ACOUSTIC EMISSION (AE) MONITORING OF BUCKLING AND FAILURE IN CARBON FIBRE COMPOSITE STRUCTURES

PhD Thesis

September 2007

Mark Eaton (MEng)

Cardiff School of Engineering
Cardiff University
Cardiff
UK

UMI Number: U585014

UMI

Dissertation Publishing

ProQuest

Declaration

This work has not previously been accepted in substance for any degree and is not currently submitted in candidature for any degree.

Signed...................................(candidate)   Date.28 - 9 - 07

Statement 1

This thesis is being submitted in partial fulfilment of the requirements for the degree of PhD

Signed...................................(candidate)   Date. 28 - 9 - 07

Statement 2

This thesis is the result of my own independent work/investigation, except where otherwise stated. Other sources are acknowledged by explicit references.

Signed...................................(candidate)   Date. 28 - 9 - 07

Statement 3

I hereby give consent for my thesis, if accepted, to be available for photocopying and for inter-library loan, and for the title and summary to be made available to outside organisations.

Signed...................................(candidate)   Date. 28 - 9 - 07

Statement 4: PREVIOUSLY APPROVED BAR ON ACCESS

I hereby give consent for my thesis, if accepted, to be available for photocopying and for inter-library loans **after expiry of a bar on access previously approved by the Graduate Development Committee.**

Signed...................................(candidate)   Date. 28 - 9 - 07

Summary:

This thesis investigates the behaviour and failure of simple aerospace type carbon fibre composite structures. The work focuses on Acoustic Emission (AE) wave propagation in composite materials, the use of advanced AE techniques to detect, characterise and locate damage and their application to the monitoring of buckling and impact failure in large-scale composite structures. The work was divided into four main areas of research:

1. Wave propagation
A thorough experimental study of AE wave propagation characteristics in anisotropic composite materials was conducted, including measurements of velocity, dispersion and attenuation behaviour. This provides the fundamental basis from which AE analysis can be confidently conducted.

2. AE source discrimination
Experiments were conducted on tensile and beam buckling coupon specimens in order to monitor the initiation and development of different source mechanisms using AE techniques. The source characterisation capabilities of signal frequency content and the Measured Amplitude Ratio of the principal plate wave modes were explored. The characterisation of source mechanisms in large-scale buckling specimens was performed using the Measured Amplitude Ratio and a novel propagation correction technique. This is a significant advance, offering more reliable source characterisation in large scale structures.

3. Large scale buckling tests
AE monitoring of large-scale buckling specimens was conducted. The work considers the detection, location and characterisation of damage throughout the test duration. DeltaT mapping, an advanced source location method, was applied to damage location in composite structures for the first time, results comparing DeltaT and time of arrival location are presented and discussed. This provided a considerable improvement to location capabilities in anisotropic materials. Additionally, the experimental results were compared with Finite Element models developed to predict the buckling behaviour of carbon fibre composite panels containing delamination. The effects of initial imperfection size and geometry were studied, providing important information to aid the design of structures prone to buckling.

4. Impact tests
Instrumented impact tests were conducted on carbon fibre panels and monitored with AE. Calculated impact and absorbed energy plus the AE parameter of absolute energy, recorded as hit and time driven data (HDD and TDD), were compared with delamination area. Absolute energy provided good correlation, with TDD offering improvement over HDD. This is the only known application of TDD AE monitoring to impact events. Furthermore, continuous waveforms were used to identify stages of damage development throughout the impact events, increasing the understanding of impact damage mechanics.

Key words: Acoustic Emission, carbon fibre composites, buckling, source characterisation, damage detection.

Acknowledgements

Glossary

Terms relating to the physical phenomenon of AE (ASTM. 1982):

Hit: A hit is the term used to indicate that a given AE channel has detected and processed an acoustic emission transient.

Event: A single AE source produces a mechanical wave that propagates in all directions in a medium. The AE wave is detected in the form of hits on one or more channels. An event therefore, is the group of AE hits that was received from a single source.

Source: A mechanical mechanism that produces AE signals.

Terms relating to the detection of the signal:

**Acoustic emission signal:** The electrical signal obtained through the detection of acoustic emission.

Noise: Signals produced by causes other than acoustic emission, or by acoustic emission sources that are not relevant to the purpose of the test.

Couplant: Substance providing an acoustic coupling between the propagation medium and the sensor.

Sensor: Device that converts the physical parameters of the wave into an electrical sensor.

Terms relating to the processing of the signal:

Threshold: The threshold is a preset voltage level, which has to be exceeded before an AE signal is detected, and processed. The following terms are made with reference to the threshold (Figure i).
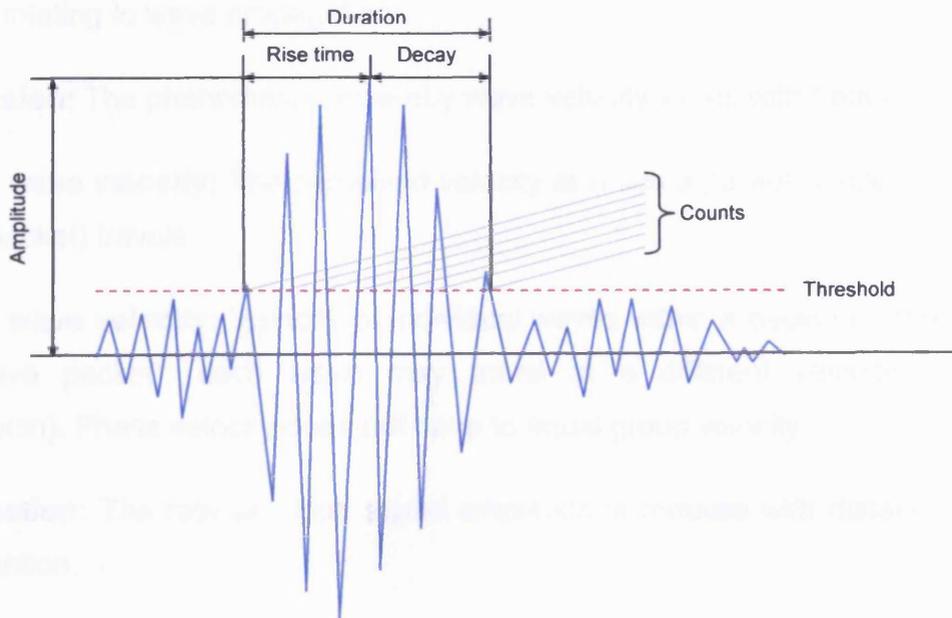
Figure i: AE Waveform features

Duration: The interval between the first and last time the threshold was exceeded by the signal.

Peak Amplitude: Maximum signal amplitude within the duration of the signal.

Counts: Number of times the signal amplitude exceeds the threshold.

Rise Time: The interval between the first threshold crossing and the maximum amplitude of the signal.

Initiation Frequency: The average frequency of the waveform from the initial threshold crossing to the peak of the AE waveform.

Energy (Absolute): The integral of the squared voltage signal divided by the reference resistance (10kOhm) over the duration of the AE waveform packet.

Time driven data: Values recorded periodically with time.

Hit driven data: Values recorded at the time of each AE hit.

Terms relating to wave propagation:

Dispersion: The phenomenon whereby wave velocity varies with frequency.

Group wave velocity: The perceived velocity at which a packet of energy (or wave packet) travels.

Phase wave velocity: Velocity of individual waves within a packet of energy (or wave packet), each wave may travel at a different velocity (see dispersion). Phase velocity does not have to equal group velocity.

Attenuation: The rate at which signal amplitude is reduces with distance of propagation.

Nomenclature

A_{ij}	Stiffness coefficients	$(N.m^{-1})$
a_i	Flexural or asymmetric wave mode	
B_{ij}	Stiffness coefficients	(N)
C_{AE}	Calculated group velocity	$(m.s^{-1})$
C_A	Asymmetric wave velocity (s_0)	$(m.s^{-1})$
C_g	Group velocity	$(m.s^{-1})$
C_p	Phase velocity	$(m.s^{-1})$
C_s	Symmetric wave velocity (a_0)	$(m.s^{-1})$
D	Bending stiffness parameter	
D_{ij}	Stiffness coefficients	$(N.m)$
d	Distance between sensor pair	(m)
d_1	Distance from source to first hit sensor	(m)
d_2	Distance from source to second hit sensor	(m)
E_{11}	Youngs modulus in material direction 1	$(N.m^{-2})$
E_{22}	Youngs modulus in material direction 2	$(N.m^{-2})$
f	Frequency	(Hz)
G_{ij}	Shear Modulus	$(N.m^{-2})$
h	Plate thickness	(m)
k_i	Mid-plane curvatures	(m^{-1})
MAR	Measured Amplitude Ratio	
M_x	Resultant in-plane moments about y-axis	$(N.m)$
M_y	Resultant in-plane moments about x-axis	$(N.m)$
M_{xy}	Resultant in-plane twisting moments about x(y)-axis	$(N.m)$
N_x	Resultant in-plane force intensity in x-direction	(N)
N_y	Resultant in-plane force intensity in y-direction	(N)

N_{xy}	Resultant in-plane shear force intensity	(N)
P_{cr}	Critical elastic buckling load	(N)
p_x	Internal body force in x direction	(N)
p_y	Internal body force in y direction	(N)
q	Lateral load	(N)
Q_x	Shear force per unit width	(N)
Q_y	Shear force per unit width	(N)
r	Radius	(m)
s_i	Extensional or symmetric wave mode	
t	Time	(s)
Δt	Time difference between arrival times at sensors	(s)
Δt^1	Difference in arrival times of s_0 and a_0 modes	(s)
u	Displacement in x direction	(m)
V_{ref}	Reference voltage at sensor	(V)
V_s	Signal voltage at sensor	(V)
v	Displacement in y direction	(m)
w	Displacement in z direction (out-of-plane)	(m)
Z	Perpendicular distance from neutral axis between two sensors to source	(m)
ε_i^0	Mid-plane strains	
λ	Wavelength	(m)
v_{ij}	Poisson ratio	
ω	Circular frequency	$(rad.s^{-1})$

Table of contents

1 Introduction

1.1 Novelty Statement

This thesis investigates the behaviour and failure of simple aerospace type carbon fibre composite structures. The work focused on Acoustic Emission (AE) wave propagation in composite materials, the use of advanced AE techniques to detect, characterise and locate damage and their application to the monitoring of buckling and impact failure in large scale structures. The novelty in the work is highlighted below:

- A thorough study of AE wave propagation characteristics in anisotropic composite materials was conducted and utilised during AE analysis in order to extract meaningful results.

- Successful discrimination between in-plane (matrix cracking, fibre failure) and out-of-plane (delamination) sources was achieved for real damage mechanisms using the Measured Amplitude Ratio (MAR) of the principal plate wave modes.

- A novel propagation correction technique was developed and used to achieve successful MAR source discrimination in large scale buckling specimens

- DeltaT mapping, an advanced source location technique, was applied to damage location in composite structures for the first time and a significant improvement was observed over the traditional time of arrival location method.

- AE monitoring of impact events on carbon fibre composites identified a relationship between impact damage size and absolute energy recorded. Data recorded as time driven data (TDD) exhibited an

improved correlation over that recorded as hit driven data (HDD). This is the only known application of TDD AE monitoring to impact events. Additionally continuous were used to identify three stages of damage development throughout the impact event.

- Full field optical measurement was conducted throughout a series of large scale instability experiments and heralded two significant results. Firstly a correlation between high levels of curvature in composite materials and AE was observed. Secondly a study of initial specimen imperfection shape on buckling performance revealed a twisted imperfection shape that provided a stiffening affect.

1.2   Background

In recent times composite materials have found widespread application in a variety of industries. Composite pressure vessels and pipelines have been used for some time in the petrochemical industry. More recently infrastructure applications, such as mobile phone masts and satellite dishes, have made use of composite materials to make cost effective and weather resistant structures. The current climate for reducing carbon emissions has lead to pressure on the aerospace and automotive industries to produce lighter and more efficient vehicles. The high specific strength and stiffness of carbon and glass fibre composite materials offer an attractive potential to manufacturers, for weight saving. This has lead to a rapid rise in the use of composite materials in both the aerospace and automotive industries, where they are increasingly used in safety critical applications. The most obvious current commercial examples are the Airbus A380, which uses 30 metric tonnes of composite material amounting to 16% of the total airframe weight (Black 2004) and the Boeing 777 for which composite materials make up 9% of the total airframe weight (Boeing 2007). Modern military aircraft utilise carbon fibre composites to an even greater extent with 25% of the SAAB JAS Gripen aircraft's airframe weight (Olson 2004) and 70% of the Eurofighter's aircraft

shell (Eurofighter 2007) consisting of carbon fibre and carbon fibre composite wing boxs and wing spars are to be used on the Airbus A400M (Airbus 2007). In light of this, it is vital that the continued integrity of composite components can be ensured during long-term service.

Many different damage mechanisms can occur in composite materials, such as matrix cracking, fibre failure and delamination, which may not be detected visually but can dramatically reduce the ultimate failure load of a component. Composite materials are also very susceptible to impact (i.e. a dropped tools, collisions, stone chips etc), which can cause large areas of internal delamination. Due to the laminar nature of continuous fibre composites, they lend themselves well to the manufacture of thin walled structures and as such are prone to failure by buckling. The presence of damage can reduce a components capacity to withstand this mode of failure, by up to 30% in the case of delamination (Abrate 1994). Thus, it is very desirable to be able to detect and characterise the development of damage in composite structures.

The Non-Destructive Testing (NDT) of composite materials is in its infancy when compared with more established materials such as steel and aluminium. The understanding of the properties and failure mechanisms of such materials is based on many years of research and experience, and there exist numerous standardised techniques for their testing and inspection. This is not the case for composite materials, where few standardised NDT methods exist and many of the established techniques for traditional materials require electrical conductivity or magnetic properties and are therefore ineffective. Ultrasound and radiography inspection have found the most successful application for the evaluation of composite materials, but there exists little guidance for the correct sizing of defects and both techniques lack the sensitivity to detect low volume defects such as matrix cracking.

Many traditional NDT techniques such as ultrasound and radiography are defined as active and require a known source input. They are commonly conducted on structures at rest and can provide information on defect size and shape within a localised area of inspection. Acoustic Emission (AE) is considered a passive technique and it differs from active techniques in that it

detects elastic waves resulting from deformation of a structure. As such it is only appropriate for use on structures under load, because a source must be active in order for it emit AE.

AE offers a number of advantages over other NDT techniques for the Structural Health Monitoring (SHM) of composite structures:-

- It has the ability to globally monitor large scale structures, detecting damage from areas that may be inaccessible to current NDT techniques.

- It provides the ability to continuously monitor structures in service or under test, allowing the direct relation of service conditions and observations with AE data.

- AE sources can be located, provided a suitable array of sensors is used to record the AE data.

- Because AE signals results from the development of damage in a structure, they potentially contain information about the source mechanism.

- It can provide an early warning of damage development, before catastrophic failure of a structure occurs.

Other online monitoring techniques, such as strain gauging, can be used for monitoring large-scale structures. However their ability to detect damage is dependant on the spacing between monitoring points. For example an area of delamination that occurs between two strain gauges is very likely to go undetected.

1.3   Acoustic Emission (AE) monitoring of composite materials

AE has been used for the monitoring of composite structures for over 20 years, with an ASTM standard for the testing of composite pressure vessels existing since 1985 (ASTM. 1989). The procedures outlined in this standard

use classical AE analysis techniques, such as the Felicity ratio (see section 2.2.3) and emission rates to determine whether damage was present in a vessel under pressure. In 1999 Lindal and Knuuttila (1999) used AE to monitor the carbon fibre composite wings and vertical stabliser of a SAAB JAS 39 Gripen combat aircraft during the static strength verification test of an almost complete airframe. They were able to detect and locate damage during the test. Rowland (2004) utilised the Felicity ratio (see section 2.2.3) to monitor damage development in carbon fibre / epoxy composite cockpits and wings structures of a Formula One car, during proof testing. Bohse (2006) presented a review of pressure tests conducted on pure composite and metallic lined composite pressure vessels containing artificially induced damage during which AE monitoring was conducted. The detection and location of damage was achieved. However, the aerospace industry has very strict pre-flight qualification tests that must be completed by any safety critical components before they can be used for in-flight service.

AE has the potential to provide in-service SHM of composite structures, to ensure their safe operation throughout a long service life. However the development of more advanced analysis techniques is required to provide more reliable and quantitative information.

1.4 Aims and objectives

The development of a complete AE based SHM system for composite structures is a vast task, that is beyond the scope of this study. Instead this work focuses on the development of advanced AE techniques for improved quantitative analysis in simple aerospace type composite structures, with a view to aiding progress towards a SHM system. Particular emphasis is given to composite structures susceptible to instability and buckling. Key objectives within this study are:-

- A thorough investigation of wave propagation in composite materials to provide a basis from which AE analysis can be confidently conducted.

- The discrimination of AE signals resulting from different composite damage mechanisms.

- The AE monitoring of impact events in carbon fibre composite materials.

- The use of Finite Element Analysis (FEA) to aid the design and understanding of a large-scale aerospace type composite instability experiments.

- Perform an initial imperfection study of the large-scale instability experiments.

- The use of AE to detect, locate and characterise damage in large-scale composite instability experiments.

1.5   Thesis organisation

This chapter outlines the requirement for improved SHM of safety critical composite structures in long-term service. The potential for AE to be used as a tool for SHM is discussed and the objectives of this research are identified.

Chapter two presents background theory and reference work. The wave propagation, source location and source characterisation of AE signals in composite structures are discussed, along with the buckling and impact response of composite materials.

Chapter three contains details of the instrumentation and experimental techniques commonly used throughout this work.

Chapter four includes an experimental investigation into the directional dependency of AE wave propagation in inhomogeneous composite materials. Additionally tensile and beam buckling coupon specimens are used to characterise signals from different damage mechanisms.

Chapter five details testing of large-scale buckling tests. Finite Element (FE) analysis is used to gain a better understanding of the material behaviour and AE monitoring is used to detect, locate and characterise damage.

Chapter six describes a series of impact tests conducted on composite plates, where AE energy recorded from the impact event is related to the area of the resulting delamination.

Chapter seven summarises the finding of this thesis and discusses potential directions for further work.

1.6 Published outputs

A total of 6 papers have been published as a result of this research:-

- Holford, K. M., Featherston, C. A., Pullin, R and Eaton, M. J. (2004) "Acoustic Emission Monitoring of Buckling Behaviour in Impact-Damaged Composite Plates". 26th International Conference on Acoustic Emission Testing, Berlin, Germany, September 15-17th, 2004, ISBN 3-931-381-58-7, pp427-434

- Eaton, M. J., Featherston, C. A., Holford, K. M. and Pullin, R. (2005) "Buckling and Postbuckling of Impact Damaged Composite Plates" SEM Annual Conference and Exposition on Experimental and Applied Mechanics, Portland, Oregon, USA, June, 2005.

- Bradshaw, T. P., Eaton, M. J., Pullin, R., Evans, S. L. and Featherston, C. A. (2006) "Determination of Damage Levels of Composite Plates After Low Velocity Impacts Using Acoustic Emission" Advanced Materials Research, Vols 13-14, 2006, ISBN-13 978-0-87849-420-0, pp253-258.

- Eaton, M. J., Holford, K. M., Featherston, C. A. and Pullin, R. (2006) "Acoustic Emission Monitoring of Defects in Buckling CFRP Composite

Panels" Advanced Materials Research, Vols 13-14, 2006, ISBN-13 978-0-87849-420-0, pp259-266.

- Eaton, M. J., Holford, K. M., Featherston, C. A. and Pullin, R. (2007) "An Investigation of Frequency as an Acoustic Emission Signal Discriminator in Carbon Fibre Composite Materials" 6th International Conference on Acoustic Emission / 50th AEWG Meeting, Lake Tahoe, NV, USA, 29th October – 2nd November, 2007. (Accepted)

- Pullin, R., Baxter, M. G., Eaton, M. J., Holford, K. M. and Evans, S. L. (2007) "Novel Acoustic Emission Source Location" 6th International Conference on Acoustic Emission / 50th AEWG Meeting, Lake Tahoe, NV, USA, 29th October – 2nd November, 2007. (Accepted)

2 Theory

2.1 Failure in composite materials

2.1.1 Buckling

To address the theory of buckling it is first necessary to introduce the concept of stability. A simple way to do so is to consider the example presented in Figure 2.1, of a sphere at rest on three different surfaces. If the sphere on the concave surface (a) is displaced from its position of equilibrium and then released it returns to its equilibrium position and hence is an example of stable equilibrium. Conversely, displacement of the sphere on the convex surface (b) causes it to roll away from its equilibrium position, demonstrating unstable equilibrium. The sphere on the flat plate is an example of neutral equilibrium, such that when the sphere is displaced and then released it remains stationary in a new equilibrium position.

Stable equilibrium without deflection exists at any load below the elastic buckling load (the critical force at which buckling of a component is induced). Once the elastic buckling load is reached and exceeded the usual case is for stable equilibrium to be reached in a deformed position, if no deformation occurs then the equilibrium is unstable (very unlikely). For symmetrical instability problems, the direction in which deformation occurs, for example in an axially loaded strut, is arbitrary and cannot be predetermined, the deformation is however of the same amplitude and mode regardless of direction. This behaviour is known as bifurcation. Once deformation has occurred a new position of equilibrium will be reached, any increases in load resulting in an increase in deformation and therefore another position of equilibrium. Figure 2.2 demonstrates the stability path followed by an axially loaded strut after deformation has occurred. The bifurcation point is quite clear at point A, where $P = P_{cr}$, as are the equilibrium paths of AE' and AE, which are both equally likely to be followed. The unstable equilibrium path (AD) that would be followed if the structure were to remain undeflected at loads above P_{cr} is also shown. In reality the elastic buckling load (P_{cr}) is unlikely to be reached without any deformation due to imperfections that exist in a structure.

Figure 2.3 demonstrates the effect of initial imperfection on the equilibrium path of an axially loaded strut. For small imperfections (ii) the elastic buckling load is reduced but as deflection increases the loads approach that of the perfect case. In the case of large imperfections (iii), considerably less load is required to achieve the same displacements. As the displacement becomes very large the load starts to approach that of the perfect case but it is likely that the effects of inelasticity will take effect before then (as shown by the dotted line DE).

For small deflections the governing differential equation for the particular case of a homogeneous thin plate (such as that examined in chapter 4) is given by Bulson (1970) in the form of Equation 2.1. The derivation of this equation from classical plate theory is included in Appendix A for completeness.

$$\frac{\partial^4 w}{\partial x^4} + 2\frac{\partial^4 w}{\partial x^2 \partial y^2} + \frac{\partial^4 w}{\partial y^4} = \frac{1}{D}\left(q + N_x \frac{\partial^2 w}{\partial x^2} + 2N_{xy} \frac{\partial^2 w}{\partial x \partial y} + N_y \frac{\partial^2 w}{\partial y^2} \right) \qquad (2.1)$$

where

w =   the transverse displacement of the mid-plane surface.

N_x, N_y, N_{xy} =   in-plane forces per unit width

q =   lateral load (0 in this case)

D = $\dfrac{Eh^3}{12(1-v^2)}$ (the bending stiffness parameter)

It is important to note the following assumptions for which this equation is valid:-

• Deflections are small.

• The middle plane of the plate does not stretch during bending.

• Plane sections rotate during bending to remain normal to the neutral surface and do not distort.

• Loads are entirely resisted by bending and twisting of the plate elements and the effects of shear forces are neglected.

- The thickness of the plate is small in comparison to other dimensions.

The analysis is greatly simplified by the assumption of small deflections but can still provide the correct elastic buckling load and differentiate between the undeformed stable and unstable conditions. However it is not possible, using this analysis, to determine the equilibrium paths after bifurcation.

For anisotropic in-homogeneous composite materials there exist complex relationships between force, momentum resultants, mid-plane strains and curvatures that must be accounted for when deriving a similar equation for the buckling behaviour of a composite plate. This is achieved using the laminate constitutive equation (Equation 2.2) the derivation of which can be found in Appendix B.

$$
\begin{pmatrix} N_x \\ N_y \\ N_{xy} \\ M_x \\ M_y \\ M_{xy} \end{pmatrix} = \begin{pmatrix} A_{11} & A_{12} & A_{16} & B_{11} & B_{12} & B_{16} \\ A_{12} & A_{22} & A_{26} & B_{12} & B_{22} & B_{26} \\ A_{16} & A_{26} & A_{66} & B_{16} & B_{26} & B_{66} \\ B_{11} & B_{12} & B_{16} & D_{11} & D_{12} & D_{16} \\ B_{12} & B_{22} & B_{26} & D_{12} & D_{22} & D_{26} \\ B_{16} & B_{26} & B_{66} & D_{16} & D_{26} & D_{66} \end{pmatrix} \begin{pmatrix} \varepsilon_x^0 \\ \varepsilon_y^0 \\ \varepsilon_{xy}^0 \\ k_x \\ k_y \\ k_{xy} \end{pmatrix}
$$

(2.2)

Where

$$ A_{ij} = \sum_{p=1}^{N} \left(z_p - z_{p-1} \right) \left(\overline{Q_{ij}} \right)_p $$

$$ B_{ij} = \sum_{p=1}^{N} \left(-\frac{1}{2} \right) \left(z_p^2 - z_{p-1}^2 \right) \left(\overline{Q_{ij}} \right)_p $$

$$ D_{ij} = \sum_{p=1}^{N} \left(\frac{1}{3} \right) \left(z_p^3 - z_{p-1}^3 \right) \left(\overline{Q_{ij}} \right)_p $$

$$\begin{pmatrix} \varepsilon_x^o \\ \varepsilon_y^o \\ \varepsilon_{xy}^o \end{pmatrix} \text{(mid-plane strains)} = \begin{pmatrix} \dfrac{du_o}{dx} \\ \dfrac{dv_o}{dy} \\ \dfrac{du_o}{dy} + \dfrac{dv_o}{dx} \end{pmatrix}$$

and

$$\begin{pmatrix} k_x \\ k_y \\ k_{xy} \end{pmatrix} \text{(mid-plane curvatures)} = \begin{pmatrix} \dfrac{d^2 w_o}{dx^2} \\ \dfrac{d^2 w_o}{dy^2} \\ \dfrac{2d^2 w_o}{dxdy} \end{pmatrix}$$

Here the (3x3) A matrix represents the in-plane strains and displacements of the mid-plane (i.e. stretching), the (3x3) D matrix represents the curvature and bending of the mid-plane and the (3x3) B matrices represent the coupling between bending and stretching of the mid-plane during transverse displacement. The coefficients A_{16}, A_{26}, B_{16}, B_{26}, D_{16} and D_{26} indicate extension-shear and/or bending-twisting coupling during plate deformation. This coupling vanishes for cross-ply lay-ups (Turvey and Marshal 1995).

For a symmetrical laminate in which the B_{ij} coefficients are zero and an equivalent governing differential equation for a thin symmetrical composite plate can be derived (Appendix C) (Turvey and Marshal 1995).

$$D_{11}\frac{\partial^4 w}{\partial x^4} + 4D_{16}\frac{\partial^4 w}{\partial x^3 \partial y} + 2(D_{12} + 2D_{66})\frac{\partial^4 w}{\partial x^2 \partial y^2} + 4D_{26}\frac{\partial^4 w}{\partial x \partial y^3} + D_{22}\frac{\partial^4 w}{\partial y^4}$$

$$= N_x\frac{\partial^2 w}{\partial x^2} + 2N_{xy}\frac{\partial^2 w}{\partial x \partial y} + N_y\frac{\partial^2 w}{\partial y^2} \tag{2.3}$$

In most cases there are no "exact" solutions to Equation 2.3 and solution requires approximation using numerical techniques. However, for a specially

orthotropic laminate subject to a uni-axial in-plane compression with all edges simply supported an "exact" closed form solution can be determined (Loughlan 2000). In this specific case $D_{16} = D_{26} = 0$ (due to the cross-ply lay-up) and $N_y = N_{xy} = 0$, and Equation 2.3 becomes

$$D_{11}\frac{\partial^4 w}{\partial x^4} + D_0 \frac{\partial^4 w}{\partial^2 x \partial^2 y} + D_{22}\frac{\partial^4 w}{\partial^4 y} = N_x \frac{\partial^2 w}{\partial x^2} \qquad (2.4)$$

where

$$D_0 = 2(D_{12} + 2D_{66})$$

The simple support conditions on all four edges mean that the transverse displacements and moments along the edges are all zero:

At $x = 0$ and a, $w = M_x = 0$

At $y = 0$ and b, $w = M_y = 0$ (2.5)

From the laminate constitutive equation, and because $D_{16} = D_{26} = 0$ the resultant in-plane moments about the y and x axis are

$$M_x = D_{11}k_x + D_{12}k_y$$

$$M_y = D_{12}k_x + D_{22}k_y \qquad (2.6)$$

Substituting for the mid-plane curvatures k_x and k_y, gives

$$M_x = D_{11}\frac{\partial^2 w}{\partial x^2} + D_{12}\frac{\partial^2 w}{\partial y^2}$$

$$M_y = D_{12}\frac{\partial^2 w}{\partial x^2} + D_{22}\frac{\partial^2 w}{\partial y^2} \qquad (2.7)$$

Using a double trigonometric series to represent the mid-plane transverse displacement surface of the plate, such that it satisfies the boundary conditions of Equations 2.5 and thus Equations 2.7 become zero at $x=0$ and a and $y=0$ and b

$$w = A_{mn} \sin \frac{m\pi x}{a} \sin \frac{n\pi y}{b} \tag{2.8}$$

where m and n are integers, and m represents a half-range sine expansion in the x-direction, and n represents a half-range sine expansion in the y-direction.

Substituting for w in Equation 2.4

$$A_{mn} \pi^2 \left[D_{11} \left(\frac{m}{a} \right)^4 + D_0 \left(\frac{m}{a} \right)^2 \left(\frac{n}{b} \right)^2 + D_{22} \left(\frac{n}{b} \right)^4 \right] = -A_{mn} N_x \left(\frac{m}{a} \right)^2 \tag{2.9}$$

As the trivial solution of $A_{mn} = 0$ is not relevant, a value of N_x is required to satisfy the equation

$$N_x = \frac{-\pi^2 \left[D_{11} \left(\frac{m}{a} \right)^4 + D_0 \left(\frac{m}{a} \right)^2 \left(\frac{n}{b} \right)^2 + D_{22} \left(\frac{n}{b} \right)^4 \right]}{\left(\frac{m}{a} \right)^2} \tag{2.10}$$

from which

$$N_x = -\pi^2 \left[D_{11} \left(\frac{m}{a} \right)^2 + D_0 \left(\frac{n}{b} \right)^2 + D_{22} \frac{\left(\frac{n}{b} \right)^4}{\left(\frac{m}{a} \right)^2} \right] \tag{2.11}$$

It can be seen from Equation 2.11 the the value of N_x required to cause initial buckling of the plate depends on the plate bending stiffness D_{ij}; plate dimensions a, b; m and n values. Now, the lowest value of N_x occurs when n = 1, as n only appears in the numerator. However, m appears in the

numerator and denominator and N_x will have to be computed for varying m, $\dfrac{a}{b}$

and D_{ij}. Thus Equation 2.11 becomes

$$N_x = -\pi^2 \left[D_{11}\left(\frac{m}{a}\right)^2 + D_0\left(\frac{1}{b}\right)^2 + D_{22}\frac{\left(\frac{1}{b}\right)^4}{\left(\frac{m}{a}\right)^2} \right] \tag{2.12}$$

the minimum value of N_x for a particular value of m occurs when

$$\frac{\partial N_x}{\partial\left(\frac{m}{a}\right)} = 0 \tag{2.13}$$

i.e.

$$2D_{11}\left(\frac{m}{a}\right) - 2D_{22}\frac{\left(\frac{1}{b}\right)^4}{\left(\frac{m}{a}\right)^3} = 0 \tag{2.14}$$

or

$$\frac{a}{b} = m\sqrt[4]{\frac{D_{11}}{D_{22}}} \tag{2.15}$$

Hence the minimum value of N_x is obtained by substituting the $\dfrac{a}{b}$ expression

from equation 2.15 into equation 2.12, this gives

$$\left(N_x\right)_{\min} = \frac{-\pi}{b^2}\left[2\sqrt{D_{11}D_{22}} + D_0\right] \tag{2.16}$$

2.1.2   Impact

Foreign object impact events are usually classified as being either low velocity or high velocity. Abrate (1991) defines a high velocity impact as having a velocity so great that the deformation of the structure, during the duration of contact, is localised to a small area surrounding the contact point. Low

velocity impact refers to situations where, during the contact duration, the entire structure deforms as waves propagate to the boundary and are reflected back several times. A velocity of less than $100m.s^{-1}$ is suggested as a low velocity impact. More generally Cantwell and Morton (1989) suggest the dividing line for low and high velocity impact lies between drop weight impactor and high powered ballistic gas guns, respectively. Low velocity impacts are of most interest because they are more likely to induce internal damage that is not detected by surface inspection.

Abrate (1991; 1994) and Cantwell and Morton (1989) identified two scenarios of damage development due to impact in continuous fibre composite materials. The first is damage initiation due to bending (Figure 2.4a), which generates high tensile stresses in the plies at the opposite surface to the impact site. This results in matrix cracking through the outer-most ply, parallel to the axis of the fibres, which is deflected at the first interface to form a delamination. The delamination is then in turn deflected by further matrix cracking in the adjacent plies as the process continues. This scenario is most common in thinner and more flexible materials. In the second scenario, damage initiates at the impacted surface due to local shear stresses created by contact with the impactor (Figure 2.4b). Upon impact, a strip of the surface ply shears parallel to the fibre orientation, inducing a shear load on the ply below, resulting in delamination at the first interface and the shearing of a strip in the second ply as the process continues. Damage development of this type is commonly observed in thicker, stiffer specimens and from high velocity impact events.

Cantwell and Morton (1989) identified an approximately linear relationship between impact energy (i.e. potential energy of the impactor) and the resulting delamination area in $(\pm45)_{8s}$ carbon fibre / epoxy plates of 2mm thickness (Figure 2.5). The plates were impacted at the centre of a 130mm diameter circular unsupported area by a 6mm diameter hemi-sperical impactor. Other researchers to report a linear relationship between impact energy and delamination area in carbon fibre composites are Hong and Liu (1989), Abrate (1991; 1994) and Davies and Zhang (1995). Cantwell and Morton (1991) also

showed that the greater the angle between adjacent plies the less impact energy is required to induce damage.

The application of AE monitoring to impact events in carbon fibre / epoxy composites was investigated by Liu et al (1999), who correlated AE energy (recorded as hit driven data) with impact damage area. Using quasi-isotropic specimens of 2 and 3.8mm thickness, varied success was shown when correlating AE energy to the impact events of 2-15J in energy. Okafor et al (2001) showed an increase in AE energy (recorded as hit driven data) with increased impact energy of high velocity ballistic impacts, although a linear relationship was not observed. The impact energy is directly linked to the resulting damage size and therefore indicates a relationship between AE energy and damage size.

2.2 Acoustic emission

2.2.1 Background

Acoustic emission is defined as the elastic energy that is spontaneously released by a material when it undergoes deformation (Miller and McIntire 1987). The release of elastic energy occurs within a material under stress, in areas of plastic deformation or crack growth. These transient elastic waves propagate to and along the material's surface where the resulting surface deformations can be detected by piezoelectric transducers. AE refers to signals existing within the frequency range of approximately 10 kHz to 1 MHz, however it is more common for signals to be within the range of 100kHz to 300kHz (Miller and McIntire 1987). Figure 2.6 and Figure 2.7 demonstrate the AE principle and the AE monitoring process chain. The recorded observations of AE in the form of "tin cry" are referenced by Drouillard (1996) and date back to the 8th century. The advent of modern AE technology began in 1950 with the work of Josef Kaiser, who most notably demonstrated the AE behaviour of irreversible plastic strain. The advent of modern computing with ever increasing acquisition rates and processing power has enabled researchers to deal with the high data rates required for AE testing, including the capture of full waveforms which has lead to a much deeper understanding of AE wave propagation.

Many traditional methods of NDT used in composites, such as ultrasound and radiography, are defined as active techniques because they require a known input source. Active NDT methods are commonly conducted on materials and structures at rest. AE is classed as a passive technique and it differs from the more traditional active NDT methods in that it detects elastic waves released from the structure itself during deformation. As such the use of AE requires the material to be under load in order for a source to be active and therefore detected. Unstressed defects will not emit AE and will therefore not be detected.

2.2.2 AE source mechanisms in composite materials

AE sources produce one of two types of signal, continuous and transient. The following definitions of continuous and transient AE signals are described by Vallen (2002). Continuous AE signals display amplitude and frequency variations but effectively the signal never ends. Sources of continuous AE include friction and flow or leakage noise. Transient (or burst signals) are discrete signals having a start and end point where the signal deviates from and returns to the level of background noise. Commonly transient signals are of more use for structural testing, originating from sources such as fractures and crack growth. Figure 2.8 shows an example of both transient and continuous AE signals. Miller and McIntire (1987) and PAC (2006a) list the common sources of AE in continuous fibre composite materials as:

- Fibre failure
- Fibre pullout
- Fibre / matrix debonding
- Matrix micro cracking
- Transverse matrix cracking
- Splitting parallel to fibres
- Delamination.

It is also noted in PAC (2006a) that complex combinations of source mechanism can occur, i.e. fibre failure with fibre pullout or simultaneous fibre and matrix failure.

2.2.3 Kaiser and Felicity effects

Dr Hans Maria Tensi established the Kaiser effect in the 1960s (Tensi 1961), based on the work by Dr Josef Kaiser (Kaiser 1950). The effect is characterised by the lack of AE activity from a material at a load to which it has already been exposed, such that when a material is unloaded and reloaded significant emission is not observed until the previous maximum load is reached. This is commonly identified on a plot of load versus cumulative AE (i.e. hits, counts or energy) (Figure 2.9a). At a certain load the Kaiser effect breaks down and significant AE activity is observed before the previous maximum load is reached, known as the Felicity effect (Figure 2.9b). This is an indication that major damage has been induced during a previous loading cycle.

In practice, materials and their structures are rarely simple enough to utilise the Kaiser effect, which is often the case for composite materials. However the Felicity effect can still provide a measure of a structure's integrity and is quantified by the use of the Felicity ratio (previous maximum load/load at which significant AE activity restarts). Both the Kaiser effect and the Felicity effect are discussed as standard test procedures in Miller and McIntire (1987).

2.2.4 Wave propagation

The propagation of acoustic waves in a solid media is a complex problem that is discussed in detail by Pollock (1986), Rindorf (1981) and Gorman and Prosser (1991). The following is a summary of the major points.

- In an infinite medium elastic waves propagate in two forms, transverse (particle motion perpendicular to propagation direction) and longitudinal (particle motion consists of localised compression and rarefraction parallel to the propagation direction) (Figure 2.10).

- If a boundary is introduced, such as a surface, the longitudinal and transverse waves combine in a region close to the surface to form what is termed a Rayleigh wave (Figure 2.11).

- In a medium bounded by two surfaces, i.e. a plate, the bulk waves couple at the surfaces to produce two surface modes, the symmetric or extensional (s_0) mode and the asymmetric or flexural (a_0) mode shown in Figure 2.12. These are known as Lamb waves.

- Given the correct geometric constraints it is possible for higher order extensional (s_0) and flexural (a_0) modes to be supported. However in general the amplitude of the modes is considerably less than that of the principal modes and therefore their use in AE monitoring is somewhat limited.

Due to the laminar nature of composite materials, they lend themselves well to the manufacture of thin walled structures and components, such as pipes and pressure vessels or aircraft wings and fuselages. As such it is the propagation of Lamb waves that is of most significance for this work.

2.2.5   Velocity and dispersion

The characteristics of Lamb waves are discussed thoroughly by Pollock (1986), Rindorf (1981) and Gorman (1990a); the following is a brief summation of the relevant points.

The propagation of Lamb wave modes is described by dispersion curves which show how velocity varies with frequency, an example of which is presented in Figure 2.13 (generated using commercially available, DISPERSE software, see section 3.1.5) for a 2.15mm thick cross-ply laminate. At low frequencies, the s_0 mode travels at a high velocity determined by the in-plane stiffness of the plate under static tension, whereas the a_0 mode is slow and highly dispersive, because the velocity is determined by the flexural stiffness of the plate (which is low) and depends strongly on thickness. It is very important when interpreting AE signals to be aware of and fully understand the effects of propagation. This is of particular importance when considering wave propagation in anisotropic materials such as composites, where the

material properties and therefore the propagation characteristics vary with direction.

The propagation of guided waves is a complex problem and one that becomes increasingly complicated in anisotropic media. Rose (1999) discusses the additional complexities that arise in anisotropic materials. A single frequency wave propagating in a given elastic media, without deformation, has a given velocity known as the phase velocity.

$$C_p = f\lambda \qquad \text{(2.17)}$$

and is directly linked to the wave number, thus

$$k = \frac{\omega}{C_p} \qquad \text{(2.18)}$$

where

C_p = Phase velocity $\qquad\qquad$ k = Wave number

f = Frequency $\qquad\qquad$ λ = Wavelength

ω = Circular frequency

When a group of waves of different but similar frequencies propagate in a given elastic media, superposition results in a modulated signal envelope which commonly propagates at a lower velocity, known as the group velocity (Figure 2.14). The group velocity is the velocity at which the energy of a signal travels and also shows variation with frequency.

$$C_g = \frac{d\omega}{dk} \qquad \text{(2.19)}$$

The group velocity is the propagation behaviour observed in AE signals, and is commonly the form in which dispersion curves are presented (Figure 2.13). The propagation vector of the phase and group velocities is in the same direction in homogeneous media or when propagating parallel to the fibre direction in anisotropic composite materials. However in bulk anisotropic

media Rose (1999) shows that propagation away from the fibre direction results in a beam-skewing phenomenon where the group velocity vector is no longer parallel to the phase velocity vector. Neau et al (2001), Lowe et al (2004), and Wang and Yuan (2007) show that this is also the case for elastic waves propagating in anisotropic composite plates. Lowe et al (2004) show that the direction of the group velocity vector is normal to the phase velocity slowness curve (a polar plot at a given frequency of inverse phase velocity versus direction of propagation); Figure 2.15 presents an example of this. The theoretical calculations of dispersion behaviour are performed in the frequency-wavenumber space (Pavlakovic and Lowe 2003) and provide a correct representation of the phase velocity dispersion behaviour, however a direct calculation of the group velocity dispersion behaviour using Equation 2.19 is not possible. Jeong and Jang (2000) and Wang and Yuan (2007) showed that it is possible to correct for the difference in phase and group velocity vectors when calculating the group velocity dispersion behaviour and both observed good agreement with experimental results. However, the process is numerically very involved and deemed to be outside of the scope of this study.

Prosser (1991) used time of arrival measurement of the s_0 mode to calculate velocity in a $((0,90)_4)_s$ carbon fibre / epoxy plate of 2.26mm thickness. Velocities of 6550, 5020 and 6450m.s^{-1} were calculated for s_0 mode propagation in the $0°$, $45°$ and $90°$ directions, highlighting the effect of the anisotropy of composite materials on propagation. Prosser (1991) also used a Fourier phase spectra technique to investigate the dispersion of the a_0 mode at low frequencies (below 160kHz). The results showed little change in the dispersion behaviour between propagation in the $0°$, $45°$ and $90°$ directions in the same $((0,90)_4)_s$ carbon fibre / epoxy plate. The maximum velocity of the a_0 mode measured in all three directions was approximately 1250m.s^{-1}; as mentioned above it is the plate thickness that has a dominant effect on the a_0 mode and as such this result is expected.

Prosser et al (1997) and Prosser and Seale (1999) later showed how the Pseudo Wigner-Ville Distribution (PWVD) can be effectively used to measure

the group velocity dispersion of Lamb wave modes in carbon fibre / epoxy composites. The PWVD decomposes an AE waveform into a time-frequency distribution and for a given mode of propagation the frequency-dependant arrival times will appear as peaks in magnitude within the distribution. The peaks in magnitude of the time-frequency distribution can therefore provide an indication of the group velocities contained within a particular mode of propagation.

Further success using time-frequency analysis to measure dispersion of AE waves was shown by Jeong and Jang (2000) and Jeong (2001), who used the Gabor wavelet transform to decompose AE signals into a time-frequency distribution. More recently Lanaza di Scalea and McNamara (2004) successfully used the Gabor wavelet transform to measure the dispersion of wave modes in steel railroad tracks. Wang and Yuan (2007) also used the Gabor wavelet transform to measure the dispersion behaviour of Lamb wave modes in carbon fibre / epoxy laminates, showing good correlation between theoretical and measured dispersion. Additionally Pullin et al (2006) used very narrow band-pass frequency filtered waveforms to measure the arrival times of different frequency components in Lamb modes for a steel plate.

2.2.6 Attenuation

Attenuation is the reduction of signal amplitude with propagation distance and is another important part of wave propagation that must be understood before undertaking any AE signal analysis. Four main causes of attenuation are identified by Pollock (1986) and are detailed below.

Geometric spreading – A wave generated by a point source has a finite amount of energy that must be distributed over a larger and larger wavefront in-order for it to propagate. In two-dimensional plate-like structures the reduction in amplitude is inversely proportional to the square root of propagation distance, making it the usual dominant mode of attenuation in the near field.

Internal friction – Is the degradation of elastic wave energy into heat through a variety of material-dependant mechanisms, also known as damping or

absorption. The effects of internal friction are typically much greater in non-metals such as composite materials, than that of metals. Losses due to internal friction in composite materials can be associated with such mechanisms as viscoelastic material behaviour, friction between surfaces that slip and incompletely bonded fibres. The amplitude reduces exponentially with distance and losses significantly increase with frequency. Consequently, attenuation in the far field is usually dominated by internal friction.

Wave dispersion – As discussed in section 2.2.5, dispersion will cause a short pulse to spread out as it propagates, thus losing amplitude accordingly. The rate of attenuation due to dispersion is dependant on the bandwidth and gradient of the dispersion curve for a given scenario.

Dissipation into adjacent media – This effect relates to the absorption of energy into adjacent media. It is however of little relevance to this work and so is not discussed in any detail.

An investigation into the attenuation of the two principal Lamb wave modes in quasi-isotropic carbon fibre / epoxy composites was conducted by Prosser (1996). The average attenuation in the $0°$, $45°$ and $90°$ propagation directions for a 1.2mm (8 ply) thick plate was shown to be $42dB.m^{-1}$ for the s_0 mode and $83dB.m^{-1}$ for the a_0 mode. The unexpectedly high attenuation rate of the a_0 mode, which is predominantly low frequency, was attributed to wave dispersion. In a 3.7mm (24ply) thick plate the average attenuation values for the three material directions were $35dB.m^{-1}$ for the s_0 mode and $51dB.m^{-1}$ for the a_0 mode.

2.3   Source location

Source location is one of the most attractive features of AE as an inspection technique. The most commonly used source location method is the "time of arrival" (TOA) technique, which is an integral part of all commercially available AE software. Other source location techniques discussed are "Single Sensor Modal Analysis Location" (SSMAL) and the recently developed "DeltaT" mapping technique.

2.3.1 Time of arrival (TOA)

A thorough explanation of the time of arrival location methodology can be found in Miller and McIntire (1987) and Rindorf (1981).

The simplest way to introduce the methodology of TOA location is to consider the one-dimensional location of a source in the beam in Figure 2.16, which is instrumented with three sensors. The most basic way to locate a source in the beam is a zonal location, which considers the order in which the sensors are hit. If, as in Figure 2.16a, sensor 2 is the first sensor hit then the area of location ranges from the mid point of sensors 1 and 2 to the mid point of sensors 2 and 3. The area of location maybe refined by considering the second sensor hit. If sensor 1 is the second sensor hit, the area of location is between sensor 2 and the mid point of sensors 1 and 2 (Figure 2.16b).

More accurate source location is achieved if both the hit sequence and the difference in arrival time between hits are known (Figure 2.16c). If as above sensor 2 is hit first followed by sensor 1 then the time difference between hits is equal to:

$$\Delta t = \frac{d_2 - d_1}{C_{AE}}$$

(2.20)

Where:

C_{AE} = Calculated wave speed

Δt = The time difference between hits

d_1 = Distance from source to first hit sensor

d_2 = Distance from source to second hit sensor

This is more commonly expressed in terms d_1

$$d_1 = \frac{D - \Delta t . C_{AE}}{2}$$

(2.21)

where D is the total distance between sensors. An event occurring outside the array (Figure 2.16d) will record a time difference equal to the time of flight (i.e. the time taken for the signal to travel from one sensor to the next) between the outer pair of sensors and the hit sequence will remain the same.

The same approach can be expanded to location in two-dimensions. Figure 2.17 considers two sensors mounted a distance of D apart on an infinite plate. If the stress wave from an event is assumed to propagate at a constant velocity in all directions, then it can be shown that

$$\Delta t C_{AE} = d_2 - d_1 \tag{2.22}$$

and

$$Z = d_1 \sin \theta_{TOA} \tag{2.23}$$

$$Z^2 = d_2^2 - (d - d_1 \cos \theta_{TOA})^2 \tag{2.24}$$

then

$$d_1^{\ 2} \sin^2 \theta_{TOA} = d_2^2 - (d - d_1 \cos \theta_{TOA})^2 \tag{2.25}$$

$$d_1^{\ 2} = d_2^2 - d^2 + 2d.d_1 \cos \theta_{TOA} \tag{2.26}$$

Substituting $r_1 = \Delta t C_{AE} + R$ from Equation 2.19 into Equation 2.23 gives

$$d_1 = \left(\frac{1}{2}\right)\left(\frac{\left(d^2 - \Delta t^2 C_{AE}^2\right)}{\left(\Delta t C_{AE} + d \cos \theta\right)}\right) \tag{2.27}$$

This is the equation for a hyperbola upon which, for a given hit sequence and time difference, the location of the source will sit. It is not possible to locate with any more accuracy, when using two sensors in two dimensions. However the accuracy can be improved by the addition of a third sensor (Figure 2.18), which effectively creates three pairs of sensors 1-2, 1-3 and 2-3. The intersection point of the three resulting hyperbola provides a more accurate two-dimensional location. The addition of further sensors increases the number of hyperbola and therefore the accuracy and confidence of location.

2.3.2   Sources of error in TOA location

A thorough investigation into the potential sources of error in TOA location techniques is presented by both Miller and McIntire (1987) and Rindorf (1981). The two most likely sources of error associated with TOA are identified by Holford (2000) as:

- Premature triggering of the timing measurement by a low amplitude extensional pre-cursor

- Dispersion of the flexural mode. The effects of dispersion can cause the arrival timing to be triggered on different phase points of the signal by different sensors. Furthermore the attenuation of higher frequency components can cause erroneous triggering from lower velocity, lower frequency components

It was observed during this research, however, that in composite materials the extensional mode amplitude is commonly above the threshold level and therefore consistently triggered the timing measurement.

Other sources of error include:

- Differing signal propagation paths due to inhomogeneity and structural complexity – This is a particular problem in composite materials due to their anisotropic nature

- Inaccurate sensor location

- Inaccurate calculation of wave velocity

2.3.3   Single Sensor Modal Analysis Location (SSMAL)

Single Sensor Modal Analysis Location (SSMAL) offers an alternative to the more conventional TOA location by exploiting the dispersive nature of Lamb waves to the practitioner's advantage. As such the approach is only appropriate for use in plate-like structures and over propagation distances

great enough to allow the development of plate waves. If a wave is detected in an appropriate manner with a suitably broadband sensor, separation of the different mode components can be observed (Figure 2.19). By determining the arrival times of particular mode components, the source to sensor distance can be calculated by equation 2.25 using the temporal separation (Holford and Carter1999).

$$d_1 = \Delta t^1 \left(\frac{C_S C_A}{C_S - C_A} \right)$$

(2.28)

where d_1 = source to senor distance

C_s = extensional (symmetric) group velocity (s_0)

C_A = flexural (asymmetric) group velocity (a_0)

A comprehensive review of studies into SSMAL is presented by Pullin (2001). Work by Maji and Setpathi (1995), Dunegan (1997) and Holford and Carter (1999) used SSMAL to successfully locate H-N sources. Additionally Surgeon and Wevers (1999b) determined the extensional and flexural mode arrival times of signals from CFRP tensile and bending tests. The measured arrival times were in good agreement with those calculated using classical plate theory.

2.3.4   DeltaT location

As discussed above, two of the major assumptions made for TOA location and SSMAL are a constant wave velocity and a direct wave path between the source and sensor. It is know that due to their inhomogeneity, wave velocities in composite materials exhibit a directional dependency, thus creating an inherent inaccuracy in location.

To overcome the location problems created by complex structures and inhomogeneous materials a novel method of source location was developed, where an AE location array is mapped with an H-N source at known positions. A detailed description of the "DeltaT" mapping technique can be found in Baxter (2007), who showed an improvement over TOA location of over 50% in

complex structures. Improved location using the "DeltaT" Technique has also been shown by Pullin et al (2007a; 2007b). The following is an overview of the processes five steps:

- **Determine area of interest** - Delta-T source location can provide complete coverage of a part or structure or it can be employed as a tool to improve source location around specific areas of expected fracture, which could be identified via finite element modelling.

- **Construct a Map System** - A grid is placed over the entire component or a specific area of interest within which AE events will be located; the higher the resolution of the grid the greater the accuracy. The grid resolution can be increased around features of interest but should not be smaller than one wavelength, this being the minimum location resolution possible. It should be noted that sources are located with reference to the grid and not the sensors and it is not required that sensors be placed within the grid.

- **Obtain time of arrival data from an artificial source** – An artificial source (nominally a H-N source) is conducted at the nodes of the grid to provide AE data for each sensor. The artificial source is performed several times at each node to provide an average result and to eliminate any erroneous data. It is not essential to have AE data from every node in the grid because missing data points can be interpolated from surrounding nodes.

- **Calculate DeltaT map** – Each artificial source results in a difference in arrival time or DeltaT for each sensor pair (an array of four sensors has six sensor pairs). The average DeltaT at each node is stored in a map

for each sensor pair. The resulting maps can be visualised as contours of constant DeltaT, such as that shown in Figure 2.20 for a steel plate containing numerous holes.

- **Locating real AE data** – The DeltaT values from a real AE event are calculated for each sensor pair. A line of constant DeltaT equivalent to that of the real AE event can then be identified on the map of each sensor. By overlaying the resulting contours, a convergence point can be found that indicates the source location. As with time of arrival, a minimum of three sensors is required to provide a point location and more sensors will improve the location. In theory all the lines should intersect at one location, however in practice this is not the case. Thus in order to estimate a location all convergence points are calculated and a cluster analysis provides the most likely location.

2.4   Source characterisation

In general the characterisation of acoustic emission signals is approached in one of 2 ways. The first is to examine changes in the relationships between different AE feature data values (e.g amplitude, duration, etc) using cross-correlation plots. These changes must then be related to the observed damage during a test. The second approach is the consideration of digitally stored AE waveforms.

2.4.1   Frequency distribution

The frequency content of recorded AE waveforms has been suggested by many as an effective method for signal characterisation. Suzuki et al (1996) showed how the source relaxation time varies for different failure modes in glass fibre / epoxy composites. It is thought that the differing source relaxation times will promote AE signals with differing frequency content. It is worth noting, however, that the specimen material, wave propagation path and the sensor will all have an effect on the recorded signal.

Bohse (2000) recorded signals from pure epoxy and single fibre tensile specimens using a PAL WD sensor. Analysis of these signals using Fast Fourier Transforms (FFTs) suggested that matrix cracks produced signals with 70% of their signal power below 350kHz and fibre failures produced signals with 70% of the signal power above 350kHz. Ramirez-Jimenez et al (2004) also used a PAL WD sensor to record signals from glass fibre / polypropylene tensile specimens with $(90)_8$, $(0)_8$, $(\pm45)_{2s}$ and $(0,90)_{2s}$ lay-ups. The peak frequency of the FFT of a signal was used to discriminate between damage modes; the identified frequency bands are shown in Table 2.1. Also using peak frequency to discriminate between damage modes de Groot et al (1995) recorded signals, using a PAL WD sensor, from carbon fibre / epoxy tensile specimens with $(0)_8$, $(10)_{16}$, $(90)_{32}$ lay-ups and pure epoxy. Additionally a double cantilever beam (DCB) test was also performed to promote delamination. The results are summarised in Table 2.1.

2.4.2   Modal analysis

Modal analysis of acoustic emission signals is the consideration of the digitised and stored waveforms, specifically the identification and interpretation of the s_0 and a_0 plate wave modes.

Plate waves were observed by Pollock (1986) in large spherical tanks of 35mm thickness, where both modes were identified. A more in-depth study of plate waves in thin aluminium and composite plates was undertaken by Gorman (1990a) where H-N sources performed on the surface and end of the plates were shown to produce larger a_0 and s_0 modes respectively. Further to this Gorman and Prosser (1991) and Prosser (1991) showed how the amplitude of the s_0 mode reduced and the amplitude of the a_0 mode increased as the source orientation changed from $0°$ to $30°$, $60°$ and $90°$, with respect to the plane of the plate.

Gorman and Ziola (1990b), Prosser et al (1995) and Prosser (1996) showed that in-plane matrix cracks occurring in carbon fibre / epoxy tensile specimens produce signals with dominant s_0 modes. Modal analysis of signals from carbon fibre / epoxy specimens with $(0,90_3)_s$, $(0_2,90_2)_s$ and (0_8) lay-ups loaded under tension and 3 point bending was conducted by Surgeon and Wevers

(1999a). Signals recorded from matrix cracking and fibre failure in tensile specimens were shown to have dominant s_0 modes and fibre failure during a 3 point bend test produced signals with dominant a_0 modes. The ratio of the s_0 mode amplitude over the a_0 mode amplitude was considered and it was found that matrix cracking under tension produced signals with a ratio of 2.5, whereas fibre failure under bending produced signals with a ratio of 0.51. The ratio of the plate mode amplitudes (s_0/a_0) was used to calculate the Measured Amplitude Ratio (MAR) by Carter (2000), which provided successful discrimination between H-N sources of different orientations in a steel I-beam. Pullin et al (2005) also used the MAR of signals to investigate the orientation of fatigue crack sources in aerospace grade steel.

It has been suggested by Carter (2000), Prosser (1991; 1996), Prosser et al (Prosser 1995) and Gorman (1990a) that sources in the plane of the plate occurring asymmetric to the centre line will produce signals with an increased a_0 mode. Johnson and Gudmundson (2001) and Johnson (2003) utilised an opposed sensor arrangement to aid the identification of plate wave modes in signals from matrix cracking in $(0_2,90_3)_s$ and $(90_2,0_3)_s$ carbon fibre / epoxy tensile specimens. It was shown that matrix cracks occurring in the mid-ply of the $(0_2,90_3)_s$ specimens produced signals with very little a_0 mode; whereas signals from asymmetric matrix cracking in the $(90_2,0_3)_s$ specimens produced signals with a considerably larger a_0 mode. This may go some way to explaining the discrepancy between the amplitude ratios measured for a matrix crack and a fibre breakage by Surgeon and Wevers (1999a), both of which are in-plane sources. The fibre breakage was induced under bending and as such is likely to be at or close to the surface of the specimen, creating a larger a_0 mode and reducing the amplitude ratio.

Gorman (1990a), Gorman and Prosser (1991) and Prosser (1991) showed that artificial sources at $90°$ to the plane of a plate produce signals with a dominant a_0 mode. This would suggest that source mechanisms with out-of-plane particle motion, such as delamination will produce similar signals. However this has as yet not been shown to be true for real AE signals from delamination sources.

2.5 Summary

It has been shown that an "exact" closed form solution of the governing buckling equation can be found for the case of a simply supported square composite plate with a specially orthotropic and symmetric lay-up, subject to a uni-axial in-plane compressive load. Because this simplifies the mathematical analysis and modelling of a buckling experiment it was decided that a (0,90) symmetric lay-up will be used for this work and large scale instability tests would be conducted on simply supported square plates.

The propagation of AE signals in composite materials is very complex, hence it is essential that the propagation characteristics are thoroughly understood for a specific material and lay-up in order to perform any meaningful analysis. The directionally dependency of the propagation velocity observed will have a detrimental effect on the calculated location of events using the traditional TOA method. For this reason it was proposed that the DeltaT location methodology be investigated for use in composite materials.

Both peak frequency content and the MAR of AE signals have been used by previous researchers to discriminate between signals from different damage mechanisms in composite materials. Signals with low frequency peaks (i.e. <150kHz) have been attribute to matrix cracking and signals with high frequency peaks (>350kHz) have been attributed to fibre failure. Modal analysis of signals from artificial H-N sources (see section 3.1.3) identified signals with a dominant s_0 mode to be from in-plane sources (such as matrix cracking) and signals with a dominant a_0 mode to be from out-of-plane source (such as delamination). This effect has been confirmed for real in-plane matrix cracking sources, but as far as the author is aware, has not been confirmed for real delamination sources. The previous investigations into signal discrimination using both frequency content and MAR have been performed in small specimens and propagation effects have not been considered. Both Frequency content and MAR were selected for further investigation and assessment of their robustness in application to large scale composite structures.

A strong correlation been between impact energy (potential) and damage area has been shown. Additionally a small number of researchers have indicated a link between AE energy, recorded as hit driven data, and impact damage area. It was decided that an investigation of the correlation between AE energy and impact damage area would be undertaken. Time driven data and continuous wave streaming were identified as helpful tools to aid the investigation.

Table 2.1 - Summation of Frequency Results

	Material	Matrix	Fibre	Debond	Pull-out	Delamination (DCB)
de Groot et al	Carbon / Epoxy	90-180kHz	Above 350kHz	240-310kHz	180-240kHz	90-180kHz
Bohse	Glass / Polyprop	70% below 350kHz	70% above 350kHz	< 70% above or below 350kHz	-	-
Ramirez-Jimenez et al	Glass / Polyprop	-	420-500kHz	~100kHz	200-300kHz	-
Russell and Henneke (from (de Groot 1995))	Graphite / Epoxy	50-150kHz	140-180kHz	-	-	-
Suzuki et al (from (de Groot 1995))	Glass / Polyester	30-150kHz	300-400kHz	-	180-290kHz	-
Suzuki et al (from (de Groot 1995))	Glass / PET	80-130kHz	250-410kHz	-	250-410kHz	-
Komai et al (from (de Groot 1995))	Carbon / Epoxy	Below 300kHz	Above 500kHz	Below 300kHz	300kHz	-
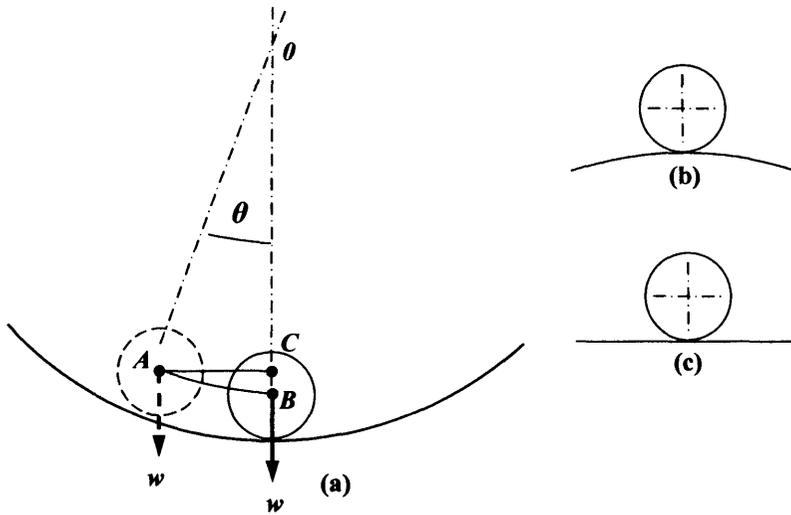
Figure 2.1 – Stability (Bulson 1970)
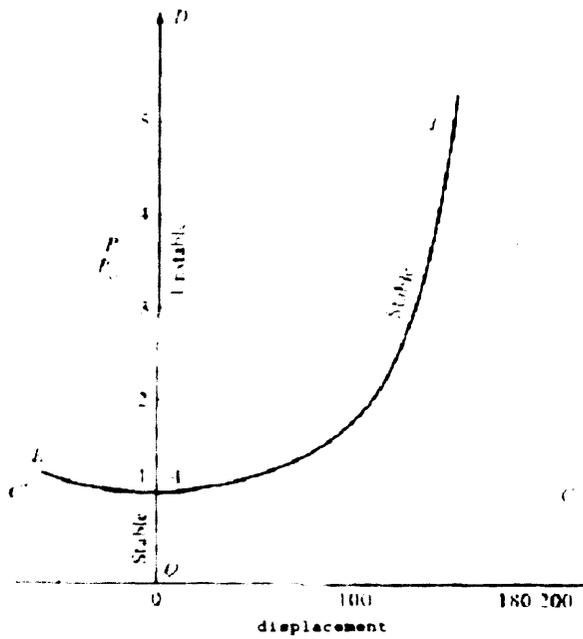
Figure 2.2 - Bifurcation buckling and stability of an axially loaded strut (Bulson 1970)
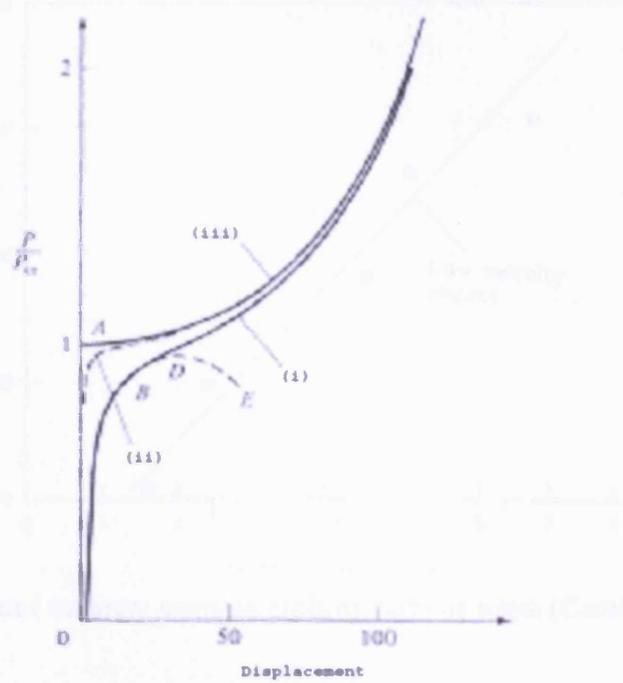
Figure 2.3 - Effects of initial imperfection on stability path (Bulson 1970)

a) Due to bending

b) Due to shear
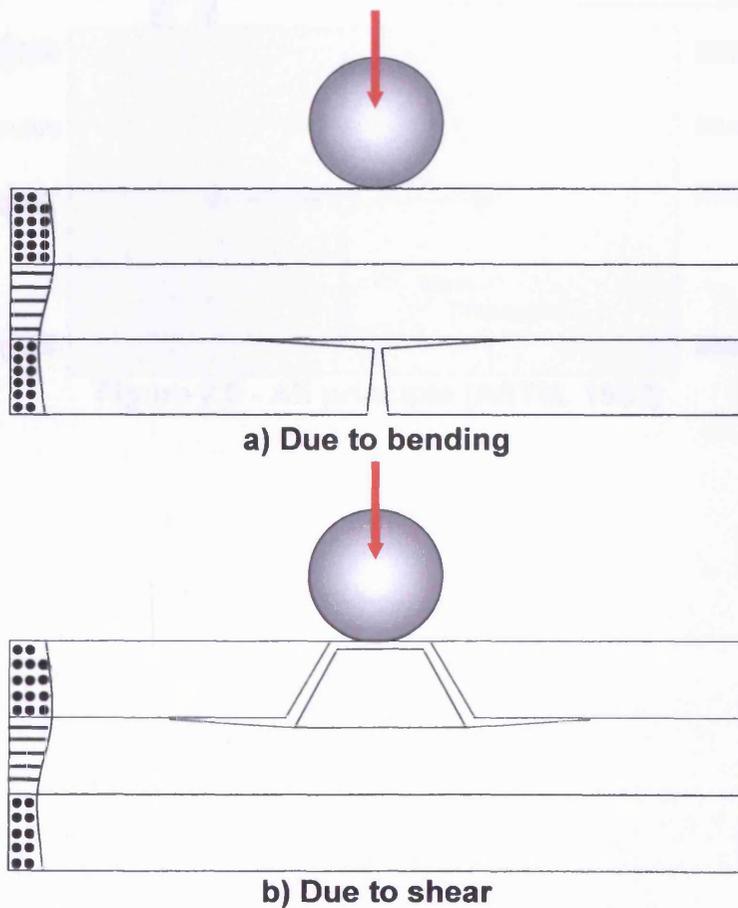
Figure 2.4 - Damage development due to impact (Abrate 1991)
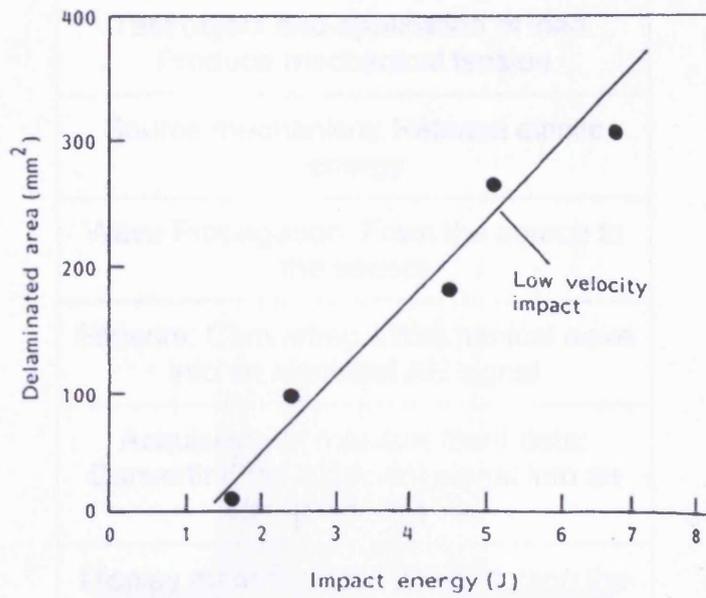
Figure 2.5 - Impact energy versus delamination area (Cantwell 1989)
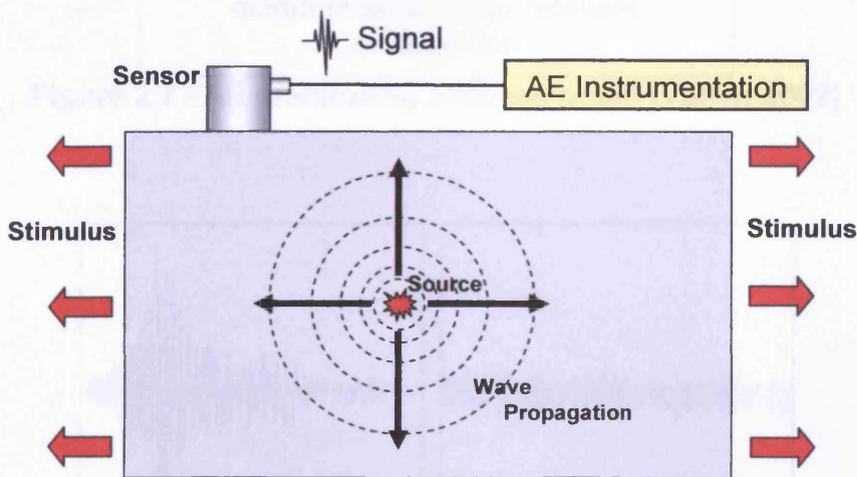
Figure 2.6 - AE principle (ASTM. 1982)

Test object and application of load: Produce mechanical tension
Source mechanism: Release elastic energy
Wave Propagation: From the source to the sensor
Sensors: Converting a mechanical wave into an electrical AE signal
Acquisition of measurement data: Converting the electrical signal into an electronic data set
Display measurement data: Plotting the recorded data into diagrams
Evaluation of the display: From diagrams to a safety-relevant intepretation

Figure 2.7 - AE monitoring process chain (Vallen 2002)

(a) Transient   (b) Continuous
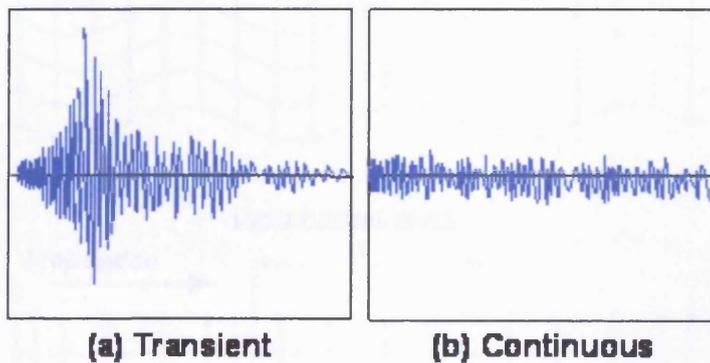
Figure 2.8 - Types of AE signal
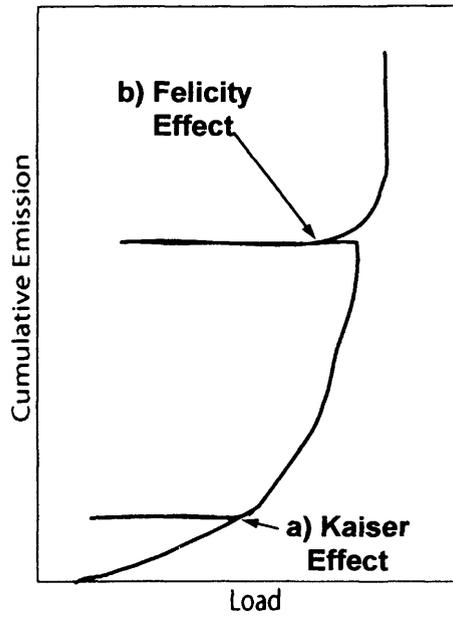
Figure 2.9 - Demonstration of the Kaiser and Felicity effects.
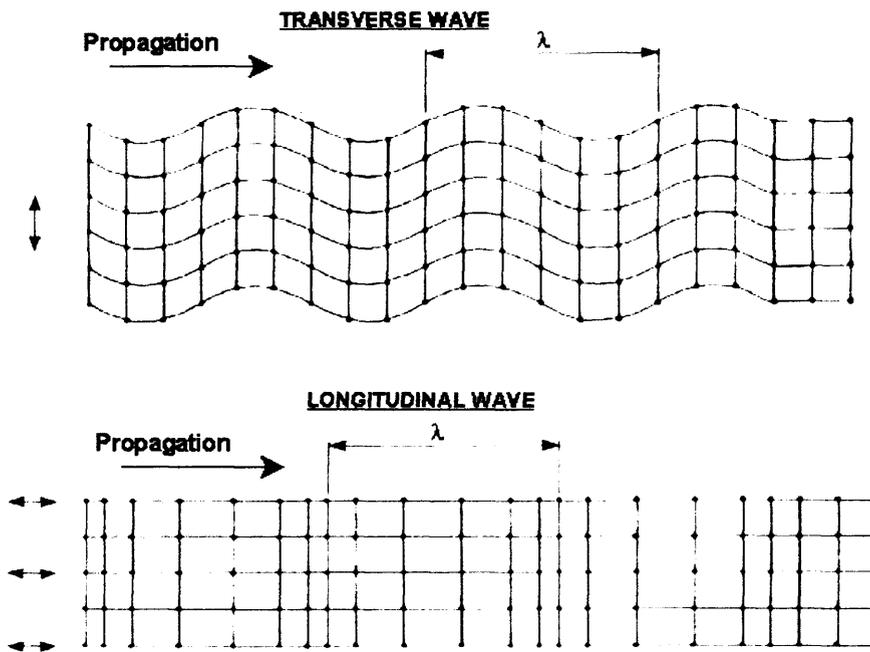
Figure 2.10 - Two basic wave modes in a solid (Rindorf 1981)

Propagation   SURFACE WAVE
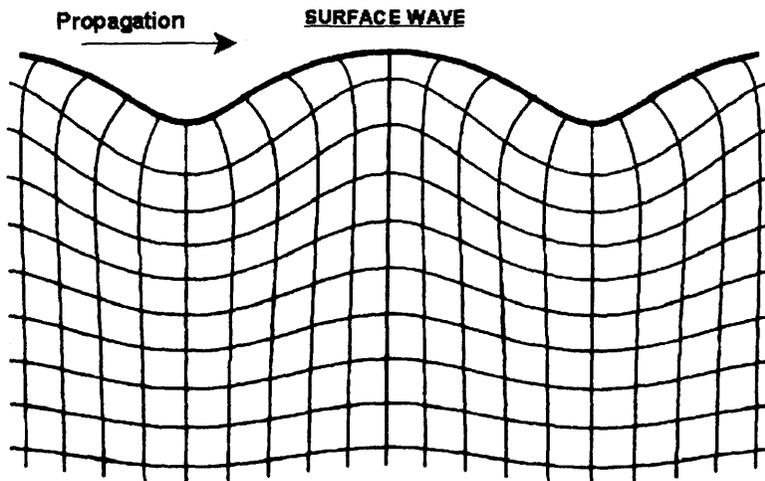
Figure 2.11 - Particle motion in a Rayleigh or surface wave (Rindorf 1981)

LAMB WAVES

Symmetric, i.e. longitudinal in centreline

Propagation

Asymmetric, i.e. transverse in centreline
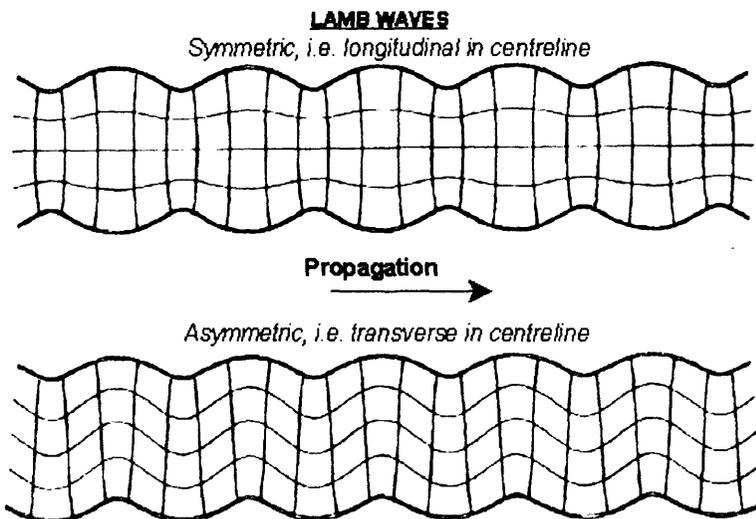
Figure 2.12 - Two principle Plate wave modes (Rindorf 1981)
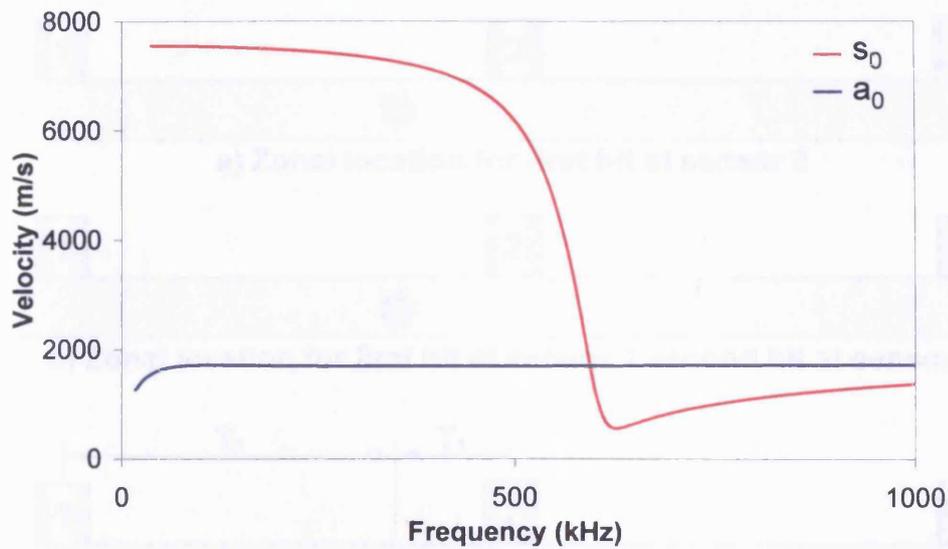
Figure 2.13 - Dispersion curve for composite material (generated using DISPERSE, see section 3.1.5)
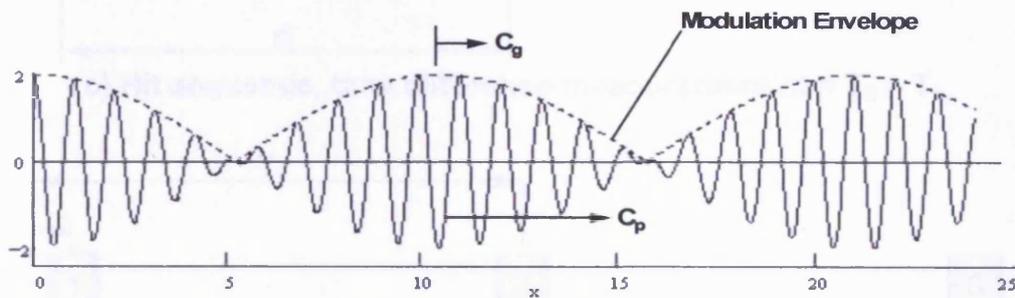
Figure 2.14 - Group velocity example
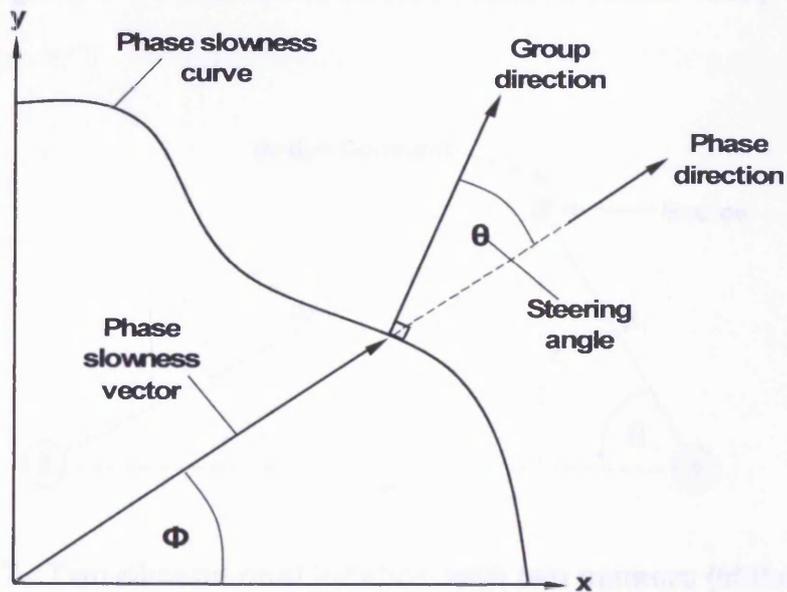
Figure 2.15 - Phase velocity slowness curve, demonstrating the group velocity vector steering angle
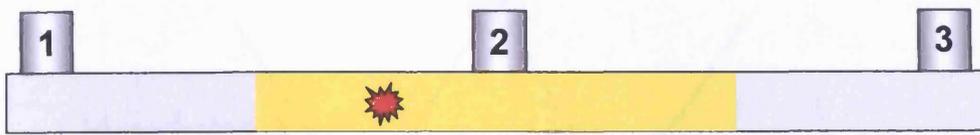
a) Zonal location for first hit at sensor 2
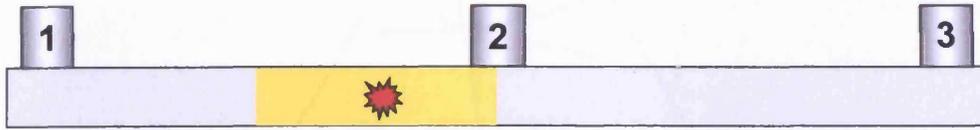
b) Zonal location for first hit at sensor 1 second hit at sensor 2
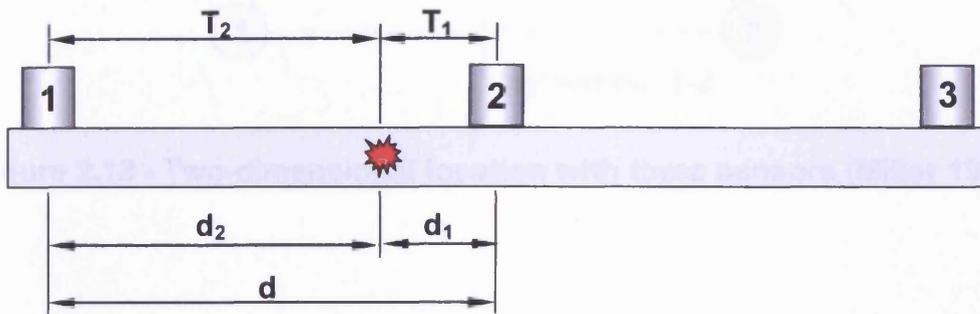
c) Hit sequence, time difference measurement $\Delta t = T_2 - T_1$
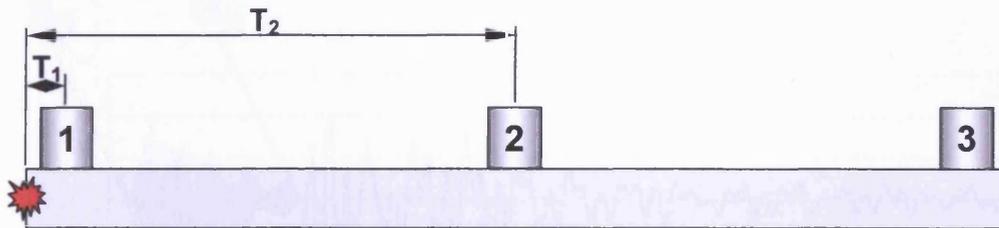
d) Source outside of the array $T_2 - T_1 = $ constant

Figure 2.16 - TOA linear source location (Miller 1987)
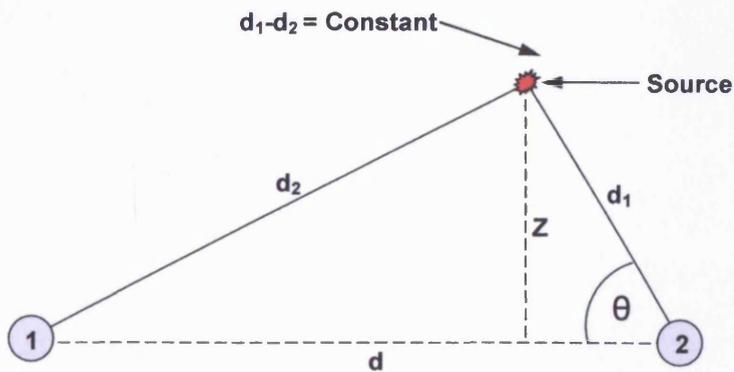
Figure 2.17 - Two-dimensional location with two sensors (Miller 1987)
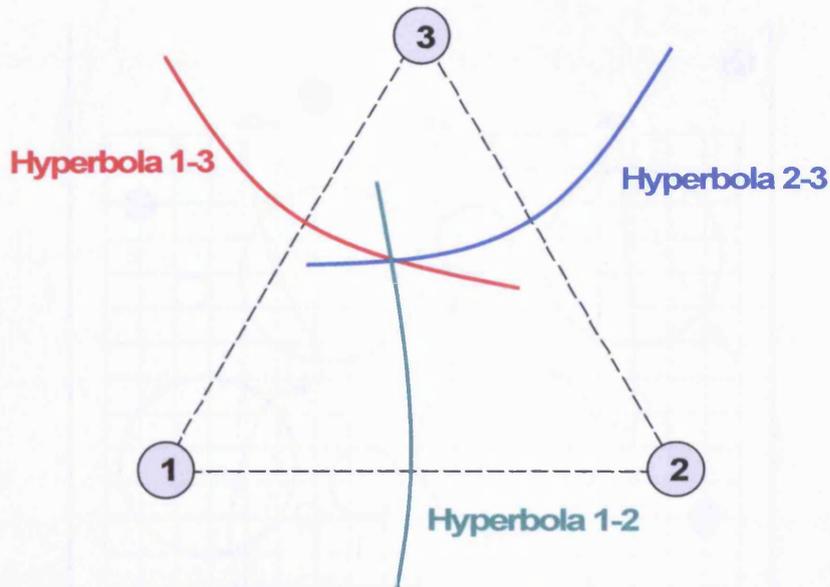
Figure 2.18 - Two-dimensional location with three sensors (Miller 1987)
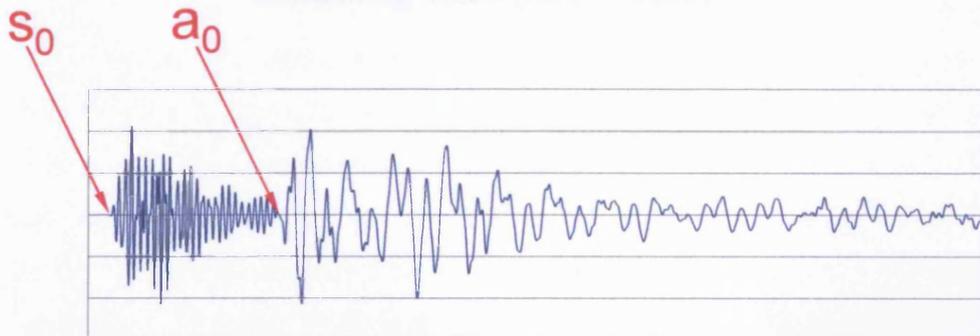
Figure 2.19 - An example of mode separation in AE signals
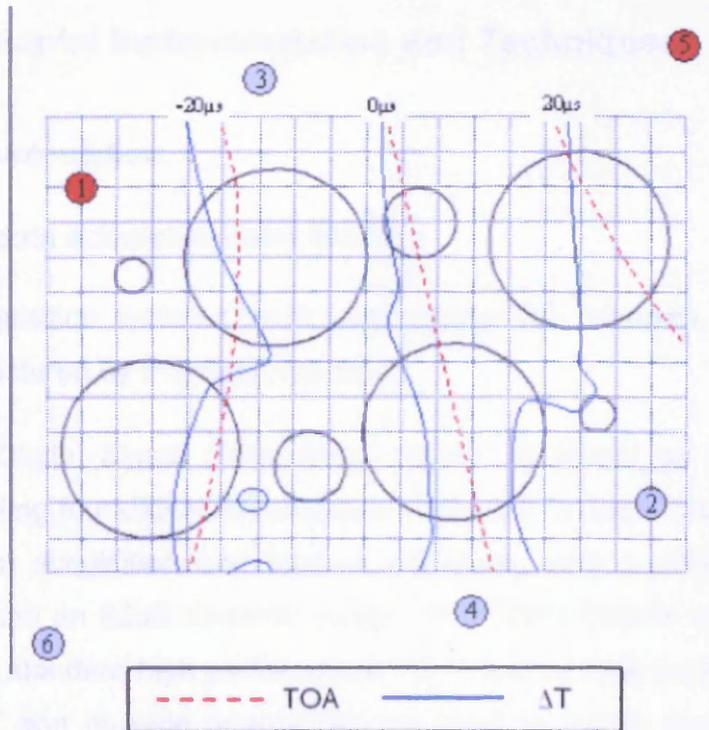
Figure 2.20 - An example of a DeltaT location map in a steel plate containing holes (Baxter 2007)

3   Experimental Instrumentation and Techniques

3.1   Instrumentation

3.1.1   AE data acquisition and storage

Two AE acquisition systems were used during this research, both of which were manufactured by Physical Acoustics.

The DiSP (Digital Signal Processing) system is based on the PCI-DSP4 board, providing four digital AE channels (Figure 3.1). Each channel performs full waveform acquisition and feature extraction, with a 16bit, 10MHz A/D conversion and an 82dB dynamic range. PCI-DSP4 boards are fitted to the PCI bus of a standard high performance PC, creating data transfer rates of up to 132Mb.s^{-1} and multiple boards can be used to create systems with 56+ channels.

The PCI-2 system utilises the PCI-2 board, which offers two low noise AE channels (Figure 3.2). Multiple boards can be used, up to a maximum of 8 channels. Each channel performs the same function as that of the DiSP system, with an improved acquisition rate using a 40MHz, 18bit A/D conversion. The most obvious difference in the PCI-2 board is the continuous data streaming function built into each channel, allowing the continuous recording of waveforms direct to the hard disk at a combined maximum rate of 10MHz (e.g. 5MHz/channel on two channels etc.).

3.1.2   Transducers

The surface displacements resulting from an AE event are commonly converted into a usable electrical signal using piezoelectric transducers. Figure 3.3 shows the construction of a typical piezoelectric transducer. The electrical signal is passed through a preamplifier, either placed close to or integrated into the sensor, that provides a gain (typically 40dB) and low frequency filtering to remove unwanted mechanical noise, before passing to the processor for digitisation via a coaxial cable. Many types of piezoelectric sensor are produced, ranging from broadband to resonant.

Broadband sensors offer a flat response across the AE frequency range (10kHz – 1MHz) effectively multiplying each frequency by the same amount. A broadband sensor produces a very high fidelity representation of the surface displacement, however this is at the cost of detection sensitivity. As such broadband sensors rarely find application outside of the research environment, but are absolutely necessary for quantitative frequency analysis.

Resonant sensors have a bias towards a particular frequency and apply a greater amplification to frequencies at or close to their resonance. This can improve the sensitivity of detection, if the sensor resonance is paired with the expected frequency of desired AE signals.

Wideband sensors aim to have a flatter frequency response than a resonant sensor but still maintain a good level of sensitivity, thus providing a high fidelity signal without the loss of too much sensitivity. Wideband sensors are often used in research applications where frequency analysis or the identification of wave modes is required (PAC 2006b).

Five types of sensor were used during this work, four manufactured by Physical Acoustics and one experimental broadband conical transducer manufactured by the National Physical Laboratory (NPL). Details of the sensor characteristics for the four Physical Acoustics sensors, rated by the manufacturer in accordance with ASTM E1106 (1986), are presented in Table 3.1. Example calibration certificates for each of the four Physical Acoustics sensors, produced by the manufacturer in accordance with ASTM E976 (1994), can be seen in Figure 3.4a-d. Additionally a plot of the transmit sensitivity for the conical transducer can be seen in Figure 3.5.

The S9208 is a broadband sensor, from its calibration certificate it can be seen that the frequency response is generally flat without any dominant peaks, however there are numerous smaller peaks and troughs. The WD sensors are wideband, achieving greater sensitivity and a flat frequency response by using a very carefully shaped piezoelectric crystal. There are, however, still a number of minor peaks observed on the calibration certificate. The WDi is effectively the same sensor as the WD, only with an integrated

preamplifier. The Nano30 is a resonant sensor with a peak frequency response at approximately 300kHz, however the Nano 30 has a relatively broad frequency response for a resonant sensor. The conical transducer supplied by NPL was developed as a traceable reference source for the characterisation of AE measurement systems, as an alternative to the H-N source (Theobald 2004). The sensor utilises a conically shaped broadband piezoelectric element that is 3mm thick with a 10 mm base and 1 mm tip. The conical transducer is used as both an artificial source (for which it requires a driving pulse, see section 3.1.4) for the investigation of source characterisation and as a high fidelity broadband receiver during this work.

3.1.3   Hsu-Nielson (H-N) source

Currently the most common method for verifying the correct mounting of sensors is the Hsu-Nielson (H-N) source, so named because of the work by Hsu and Breckenridge (1981) and Nielson (1980) that led to its development. It can also be used as an artificial source of acoustic emission. The H-N source gained favour because it is repeatable, very practical and very low cost. Utilising a standard 0.5mm (alternatively 0.3mm) propelling pencil with a type 2H lead, the addition of a PTFE guide ring facilitates a repeatable angle of fracture reducing the likelihood of spurious signals (Figure 3.6).

The recommended procedure for performing the H-N source, as agreed by the European Working Group on Acoustic Emission (EWGAE) in October 1980, is as follows:

a.   The lead feed button on the pencil is pressed repeatedly until the lead protrudes.

b.   The end of the lead is levelled with the end of the guide tube by pressing the tip of the pencil perpendicularly towards an even surface while the feed button is pressed down.

c.   The button is pressed six times causing the lead to protrude 3mm.

d. The pencil is guided obliquely towards the structure until the guide ring rests on the specimen

e. The pencil is pivoted about the point of contact towards a steeper position thus causing the lead to break.

It is also noted that the AE signal is generated as a result of the rapid stress release of the surface at the point of contact with the lead (ASTM E9761994)

3.1.4 Pulse generation

Electronically generated pulses were used to drive the conical transducer (section 3.1.2), when used as an artificial AE source. The pulse generation was provided by a Physical Acoustics ARB-1410 Arbitrary Waveform Generator Board or "wavegen" board (Figure 3.7). The "wavegen" board interfaces with a standard PC's PCI-bus and with its accompanying software is capable of producing analogue signals with frequencies of up to 15MHz and amplitudes of up to ±150V, using a 14bit, 100MHz Digital to Analogue Converter (DAC) (PAC 2003b). The control software allows a range of output signals (i.e. square wave, saw tooth, sine wave etc.) to be both frequency and amplitude modulated, making it possible to generate a wide variety of signals. The conical transducer and the pulse generator can provide an artificial source of varying frequency (i.e. replicating differing relaxation times of different damage modes), hence it can be used to replicate different damage mechanisms.

3.1.5 Dispersion curve calculation

Theoretical dispersion curves are used for the validation of experimental propagation results. All theoretical dispersion results presented in this thesis are generated using the commercially available DISPERSE 2.0.16 software, distributed by the Non-Destructive testing Laboratory, Imperial College, London. The software allows the user to define the properties of a single lamina and then construct the desired material lay-up. Propagation can be modelled in any desired direction, however as discussed in section 2.2.5,

appropriate group velocity dispersion curves can only be generated for propagation along fibre directions, without further post processing.

3.1.6 Finite element analysis software

The development of the Finite Element (FE) model and mesh were conducted using MSC's Patran software, due to the author's familiarity with this package. However analysis of the model was undertaken using Simulia's ABAQUS/standard software. The ABAQUS software was developed to address non-linear physical behaviour such as buckling and instability. The FE analysis was firstly used to aid the design of the large scale instability tests, i.e. predicting loads and displacements. Secondly the postbuckling analysis forms an integral part of the imperfection study.

3.1.7 Digital Image Correlation (DIC)

Digital image correlation (DIC) can be thought of as stereo vision. Images from two calibrated cameras are processed to provide accurate three-dimensional full field measurements. The cameras are calibrated for a given test space using a calibration target of known geometry. A specimen or component of interest must first have a black and white speckled pattern applied, from which the software generates a greyscale pattern for each image that can be correlated to calculate special position. The displacement and deformation of the pattern is tracked throughout the test and therefore values of strain and curvature can also be found through additional post processing. During this work a LIMESS DIC system was used. Images were captured using two black and white digital cameras with a 1Mpixel resolution, and synchronised using Correlated Solutions VicSnap software. The captured images can be recorded at rates up to 5Hz and are stored on a standard PC laptop as .tiff files for post processing using Correlated Solutions Vic3D software. The use of full field DIC facilitates non-intrusive measurement of displacement during instability experiments, enables easy identification of buckling mode shapes and also identifies areas of high strain and curvature.

3.2 Experimental techniques

3.2.1 Sensor mounting

The correct mounting of AE sensors is essential to maintaining repeatability of signals and avoiding any loss of sensitivity. Correct mounting requires two things; firstly the physical restraint of the sensor and secondly the provision of an acoustic coupling between the sensor and the test material. Both requirements can be fulfilled by the use of adhesives, such as cyanoacrylates, however this can result in damage to the sensors upon removal and, as such, is not appropriate for research applications.

The ASTM guidelines (ASTM. 1985) for the mounting of piezoelectric AE sensors, identifies several key points for the successful mounting of AE sensors:

- Adequate pressure should be applied to ensure intimate contact between the sensor and the structure is maintained throughout a test.

- Movement of the sensor relative to the surface should not be allowed.

Common mounting methods suggested include springs, screw threads, magnets, tape and elastic bands. The sensor mounting methods utilised during this work are:

- Electrical tape – The elasticity of the tape provides an appropriate force for mounting sensors, however its use is limited to smaller specimens

- Magnetic clamps – Two types of magnetic clamp were utilised; for the larger sensors, clamps such as that shown in Figure 3.8a were used, where the magnets secure the clamp and the central spring applies a force to the sensor. For the miniature sensors, smaller magnetic clamps (Figure 3.8b), used to good effect by Baxter (2007), were utilised. The magnets were attached either using small steel tabs bonded to the carbon fibre material using hot melt glue (Figure 3.9a) or

via opposed magnets from the opposite side of the specimen (Figure 3.9b). Additionally the conical transducer was mounted using the arrangement of magnets presented in Figure 3.10, due to its top exiting connector.

- Self adhesive tabs and zip ties – Self adhesive tabs were attached to a specimen either side of the sensor and a zip tie running between them was used to secure the sensor in position. Foam placed between the sensor and the zip tie was used to regulate the applied force (Figure 3.11).

The ASTM guide (ASTM. 1985) for mounting piezoelectric AE sensors does not recommend any specific couplants, stating that most liquids or greases will work if they wet the surface of both the structure and the sensor. Additionally guidelines on couplant properties for specific experimental set-ups and operating environments are offered. PAC (2003a) suggest a range of potential couplants for different environments; including high vacuum grease, silicone grease, petroleum grease, water, sealant and dental cement. Work by Hensman (2006) investigated the repeatability of various commonly used couplants using cross-correlation. They found that water based ultrasound gel provided the most repeatable acoustic coupling, although its use is only recommended for short tests (<1 day) due to evaporation. For longer-term tests they found ordinary brown grease to produce the most repeatable coupling. Interestingly they found silicone grease (often recommended as a couplant for AE sensors (Vallen 2006)) to be one of the worst performing couplants for repeatability.

Once mounted, the sensitivity of a sensor should be assessed through the use of an artificial AE source. Throughout this work the H-N source (section 3.1.3) was used. A correctly mounted sensor should produce a signal amplitude of 97-100dB (broadband sensors will produce a lower amplitude response due to reduced sensitibty) in response to an adjacent H-N source. Sensors not achieving this level of sensitivity should be remounted and

retested. If the problem persists the offending sensor should be replaced and assessed for damage.

3.2.2 Measurement of wave velocity

In order to calculate the location of an AE event, both the TOA and SSMAL techniques require a wave velocity (velocities of both wave modes are required in the case of the SSMAL). As discussed in section 2.2.5 this is additionally complicated for composites due to the directional dependency of the velocity.

The velocity of wave both modes can be practically determined as follows. Two sensors are placed at a set distance apart on a structure. A H-N source is performed adjacent to sensor 1, as shown in Figure 3.12. A synchronous trigger is used, so that when the signal crosses the threshold at channel 1, channel 2 begins recording. As such the arrival times of the wave modes identified in the recorded waveform at channel 2 (Figure 3.13) provide an accurate measurement of the wave modes times of flight between the two sensors. Hence the velocity along that specific material direction can be determined using Equation 3.1.

$$C_{S/A} = \frac{T_{S/A}}{d_1}$$
(3.1)

Where: $C_{S/A}$ = Velocity of the s_0 or a_0 wave mode

$T_{S/A}$ = Time of arrival of a_0 or s_0 wave mode

d_1 = Distance from source

3.2.3 Graphical representation

Much of the data, be it AE, DIC or C-scan, considered in this work is presented in a graphical format. The following is a description of the more commonly used graphical displays.

Historical Plots – Can be plotted in terms of time history or load history. Time history plots, such as that shown in Figure 3.14, illustrate the change in an AE

parameter with time and provide an indication of damage development throughout a test. Load history plots allow the operator to assess changes in AE parameters (i.e. cumulative counts or energy) relative to load application, they are particularly useful when investigating the Kaiser and Felicity effects (Figure 3.15)

Location plots – Three different location methodologies were utilised during this work. Linear TOA location, Two-dimensional TOA location and DeltaT location, all of which are discussed in Chapter 2. Linear locations are presented as a histogram of located energy plotted against position between sensor pairs (Figure 3.16). The two-dimensional locations and the DeltaT locations are presented as scatter plots of x and y position, in which the points are coloured by the density of events (Figure 3.17).

Correlation plots – Are point plots that show the relationship between two AE parameters. Plots of certain AE parameters can give an indication of damage levels and source type. Amplitude versus log duration plots (Figure 3.18) are identified by PAC (2006a) as being of particular use for the monitoring of composite materials, suggesting that high amplitude hits are indicative of fibre failure and hits with high amplitude and long durations are indicative of delamination.

Waveforms – Are the time domain representation of an AE signal. The vertical axis is the amplitude of a signal in volts and the horizontal scale is the elapsed time from the point of triggering. An example of a recorded AE waveform is presented in Figure 3.19. The amplitude in dB_{AE} of an AE signal is calculated, relative to a $1\mu V$ reference voltage at the transducer, by an AE acquisition system, using Equation 3.2.

$$Amplitude = 20\log_{10}\left(\frac{V_s}{V_{ref}}\right)$$
(3.2).

Digital Image Correlation (DIC) contour plots – The DIC system provides full field measurements of displacement and through post processing can provide values of curvature. A chosen data parameter (i.e. displacement in the

x-direction, strain in the y-direction, principal curvature etc.) is plotted as a series of coloured contours overlaying the original image (Figure 3.20). Plots of out-of-plane displacement and both minor and major principal curvature are utilised in this work. The direction in which a specimen deflects under bifurcation buckling dictates whether the curvature is viewed as being positive or negative by the DIC system. If the curvature is positive then the greatest curvature will be positive and will be assigned as the major principal curvature. If the curvature is negative then the greatest curvature will be negative and will be assigned as the minor principal curvature. Thus, when principal curvature data is presented the most appropriate plot will be selected depending on the displacement of the specimen. The AE location data is presented as if looking at the specimen from the side on which the sensors are mounted and the C-scans were performed such that the images would be in the same orientation. However, because the optical measurements are made from the opposite side of the specimen they are not in the same orientation. In order to simplify the comparison of DIC, C-scan and AE data the DIC contour plots presented are mirrored about the vertical axis such that their orientation is the same as the C-scan and AE data (Figure 3.20a and b).

C-scan images – The colours presented in a C-scan image are scaled relative to the amount of signal lost at that specific position in the scan area. Damage causes diffraction and attenuation of the signal resulting in greater signal loss, identified by the dark brown areas in the C-scan image presented in Figure 3.21.

Table 3.1 - Manufacturer's specification of sensors in accordance with ASTM E1106 (1986)

Sensor Type	Operating Frequency Range (kHz)	Resonant Frequency (shear[compression]) (kHz)	Dimensions Dia x Ht (mm)
S9208 (broadband)	20 – 1000	500 [500]	25 x 25
WD (wideband)	100 – 1000	125 [650]	18 x 17
WDi (wideband)	100 – 1000	125 [500]	29 x 30
Nano30 (resonant)	125 - 750	140 [300]	8 x 8
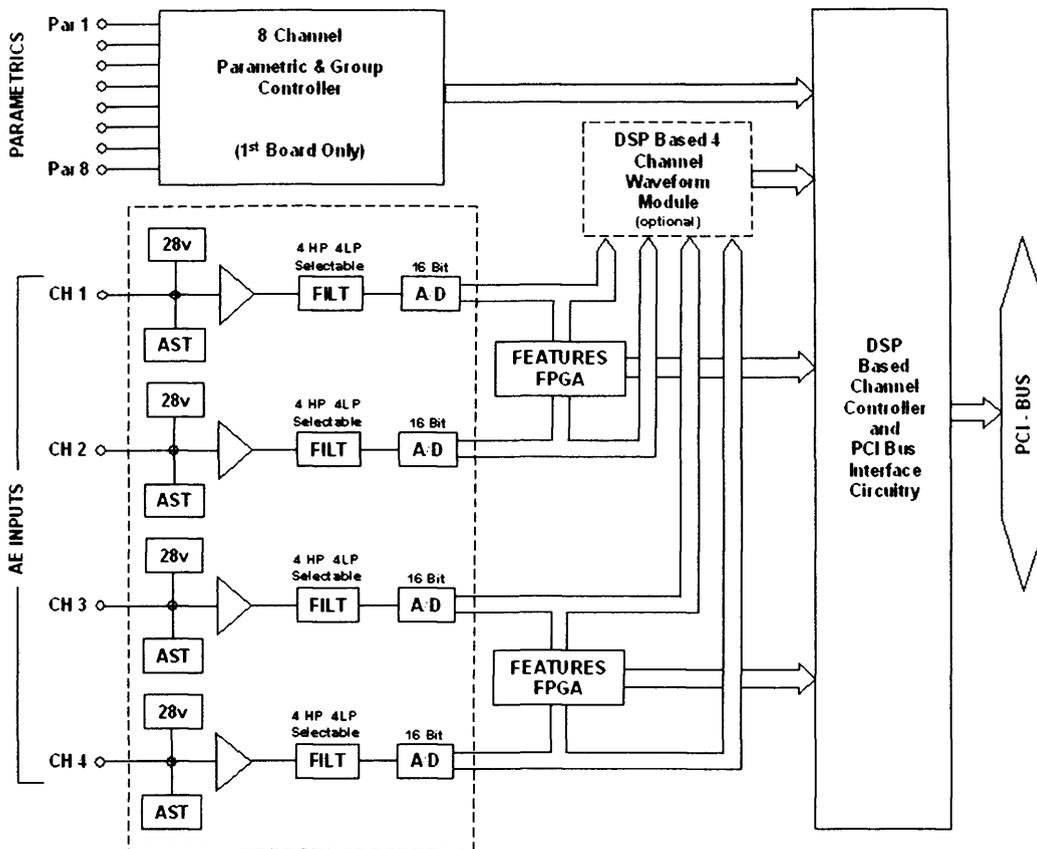
Figure 3.1 - PCI-DSP4 board block diagram (PAC 2003a)
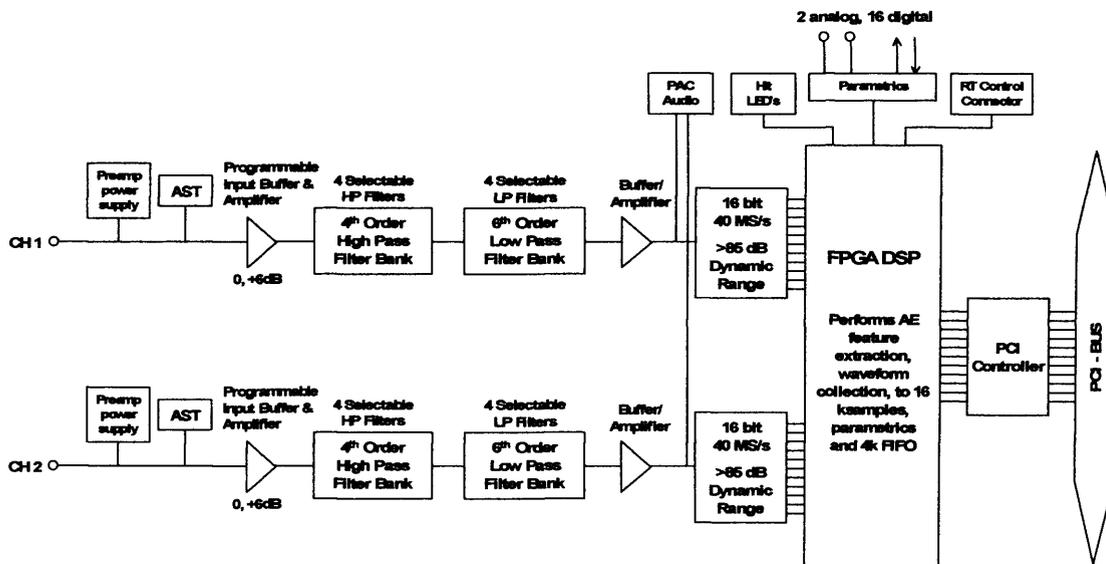
Figure 3.2 - PCI-2 board block diagram (PAC 2004)
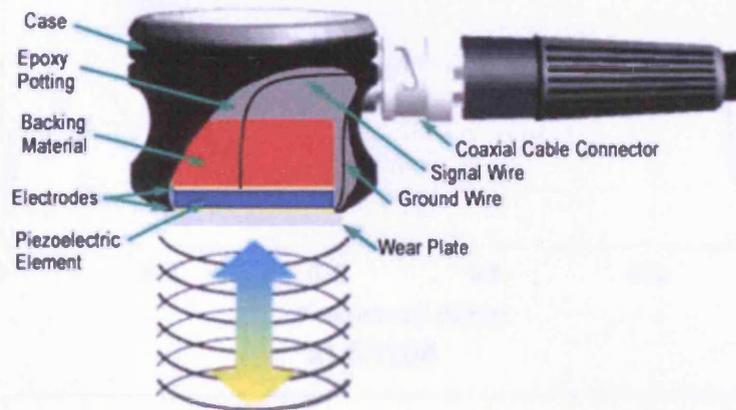
Figure 3.3 - Typical piezoelectric sensor construction

a) S9208

b) WD

c) WDi

d) Nano30

Figure 3.4 - Calibration certificates for S9208, WD, WDi and Nano30 sensors (Sensitivity dB ref 1V/µbar)
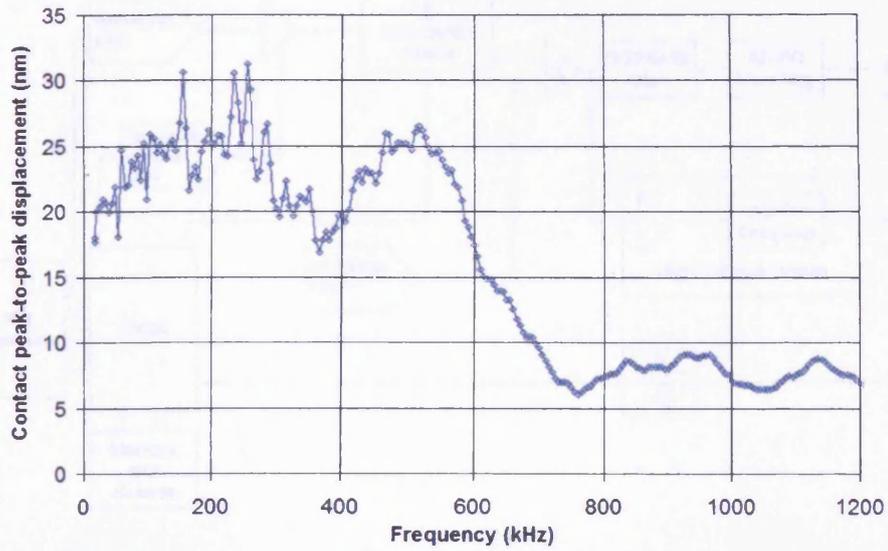
Figure 3.5 - Conical transducer transmit sensitivity

Diameter	GT (± 0.05 mm)
0.3 mm	0.84 mm
0.5 mm	0.92 mm

a) Neilson Shoe

b) Neilson Shoe on a H-N pencil

Lead (2H and 3mm long)
Nielsen Shoe
Pencil
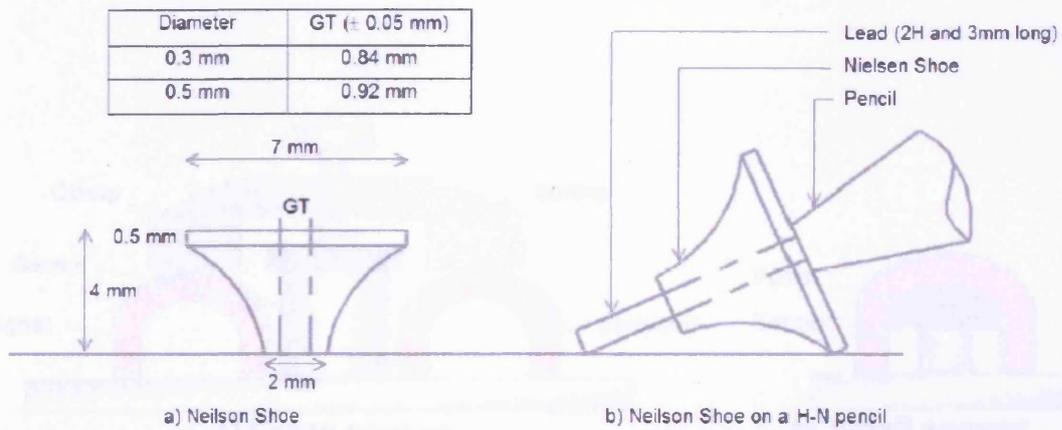
Figure 3.6 - Hsu-Nielson source (ASTM. 1994)
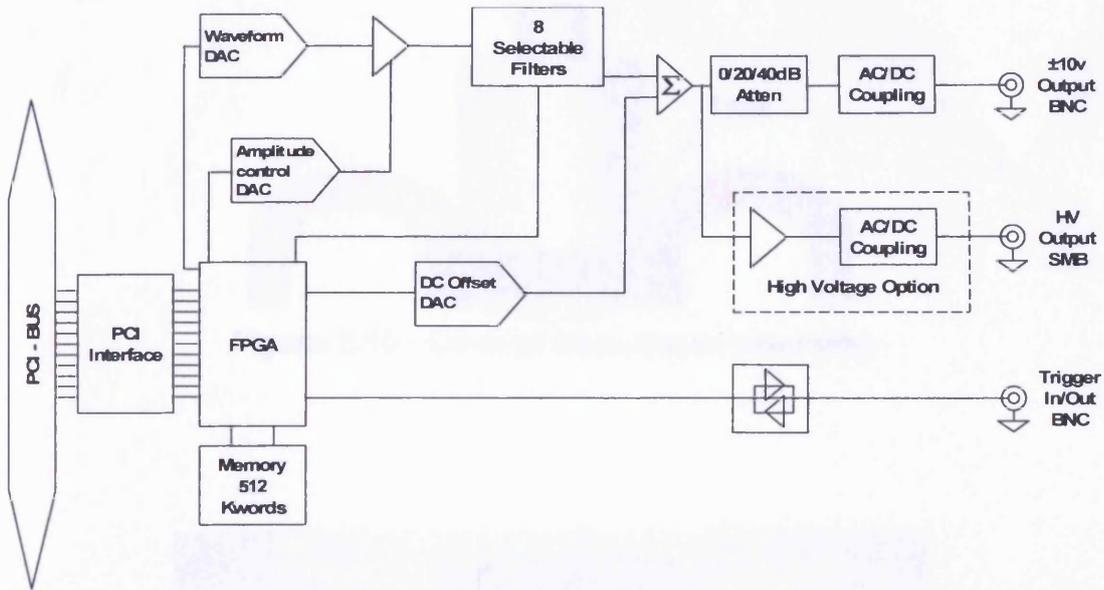
Figure 3.7 - ARB-1410 arbitrary waveform generator board block diagram (PAC 2003b)
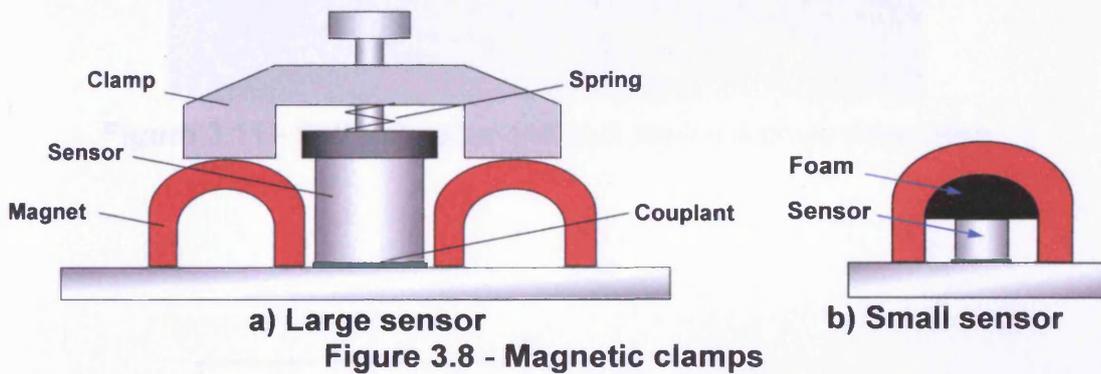
a) Large sensor
Figure 3.8 - Magnetic clamps

b) Small sensor
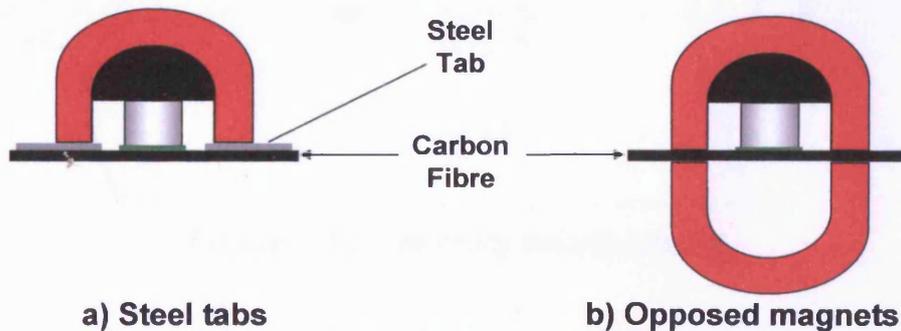
a) Steel tabs   b) Opposed magnets
Figure 3.9 - Magnet attachment
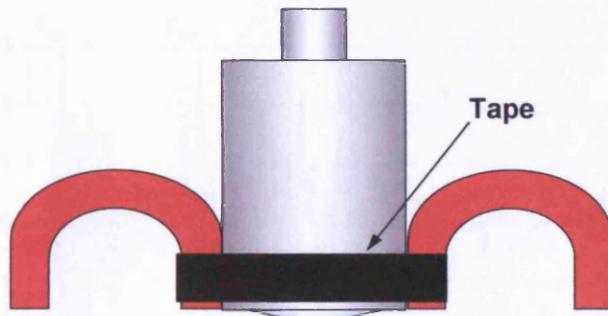
Figure 3.10 - Conical transducer mounting
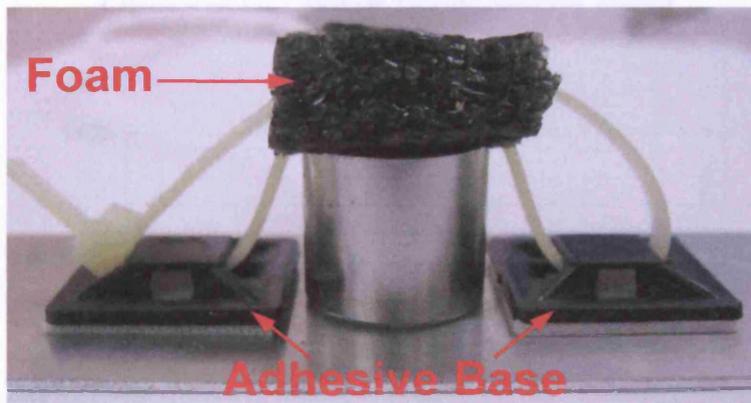
Figure 3.11 - Self adhesive tab and zip tie sensor mounting
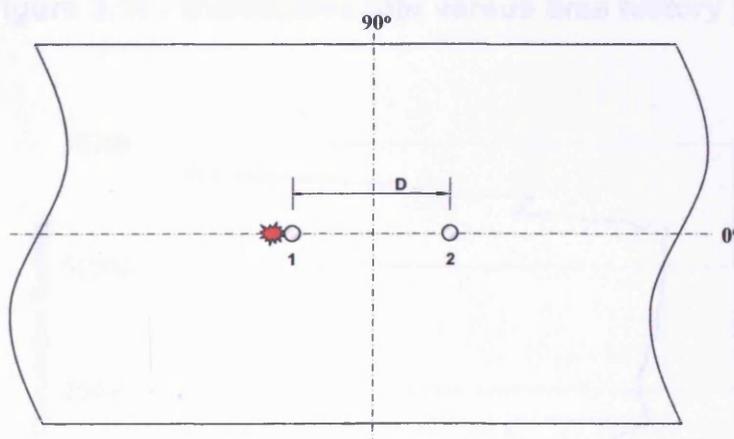
Figure 3.12 - Velocity measurement
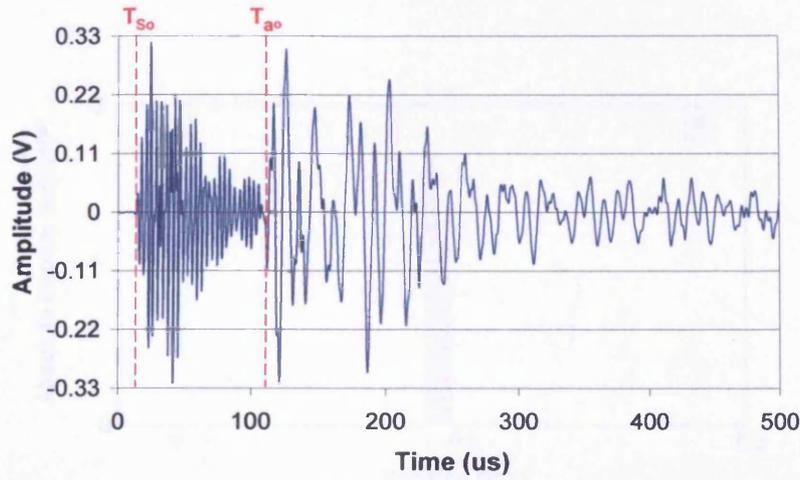
Figure 3.13 - Wave mode arrival times
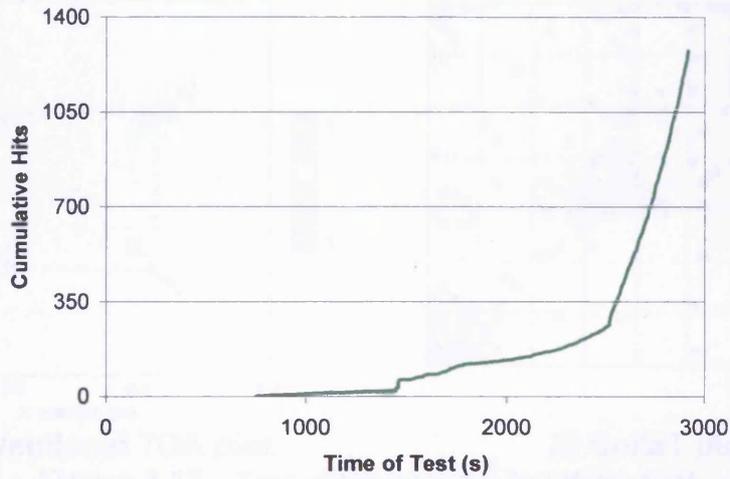
Figure 3.14 - Cumulative hits versus time history plot
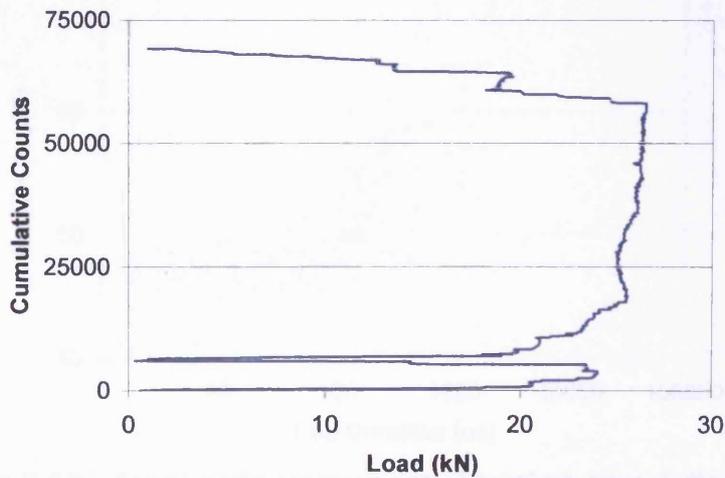
Figure 3.15 - Cumulative counts versus load history plot
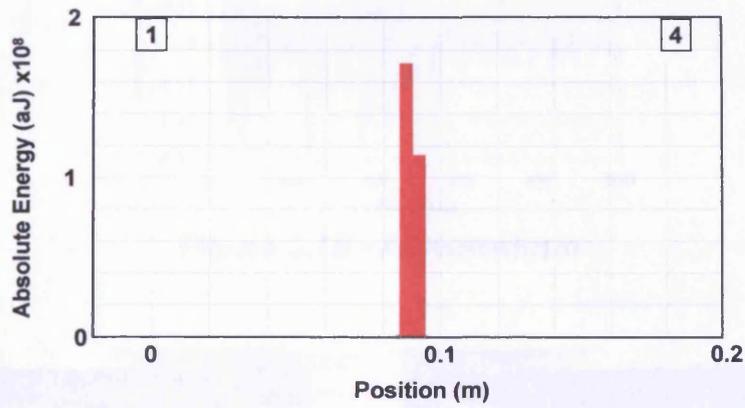
Figure 3.16 - Linear location plot
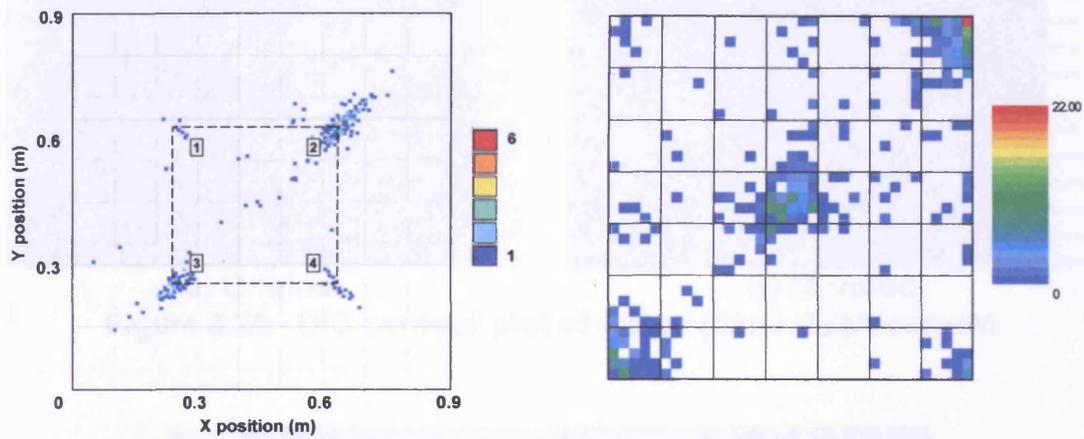
a) Conventional TOA plot   b) DeltaT plot

Figure 3.17 - Two-dimensional location plot
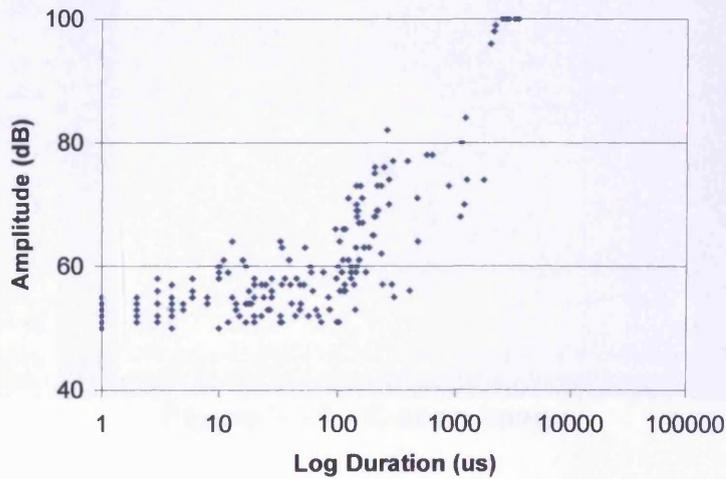
Figure 3.18 - Amplitude versus log duration correlation plot
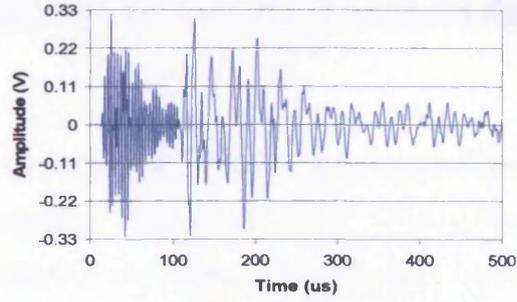
Figure 3.19 - AE waveform
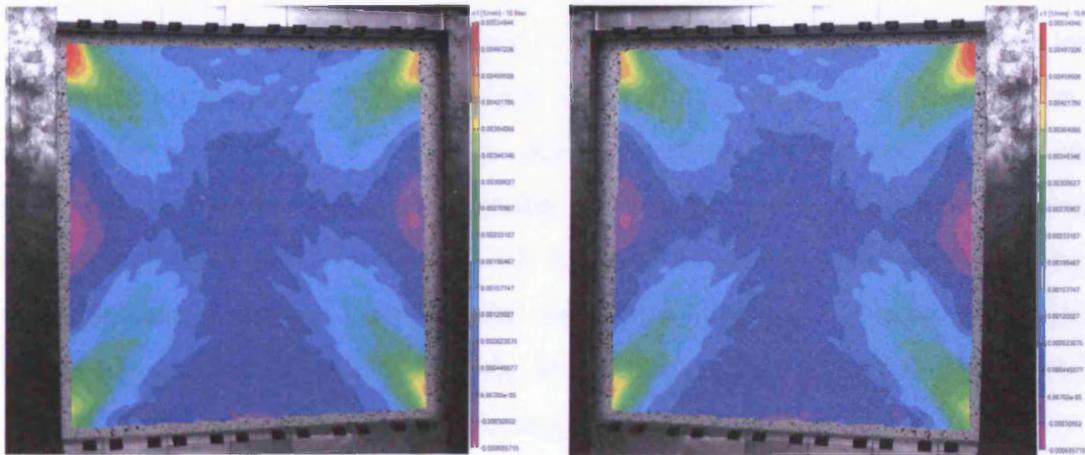
| a) Original | b) Mirrored |

Figure 3.20 - DIC contour plot of out-of-plane displacement
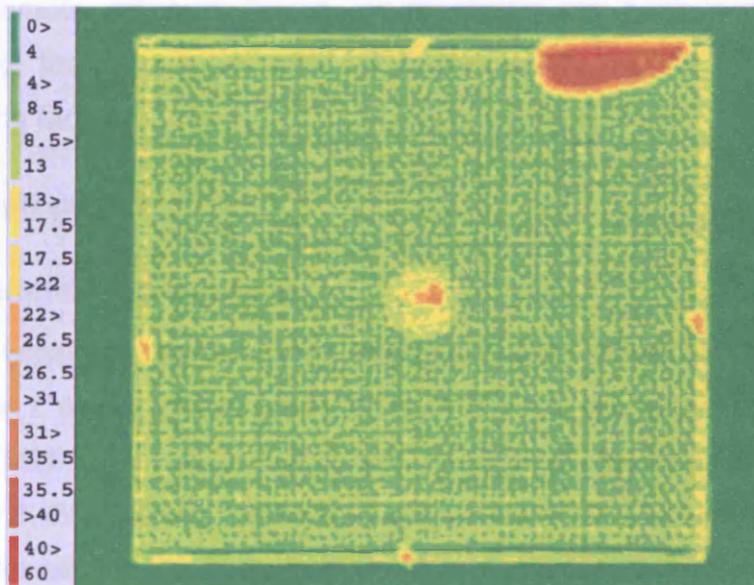
Figure 3.21 - C-scan image

4 Wave Propagation and Source Characterisation

4.1 Introduction

The ability to discriminate between AE signals generated by different source mechanisms is extremely desirable and is the primary focus of the work in this chapter. In order to attempt a correct discrimination between AE signals there must first be a better understanding of the effects that source type, material, geometry, propagation and sensor response have on a recorded signal.

This chapter is split into two sections. The first section is an investigation into the effects of propagation and sensor response on artificial AE sources in a composite material. The velocity, attenuation and dispersion of the two principal plate wave modes were measured for varying propagation directions between $0°$ and $90°$. The effect of differing source mechanisms on their resulting signals was investigated using an artificial source of varying frequency. In addition to this a study of the effect of grid resolution on DeltaT source location (section 2.3.4) accuracy was undertaken.

The second section focuses on the discrimination between real AE signals from different damage modes. Tensile and beam buckling coupon tests were used to promote different failure mechanisms and both peak frequency content and the amplitude ratio of plate wave modes were used as discriminating factors.

4.2 Wave propagation

4.2.1 Experimental procedure

A series of wave propagation tests were conducted on a 500mm x 1400mm carbon fibre / epoxy plate made from 16 plies of Advanced Composite Group's MTM28-1/HS-135-34%RW with a $((0,90)_4)_s$ lay-up giving a nominal thickness of 2.15mm (manufacturing details are included in Appendix D). Data acquisition for all wave propagation tests was conducted using a PAC PCI-2 system.

The velocity of both plate wave modes was measured in the $0°$ and $180°$ in $10°$ increments using two PAC Nano30 sensors. These sensors were selected

for their small diameter which increases the accuracy of measurement. The calibration certificates for both sensors are presented in Figure 4.1. The sensors were mounted 200mm apart (Figure 4.2) using opposed magnets (as detailed in section 3.2.1) and ultrasound gel was used as a couplant. The sensitivity of both sensors was checked using a H-N source (ASTM. 1994) each time the sensors were moved and their response was above 97dB in all cases. A H-N source (ASTM. 1994) was used to generate a broadband artificial AE signal adjacent to sensor 1 and a synchronous trigger was used to record the signals at sensor 2. The velocities were calculated from the arrival times of the s_0 and a_0 modes at sensor 2. The time of arrival was taken to be the peak of the first cycle of each mode and was selected manually. By measuring the arrival time in this way the effects of threshold level and sensor response are limited.

The measurement of attenuation was conducted using 4 PAC WD sensors amplified by PAC 2/4/6 amplifiers providing 40dB gain. Calibration certificates for all four sensors are presented in Figure 4.3. These sensors were chosen because they offer a relatively flat frequency response over a wide frequency range, but still achieve a higher sensitivity than a broad-band sensor. This makes them an effective sensor for use in source characterisation. The sensors were arranged in a straight line having a $0°$, $22.5°$, $45°$ or $67.5°$ angle to the principal material direction, with a regular spacing of 100mm, as seen in Figure 4.4. Data from the $90°$ direction is not included because reflections from the plate boundaries in this direction made identification of the plate modes and their peak amplitudes very difficult. Each time the sensors were moved the sensitivity was checked with a H-N source ((ASTM. 1994)) and responses were above 97dB in all cases. Ten H-N sources were performed at 100mm distance from sensor 1, in line with the sensor array, for each propagation direction considered. No amplitude measurements were made adjacent to the source because the plate wave modes do not develop within a propagation distance of 8-10 times the plate thickness and therefore no measurement could be made. Waveforms were recorded from all 4 sensors and the amplitudes of the principal plate wave modes were measured manually.

The measurement of dispersion in this material was undertaken using the Vallen Systems wavelet software package (Vallen 2006). The software uses a Gabor wavelet to decompose the AE signal into a 2D time-frequency plot. Details of the wavelet set-up used are shown in Table 4.1. Peaks in the wavelet magnitude at a particular frequency can be inspected and are an indication of the group velocities of different modes at that frequency. An example of the wavelet transformation and data extraction can be seen in Figure 4.5. To limit the effects of sensor resonance and the averaging of small wavelengths across the sensor face, a broadband conical transducer (Supplied by NPL, see section 3.1.2) was used to record the propagating signal. The PCI-2 system was operated in Transient Record Analysis (TRA) mode, using a synchronous trigger and a PAC pico as a trigger sensor. The sensors were arranged (shown in Figure 4.6) 200mm apart at the centre of the plate to maximise the time before the arrival of the first reflection. Waveforms were recorded for 5 signals, generated by a H-N source ((ASTM. 1994)), in each of the $0°$, $22.5°$, $45°$, $67.5°$ and $90°$ propagation directions relative to the principal material axis. Arrival times of the a_0 and s_0 mode group velocities were measured manually at 10kHz intervals, an average velocity was calculated at each frequency and used to plot dispersion curves. Theoretical dispersion curves were generated for the $0°$ and $90°$ material directions using DISPERSE 2.0.16 (Imperial College, London). As discussed in section 2.2.5, for waves not propagating in a direction parallel to the principal material directions (i.e. in-line with the fibres) the phase direction differs from that of the group direction. As such, direct calculation of the group velocity dispersion behaviour is not possible for propagation in directions other than those parallel to the fibre orientation. It has been shown by a number of researchers (Jeong and Jang 2000; Wang and Yuan 2007) that it is possible to correct for the difference in propagation direction of the phase and group velocity, to produce theoretical dispersion curves for propagation off of the fibre axis. However this approach is numerically very involved and deemed to be outside the scope of this work. The dispersion behaviour calculated in the $0°$ and $90°$ is considered to be a sufficient verification of the dispersion measurements.

A study of sensor response to different artificial sources was undertaken for both PAC WD and S9208 sensors. The S9208 is a true broadband sensor and provides a high fidelity measurement of out-of-plane displacements in the plate. The WD sensors are more suitable for practical applications and are included in this test for comparison with the S9208 broadband sensors. The broadband conical transducer, powered by a PAC "wavegen" board, provided an artificial source of varying frequency. The high voltage output of the "wavegen" board produced a single cycle square wave with an amplitude of 160V, to drive the conical transducer and the frequency was varied in 100kHz increments from 100 – 900kHz. Before conducting the testing the output signal from the "wavegen" board was verified using a Digital Storage Osciliscope. One sensor was mounted adjacent to the conical transducer and a second sensor, mounted at 200mm from the conical transducer in the 0° direction (see Figure 4.7), were used to recorded the resulting signals. The test was repeated with the two sensors mounted in opposite positions. The sensors were mounted using opposed magnets (detailed in section 3.2.1) and ultrasound gel was used as a couplant. The recorded waveforms and their FFTs were used to assess the effect of source frequency on the frequency content of the resulting signal.

The investigation of DeltaT mapping grid resolution on location accuracy was conducted on a 200mm x 200mm grid constructed at the centre of the large carbon fibre plate. Eight nano30 sensors, again chosen for their small size, were arranged at a distance of 20mm from the grid boundary, one at each corner and the mid-point of each side (Figure 4.8). Time of arrival data was collected at mapping grid resolutions of 10cm, 5cm, 2cm and 1cm with a threshold level of 45dB and used to create DeltaT location grids. Four arbitrary locations were selected within the grid shown in Figure 4.8 and 5 H-N sources were performed at each location. DeltaT Locations were calculated using all four grid resolutions and compared with the TOA locations from AEwin calculated using the wave velocity measured at 45°. The location error for each DeltaT grid resolution and for the TOA locations were measured as the distance (in mm) between the actual source location and the calculated source location.

4.2.2 Results and discussion

The variation of the principal plate wave mode velocities with direction of propagation is presented in Figure 4.9. The a_0 mode shows little variation of velocity with direction having a maximum and minimum velocity of 1603m.s^{-1} in the $40°$ direction and 1499m.s^{-1} in the $90°$ direction. The velocity of the s_0 mode has a much greater dependency on direction of propagation, varying between 7429 m.s^{-1} in the $0°$ direction and 5282m.s^{-1} in the $40°$ direction. Such a variation in velocity can be the cause of location errors. As discussed in section 2.3 the often used TOA location method relies heavily on accurate arrival times and an accurate wave velocity. If the arrival of the s_0 mode is used to calculate the location it will invariably lead to errors. An example of the location accuracy of TOA in composites can be seen below where a comparison is made with the Delta T location method.

Figure 4.10 shows the attenuation by presenting the amplitude in dB of the two principal plate wave modes versus distance for a wave propagating in the $45°$ direction. A linear least squares fit of the data provided a best fit line, the gradient of which is a measure of signal attenuation with distance. The average attenuation value of the 10 signals in the each of the $0°$, $22.5°$, $45°$ and $67.5°$ material directions are shown in Table 4.2. It can be seen in Figure 4.10 and Table 4.2 that the a_0 mode has a much higher rate of attenuation than the s_0 mode. The same effect was observed by Prosser (1996) in an 8ply quasi-isotropic lay-up. The attenuation rate of the a_0 mode is so great in this material that an a_0 mode with an amplitude of 100dB will have attenuated to 40dB within 0.6m in all directions. The s_0 mode will propagate little more than 1.2m before attenuating to 40dB. The difference in the attenuation rates of the two principal plate wave modes will have a bearing on any modal analysis (such as that performed by Surgeon and Wevers (1999a), Johnson and Gudmundson (2001) and Johnson (2003)) performed on signals recorded at a distance from the source in composite materials.

The theoretical and measured dispersion behaviour of the s_0 and a_0 plate wave modes is presented in Figure 4.11 and Figure 4.12 for the $0°$ and $90°$ material directions. Excellent agreement is seen between the measured and

theoretical a_0 values in both cases. Good agreement is also seen between the measured and theoretical s_0, although not as good as that observed for the a_0 mode. Potential differences in the results may arise due to the manufacturers stated material properties (those used to calculate the theoretical dispersion curves) differing slightly different from the properties of the cured material. From the theoretical dispersion curves it can be seen that up to 400kHz the s_0 mode remains relatively non-dispersive in both cases, however above this it becomes very dispersive. The s_0 mode was only apparent in the wavelet transforms at frequencies within the non-dispersive region (<400kHz). The a_0 mode is very dispersive at low frequencies (below ~100kHz) and non-dispersive at higher frequencies (above ~100kHz) in both the $0°$ and $90°$ material directions. In the wavelet transforms the a_0 mode was apparent at low, dispersive, frequencies and up to ~400kHz where no dispersion is observed. A comparison of the measured dispersion behaviour of both the s_0 and a_0 plate wave modes in the $0°$, $22.5°$, $45°$, $67.5°$ and $90°$ material directions can be seen in Figure 4.13. Good correlation can be seen between the a_0 mode dispersion behaviour in all material directions. As discussed in section 2.2.5, this is expected because the propagation of the a_0 mode is strongly dependant on the material thickness which does not vary with material direction and also the flexural stiffness. In all directions the s_0 mode was only apparent in the wavelet transform within the non-dispersive region (<400kHz), this is reflected in the measured dispersion curves where there is very little slope to the s_0 mode data in all directions. Concurrently with the wave velocities presented in Figure 4.9, the s_0 mode propagates at the highest velocities in the $0°$ and $90°$ and the lowest velocity in the $45°$ direction, with the velocities in the $22.5°$ and $67.5°$ being in between.

The output signals measured from the "wavegen" board when instructed to produce a single cycle square wave of 100, 500 and 900kHz with a 160V amplitude are presented in Figure 4.14a, b and c, respectively, with the desired output overlaid. As the required frequency increases, the output pulse deviates increasingly from the requested square wave, however the frequency of the signals remains consistent with that requested. It can be seen in Figure

4.14c that at 900kHz there is a loss in the amplitude of the negative voltage of over 75V.

The waveforms and FFTs of the signals recorded by two S9208 sensors mounted adjacent to the conical transducer are shown in Figure 4.15a, b and c for driving pulses of 100kHz, 500kHz and 900kHz respectively. The response of both the S9208 sensors to a 100kHz driving pulse shows that most of the energy in the signal is contained below 100kHz. As the frequency of the driving pulse increases so the frequency content of the recorded signal expands to higher frequencies. The response to a 500kHz artificial source shows that the frequency content of the signals has increased with most of the energy contained below 400kHz and very little energy is seen above 600kHz. This effect is expected because an increase in frequency of the driving pulse reduces the pulse duration and hence increases the frequency content of the pulse. However as the frequency of the driving pulse is increased above 500kHz there is little increase in the frequency content of the signal, which can be seen in the response to a 900kHz source where, again, most of the energy is contained below 400kHz and very little is seen above 600kHz. When the sensors are moved away from the conical transducer the response becomes very different. Figure 4.16a, b and c show the recorded signals and their FFTs for both the S9208 sensors mounted at a distance of 200mm from the conical transducer with driving pulse frequencies of 100kHZ, 500kHz and 900kHz respectively. Both the s_0 and a_0 plate modes are observed in all the waveforms recorded at 200mm. The response of the S9208 sensors to a 100kHz driving pulse has an a_0 mode that is much larger than the s_0 mode. This is reflected in the FFT by most of the energy being contained below 100kHz, due to the lower frequency of the a_0 mode. The half cycle times for the peak of the a_0 modes equates to a frequency of approximately 52kHz and 55kHz for S9208-1 and 2 respectively. The 500kHz and 900kHz driving pulses generate a response with s_0 and a_0 modes of similar amplitude, this is reflected by the observation of higher frequencies peaks in their FFTs between 200kHz and 500kHz. The two regions of frequency content can be attributed to the fundamental plate wave modes a_0 (lower frequency) and s_0 (higher frequency). This is ratified by measuring the half cycle times for the

peak cycle of the s_0 and a_0 modes from S9208-1 for a 500kHz source, which have corresponding frequencies of 374kHz and 39kHz respectively, suggesting that geometry has a considerable effect on the frequency content of a signal. Concurrently (Hill 1976) in (Prosser 1991) observed the variation of AE feature data with geometry.

The response of two WD sensors when mounted adjacent to the conical transducer are presented in Figure 4.17a, b and c for driving pulses with frequencies of 100kHz, 500kHz and 900kHz respectively. The WD sensors response to a 100kHz driving pulse contains most of its energy below 150kHz, which is similar to the response of the S9208 sensors to the same source. As expected and also observed in the S9208 sensor response, the frequency content of the recorded signal expands to higher frequencies as the driving pulse frequency is increased. For a 500kHz driving pulse the majority of the signal energy is contained below 600kHz as opposed to below 500kHz for the S9208 sensor response to the same source. For a driving pulse of 900kHz there is still very little energy contained above 600kHz. The increase in higher frequency content is thought to be an attribute of the sensors because it is not observed for the broadband S9208 sensors and indeed the sensor calibration certificate for a WD sensor (Figure 4.3) shows a peak at approximately 525kHz. The observation of most interest from this test is the difference in response between the two WD sensors to the same source. It can be seen in Figure 4.17b that the two WD sensors have a considerably different response to a 500kHz driving pulse. The signal recorded by WD-1 has more low frequency content than that of WD-2 and its peak is approximately 100kHz. The signal recorded by WD-2 however has more high frequency content than that of WD-1 with significant content observed at approximately 475kHz and a peak at 550kHz. This demonstrates how the response of a sensor can affect the frequency content of a recorded signal and how the response can vary, even within sensors of the same model. Autieri(2007) also observed variation in the feature data recorded from a repeatable pencil lead fracture source, when using different WD sensors.

The waveforms and their FFTs, recorded by both WD sensors mounted at a distance of 200mm from the conical transducer are shown in Figure 4.18a, b and c for source driving pulses of 100kHz, 500kHz and 900kHz respectively. Both of the principal plate wave modes are observed in a signal recorded from a 100kHz driving pulse but as the frequency of the driving pulse increases the a_0 mode rapidly diminishes and for a 500kHz driving pulse is no longer observed. The FFTs of these waveforms have three distinctive peaks occurring at approximately 100kHz, 275kHz and 550kHz. The amplitudes of these peaks are seen to vary with the frequency of the driving pulse. As expected, more energy is contained in the lower frequencies for a low frequency driving pulse and more energy is contained in the higher frequencies for a higher frequency driving pulse. The lower and middle frequency peaks can be attributed to the a_0 and s_0 modes in accordance with the results presented in Figure 4.16 for the S9208 sensors. It can also be seen that as the a_0 mode loses amplitude with increasing driving pulse frequency, a corresponding reduction in the amplitude of the low frequency peak in the FFT is observed. The higher frequency peak centred about 550kHz is considered to be an artefact of the sensor because it is not observed in the results from the broad band S9208 sensors. Additionally it appears that the frequency content at this level is very different for the two WD sensors, suggesting that the frequency response of the two sensors is different. A difference in sensor response such as this could lead to confusion when considering frequency as a discriminating factor. For example the two FFTs seen in Figure 4.18b for a 500kHz driving pulse both have a peak frequency of approximately 275kHz. WD-1 has a very dominant peak at 275kHz, whereas WD-2 has a peak at 275kHz whose amplitude is only slightly larger than that of the peak at 550kHz. It is clear that a small variation in the source could quite easily produce a significantly different result from sensor WD-2. It is interesting to note that de Groot (1995), Bohse (2000) and Ramirez-Jimenez (2004) all observed frequencies in low, medium and high frequency bands using PAL WD sensors that correspond to the three frequency peaks (100kHz, 275kHz and 550kHz) seen in the FFTs in Figure 4.18. In particular the results taken from Ramirez-Jimenez (2004) presented in Figure 4.19 show how the frequency bands observed centralise around

100kHz, 275kHz and 550kHz. Suggesting that specimen geometry and sensor response played a significant part in the frequency banding observed by other researchers.

The results of the DeltaT location investigation are presented in Figure 4.20 for locations 1, 2, 3 and 4. The figure presents a comparison of the average location error for each DeltaT grid resolution and for the TOA location calculated by AEwin for each source position. It is worth noting that for TOA locations the minimum confidence in a located position is limited to the diameter of the sensors, which in this case is 8mm. The DeltaT location technique was shown to be more accurate than the TOA technique in all cases with a maximum location error of 7.7mm from the 100mm grids resolution at location1. The most notable difference is from locations 1, 2, and 3 with the average TOA location errors being 22.8mm, 17.2mm and 33.5mm respectively, resulting in 67%, 83% and 97% improvements in location error using the DeltaT technique. A high location accuracy was achieved in all cases at location 4, which is close to the centre of the grid, with the maximum location error being below 2mm, however the DeltaT technique still provided 12% improvement in location error. The TOA location algorithm is known to produce more accurate location of signals originating in the central region of a sensor array, which may explain the higher accuracy achieved by the TOA technique at this location. Additionally the proximity of the centre of the grid provided a similar location path to all four sensors of approximately $45°$, the velocity for which was used in the TOA algorithm.

4.2.3 Conclusions

It has been shown that the wave propagation in cross-ply composites is very dependant on direction, with velocity of the s_0 mode in particular varying greatly. This was shown to have an adverse effect on the accuracy of source location calculated with the TOA algorithm. However it was shown that greater location accuracy could be achieved using the DeltaT location technique.

The composite material was shown to be highly attenuative, with even large signals attenuating to below 40dB within 1.2m. This is a very important consideration when monitoring large-scale composite structures as maximum

sensor spacing maybe an issue. Additionally the two fundamental plate wave modes were shown to attenuate at different rates which could lead to erroneous results when considering the amplitude ratio of the plate wave modes at any distance from the source.

The dispersion behaviour was calculated theoretically for the $0°$ and $90°$ material directions and measured in the $0°$, $22.5°$, $45°$, $67.5°$ and $90°$ material directions. Frequencies observed in the s_0 mode were seen to be non-dispersive, whereas the a_0 mode contained dispersive low frequencies and non-dispersive higher frequencies.

Source frequency was shown to have an effect on the frequency content of the resulting signals. However it was seen that geometry and sensor response had an over-riding effect on the frequency content of the resulting waveforms. This indicates that the use of peak frequency as a signal discriminator should be approached with great care and an understanding of the sensor response and the propagation characteristics of the material are essential.

4.3 Source characterisation

4.3.1 Experimental Procedure

A series of beam buckling and tensile specimens were manufactured from ACG's HTM45/HS-135-34%RW Uni-Directional carbon fibre / epoxy pre-preg and cured in a hotpress (manufacturing details are included in Appendix D). Details of the specimen lay-ups used and the expected failure modes are shown in Table 4.3. A water-cooled, diamond tipped cutting wheel was used to cut the specimens to size and the edges were finished with emery cloth.

Six tensile specimens were cut to a width of 30mm and had an overall length of 240mm. Aluminium end tabs were bonded to the tensile specimens, with epoxy resin; in order to avoid slipping and grip noise, these reduced the unsupported length to 150mm. Monitoring of the tensile specimens was conducted with a single PAL WDi sensor (the calibration certificate of which is presented in Figure 4.21) mounted at the centre of the specimen using electrical tape and Electrolube multi purpose grease was used as a couplant. The specimen dimensions and sensor arrangement used for the tensile tests

is presented in Figure 4.22a. The specimens were held in self-tightening grips and loaded to failure under displacement control at a rate of $0.125mm.min^{-1}$ using an Avery Denison universal testing machine. AE data was recorded throughout the test using a PAC μicroDiSP system and the channel settings used are shown in Table 4.4.

The beam buckling specimens were subject to an in-plane uniaxial compressive load along their length. The long edges remain unsupported and the short edges were built-in. The loading cage seen in Figure 4.23 provides the built in supports and ensures the supports remain aligned throughout the test. The width of the six beam buckling specimens was 30mm and they had an overall length of 200mm, which was reduced to an unsupported length of 170mm once they were mounted in the loading cage. The specimens were monitored by two PAC WD sensors placed at ¼ of the length or 42.5mm from the supports, which coincides with the two inflection points and hence ensured the sensors had maximum contact with the deformed specimen. Self-adhesive tabs and zip ties, as detailed in section 3.2.1, were used to mount the sensors and ultrasound gel was provided a couplant. Details of the specimen dimensions and sensor placement are shown in Figure 4.22b. The specimens were loaded to failure at $0.5mm.min^{-1}$ and $1mm.min^{-1}$ for the (0,90) and (±45) lay-ups respectively. Data was recorded throughout the test using a PAC PCI-2 system and the channel settings used can be seen in Table 4.4. In addition to acoustic emission monitoring, full-field displacement and strain measurements were taken throughout the test using a LIMESS Digital Image Correlation (DIC) system.

4.3.2 Results and discussion

The failure of tensile specimens 1-3 ((0,90) lay-up) occurred in one of two ways. Specimens 1 and 2 failed in a straight line across the width of the specimen perpendicular to the loading direction, just inside the area enclosed by the end tabs. An example of this is shown in Figure 4.24a. The presence of matrix cracking in the thicker 90° central layer of both specimen 1 and 2, was observed at their edges with a microscope, as seen in Figure 4.24b. The failure of specimen 3 can be seen in Figure 4.24c, where the failure occurred

within the unsupported area between the end tabs. It can be seen that there is considerably more damage induced at the failure site in particular fibre/matrix debonding and matrix cracking. There was no visible evidence of damage during the tests until the final failure in any of the (0,90) specimens.

During the testing of tensile specimens 4-6 ((0) lay-up) numerous audible cracking noises were observed before the final failure in all three cases. A single longitudinal shear crack with a corresponding crack noise was observed in specimens 4 and 6 before final failure occurred. After failure all three specimens contained numerous longitudinal splits running the full length of the specimens. Fibres failed adjacent to the end tabs at both ends of specimen 4 (Figure 4.25a), leaving the majority of the specimen unattached from the end tabs. An example of the failure observed in specimens 5 and 6 is shown in Figure 4.25b, where the failure occurred adjacent to the end tabs but only at one end.

Beam buckling specimens 1-3 ((0,90) lay-up) all failed through thickness at one end, inline with the support. The failure event induced delamination between multiple plies (Figure 4.26) local to the failure, not visible prior to failure. Numerous cracking noises were observed during the test and small areas of the surface ply delaminated adjacent to the supports on the compressive side of the specimens.

Numerous audible cracking noises were observed throughout the tests of beam buckling specimens 4-6 ((±45) lay-up). Small areas of the surface plies were seen to delaminate adjacent to the supports on the compressive side of the specimen. Additionally, delamination at the mid-plies adjacent to the supports (Figure 4.27a), was observed from the edge of the specimen during all three tests. Loading was stopped for specimens 4 and 5 after the specimens failed at one end on the tensile side adjacent to the supports (Figure 4.27b). The loading of specimen 6 was stopped before failure of the tensile side. Figure 4.28 presents the curvature measured by the DIC system from beam buckling specimen 5, at the point of test when the first mid-ply delamination was observed adjacent to the supports. The maximum curvature adjacent to the supports was 0.00618mm^{-1}. The curvature values for beam

buckling specimens 4-6 ((±45) lay-up) measured at the initiation of delamination are presented in Table 4.5.

The results of the frequency analysis are presented in the same way for all of the coupon tests. The hits for each test are separated using the peak frequency recorded by AEwin into three frequency bands 0-150kHz, 150-400kHz and >400kHz. The hits within each band are then plotted cumulatively against time.

The results from tensile specimens 1-3 having a (0,90) lay-up presented in Figure 4.29a, b and c show that signals with a low frequency peak (i.e. between 0-150kHz) are the most prominent in all three tests. The expected and observed damage modes from the (0,90) lay-up tensile specimens are predominantly matrix based, i.e. matrix cracking and fibre / matrix debonding. This is in keeping with the results presented by others (section 2.4.1) in which signals with a low frequency peaks were unanimously related to matrix cracking and debonding. This is further supported by the more extensive matrix damage observed in specimen 3 being accompanied by a corresponding increase in recorded hits with low peak frequencies.

Less matrix damage and more fibre failure was expected in the tensile specimens with a (0) lay-up, Indeed the only matrix damage identified was that of the longitudinal crack that occurred during the test of specimens 4 and 6 and the multiple longitudinal cracks that occurred during the final failure of all specimens. This is reflected in the frequency results presented in Figure 4.30a, b and c for the tensile specimens with a (0) lay-up. The signals with low peak frequencies are no longer dominant and much more activity is seen at higher frequencies, in particular above 400kHz band. The increase in activity in the >400kHz band would suggest that signals with higher peak frequencies are generated by fibre failures. The results presented by others suggest that fibre failures create signals with high peak frequencies, the suggested frequencies vary from 250kHz to above 500kHz. The only exception to this is Russell and Henneke (1977) from de Groot (1995) who believed signals from fibre failures to have a peak frequency of 140kHz – 180kHz. For specimens 4 and 6 (Figure 4.30a and c) there is a rapid increase in hits recorded in all

three of the frequency bands, which corresponds to the observation of the longitudinal crack in both specimens. It is thought that fretting between the two crack surfaces could have generated the increase in low frequency hits and that the increase in high frequency hits is generated by the failure of fibre bridges between the crack surfaces.

As yet the cause of activity in the 150kHz-400kHz band has not been addressed. The previous work presented by others (section 2.4.1) has suggested that frequencies in this range may be attributed to fibre pull-out. The physical identification of fibre pull-out is very difficult, so it is not possible to confirm or refute this. It is worth noting however that the work conducted in the first half of this chapter showed that the s_0 mode generated a peak on a waveforms FFT within this range. Therefore it is not unreasonable to consider that activity in this band maybe a result of the specimen geometry and/or the sensor response. Additionally the frequency content of a signal may be further complicated by different source mechanisms occurring simultaneously, for example a fibre break is likely to be accompanied by some fibre pull-out or movement.

The frequency analysis results from the beam buckling tests are presented in the same way as above, the only difference being that the results from the two channels are presented separately. In doing so, the complications that sensor response can introduce in this type of approach to source characterisation will be highlighted.

The frequency analysis results from the beam buckling specimens 1, 2 and 3 with a (0,90) lay-up are presented in Figure 4.31, Figure 4.32 and Figure 4.33 respectively. It can be seen that in all three tests there is a considerable amount of activity in the low frequency 0-150kHz band which has been previously attributed to matrix damage. The delamination of surface plies adjacent to the supports is a contributing factor to this, additional matrix cracking is likely to have occurred internally. The delamination observed post-failure is believed to have occurred during the final failure, this is concurrent with the sharp increase observed in hits recorded in the 0-150kHz frequency band at the end of the tests. Of more interest is the activity in the 150-400kHz

and >400kHz frequency bands. For channel 1 of specimen 1 (Figure 4.31a) the most activity is seen in the 150-400kHz band and the least activity is seen in the >400kHz band, whereas for channel 2 (Figure 4.31b) the most activity is seen in the >400kHz band and the least activity is seen in the 150-400kHz band. Indeed the rate of hits recorded on channel 1 between 150-400kHz is very similar to that of hits recorded above 400kHz on channel 2 and vice versa. A similar effect is observed in both specimen 2 and 3. The two WD sensors used for these tests are the same two sensors used in the first half of this chapter to assess the sensor response to different frequency sources. Figure 4.18 shows how the different sensors can produce a different response to the same source. In particular Figure 4.18b shows that for the same source the peak frequency might lie in either the 150-400kHz band or the >400kHz band depending on the sensor. These results highlight the effects that individual sensor response can have on the frequency content of a signal and the potential confusion it can cause, even for sensors of nominally the same frequency response.

The results of the beam buckling specimens 4, 5 and 6 with a (±45) lay-up, seen in Figure 4.34, Figure 4.35 and Figure 4.36 respectively, show the activity in the 0-150kHz band to be dominant in all cases. This is as expected due to the greater amount of matrix damage observed in the form of delamination during the tests of the (±45) lay-up specimens compared with those of (0,90) lay-ups. The same effect is observed in specimens 4-6 whereby the hit rate in the 150-400kHz band on one sensor is similar to that of the >400kHz band on the other and vice versa. As above this is attributed to a difference in sensor response.

The amplitude ratio, i.e. the ratio of s_0/a_0 amplitudes, was calculated for signals from all the coupon tests. The amplitude of the plate wave modes were measured manually and, due to limits in processing time, only signals with an amplitude of 80dB or greater were considered. The results are presented as a distribution of the amplitude ratio of signals within a test.

The distribution of amplitude ratios from the tensile tests with a (0,90) lay-up are presented in Figure 4.37. It can be seen that the amplitude ratios from

these tests are quite widely distributed with most of the activity having ratios between 0.5 and 4.0. Signals with low amplitude ratios (i.e. less than 1) recorded during tensile tests have previously been attributed to grip noise by Gorman and Ziola (1990b), Prosser et al (1995), Prosser (1996) and Surgeon and Wevers (1999a). This would explain the presence of so many signals with low amplitude ratios from a specimen that should produce predominantly in-plane failure mechanisms, normally associated with higher s_0/a_0 amplitude ratios. The signals with higher amplitude ratios can be attributed to the observed in-plane damage mechanisms, in particular matrix cracking. The amplitude ratios of signals are distributed about an approximate centre of 2.5, which is the amplitude ratio quoted by Surgeon and Wevers (1999a) for a matrix crack. The wide distribution of the amplitude ratios is likely to be a result of either the position within the cross-section at which the cracking occurred or the distance of propagation from source to sensor.

The amplitude ratio distributions for the beam buckling specimens with a (0,90) lay-up are presented in Figure 4.38. As for the tensile tests, the amplitude ratios are quite widely distributed, however for the beam buckling tests there is a general shift towards the lower ratios, with most of the activity having ratios between 0 and 2.75. The presence of lower amplitude ratios is expected due to the observation of surface ply delamination during the tests. The higher amplitude ratios can again be attributed to in-plane matrix damage and the shift towards lower amplitude ratios is thought to be a result of the damage mechanisms occurring asymmetric to the mid-plane of the specimen due to its curvature. As discussed in section 2.4.2, an in-plane source occurring asymmetrically to the mid-plane of a plate is expected to produce a signal with increased amplitude of the a_0 mode.

The amplitude ratio distribution of signals recorded during the beam buckling tests for specimens with a (±45) lay-up is considerably different, with most of the activity having amplitude ratios below 0.75. This is attributed to the extensive amount of delamination observed during the tests and is in keeping with the literature in section 2.5.2 that suggests a source mechanism with out-of-plane displacement will produce signals with large a_0 modes.

Figure 4.40 presents a comparison of the sum of all the hits from each different test where it is clear to see how the amplitude ratios differ for the source mechanisms observed with different orientations.

4.3.3 Conclusions

It has been shown that the peak frequency of an AE signal can be used to provide some information about its source. However it has been demonstrated how the overriding effects of geometry and sensor response can produce misleading results. As such this technique should be approached with great care and an understanding of the wave propagation and sensor response for a specific case is essential.

The amplitude ratio of signals from coupon specimens have been successfully used to distinguish between in-plane matrix cracking source mechanisms and out-of-plane delamination source mechanisms.

4.4 Summary

Due to the improvements in source location accuracy observed, it was decided that the DeltaT location methodology would be utilised for all large scale tests. A grid resolution of 50mm was selected, because it offered the best combination of data collection required and confidence of location.

The use of peak frequency content as a signal discriminator was shown to be potentially misleading due to its dependency on geometry and sensor response. For this reason the use of frequency as a signal discriminator was abandoned and the MAR of signals was selected for use during further testing. Additionally the propagation behaviour of AE signals is to be used to aid the interpretation of MAR results.

Table 4.1 - Wavelet set-up

Maximum Frequency (kHz)	800
Frequency Resolution (kHz)	10
Wavelet Size (samples)	500
Number of Samples	8192
Offset Samples	0
Wavelet table scale factor	1

Table 4.2 – Average attenuation of plate wave modes

Propagation Direction (Degrees)	s_0 Attenuation (dB.m^{-1})	a_0 Attenuation (dB.m^{-1})
0	41	110
22.5	51	105
45	43	104
67.5	60	100

Table 4.3 - Details of Specimen Lay-ups

Specimen Type	Specimen Numbers	Lay-up	Nominal Thickness	Expected Failure Modes
Tensile	5-7	$(0)_8$	1.08mm	Fibre breakage Matrix cracking
Tensile	1-3	$((0,90)_2)_s$	1.08mm	Matrix cracking Fibre/matrix debonding Fibre breakage
Beam Buckling	1-3 and 7-9	$((0,90)_4)_s$	2.16mm	Matrix cracking Fibre/matrix debonding Fibre breakage
Beam Buckling	4-6 and 10-12	$((\pm45)_4)_s)$	2.16mm	Matrix cracking Fibre/matrix debonding

Table 4.4 – Channel settings

Tensile tests								
Channel	Threshold (dB)	Analogue Filter	Sample Rate	Pre-Trigger (μs)	Hit Length	PDT (μs)	HDT (μs)	HLT (μs)
1 (WDi)	45	20kHz-2MHz	10MSPS	100	6k	20	40	40
Beam buckling tests								
Channel	Threshold	Analogue Filter	Sample Rate	Pre-Trigger (μs)	Hit Length	PDT (μs)	HDT (μs)	HLT (μs)
1 & 2 (WD)	45	20kHz-2MHz	10MSPS	100	6k	20	40	40

Table 4.5 - Curvature values at delamination initiation for beam buckling specimens 4-6

Specimen	Curvature Value (mm^{-1})
4	0.00648
5	0.00618
6	0.00650
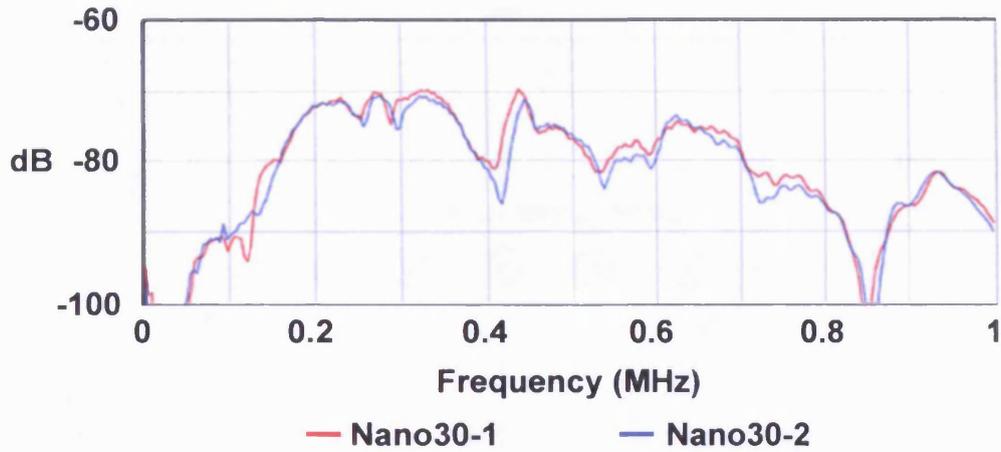
Figure 4.1 - Calibration certificates for two PAC Nano30 sensors
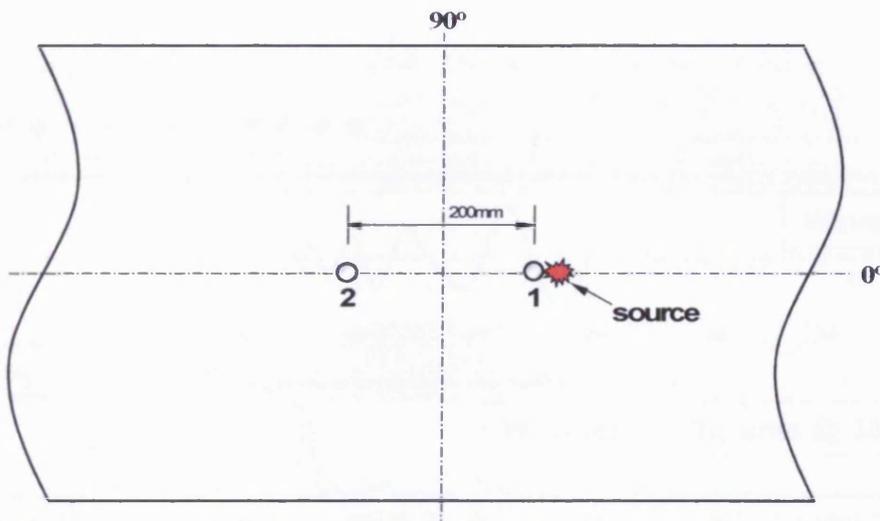
Figure 4.2 - Arrangement of sensors for velocity measurement
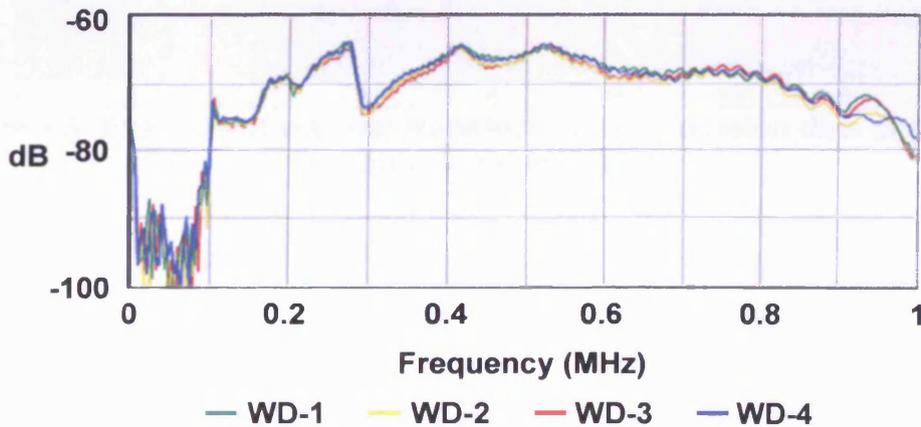
Figure 4.3 - Calibration certificates for four PAC WD sensors
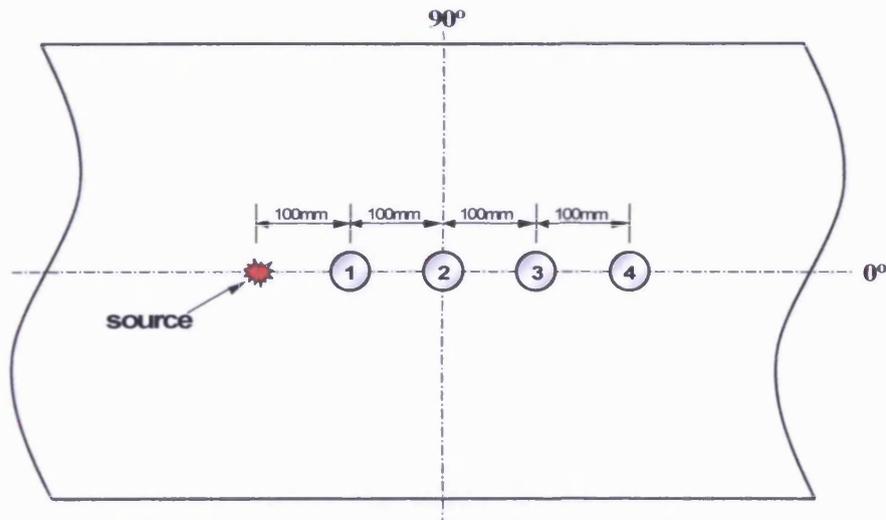
Figure 4.4 - Arrangement of sensors for attenuation measurement
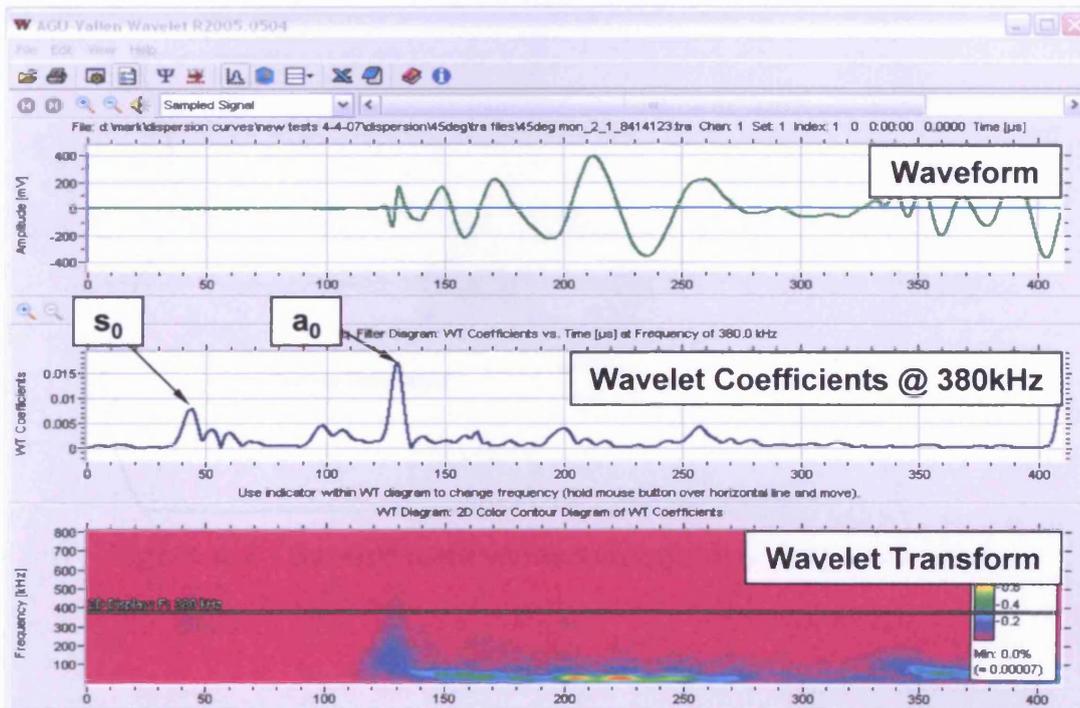
Figure 4.5- Example of wavelet transform and dispersion data extraction (time scale in µs)
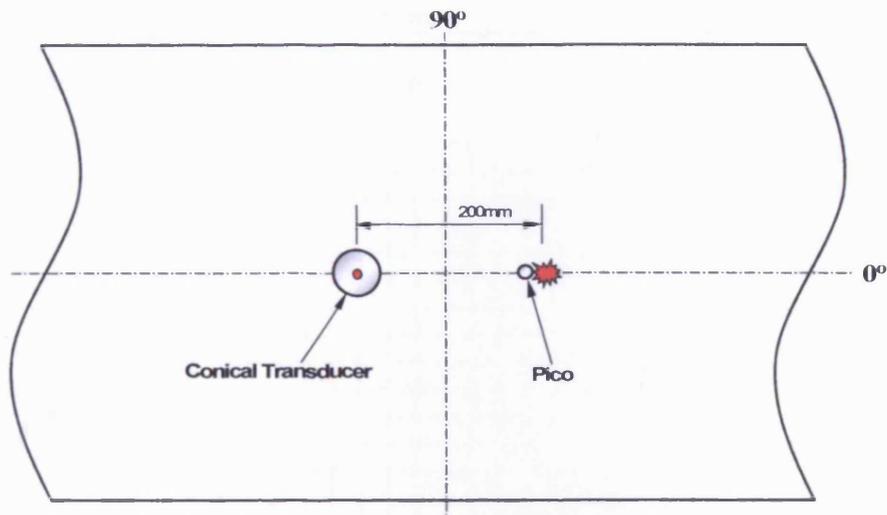
Figure 4.6 - Sensor arrangement for dispersion measurement
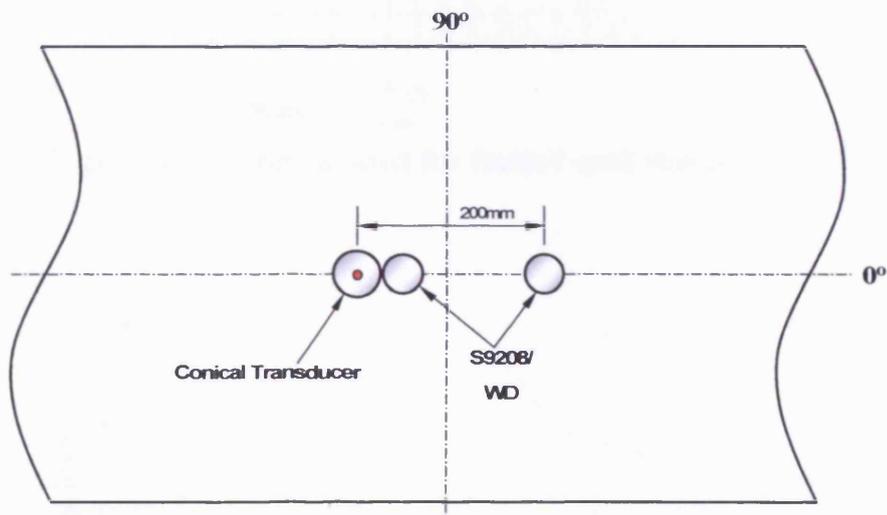
Figure 4.7 - Sensor arrangement for sensor response tests
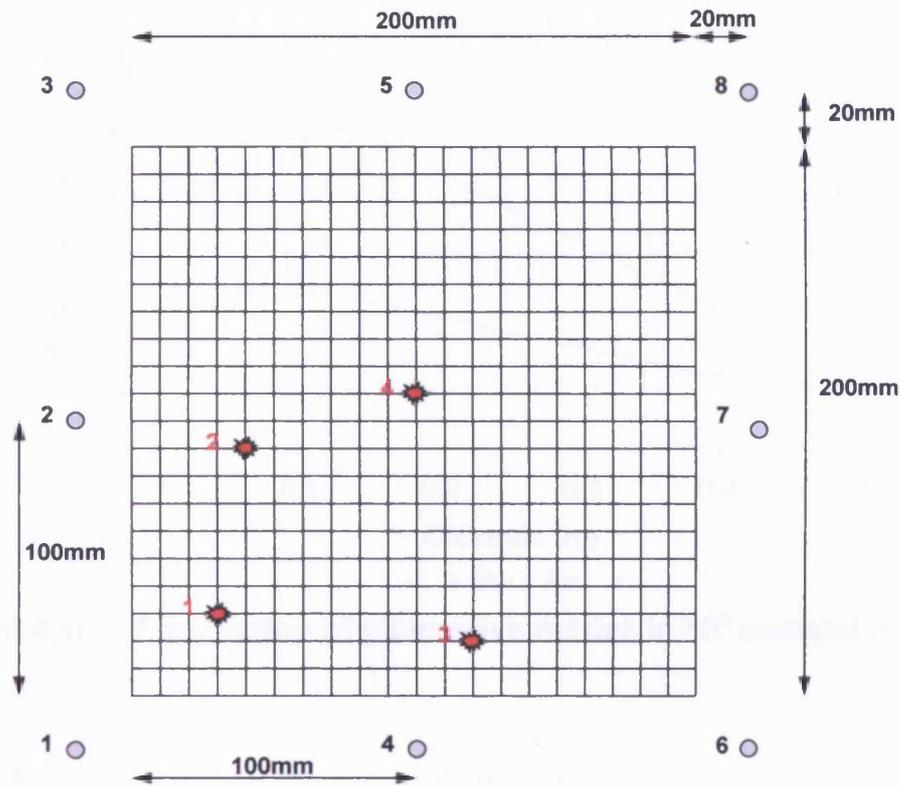
Figure 4.8 - Grid lay-out for DeltaT grid resolution tests
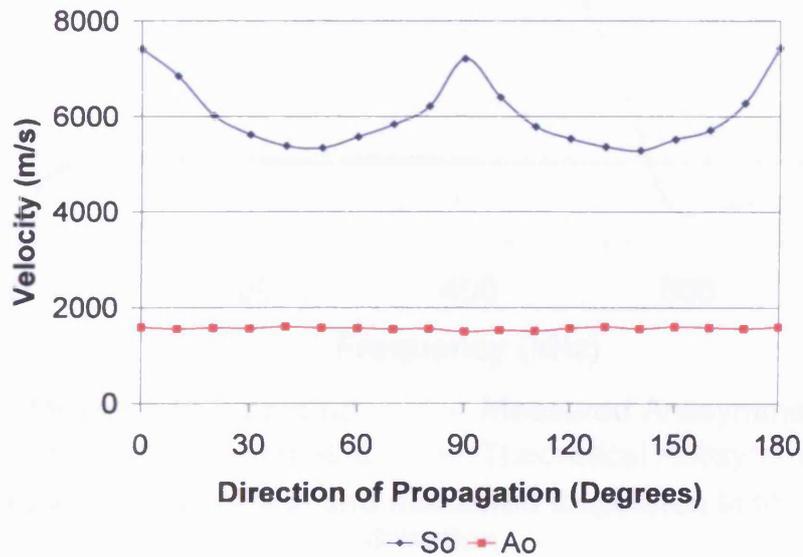
Figure 4.9 - Velocity of principal plate wave modes versus direction of propagation
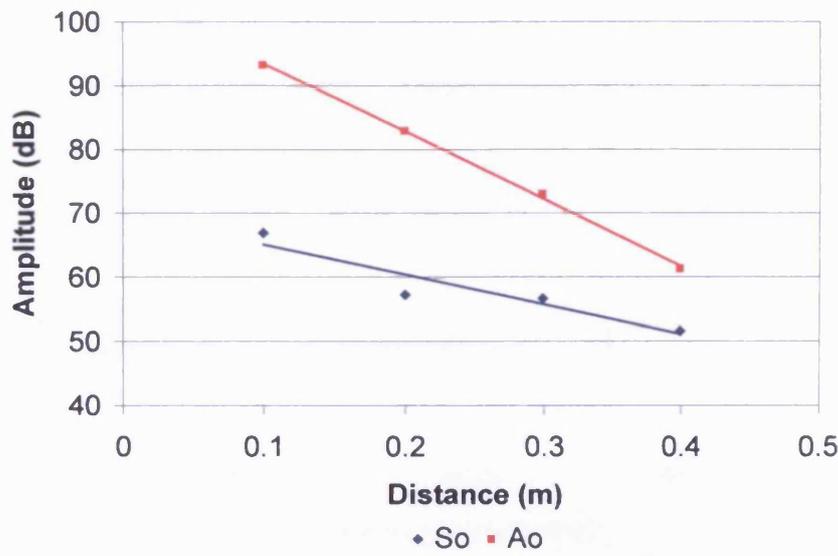
Figure 4.10 – Attenuation of plate wave modes in 45° material direction
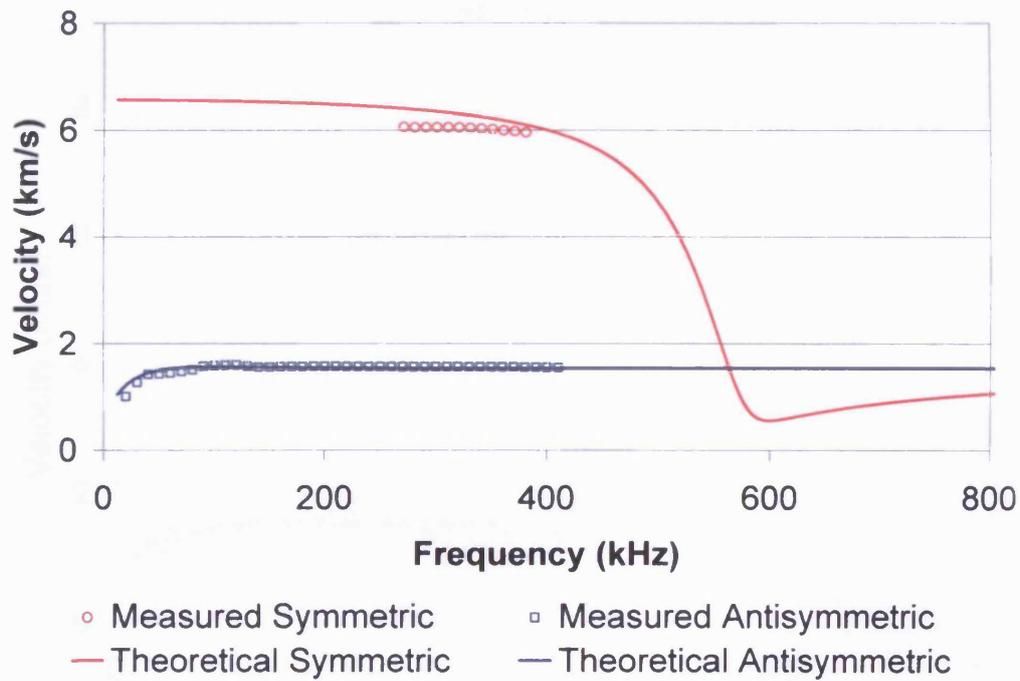
Figure 4.11 - Theoretical and measured dispersion in 0° material direction
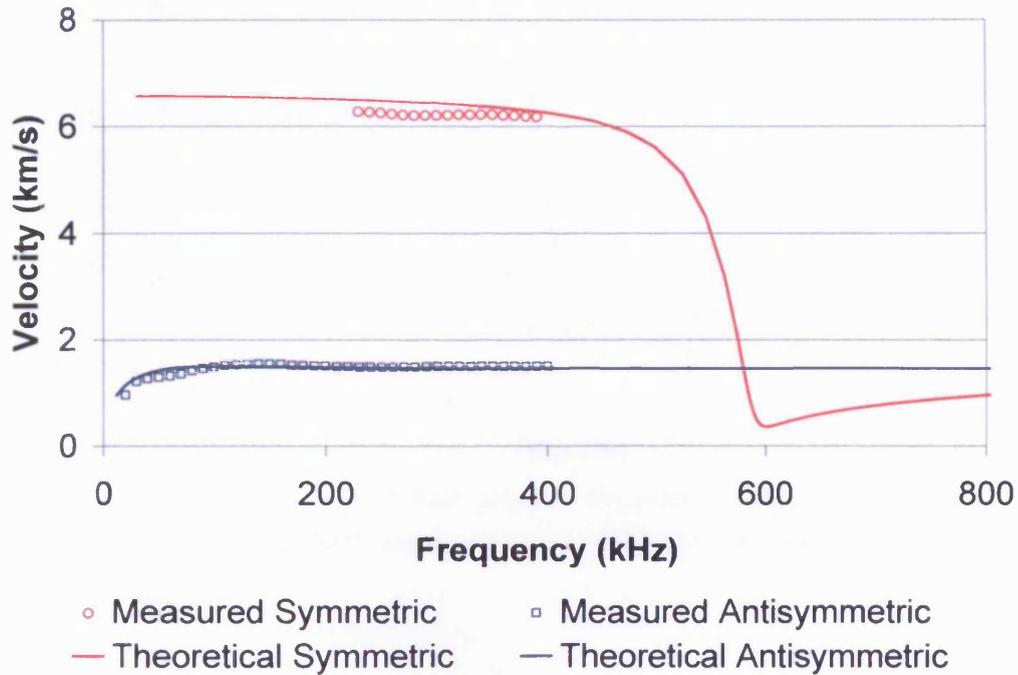
Figure 4.12 - Theoretical and measured dispersion in 90° material direction
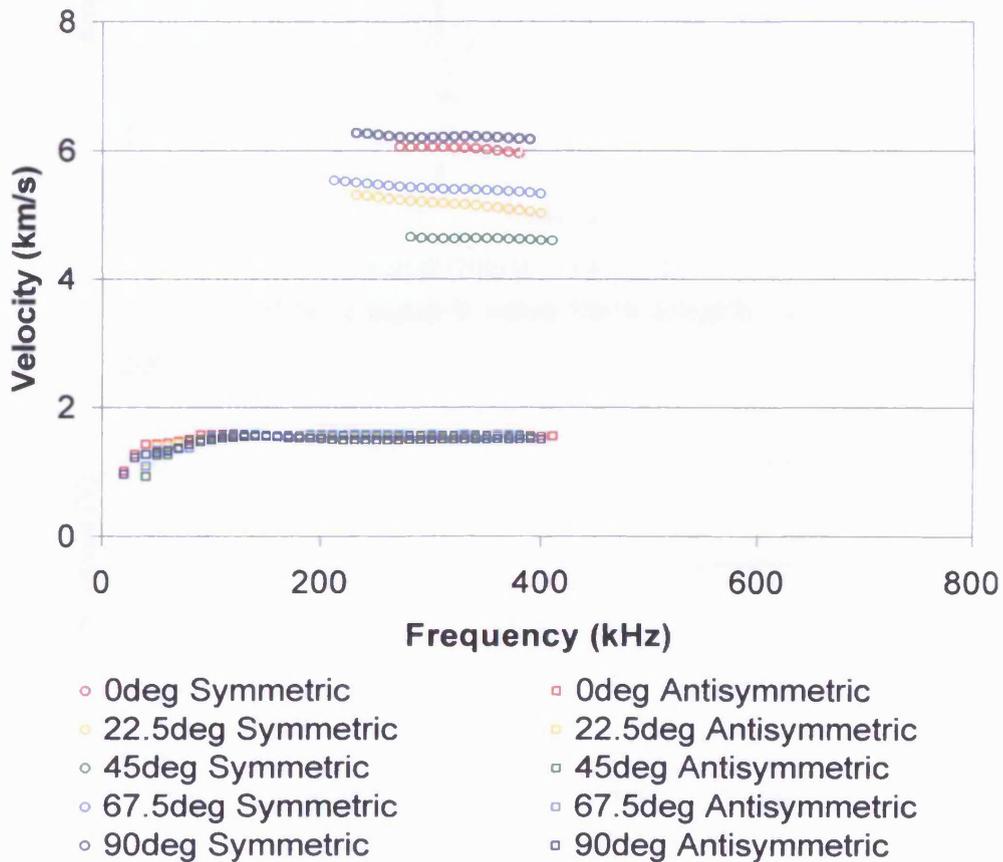
Figure 4.13 - Comparison of measured dispersion in 0°, 22.5°, 45°, 67.5° and 90° material directions
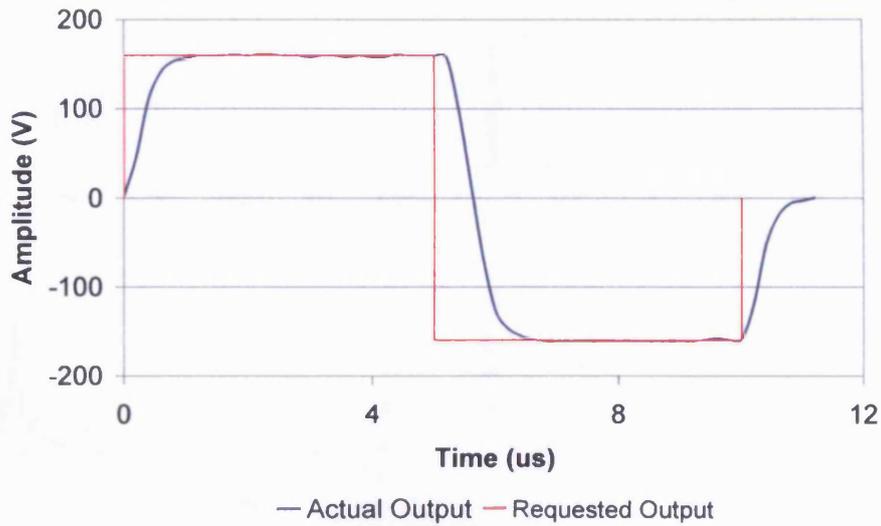
a) 100kHz square wave 160V amplitude
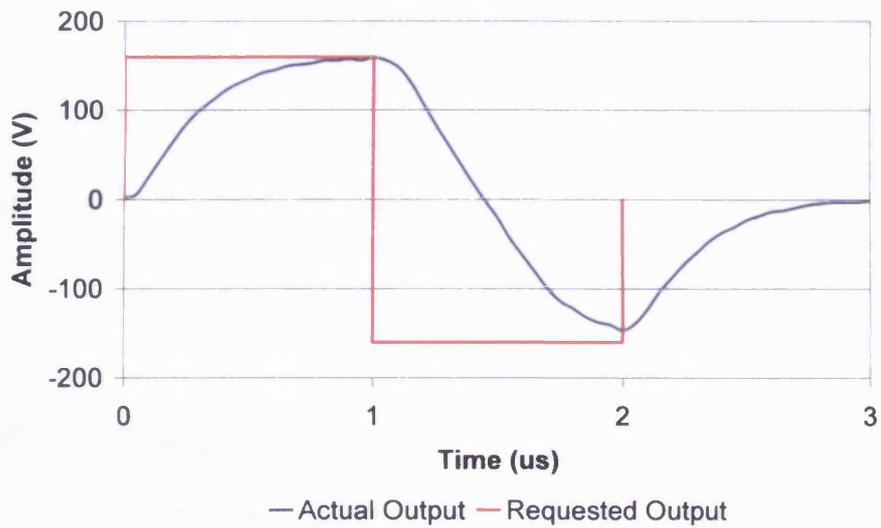
b) 500kHz square wave 160V amplitude
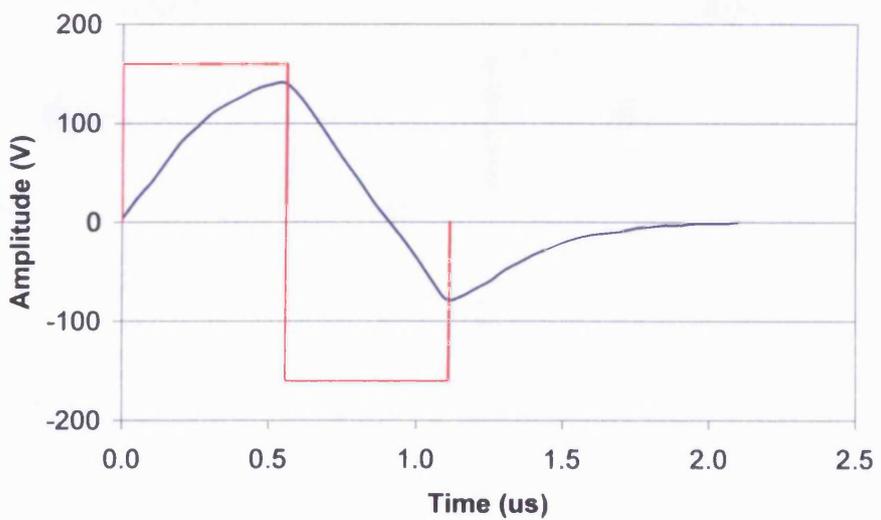
c) 900kHz square wave 160V amplitude
Figure 4.14 - Measured PAC "Wavegen" output

a) 100kHz source

b) 500kHz source
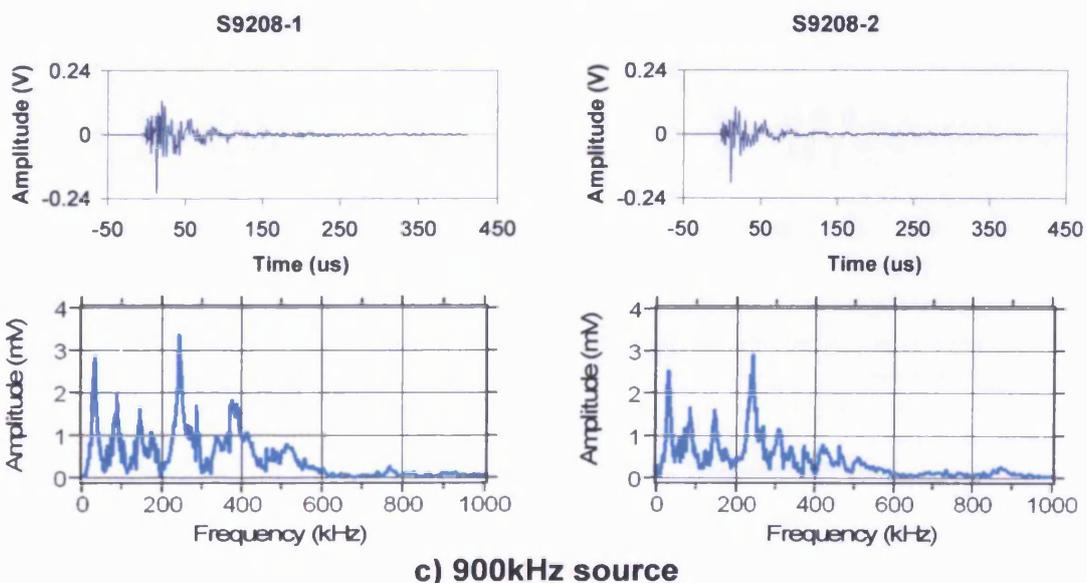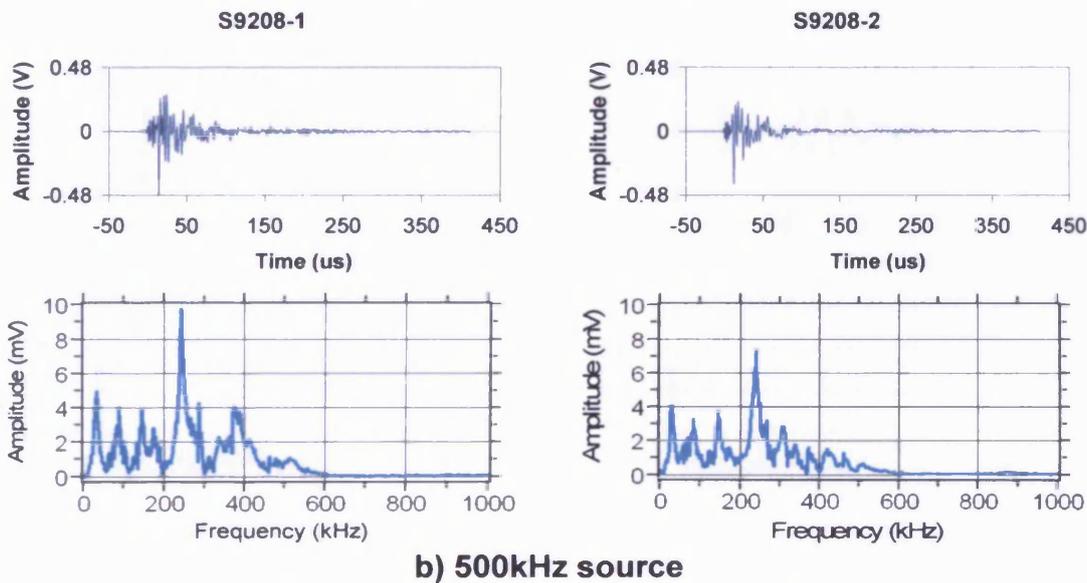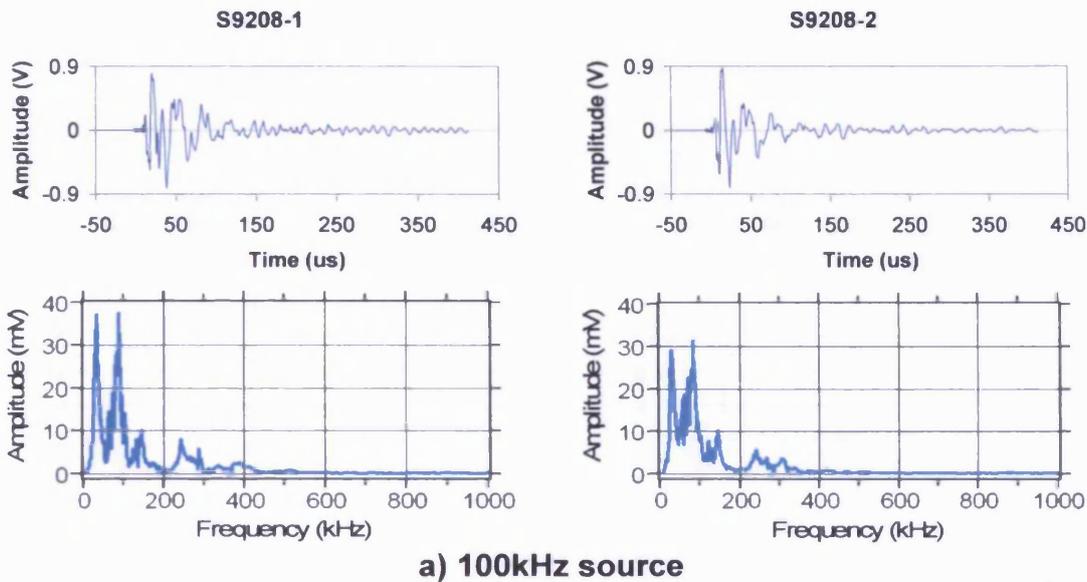
c) 900kHz source

Figure 4.15 - Waveforms and FFTs recorded by S9208 1 and 2 adjacent to 100kHz, 500kHz and 900kHz sources
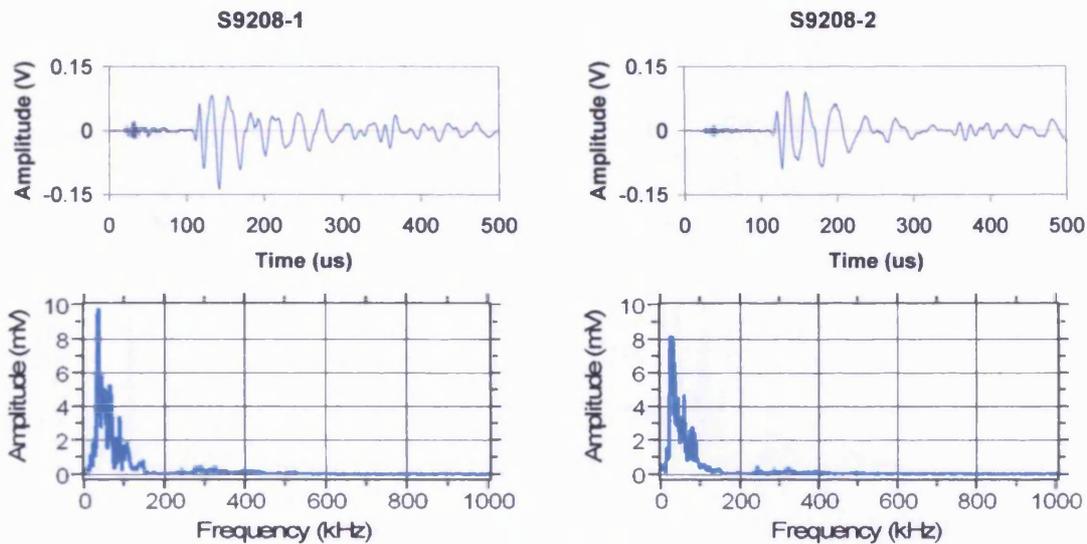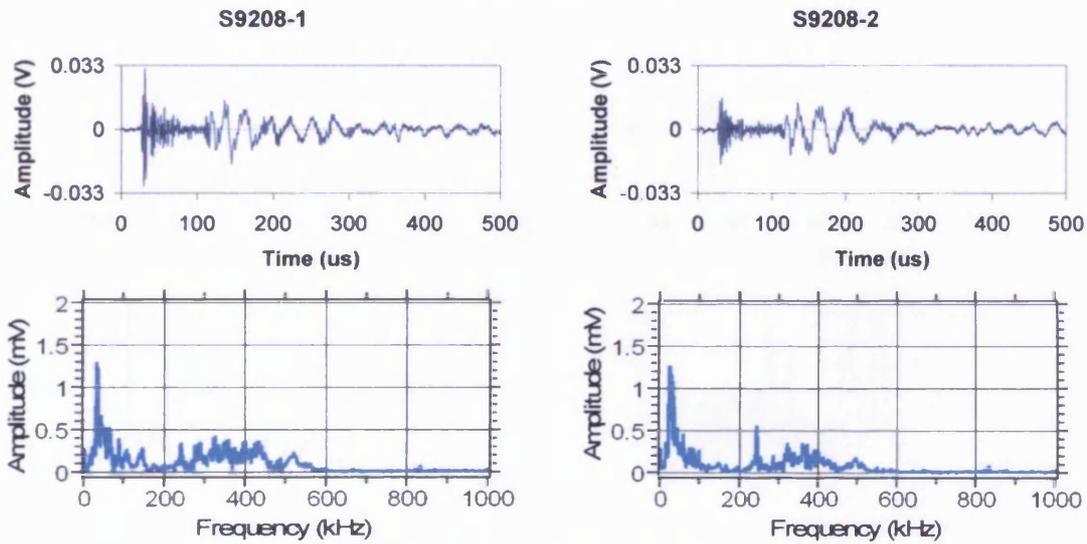
a) 100kHz source
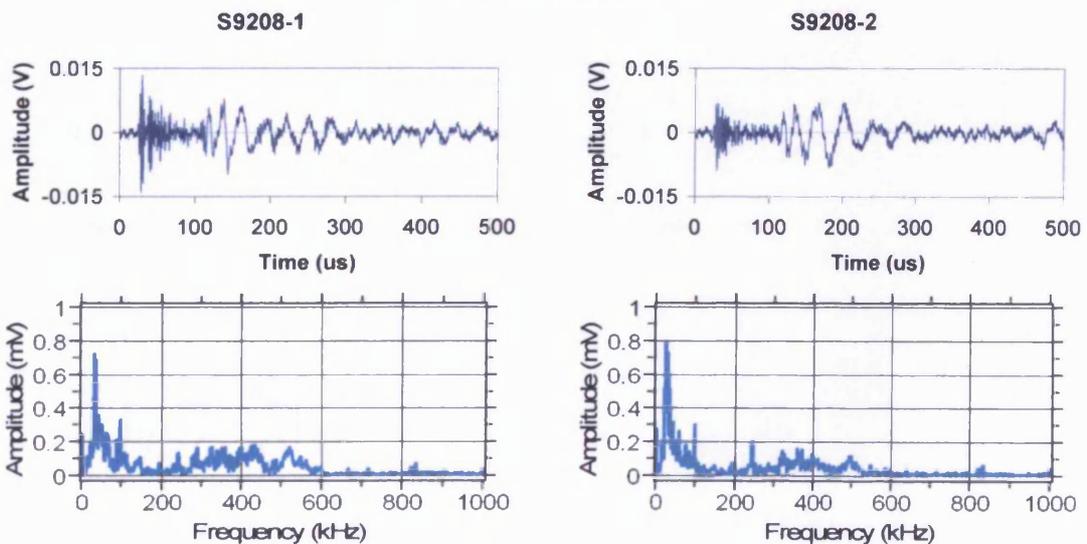
b) 500kHz source

c) 900kHz source

Figure 4.16 - Waveforms and FFTs recorded by S9208 1 and 2 at 200mm from 100kHz, 500kHz and 900kHz Sources

a) 100kHz source

b) 500kHz source
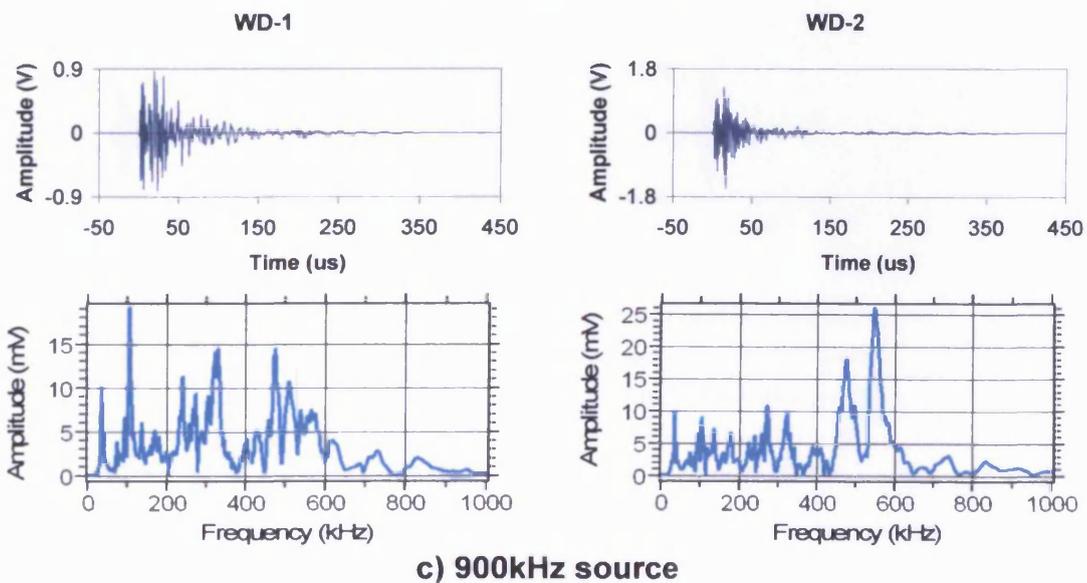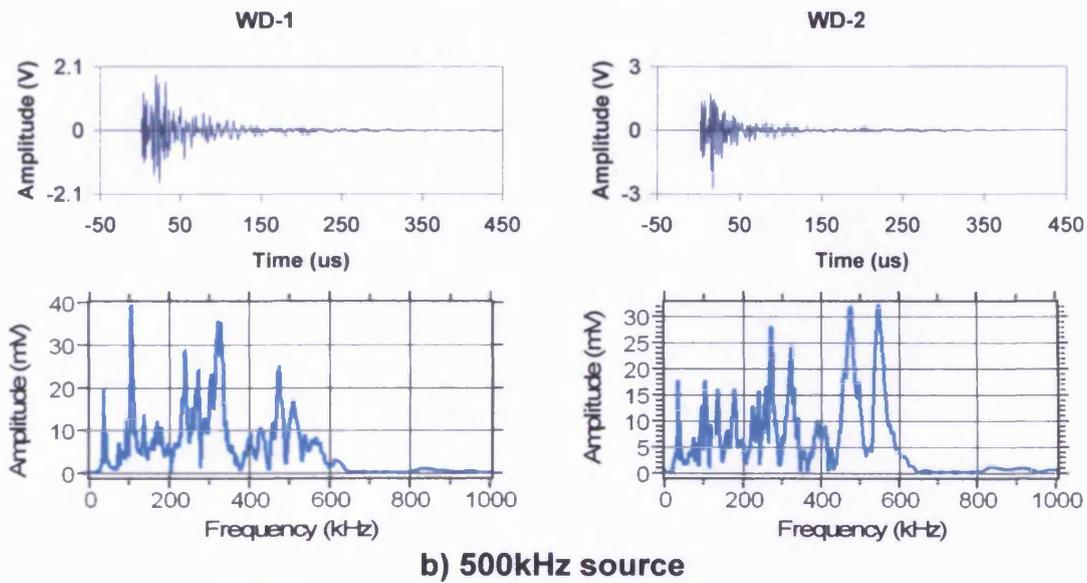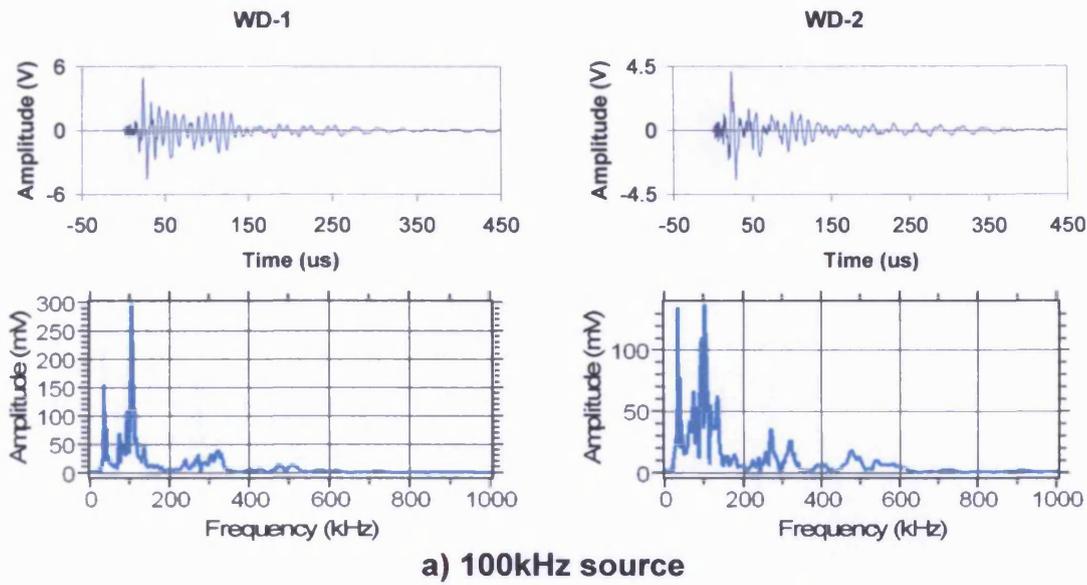
c) 900kHz source

Figure 4.17 - Waveforms and FFTs recorded adjacent to artificial source by WDs 1 and 2
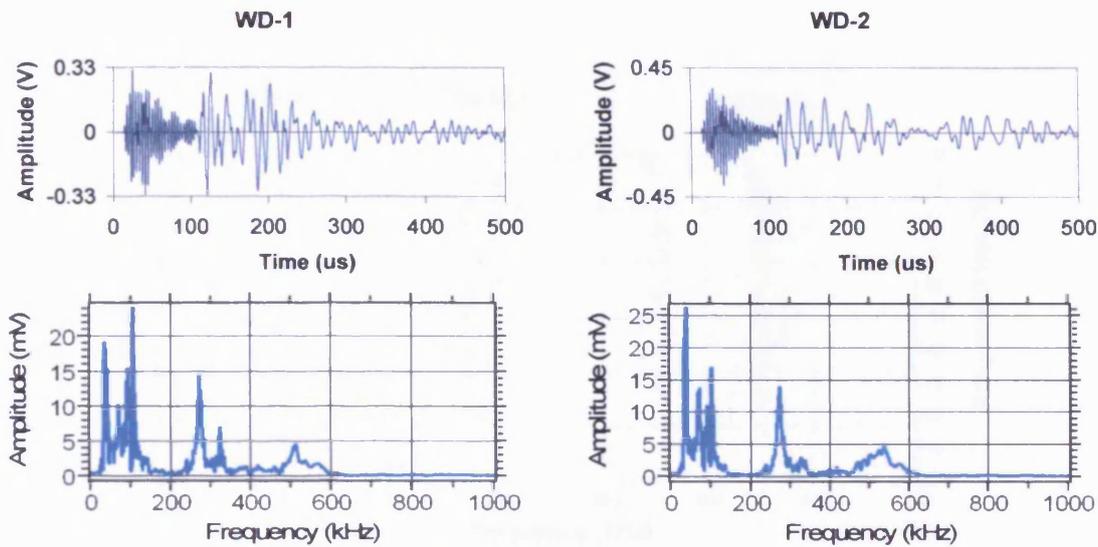
a) 100kHz source
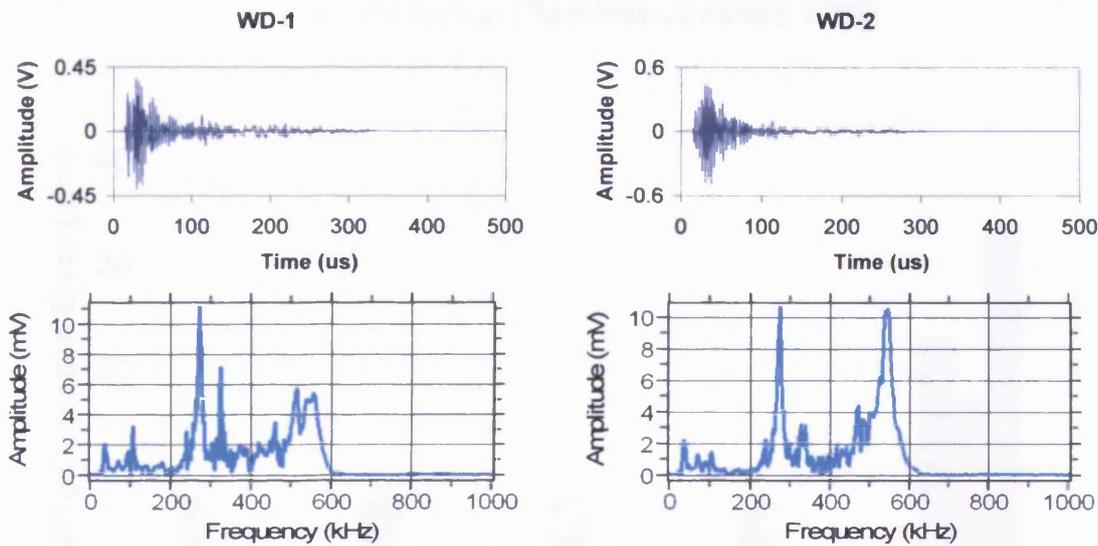
b) 500kHz source
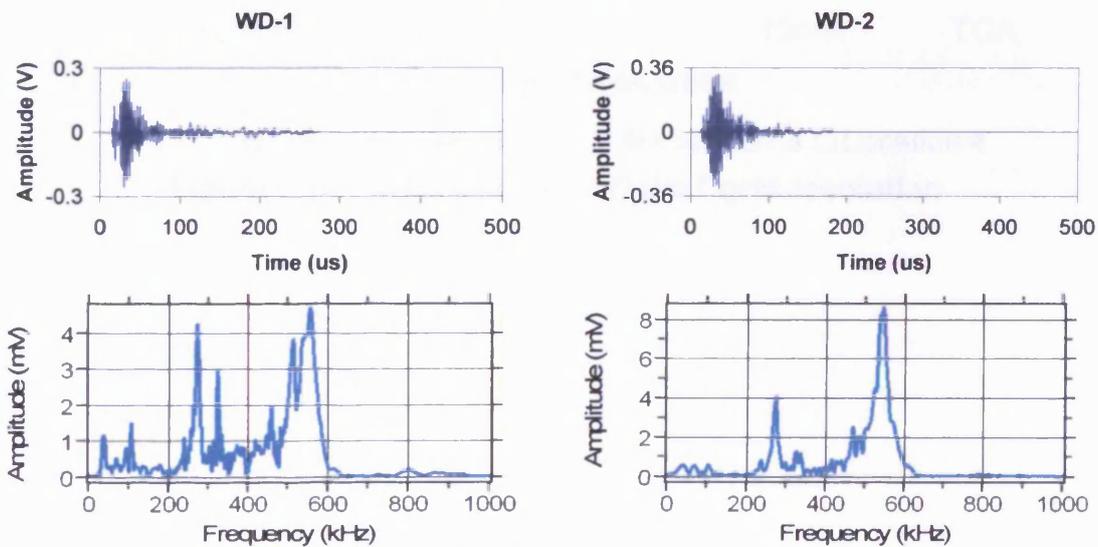
c) 900kHz source

Figure 4.18 - Waveforms and FFTs recorded 200mm from artificial source by WD 1 and 2
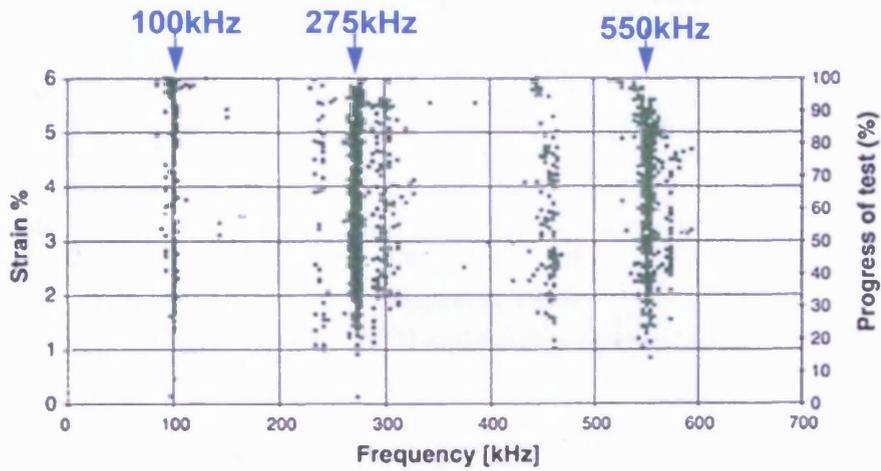
Figure 4.19 - Time of test versus peak frequency from a uni-directional tensile specimen (Ramirez-Jimenez 2004)
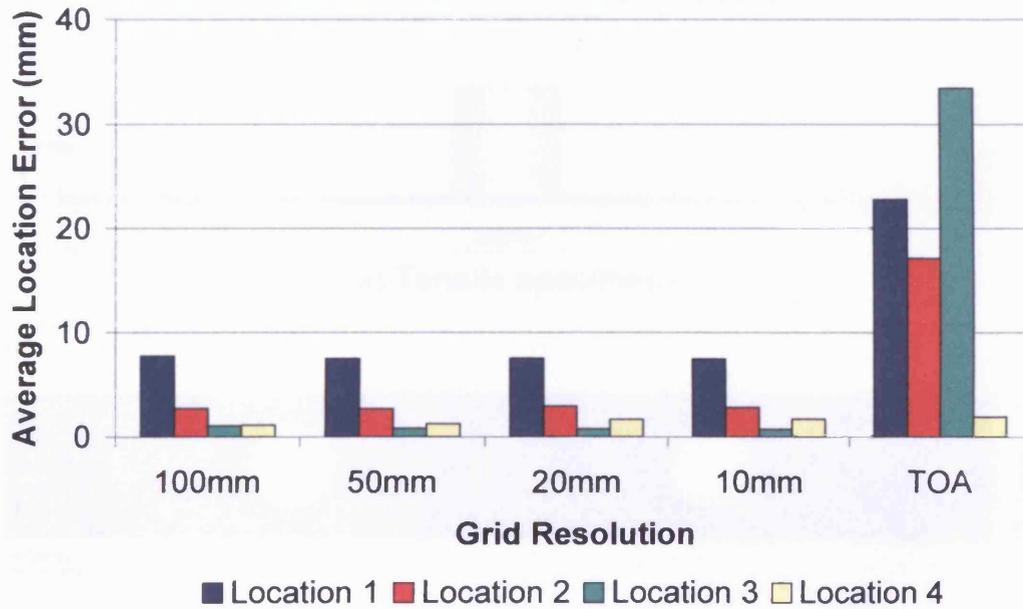
Figure 4.20 - Comparison of DeltaT grid resolution
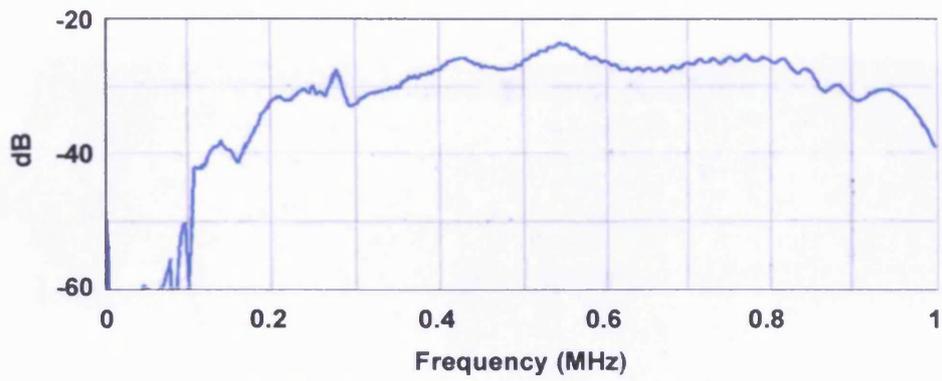
Figure 4.21 - WDi calibration certificate

a) Tensile specimens

b) Beam buckling specimens
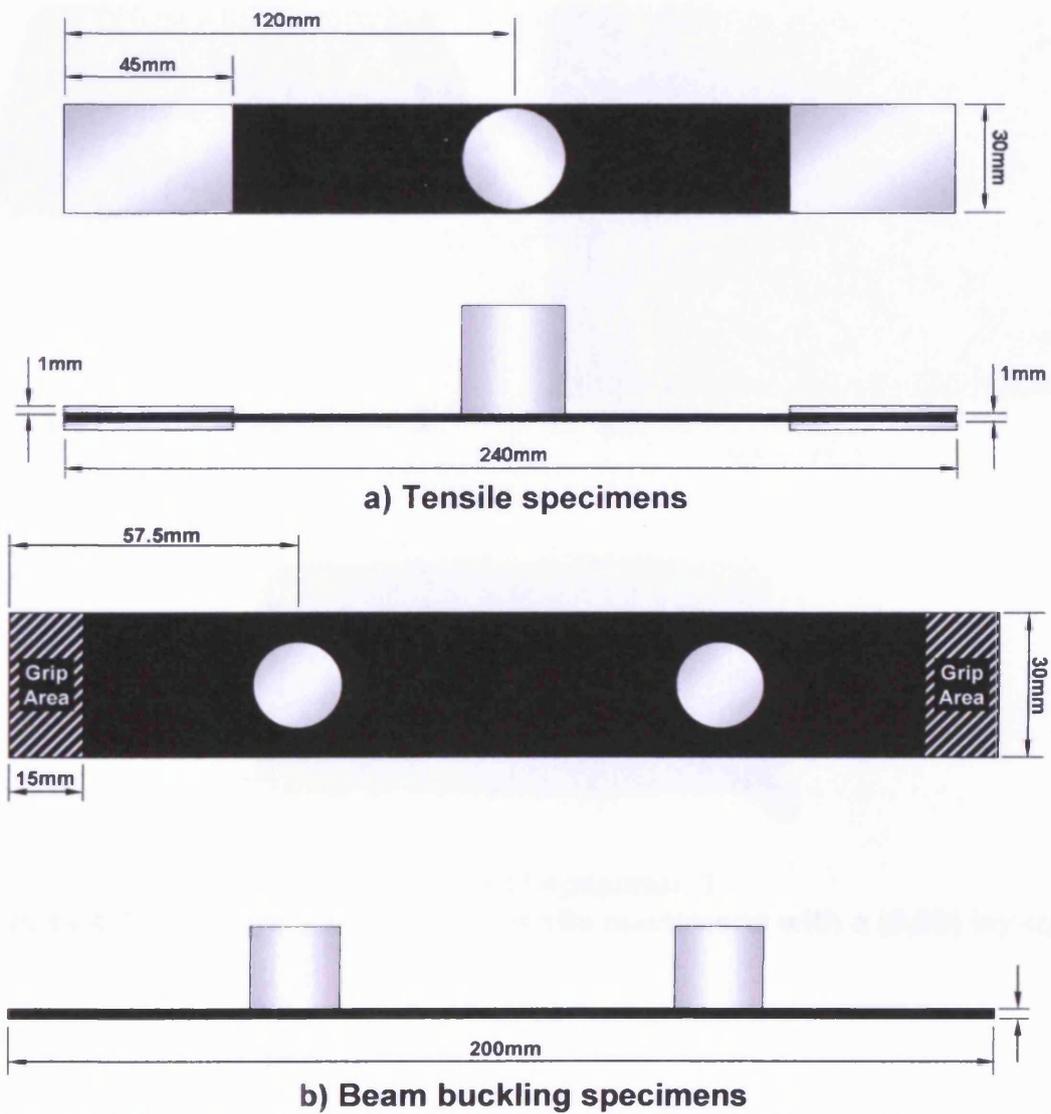
Figure 4.22 - Specimen dimensions and instrumentation a) Tensile b) Beam buckling
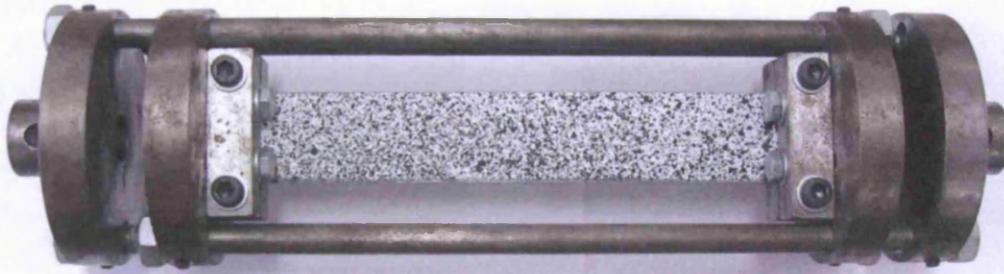
Figure 4.23 - Loading cage for beam buckling specimens

(a) Failure of specimen 2
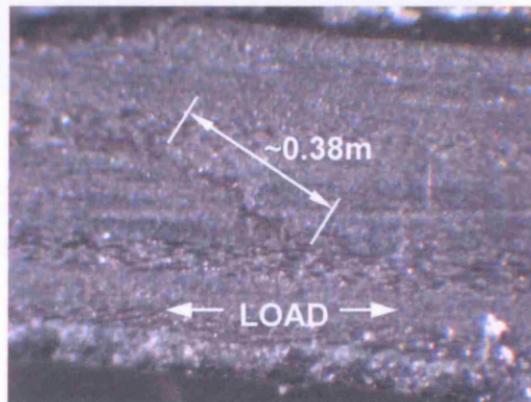
(b) Matrix crack observed in specimen 2
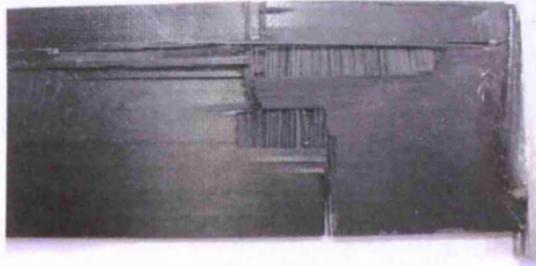
(c) Failure of specimen 3
Figure 4.24 - Failure observed in tensile specimens with a (0,90) lay-up
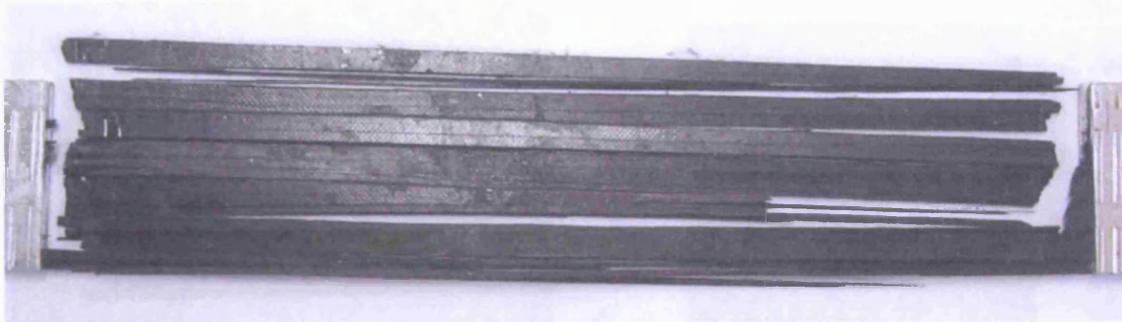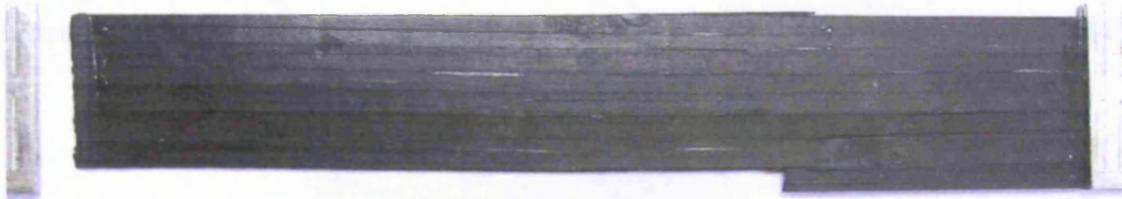
(a) Specimen 4

(b) Specimen 5
Figure 4.25 - Failure observed in (0) tensile specimens
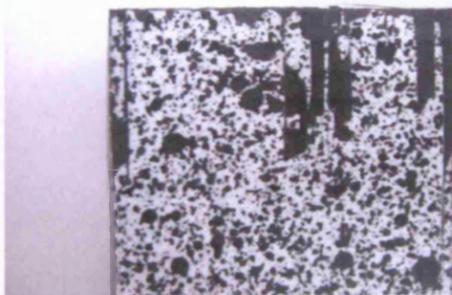
a)
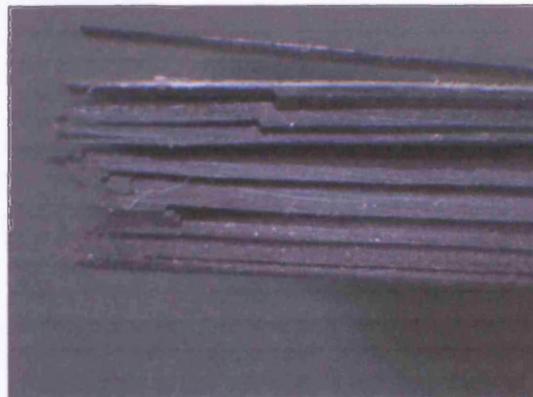
b)
Figure 4.26 - Failure observed in beam buckling specimens with a (0,90) lay-up
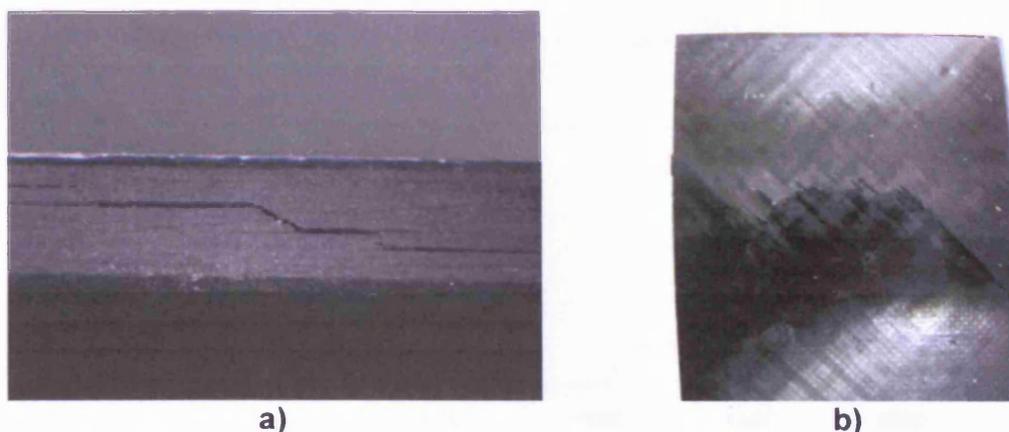
a)   b)

Figure 4.27 - Damage observed in beam buckling specimens with a (±45) lay-up
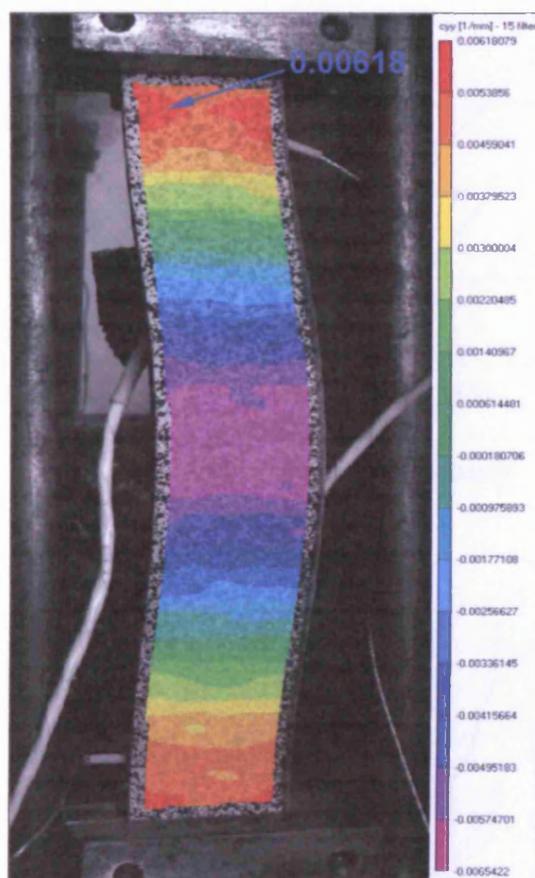
Figure 4.28 - Beam buckling specimen curvature
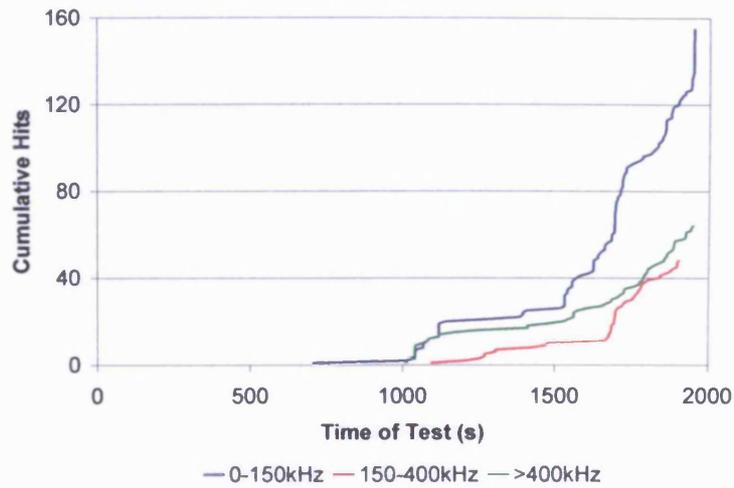
a) Specimen 1
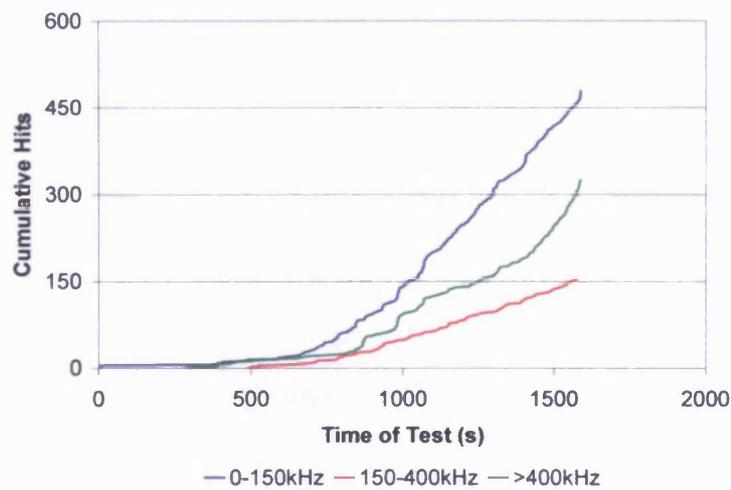
b) Specimen 2
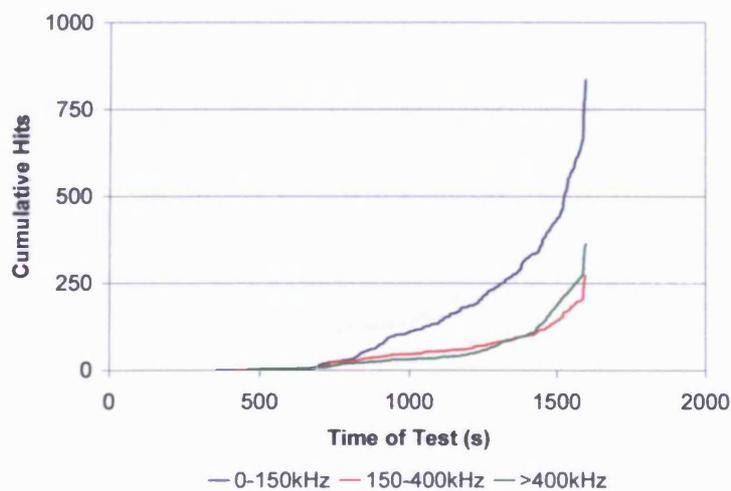
c) Specimen 3

Figure 4.29 - Cumulative hits versus time for tensile specimens with a (0,90) lay-up
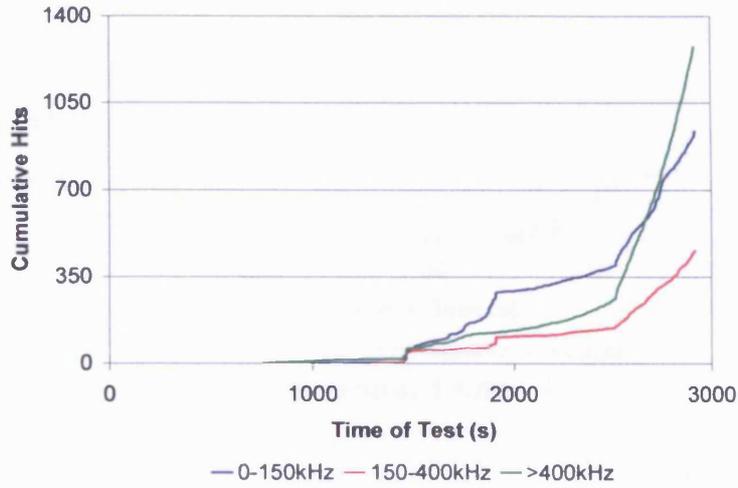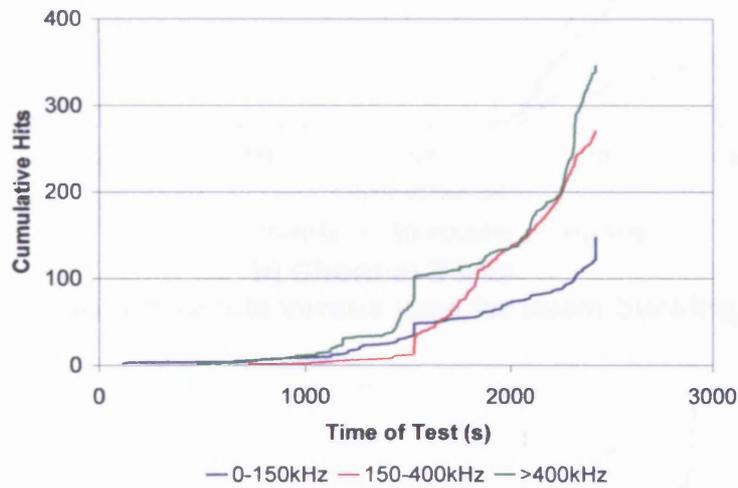
a) Specimen 4
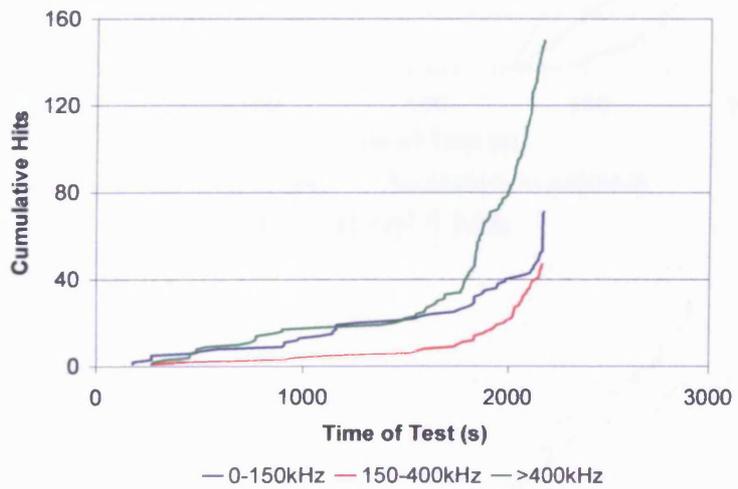
b) Specimen 5

c) Specimen 6

Figure 4.30 - Cumulative hits versus time for tensile specimens with a (0) lay-up

a) Channel 1 hits
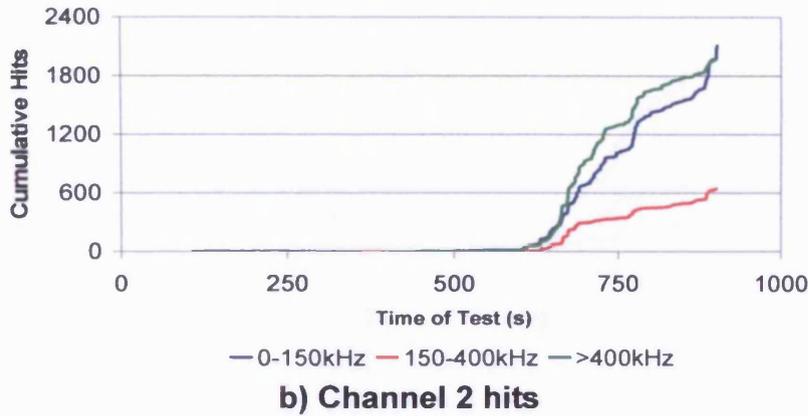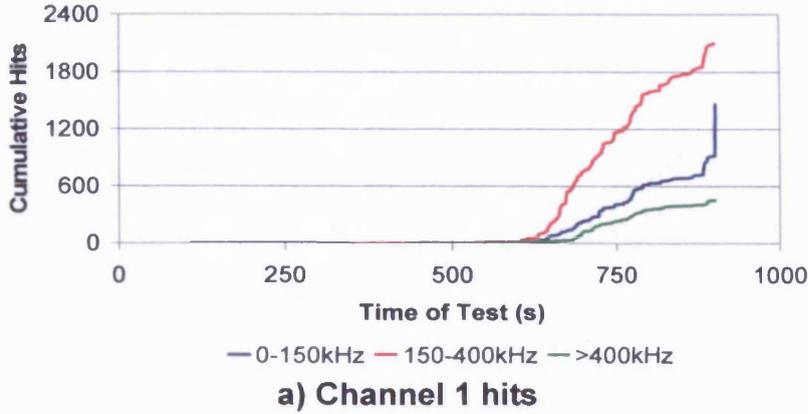
b) Channel 2 hits

Figure 4.31 - Cumulative hits versus time for beam buckling specimen 1

a) Channel 1 hits
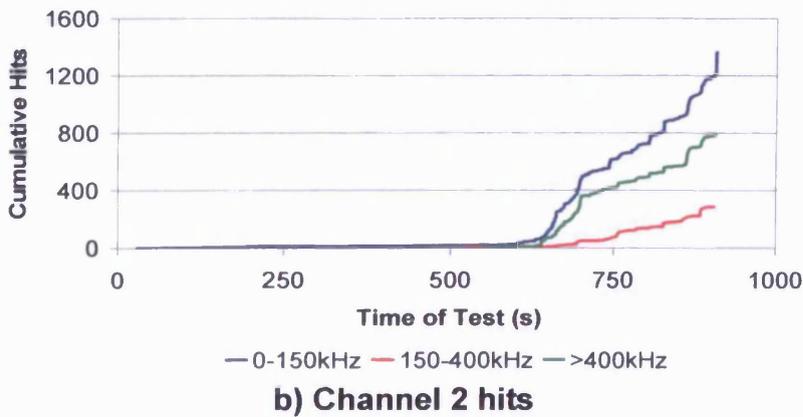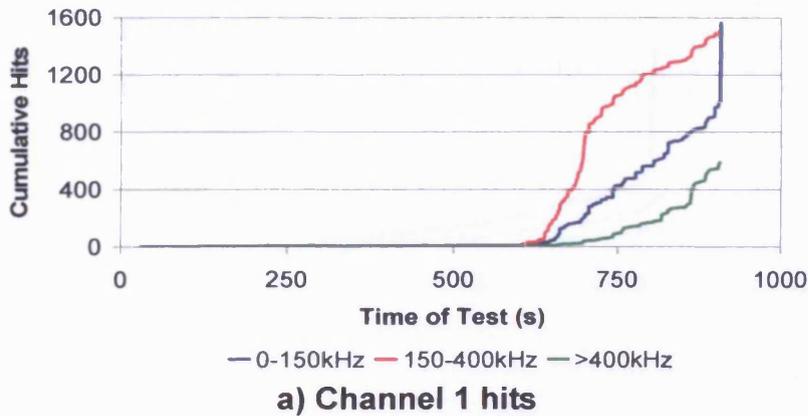
b) Channel 2 hits

Figure 4.32 - Cumulative hits versus time for beam buckling specimen 2
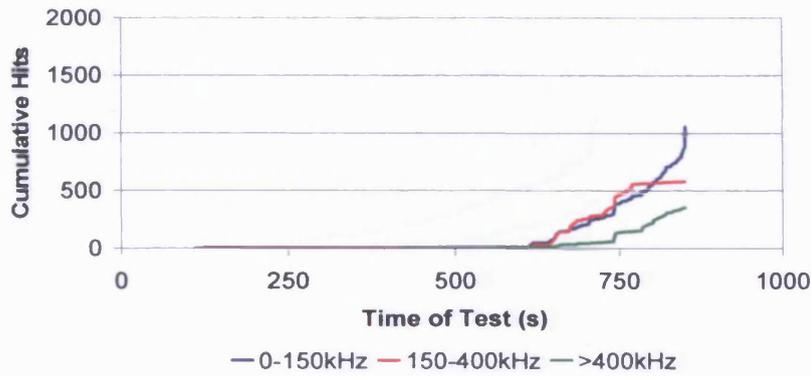
a) Channel 1 hits
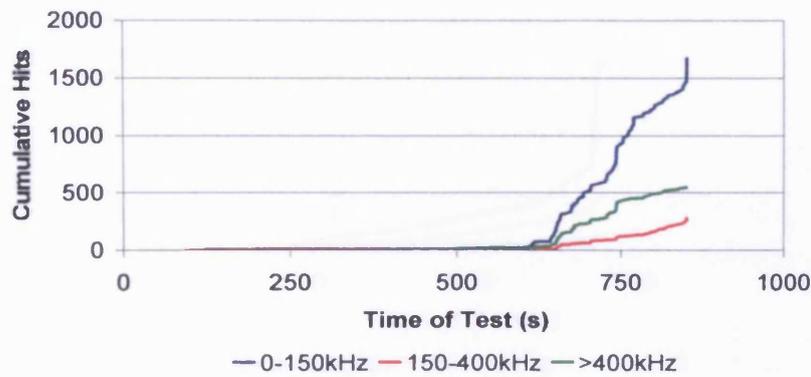
b) Channel 2 hits

Figure 4.33 - Cumulative hits versus time for beam buckling specimen 3
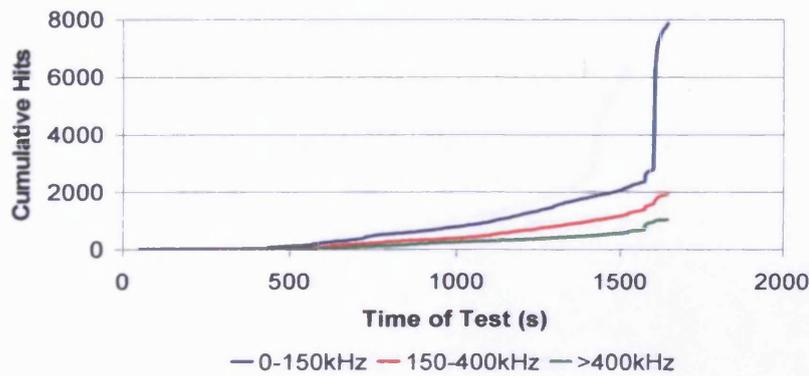
a) Channel 1 hits
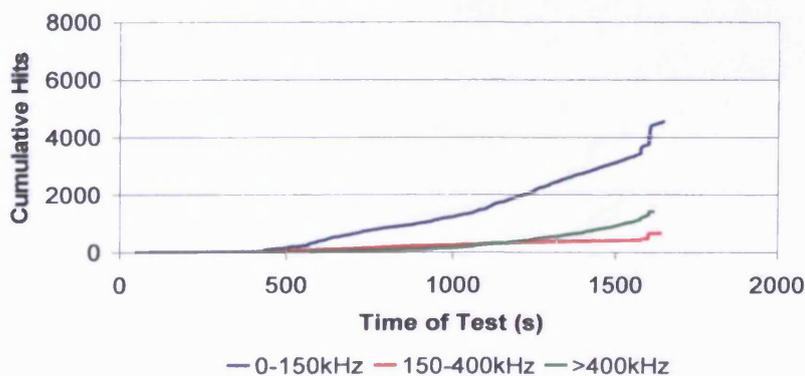
b) Channel 2 hits

Figure 4.34 - Cumulative hits versus time for beam buckling specimen 4

a) Channel 1 hits

b) Channel 2 hits
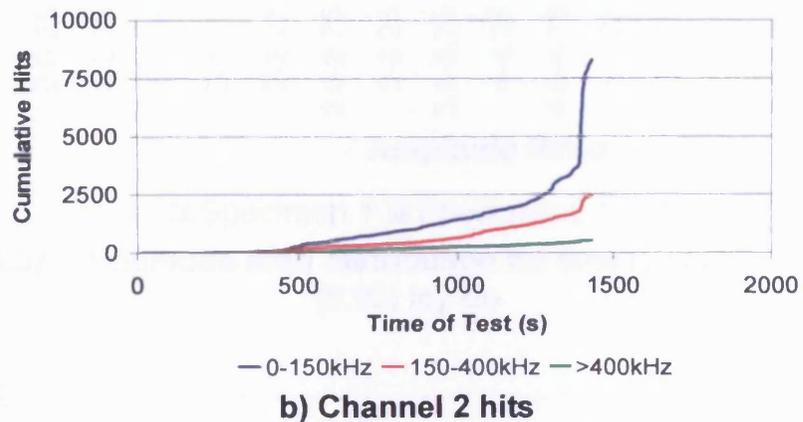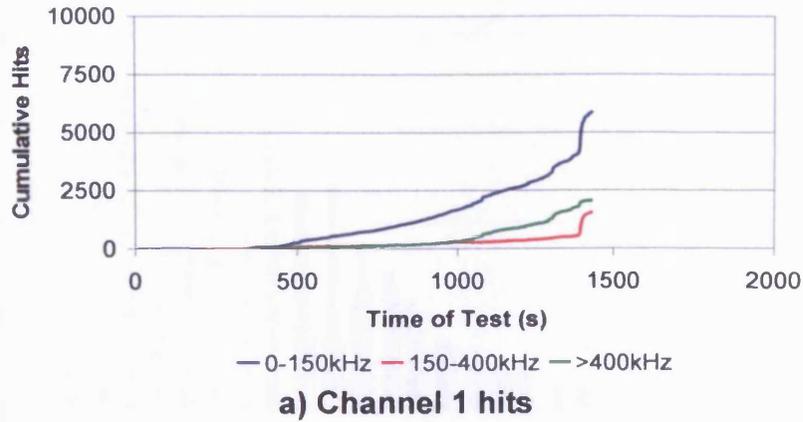
Figure 4.35 - Cumulative hits versus time for beam buckling specimen 5


a) Channel 1 hits

b) Channel 2 hits
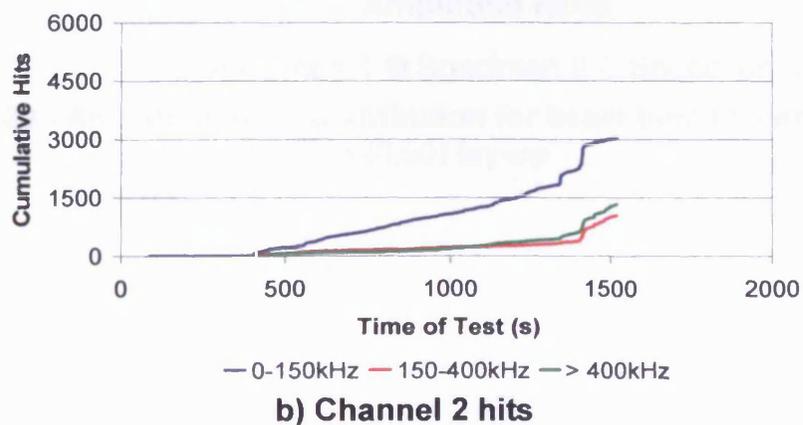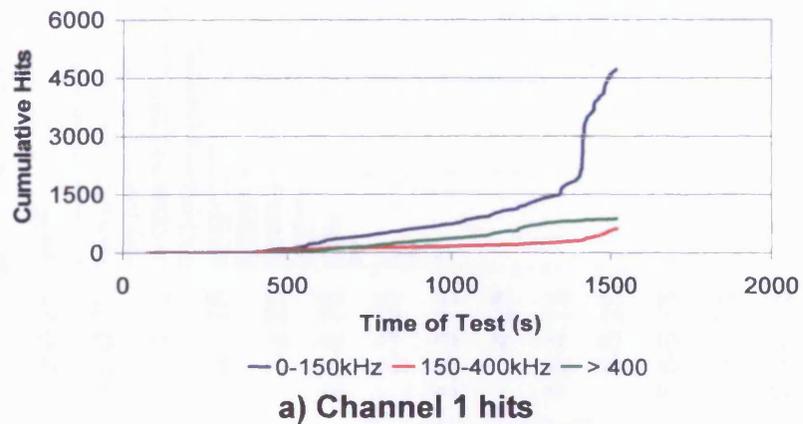
**Figure 4.36 - Cumualtive hits versus time for beam buckling specimen 6**
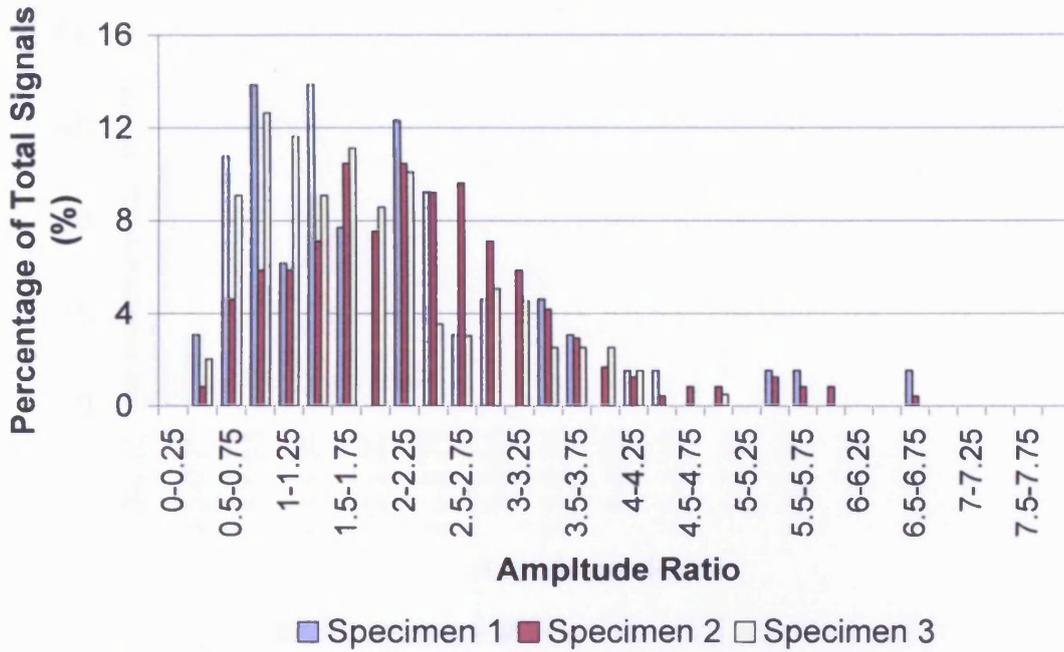
Figure 4.37 - Amplitude ratio distribution for tensile specimens with a (0,90) lay-up
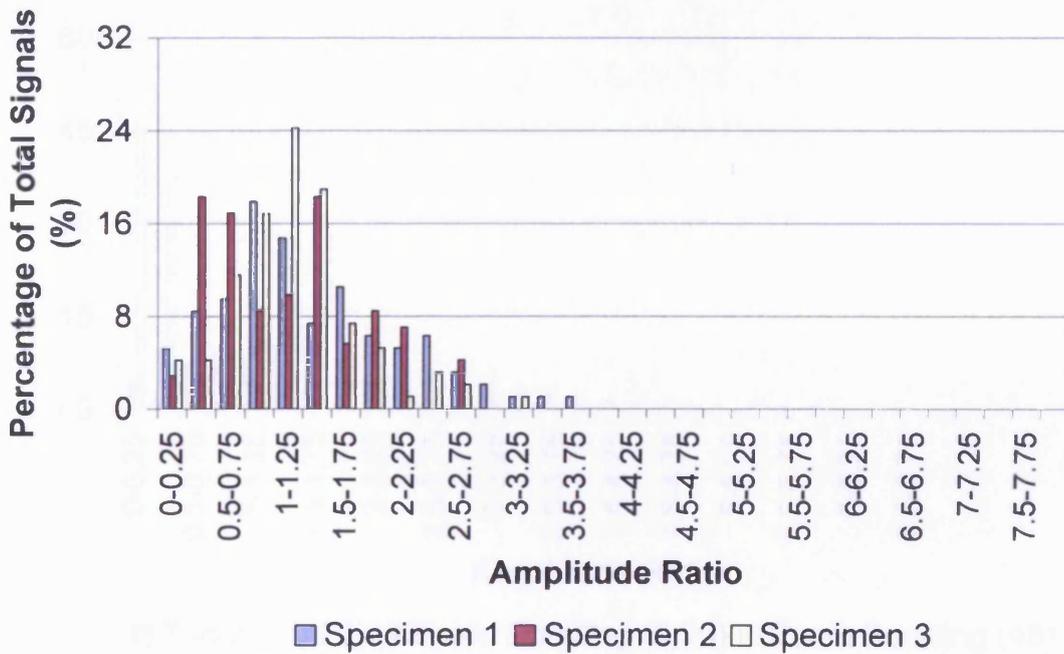

Figure 4.38 - Amplitude ratio distribution for beam buckling specimens with a (0,90) lay-up
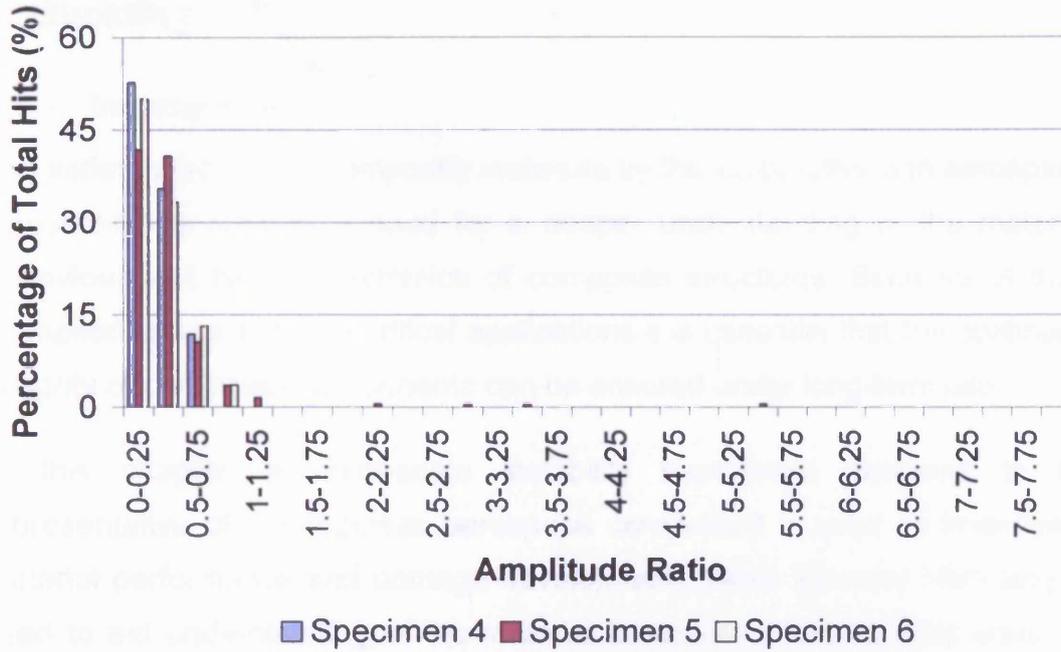
Figure 4.39 - Amplitude ratio distribution for beam buckling specimens with a (45) lay-up
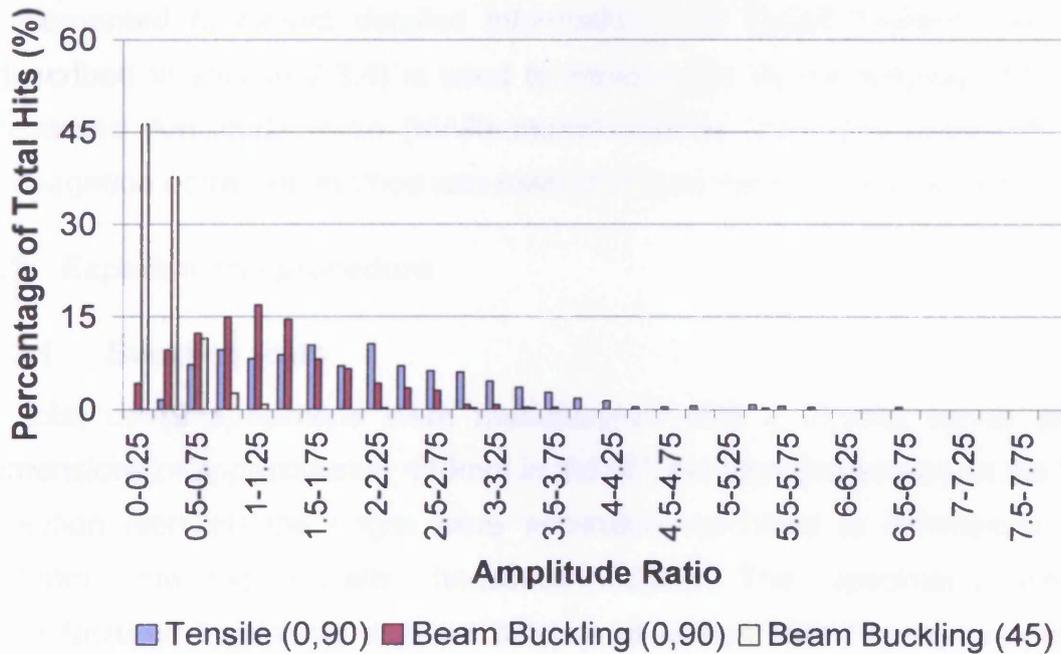

Figure 4.40 - Comparison of amplitude ratios from all coupon tests

5 Buckling

5.1 Introduction

The widespread use of composite materials by the automotive and aerospace industries has created a need for a deeper understanding of the material behaviour and failure mechanics of composite structures. Because of their increased usage in safety critical applications it is essential that the continued integrity of composite components can be ensured under long-term use.

In this chapter, a large-scale instability experiment designed to be representative of a composite aerospace component is used to investigate material performance and damage development. Finite Element Modelling is used to aid understanding of the material behaviour and to predict areas of potential failure. Classical AE monitoring techniques are used to detect and monitor the development of damage; with more advanced techniques implemented to extract detailed information. The DeltaT location method (described in section 2.3.4) is used to improve the source location and the Measured Amplitude Ratio (MAR) modal analysis technique along with a propagation correction method was used to characterise damage signals.

5.2 Experimental procedure

5.2.1 Buckling tests

A total of 19 specimens were manufactured with a $(0,90)_{4s}$ lay-up and dimensions of approximately 410mm in the 90° direction (horizontal). In the 0° direction (vertical) the edges were accurately machined to dimensions of 380mm, creating parallel horizontal edges. The specimens were manufactured from three different batches of carbon fibre / epoxy pre-preg each having similar properties, due to the availability of materials at the time of manufacture. The first three specimens were manufactured from Hexcel's 914C-T300H-5-34% uni-directional pre-preg and cured in an autoclave (details of the curing process are included in Appendix D). A drop weight impactor with a mass of 1.46kg was used to induce damage at the centre of all three specimens at impact energies of 5J, 6.5J and 8J, in accordance with British Standard for the impacting of rigid plastics (BSI 2000). A further 8

specimens were then manufactured from ACG's MTM28-1/HS-135-34%RW and cured in a vacuum bag (details of the curing process are included in Appendix D) and impacted in the same way with impact energies of 5J, 6J, 8J and 10J. The remaining 8 specimens were manufactured from ACG's HTM45/HS-135-34%RW and cured in an autoclave (details of the curing process are included in Appendix D). One of the specimens was left undamaged, one had a single 200mm diameter PTFE disc embedded 2 plys from the surface at its centre, three had a 100mm diameter PTFE disc embedded 2 plys from the surface at their centres and the remaining three had a 50mm diameter PTFE disc embedded 2 plys from the surface at their centres. Table 5.1 summarises the specimen details. A black and white speckled pattern was applied to one side of each specimen to enable the Digital Image Correlation (DIC) system to be used. The impacted specimens were speckled on their non-impacted side and the artificially delaminated specimens were speckled on the surface closest to the PTFE insert.

The buckling rig, shown in Figure 5.1a, was designed to provide simple supports to all four sides of the specimens whilst facilitating the application of a uni-axial in-plane compressive load. The buckling rig supports are described in accordance with the coordinate system shown in Figure 5.2. The vertical (unloaded) specimen edges are held between opposed knife edges (Figure 5.1b) which allow both rotation of the specimen about the y axis and the applied in-plane load to be transferred down through the specimen, whilst still restraining any out-of-plane displacement. It can be seen how the use of knife-edge supports reduced the effective width of the specimen to 380mm, creating a simply supported buckling area of 380mm x 380mm. To prevent jamming of specimens during loading, the knife-edges have approximately 3mm of sprung movement in the z direction. Figure 5.1c demonstrates how the loaded (horizontal) edges of the specimens are seated in a slot running through 7 sections of 20mm round bar. The sections of round bar are housed in roller bearings which allows the specimen to rotate whilst under load. The bearings along the top edge of the specimens are mounted to a cross-head which is guided to allow only vertical movement and is used to apply load to the specimen.

In the first stage of loading, specimens 1-11 were loaded (beyond their buckling point) under displacement control at a rate of $0.25mm.min^{-1}$ using a Howden universal test machine. Loading was stopped at the onset of damage and the specimens were unloaded. The detection of AE signals with an amplitude greater than 80dB is believed to be a good indication of damage onset in composite materials and as such the loading was stopped when the first AE signals of 80dB or greater were recorded. The specimens were instrumented using four PAC Nano30 sensors mounted using magnetic clamps with brown grease as a couplant. The sensors were arranged 260mm apart in a diamond shaped array, as shown in Figure 5.3. The sensitivity of the installed sensors was found to be above 97dB in response to a H-N source in all cases. Images for DIC were captured at 0.5kN intervals throughout the loading of each specimen.

During the second stage of loading, all 19 specimens were loaded to failure at a rate of $0.25mm.min^{-1}$ under displacement control using a Howden universal test machine. The specimens were instrumented with eight sensors (Figure 5.4), four PAC WD sensors arranged in a 280mm x 280mm square array and four PAC Nano30 sensors arranged 260mm apart in a diamond shaped array. The WD sensors were mounted using zip ties and adhesive pads and the Nano30 sensors were mounted using magnetic clamps (section 3.2.1). All sensors were coupled with ultrasound gel and monitoring was conducted with a PAC PCI-2 system. DeltaT location grids of 350mm x 350mm (seen in Figure 5.4) were drawn on all 19 specimens with a grid resolution of 50mm. Before each test, data were recorded from five H-N sources at each grid point, in order to construct DeltaT location maps for the specimens. Images for DIC were captured at a rate of 0.5Hz until failure and the test load at the point of capture was recorded with each image.

All 19 specimens were inspected post failure using an ultrasound C-scanner with a 5MHz probe. Sizing of delamination defects was achieved using the "-6dB drop" method, for which a drop of 6dB in signal is used to determine the position of a defect edge. The supporting research for this approach was conducted by the National Physical Laboratory (NPL) and is presented in a

series of papers. Broughton et al (1998), Smith et al (1998c), Zeqiri (1998b), Zeqiri and Hodnett (1998a) and Smith et al (1998a; 1998b).

5.2.2 Finite Element models

Three types of FE meshes were created to represent the above buckling experiments. The first represented an undamaged plate and the latter two attempted to make approximations of the impact damage in the specimens. The first approximation was to remove a circular section of the specimen from its centre and the second approximation modelled the presence of a single circular delamination at the centre of the specimen. The models were constructed using the coordinate system presented in Figure 5.2. The mesh of the undamaged specimen was constructed from S8R5 quadrilateral elements that behave in a manner consistent with thin shell theory. The S8R5 is a shell element with eight nodes and has five degrees of freedom per node (three displacement and two in-plane rotations). It uses reduced integration with four integration points instead of the standard eight to reduce processing time. The element size was selected as 19mm x 19mm, as seen in Figure 5.5, in accordance with a convergence study conducted using meshes of 9.5mm, 19mm, 38mm and 76mm elements. The meshes containing a central hole were also constructed from S8R5 quadrilateral shell elements. Starting with 20 elements of 19mm edge length along each edge of the specimen, the elements tapered towards a central hole of 50, 100 or 200mm in diameter, as demonstrated in Figure 5.6 for a 100mm hole. The delamination models were created using the mesh containing a hole as a starting point. Two identically meshed circular surfaces were joined around their circumference only and then joined to the circumference of the hole in the starting mesh, thus filling in the hole as shown in Figure 5.7 for a 100mm diameter delamination.

The material properties of the specimens were defined using the composite builder within the MSC Patran software. This allows the user to define the properties of a single ply and then define the material lay-up used. The material properties used were for ACG's HTM45/HS-135-34%RW uni-directional prepreg which are included in Table 5.2. A $(0,90)_{4s}$ lay-up was used in keeping with that of the specimens. The delamination surfaces on the

positive (thin delamination surface) and negative (thick delamination surface) z faces of the specimen were given lay-ups of (90,0) and (0,90,0,90,0,90,0,90,90,0,90,0,90,0) and offsets of +3.5 and - 0.071429 mm respectively, thus representing a delamination at a depth of 2 plys from the positive z surface (Figure 5.8). The contact between the two delamination surfaces was also modelled in order to prevent the surfaces passing through each other and producing erroneous results.

The boundary conditions applied to the models are described below with reference to the coordinate system presented in Figure 5.2. The bottom edge was restricted from moving in the x, y and z directions and from rotating about the y and z axis, leaving it free to rotate about the x axis only. The vertical edges were restricted from moving in the z direction and from rotating about the x axis, leaving them free to move in the x and y directions and to rotate about the y and z axis. The top edge was restricted from moving in the x and z directions and from rotating about the y and z axis, leaving it free to move in the y direction and to rotate about the x axis. A uniaxial in-plane load of 1kN (the calculated loads are given as a scale factor relative to the applied 1kN load) was applied in the negative y direction to a single node above the top edge that was rigidly linked to all the nodes on the top edge using a Multi-Point Constraint function.

An eigenvalue analysis was conducted for each of the models to give an initial buckling load and mode shape for the idealised case. The delamination models were analysed twice, once with the two surfaces free to move independently, to promote a local buckling mode of the thin delamination surface and once with the two surfaces tied together to prevent them from moving independently, to force an overall buckling mode. The mode shape calculated is scaled between 0 and 1, such that the largest displacement has a value of 1 and the other displacements are scaled relatively between 0 and 1.

Non-linear Riks analyses were conducted for the undamaged model and the delamination models, to predict their post buckling behaviour. The models containing holes were considered to be too approximate for further analysis

and do not feature in the postbuckling analysis. The Riks analysis predicts the load and displacement behaviour of the specimens in the postbuckling region. An initial imperfection is required to start the non-linear analysis and is provided by the mode shape predicted by the eigenvalue analysis. The size of the initial imperfection is controlled by the imperfection value (a scale factor) in units of mm, which is applied to the eigenvalue analysis mode shape such that the point of largest deflection is equal to the imperfection value. The undamaged plate was analysed using imperfection values of 0.125, 0.25, 0.5 and 1. The delamination models were analysed using the local buckling modes with applied imperfection values of 0.125, 0.25 and 0.5 and the overall buckling modes using applied imperfection values of -0.125, -0.25, -0.5, -1.0, 0.125, 0.25, 0.5 and 1.0. The orientation of the overall imperfection values is described by Figure 5.9a and b. Before beginning the Riks analyses using the overall modes, the two delamination surfaces were untied to allow independent movement. The local modes are only considered with a positive imperfection value because it is only possible for the thin delamination surfaces to locally buckle in this direction, whereas the overall buckling mode can occur in both the positive and negative directions.

5.3 Results and discussion

5.3.1 Buckling

The experimental buckling loads were taken as the intersection of tangents to the pre- and postbuckling gradients of the load versus displacement curves (Figure 5.10), as presented by Zaal (1998). Table 5.3 presents the buckling loads extracted from the load versus out-of-plane displacement measured at the specimen centre using the DIC system, for the first and second stages of testing. Data is not included from the first stage for specimen 1 and from the second stage for specimens 7 and 11, due to corruption of load data. Additionally data from second stage tests for specimens 9, 10 and 19 are not included because the buckling rig became stuck during the initial stages of the test. There is a noticeable amount of scatter between the results, which is quite common for instability experiments. This can also be seen in the load versus displacement behaviour for the first and second stages of testing

presented in Figure 5.11 for specimens 1, 2 and 3 (Impacted Hexcel 914C-T300H-5-34%), Figure 5.12 for specimen 4 (undamaged ACG HTM45/HS-135-34%RW), Figure 5.13 for specimens 5, 6 and 7 (50mm delamination ACG HTM45/HS-135-34%RW), Figure 5.14 for specimens 8, 9 and 10 (100mm delamination ACG HTM45/HS-135-34%RW), in Figure 5.15 for stage 1 testing of specimen 11 (200mm delamination ACG HTM45/HS-135-34%RW) and Figure 5.16 for stage two testing of specimens 12-18 (Impacted ACG MTM28-1/HS-135-34%RW). It should be noted that due to a manufacturing error specimen 18 was found to have two additional plies making it thicker and thus stiffer than the other specimens. The average buckling loads (not including specimen 18) are 2.62kN and 2.54kN and the standard deviations (not including specimen 18) are 0.637 and 0.699 for the first and second stages of testing respectively.

5.3.2   Finite Element Analysis

The buckling loads resulting from the eigenmode analysis are presented in Table 5.4 for the undamaged model, the hole models and the delamination models. Additionally the table contains the buckling load for an undamaged plate, calculated using equation 2.16, for comparison. The undamaged plate has a FE predicted buckling load of 3.42kN, this corresponds to a calculated buckling load of 3.403kN. Thus providing validation of the FE model and the applied boundary conditions. It can be seen that the predicted buckling load for the 50mm hole model is only slightly less than that of the undamaged plate at 3.21kN, however a more noticeable drop in buckling load is observed as the hole is increased in size to 100 and 200mm. The 50mm local mode delamination model buckles with an overall mode, which is represented by a buckling load of 3.44kN. This means that the 50mm local mode model has no local mode that exists below the load of the overall buckling mode. The 100 and 200mm local mode delamination models have dramatically smaller buckling loads due to the local buckling of the thin delamination surface. The overall mode delamination models all have a buckling load of 3.44kN because they effectively act as an undamaged plate when the two delamination surfaces are tied together. It is worthy of note that the buckling loads predicted

by the eigenvalue analysis are for a perfect case without any consideration for imperfections in geometry.

The non-linear Riks analysis does not directly output a buckling load in the way the eigenmode analysis does. However, using the method presented by Zaal (1998) and discussed in section 5.3.1, the buckling load can be taken as the intersection of tangents to the pre- and postbuckling gradients of a load versus displacement curve. The extracted buckling loads from the Riks analyses are of interest because they are affected by the initial imperfection applied to the model. The resulting buckling loads from the Riks analysis of the undamaged plate are presented in Table 5.5. For an initial imperfection value of 0.125mm the predicted buckling load is reduced to 2.5kN compared with 3.42kN predicted by the eigen mode analysis for a perfect case. As the size of imperfection is increased so the buckling load decreases down to 1.25kN with an imperfection value of 1mm.

The buckling loads from delamination models were extracted from the load and displacement data of both the thick and the thin delamination surfaces at the centre of the plates. The buckling loads resulting from the Riks analyses, using the local mode delamination eigenvalue results as an initial imperfection, are presented in Table 5.6. The results of the 50mm local mode model are omitted due to the lack of a local buckling mode. The 100 and 200mm delamination models had initial imperfections in which the thin delamination buckled locally and the thick section had no imperfection and therefore maintains the same buckling load. The thin delaminations buckle at increasingly lower loads as the size of the imperfection increases, as expected. It can be seen that the buckling load of the 100mm thin delamination surface is approximately four times larger than that of the 200mm thin delamination surface at all three imperfection values. If the critical buckling load of a homogenous circular plate, radius r, subject to an in-plane uniform radial load with clamped edges is considered (Brush and Almroth1975)

$$P_{cr} = 14.68 \frac{D}{r^2} \tag{5.1}$$

Where D is the bending stiffness parameter, given as

$$D = \frac{Eh^3}{\left[12(1-v^2)\right]}$$

It can be seen that if the radius is doubled the buckling load becomes four times smaller. Although the load case for Equation 5.1 is not identical to that of the experiment and it is for a homogeneous material, it still provides a good approximation of the buckling behaviour observed in Table 5.6 for the 100mm and 200mm diameter thin delamination surfaces. Once buckled the thin delaminations will support little of the applied load, which will then be supported by the thick delamination sections. This is thought to be the reason for the difference in thick delamination surface buckling load between the 100 and 200mm models; the 200mm delamination naturally being more unstable and having a slightly lower buckling load.

The buckling loads resulting from the Riks analysis of the overall mode delamination models are presented in Table 5.7 and Table 5.8 for negative and positive imperfection values respectively. It can be seen that with a negative imperfection value, the buckling loads are very similar to that of the undamaged plate for all three models and for both thick and thin delamination surfaces. This occurs because the thin delamination surface cannot pass through the thick surface when displacement is in the negative z direction and as can be seen in Figure 5.17, the thin delamination surface remains in contact with the thick surface beyond the point of buckling. Thus the models are effectively acting as undamaged plates. Using positive imperfection values the thick delamination surface of the 50mm model has the same buckling loads as those of the undamaged plate. The thin surface, being less stiff, buckles just before the rest of the plate with a slightly smaller buckling load at all values of imperfection. This behaviour is exaggerated for the 100mm and 200mm thin delamination surfaces both having much lower buckling loads in accordance with Equation 5.1 that predicts a reduction in buckling load by a factor of four when the delamination radius is doubled. It was not possible to extract a buckling load for the 200mm thin delamination surface with an imperfection of 1, because the buckling load is so small (~0.075kN predicted

by the relationship in Equation 5.1) and the imperfection so large, that the analysis started at a displacement past the point of buckling. The thick delamination buckling loads for positive imperfection values are seen to reduce as the size of the delamination is increased, as would be expected.

The initial imperfection used in the above analysis can be considered a worst-case scenario, because the induced shape is that of the actual buckling mode. In reality however, any initial imperfection of the specimens is likely to be of a different geometry and the effect of this on the buckling load is thus not easily predicted. Table 5.9 presents the buckling loads extracted from the experimental results and the actual maximum and minimum out-of-plane initial imperfection measured using the DIC system. Additionally the table includes information on the shape of the initial imperfection, a + or − symbol indicates an imperfection shape that is similar to the buckling mode shape (Figure 5.18) and a T indicates a slight twist in the specimen at the start of the test (Figure 5.19). There is a noticeable amount of scatter in the results, which is quite common for an instability experiment. Specimen 4 (undamaged) however, correlates very well with the FE results having buckling loads of 2.7kN and 2.5kN for the first and second stages of testing, which are very close to the predicted buckling load with an imperfection of 0.125mm of 2.5kN. Specimens 5, 6 and 7 (50mm delamination) have higher buckling loads for the first stage loading, all of which are above 3kN, their correspondingly smaller imperfections are still greater than that of the 0.125 FE model. The buckling loads of specimen 5 and 6 (specimen 7 had corrupted load data) for the second stage of testing are lower at 2.25kN and 2.4kN respectively with slightly larger imperfections. Interestingly, for the first stage of testing, specimen 8 has the largest imperfection values of −0.77 and 0.31mm but still has a buckling load of 2.25kN, whereas the second stage test has imperfection values of −0.20 and 0.25 with only a slightly larger buckling load at 2.3kN. It is thought that the twisted imperfection shape of the specimen in the first stage may have had a stiffening effect. Indeed specimen 2 had a twisted imperfection shape in both stages and the second stage had both a larger imperfection and a larger buckling load. This is supported by the results of specimens 12 − 19 where a general trend for the specimens with a twisted

imperfection shapes to have higher buckling loads is apparent. It is though that the twisted initial imperfection of the specimens induces an in-plane tensile field, which acts to limit out-of-plane displacement and therefore increases the buckling load.

The load versus displacement behaviour of the specimens agrees very well with the FE models up until the buckling load, beyond which the FE models become stiffer. Figure 5.20 shows the load versus displacement behaviour for specimen 4 and the FE models resulting from different initial imperfection values. Observations throughout testing suggested that local buckling of the thin delamination did not occur in any of the tests. Additionally post test C-scan images showed that the inserted PTFE delaminations still had a good level of cohesion with the specimen. As such the experimental load versus displacement data of the delamination specimens is compared with the FE data for the thick delamination only. Figure 5.21 compares FE results from the 50mm delamination model with that of specimen 5's second stage test. Figure 5.22 compares FE results from the 100mm delamination model with that of specimen 8's second stage test and Figure 5.23 compares FE results from the 200mm delamination model with that of specimen 11's first stage test. The undamaged plate, the 100mm delamination and the 200mm delamination all agree very well up to the point of buckling with the 0.125mm imperfection models. The only exception to this is the 50mm delamination which has a close correlation with the 0.25mm imperfection model. In the postbuckling region the FE model is stiffer in all cases. The difference in stiffness can be attributed to the movement of the sprung knife edges in particular and also damage accumulation in the material, both of which are not accounted for in the FE models.

5.3.3 Damage observations

During the first stage of testing the loading of specimens 1-11 was stopped at the point of damage initiation (determined by the arrival of signals having amplitudes greater than 80dB) consequently only limited damage was observed in the specimens. Visually there was no apparent damage observed at all, however ultrasonic C-scanning revealed internal damage in specimens

4 and 7. Both specimens exhibited a small area of delamination (Figure 5.24a and b) corresponding to the areas of high curvature at the specimen corners. Growth of the central delaminations, whether induced by impact or embedded PTFE, was not observed in any of the specimens. Figure 5.25 presents C-scan images of both embedded PTFE and impact induced delamination from before (a and c) and after (b and d) the first stage of testing, it can be seen that no growth of delamination had occurred.

During the second stage of testing all 19 buckling specimens were loaded to failure. The final failure occurred at one or more of the specimen corners in all cases, in the form of a through thickness shear crack (Figure 5.26). This occurs because of the constraints of the boundary conditions; at high levels of curvature the roller supports are trying to rotate and the knife-edges are trying to keep the specimen straight, resulting in at "tearing" action at the corners. This "tearing" propagated to a maximum length of approximately 30mm along a 45° line from the point of initiation at the corners, where cracking could be seen on both sides of the specimen. Specimens 12-19 also exhibited a small amount of surface ply delamination along the propagation path of the shear crack which were only visible on the compressive side (Figure 5.27). C-scan inspection of the specimens after the second stage of loading revealed an increase in size of the delamination previously observed in specimen 4 (Figure 5.28). The smaller delamination observed in specimen 7 did not increase in size, however a much larger area of delamination occurred at the top right corner (Figure 5.29). The small areas of signal loss observed in the centre of all four sides are a result of the supports used during the C-scanning process and not from actual damage. Similar areas of extensive delamination were observed in specimens 1,2,3,5,6,9,10 and 11. Smaller amounts of delamination resulting from the "tearing" action of the shear cracking (see Figure 5.26) were observed in specimens 8,10 and 12-19, examples of this are presented in Figure 5.30, Figure 5.31 and Figure 5.32. Details of the delamination sizes (estimated using the -6dB method) and their location are included in Table 5.10. It is also noted that the induced delamination at the centre of the specimens was not seen to have grown during any of the second stage testing. The major damage observed in the form of delamination and

shear cracking (or "tearing") are damage mechanisms that have their particle motion perpendicular to the plane of the plate/specimens. In accordance with the modal analysis techniques discussed in section 2.4.2, these are considered to be out-of-plane sources.

5.3.4   Damage detection

Correlation plots are used extensively in classic AE testing, for the detection and potentially the characterisation of damage. A correlation plot of amplitude versus log duration is commonly used for the testing of composite materials, where high amplitude hits are thought to be from fibre failure and high amplitude plus long duration hits are thought to be from delamination (section 3.2.3). The definition of what is deemed to be a high amplitude or a long duration is open to a large amount of interpretation. Because the range of amplitudes and durations will vary with sensor type and test set-up, there are no guidelines as to what constitutes a high amplitude or long duration. Figure 5.33a-i presents the correlation plots of amplitude versus log duration for the first stage loading of specimens 2-10. By considering the range of amplitudes and durations recorded, approximate limits were set at 90dB and 2000μs for high amplitudes and long durations respectively. As expected, a group of hits is observed in the high amplitude long duration region for both specimen 4 and 7 (Figure 5.33c and f) in which delamination was observed. However a number of hits were also observed in this region for specimens 3, 5, 9 and 10, in which no major damage was identified. It should be noted, however, that the identification of transverse defects, such as matrix cracking, is particularly difficult using both visual and ultrasound C-scan inspection. The high amplitude and long duration hits from all specimens were recorded in the final moments of the first stage of testing (the recording of hits above 80dB was the point at which the first stage testing was stopped, section 5.2.1) and are thought to be a result of damage initiation. There appears to be little appreciable difference between the correlation plots of specimens 4 and 7 (containing delamination) and those of specimens 3, 5, 9 and 10 also exhibiting high amplitude long duration hits, but containing no identified major damage, making it difficult for an operator to perform any characterisation based on the correlation plots. Specimen 6 (Figure 5.33e) exhibits the least

amount of hits with high amplitudes and/or long durations, suggesting it sustained the least amount of damage during the first stage of testing. The correlation of amplitude versus log duration was found to be a useful tool for the detection of damage initiation, with a trend of high amplitude long duration hits corresponding to damage initiation. However the ability to characterise damage or estimate its severity has been shown to be limited.

For components subject to repeated loading, the Felicity effect (section 2.2.3) can be utilised to investigate the onset and development of damage in a component. Figure 5.34a-i present the cumulative counts versus load for the first and second stage testing of specimens 2-10 respectively, where only hits recorded by the Nano 30 sensors (channels 5-8) are included from the second stage testing. It can been seen in all cases during the second stage loading that AE activity begins before the previous peak load is reached, indicating that the specimens sustained permanent damage during the first stage of loading. However, it is difficult to determine the load at which the significant AE activity is deemed to have begun. With careful consideration of the observations made during the second test, in particular the movement of the knife-edges, it is possible to make a sensible estimation. The resulting Felicity ratios are presented in Table 5.11 along with the final failure loads of the specimens. As expected, specimens 4 and 7 (containing observed delamination) have the lowest Felicity ratios at 0.815 and 0.367 respectively. It was also expected that specimens 3, 5, 9 and 10 (exhibiting numerous hits with high amplitudes and long durations) would produce low Felicity ratios, however specimens 5 and 8 have the highest Felicity ratios at 0.956 and 0.950 respectively. Furthermore, specimen 6 exhibited the least high amplitude and long duration activity during the first stage of testing but has the lowest Felicity ratio after specimens 4 and 7 at 0.862. Figure 5.35 presents a correlation of specimen failure loads with Felicity ratios, it can be seen that there is no trend for specimens with lower Felicity ratios (and supposedly more existing damage) to have lower failure loads. The identification of existing damage using the Felicity ratio was successful, however the ability to estimate the damage severity or the future performance of a structure are again limited and open to interpretation by an operator.

The correlation of amplitude with log duration and the Felicity ratio both provide useful tools for damage detection in composite structures. However their use for damage characterisation and quantitative SHM was demonstrated to be limited. This highlights the need for the development of more advanced AE techniques for composite SHM.

5.3.5 Location

The location of events from the boundary of a plate is always problematic because invariably the AE source is outside of the sensor array. The details of potential TOA source location problems are discussed in section 2.3.2. This problem is exacerbated by the directionally dependent wave speed observed in composite materials (section 4.2). Figure 5.36 demonstrates the potential for large location errors for signals originating from the plate corners, using a square array of sensors as in the first stage of testing. In reality, the effect is so extreme that events can be falsely located over 150m from the plate. Furthermore, very slight differences in arrival times will result in large changes in location. However, it is still possible to extract some information about the source location. Figure 5.37a and b show the TOA locations from the first stage of testing for specimens 4 and 7, respectively. The green dot at the centre of each figure represents the sensor positions on the plate, however at this scale the positions appear overlaid. As indicated by Figure 5.36, the located events in Figure 5.37a and b lie approximately on a 45° line extending from the corners of the plate. Comparing these locations with the C-scan images of specimens 4 and 7 in Figure 5.24a and b it is clear to see that the majority of events in Figure 5.37 are located on a 45° line extending away from the damaged corners, seen in Figure 5.24. This is supported when the linear locations across the specimen corners are considered. Figure 5.38 and Figure 5.39 present the linear locations from the sensor pairs spanning each corner for specimens 4 and 7 respectively. The location algorithm is controlled such that the opposite pair of sensors act as guard sensors, to avoid erroneous locations from the opposite corner (i.e. the location between sensors 1 and 2 has sensors 3 and 4 as guard sensors). It can be seen that events are located near the centre of the location arrays, corresponding to the specimen corners in all cases except the bottom right hand corner of

specimen 4. Consideration of the absolute energy located at each corner identifies more energy by approximately a factor of 4 at the top right corner of specimen 4 and the top left corner of specimen 7, where damage was identified by the C-scans. Events located at the other corners are thought to be a result of micro damage caused by the high rates of curvature at the specimen corners (Figure 5.40). Signals from micro damage were not located in two-dimensions because the required third sensor was not hit due to the high signal attenuation in composite materials.

The same location error (Figure 5.36) was observed for two-dimensional location using the Nano30 sensor array during the second stage testing (Figure 5.41a and Figure 5.42a). The same pattern of located events is observed with most locations lying approximately on a 45° line extending from the corners and events being located up to 250m outside the plate boundary. Figure 5.41b and Figure 5.42b demonstrate the greatly improved location, for specimens 4 and 7 respectively, when the WD sensor array is used. The events are now clustered around the four corners of the specimens and those located furthest from the plate corners are still within 20cm. The clusters of events around the corners are still quite spread out with a large proportion of hits being located outside the plate boundary. The point of most intensely located events in specimen 4 is on the point of the top right corner, with only 4 events, which corresponds to the damage observed in Figure 5.28. In specimen 7 the point of most intensely located events, again with 4 events, is approximately 10cm from the bottom right hand corner, which does not correspond to the damage observed at the top right hand corner in Figure 5.29. There are, however, two points containing 3 events each located at 2.9cm and 5.5cm from the top right hand specimen corner. It is thought that the signals located at the bottom right hand corner are due to micro damage resulting from the high curvature. Indeed, the largest absolute energy content of the 4 located signals at the bottom right hand corner is 212.5×10^5aJ; whereas out of the 6 signals located at the top right hand corner, the largest absolute energy content is 247.5×10^6aJ. Suggesting that the signals located at the top right hand corner contain more energy resulting from the delamination observed in Figure 5.29. The locations calculated using the

DeltaT location methodology developed by Baxter (2007) are presented in Figure 5.41c and Figure 5.42c for specimens 4 and 7 respectively. The DeltaT locations have been calculated using both the WD and Nano 30 sensor, because the mapping stage of the methodology accounts for any triggering error due to differing sensor response. Due to the nature of the technique it is not possible to locate events outside of the grid created during the mapping stage, hence there are no events located outside of the specimen or within a short distance of the edges due to the supports. The events are clustered quite closely at the corners of the grid, indeed the point of most intensely located events is at the very top right hand corner of the grid, 2.12cm from the position of damage initiation, for both specimens. The points have 22 and 18 located events for specimens 4 and 7 respectively and considerable numbers of events are located at adjacent points, which correspond to the observed damage at the top right hand corners. compared to the largest location error observed of 5.5cm this offers a 61% improvement in location. There are also less intensely located events observed at the other specimen corners, corresponding to the locations observed from TOA analysis. It is believed that the locations observed at the other corners again result from minor damage induced at the corners by localised high levels of curvature. Figure 5.43a and b present the principal curvature for specimens 4 and 7 respectively, measured using the DIC system just prior to final failure. The images have been flipped horizontally (as described in section 3.2.3) inorder for the curvature pattern to relate directly to the AE locations. The localised increase in curvature is clearly seen towards the specimen corners and the maximum curvature is observed at the corner where failure eventually occurred in both cases.

The cluster of events observed at the centre of both DeltaT location plots in Figure 5.41c and Figure 5.42c has thus far not been considered and is the source of some concern. Specimen 4 has no initial damage at its centre, no damage was observed at the centre of the specimen post-test and the centre of the specimen is the region subject to the least strain/curvature. Specimen 7 contained a 50mm delamination at its centre, however this was shown not to have grown during the second stage testing (Figure 5.29). Additionally no

location clusters were identified at the centre of the specimen using TOA location, a region where the TOA location would be expected to have greatest sensitivity and accuracy. Hence it is concluded that the events located at the specimen centre using DeltaT are incorrectly located. Figure 5.44a, b and c present the DeltaT contour maps of constant time difference for sensor pairs 1-5, 4-6 and 1-4 respectively. It can be seen in all three maps that contour lines passing through or near the top right hand corner also pass though the centre of the specimen. Figure 5.44d shows the resulting crossing points produced by overlaying the three DeltaT maps (as discussed in section 2.3.4). It can be seen that crossing points occur at both the corner and the centre of the specimen for the same recorded time differences. This effect can be seen in the location file produced by the DeltaT software in which the coordinates of the three most likely locations of each event are stated. In a small number of cases, events having their most likely location at the centre were seen to have their second or third most likely location at the corner. This further supports the belief that the locations at the centre are in fact events occurring at the specimen corners that have been incorrectly located. The addition of a sensor at the middle of the specimen would reduce the number of erroneous locations at the centre, further improving the DeltaT locations. Alternatively a random arrangement of sensors would avoid the symmetric pattern of constant time difference contours seen in Figure 5.44 and thus could also reduce the number of erroneous locations at the centre of the specimen.

During the second stage testing of specimen 15 a sharp "jerk" of the specimen was observed that resulted in sensor 8 becoming unattached and the other Nano30 sensors shifting position slightly. Sensor 8 was immediately remounted and monitoring continued until the end of the test. Figure 5.45a, b and c present the TOA location data from the Nano30 and WD sensor arrays and the DeltaT location data, respectively. The TOA location plots appear unaffected by the sensor movement, having similar location patterns and accuracy to the location plots shown previously for specimens 4 and 7. The DeltaT location plot, however, does not display the same clustering at the corners observed in specimens 4 and 7. Instead the locations are widely spread, over a large proportion of the specimen. One point of clustered hits is

identified towards the top right hand corner of the specimen which is approximately 5cm away from the nearest damage. Similar errors in DeltaT locations were observed in specimens 12-14 and 16-19 where sensor movement was experienced during testing. So for successful location of AE events using the DeltaT methodology it is vital that the sensors remain in their mapped positions.

5.3.6   Source Characterisation

Characterisation of signals from the buckling tests was conducted using the Measured Amplitude Ratio (MAR) modal analysis method investigated in section 4.3. Figure 5.46 - Figure 5.64 present the amplitude ratio distribution of signals with amplitudes greater than 70dB recorded by Sensor 1 during second stage testing of specimens 1-19 respectively. Being that most of the damage mechanisms identified in section 5.3.3 produce particle motion perpendicular to the plane of the specimens and as such are classed as out-of-plane sources, it was expected that the majority of hits would have an amplitude ratio of less than 1. Specimens 1-3, manufactured from Hexcel's 914C-T300H-5-34% material, have a considerable proportion of hits recorded with amplitude ratios of greater than 1. Specimen 1 has nearly 75% of total hits with amplitude ratios greater than 1 and Specimens 2 and 3 both have over 50% of hits with amplitude ratios greater than 1. This is in contradiction to the relationship between out-of-plane sources and low amplitude ratios observed in section 4.3.2. A similar trend is observed for specimens 4-11, manufactured from ACG's HTM45/HS-135-34%RW material, having between 35 and 45% of total hits with an amplitude ratio of greater than 1. The only exceptions being Specimens 7 and 9, having 15% and 6% of hits with an amplitude ratio greater than 1, respectively. The trend is even worse in specimens 12-19, manufactured from ACG's MTM28-1/HS-135-34%RW, with specimen 13 having over 80% of its hits with amplitude ratios greater than 1 and specimens 15, 16, 18 and 19 all having over 70% of their hits with amplitude ratios greater than 1. Specimen 14 is the only exception with only 17% of hits having amplitude ratios greater than 1.

It is clear that the MAR method of signal characterisation does not transpose well into larger scale structures. The cause of this is the extended propagation distances from source to sensor experienced in larger structures. This is confirmed by considering the amplitude ratio distribution of signals recorded by the sensor closest to the damage, which is presented in Figure 5.65, Figure 5.66 and Figure 5.67 for specimens 5, 12 and 15. A dramatic difference is observed, with over 90% of the signals having amplitude ratios less than 1, in all three cases. Figure 5.68a and b demonstrate how propagation distance can affect the amplitude ratio of a signal. The signals presented for channel 2 and 1 respectively are believed to originate from the same event at the top right hand corner. Using the velocities presented in Figure 4.9, the difference in propagation time of a signal from the top right hand corner is calculated to be $40.3\mu s$ and the difference in arrival times of the signals in Figure 5.68 is $45.8\mu s$. In addition to this the temporal separation of the wave modes is concurrent with the propagation distances from source to sensor. It can be seen, due to the difference in attenuation rates of the plate wave modes, that the amplitude ratio changes from 0.323 at sensor 2 (71mm from source) to 2.181 at sensor 1 (334mm from source).

However, using the detailed understanding of wave propagation gained in chapter 4 it is possible to apply a propagation correction to the recorded amplitude ratios. The temporal separation of a signals wave modes can be used to estimate the distance the signal has propagated from its source and hence the amount of attenuation expected for each wave mode can be predicted using the attenuation rates presented in Table 4.2. The measured wave mode amplitudes can then be corrected by the addition of the calculated attenuation values and a propagation corrected amplitude ratio can be calculated. The attenuation measurements made in section 4.2.1 were conducted in a plate manufactured from ACG's MTM21-1/HS-135-34%RW material, therefore propagation corrections can only be made for specimens 12-19. Figure 5.69 - Figure 5.76 present the propagation corrected amplitude ratio distributions for channel 1 of specimens 12-19. The improvement is very apparent with the majority of signals having amplitude ratios of less than 1 for all specimens. A comparison of the propagation corrected amplitude ratio

distribution from channel 1 with that of the sensor closest to the damage for specimens 12 and 15 (Figure 5.77a and b) reveals agreement with the previous findings.

The delamination observed in specimens 4 and 7, from the first stage of testing, indicates that the more extensive delamination observed in specimens 1-11 during the second stage testing may have developed prior to the final failure. It is proposed that the arrival of signals having an amplitude greater than 90dB and an amplitude ratio of less than 1 can provide an indication of delamination onset. The time of test at which this occurs can be correlated with the DIC data and a measure of the curvature at which delamination initiates can be found, thus allowing comparison with the delamination observations made in the beam buckling coupon specimens. Figure 5.78 presents the amplitude ratios versus time of test for hits recorded from specimen 4 with an amplitude greater than 90dB, during the second stage of testing. The first hit with an amplitude ratio of less than 1 was recorded at 388s and the curvature data recorded by the DIC system at this point in the test is presented in Figure 5.79. The image has been flipped horizontally (as described in section 3.2.3) in order that the curvature pattern is presented in the same orientation as the C-scan image (Figure 5.28). A direct measurement of the curvature at the delamination site is not possible because the specimen supports obstruct the view. However, an approximation can be made by extrapolating from the trend in curvature along a 45° line leading towards the corner (Figure 5.79). Figure 5.80 demonstrates the extrapolation process using a trend line fitted to the curvature data, resulting in an estimated curvature of $0.00476mm^{-1}$ for specimen 4. Table 5.12 contains the extrapolated curvature values corresponding to the arrival of the first delamination signals for specimens 4-11. Although only an approximation, the curvature values correspond well to those observed at the onset of delamination in the beam buckling tests for the (±45) specimens of 0.00648, 0.00618 and $0.00650mm^{-1}$ (Table 4.5). This supports the proposal that the delamination developed prior to the final failure and highlights the potential for AE to detect and characterise delamination failures in composite materials.

5.4 Conclusions

The FE results were shown to agree well with the experimental data in the initial buckling stage. However, in postbuckling the simplicity of the model produced a stiffer result in all cases, though to be a result of the sprung knife-edges. Additionally a trend was observed for specimens exhibiting a twisted initial imperfection geometry to have an increased buckling load.

The classic AE analysis of amplitude versus duration correlation plots and the Felicity ratio were shown to be useful indicators of damage onset. However the information they provide is limited and careful interpretation is required to produce reliable results.

More advanced AE techniques were successfully used to detect, locate and characterise damage from composite materials although some limitations were demonstrated. The DeltaT location technique was shown to have great potential for improving the accuracy of location within inhomogeneous composites, although some limitations were demonstrated. The use of MAR modal analysis was shown to successfully identify the out-of-plane sources resulting from delamination and through-thickness shear cracking. Additionally, a propagation correction methodology was proposed and shown to improve the source characterisation capability of MAR analysis in large-scale structures.

Table 5.1 Buckling specimen details

Specimen No.	Material	Damage
1	Hexcel	6.5J Impact
2	Hexcel	8J Impact
3	Hexcel	5J Impact
4	ACG HTM45	Undamaged
5	ACG HTM45	50mm PTFE
6	ACG HTM45	50mm PTFE
7	ACG HTM45	50mm PTFE
8	ACG HTM45	100mm PTFE
9	ACG HTM45	100mm PTFE
10	ACG HTM45	100mm PTFE
11	ACG HTM45	200mm PTFE
12	ACG MTM28-1	8J Impact
13	ACG MTM28-1	8J Impact
14	ACG MTM28-1	10J Impact
15	ACG MTM28-1	10J Impact
16	ACG MTM28-1	6J Impact
17	ACG MTM28-1	6J Impact
18	ACG MTM28-1	5J Impact
19	ACG MTM28-1	5J Impact

Table 5.2 - FE model material properties

E_{11} (MPa)	E_{22} (MPa)	V_{12}	G_{12} (MPa)
124400	8900	0.33	4430

Table 5.3 - Experimental buckling loads

Specimen	First Stage Buckling Load (kN)	Second stage Buckling Load (kN)
1	#	1.75
2	2.2	2.65
3	1.1	1.25
4	2.7	2.5
5	3.15	2.25
6	3.1	2.4
7	3.2	#
8	2.25	2.3
9	3.0	*
10	2.75	*
11	2.75	#
12	-	2.15
13	-	3.85
14	-	3.4
15	-	3.0
16	-	2.25
17	-	3.25
18	-	4.0
19	-	*

 # Load data corrupted   * Buckling rig stuck during initial stage of test

Table 5.4 - Eigen mode analysis results

Damage Approximation Method	No Damage	50mm Ø Delamination	100mm Ø Delamination	200mm Ø Delamination
Calculated (Equation 2.16)	3.64kN	-	-	-
Undamaged	3.42kN	-	-	-
Hole	-	3.21kN	2.84kN	2.49kN
Delamination (Local)	-	*	1.30kN	0.34kN
Delamination (Overall)	-	3.44kN	3.44kN	3.44kN

* No local mode exists for the 50mm delamination model

Table 5.5 - Undamaged plate Riks analysis buckling loads

Imperfection Size (mm)	Buckling Load (kN)
0.125	2.5
0.25	2.2
0.5	1.75
1.0	1.35

Table 5.6 – Local imperfection Riks analysis buckling loads

Imperfection Size (mm)	50mm Buckling Load (kN)	100mm Buckling Load (kN)	200mm Buckling Load (kN)
Thick			
0.125	-	3	2.35
0.25	-	3	2.35
0.5	-	3	2.35
Thin			
0.125	-	1.375	0.33
0.25	-	1.35	0.32
0.5	-	1.325	0.31

Table 5.7 - Negative overall imperfection Riks analysis buckling loads

Imperfection Size (mm)	50mm Buckling Load (kN)	100mm Buckling Load (kN)	200mm Buckling Load (kN)
Thick			
0.125	2.5	2.5	2.5
0.25	2.2	2.2	2.2
0.5	1.75	1.75	1.75
1.0	1.35	1.35	1.35
Thin			
0.125	2.5	2.5	2.5
0.25	2.2	2.2	2.2
0.5	1.75	1.75	1.75
1.0	1.35	1.35	1.35

Table 5.8 - Positive overall imperfection Riks analysis buckling loads

Imperfection Size (mm)	50mm Buckling Load (kN)	100mm Buckling Load (kN)	200mm Buckling Load (kN)
Thick			
0.125	2.5	2.35	1.9
0.25	2.2	2	1.65
0.5	1.75	1.55	1.25
1.0	1.35	1.25	1
Thin			
0.125	2.45	0.75	0.175
0.25	2	0.55	0.13
0.5	1.65	0.4	0.095
1.0	1.25	0.3	-

Table 5.9 - Experimental buckling loads and specimen imperfections

Specimen (damage)	First Stage				Second Stage			
	Buckling Load (kN)	Imperfection			Buckling Load (kN)	Imperfection		
		- (mm)	+ (mm)	Shape		- (mm)	+ (mm)	Shape
1 (6.5J)	#				1.75	-0.15	0.19	-
2 (8J)	2.2	-0.29	0.15	T	2.65	-0.39	0.23	T
3 (5J)	1.1	-0.52	0.5	+	1.25	-0.36	0.39	+
4 (None)	2.7	-0.21	0.34	-	2.5	-0.32	0.42	-
5 (50mm)	3.15	-0.19	0.23	-	2.25	-0.22	0.32	-
6 (50mm)	3.1	-0.12	0.24	-	2.4	-0.25	0.42	-
7 (50mm)	3.2	-0.15	0.25	-	#	-0.19	0.26	-
8(100mm)	2.25	-0.77	0.31	T	2.3	-0.20	0.25	-
9(100mm)	3	-0.38	0.44	T	*	-0.23	0.34	-
10(100mm)	2.75	-0.38	0.18	+	*	-0.18	0.35	-
11(200mm)	2.75	-0.19	0.31	T	#	-0.23	0.28	
12 (8J)					2.15	-0.40	0.23	+
13 (8J)					3.85	-0.31	0.23	T
14 (10J)					3.4	-0.29	0.28	T
15 (10J)					3.0	-0.16	0.08	+
16 (6J)					2.25	-0.13	0.20	-
17 (6J)					3.25	-0.28	0.18	T
18 (5J)					4	-0.28	0.09	T
19 (5J)					*	-0.15	0.08	+

\# Load data corrupted   * Buckling rig stuck during initial stages of test
- Negative imperfection shape (Figure 5.18)   + Positive imperfection shape
T Twisted imperfection shape (Figure 5.19)

Table 5.10 - Damage observations from buckling specimens

Specimen	Damage Location	Damage Size (mm^2)
1	Bottom left	1267
2	Top left	2338
3	Top right	2301
4	Top right	3106
5	Bottom left	1471
6	Bottom left	1819
7	Top right	3317
8	Bottom right	313
9	Bottom right	314
10	Top right/ Bottom left	748/ 75
11	Top right	983
12	Top right	352
13	Top right	315
14	Top right/ Top left	411/ 236
15	Top right	317
16	Top right	249
17	Top right	312
18	Top right	197
19	Top right	292

Table 5.11 - Felicity ratios

Specimen	Felicity Ratio	Failure Load (kN)
2	0.901	23.32
3	0.897	20.66
4	0.815	26.31
5	0.956	27.85
6	0.862	29.21
7	0.367	27.65
8	0.950	25.12
9	0.918	26.63
10	0.893	25.12

Table 5.12 - Extrapolated curvature values at delamination initiation

Specimen	Curvature (mm^{-1})
4	0.0048
5	0.0040
6	0.0050
7	0.0039
8	0.0045
9	0.0050
10	0.0051
11	0.0057
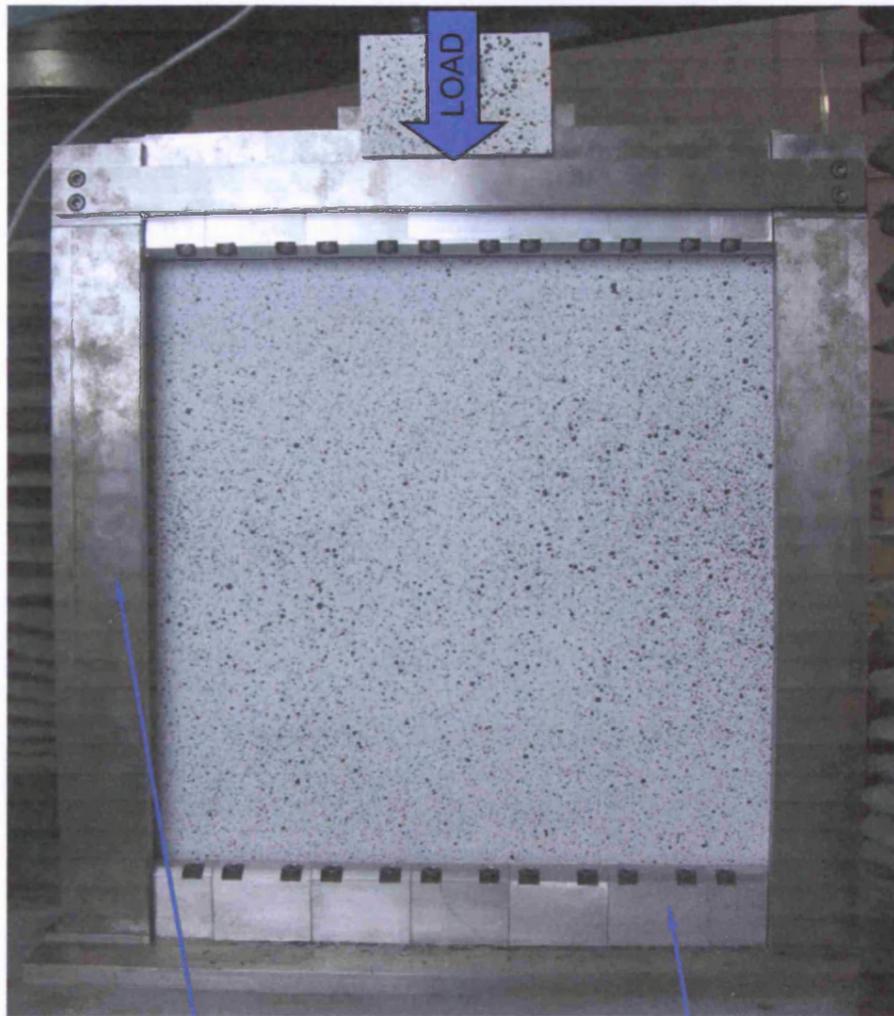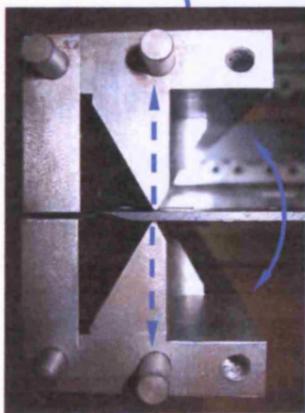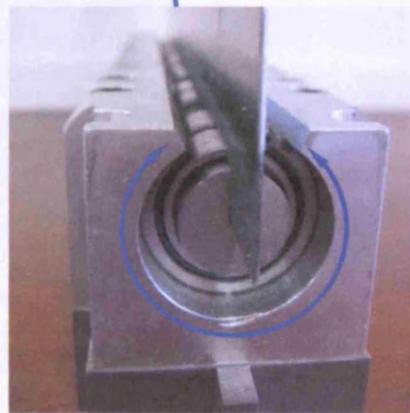
Figure 5.1 - Buckling test rig a) whole rig b) knife edge detail c) roller support detail
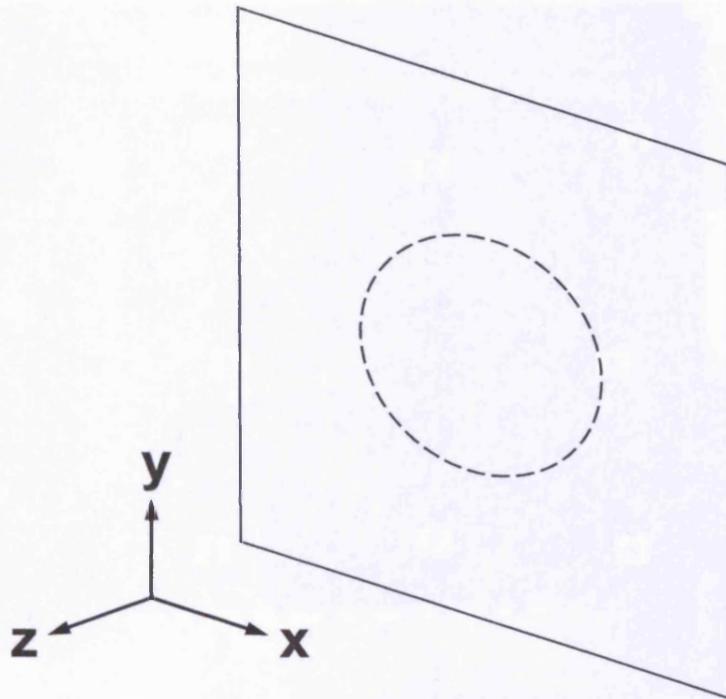
Figure 5.2 - Coordinate system
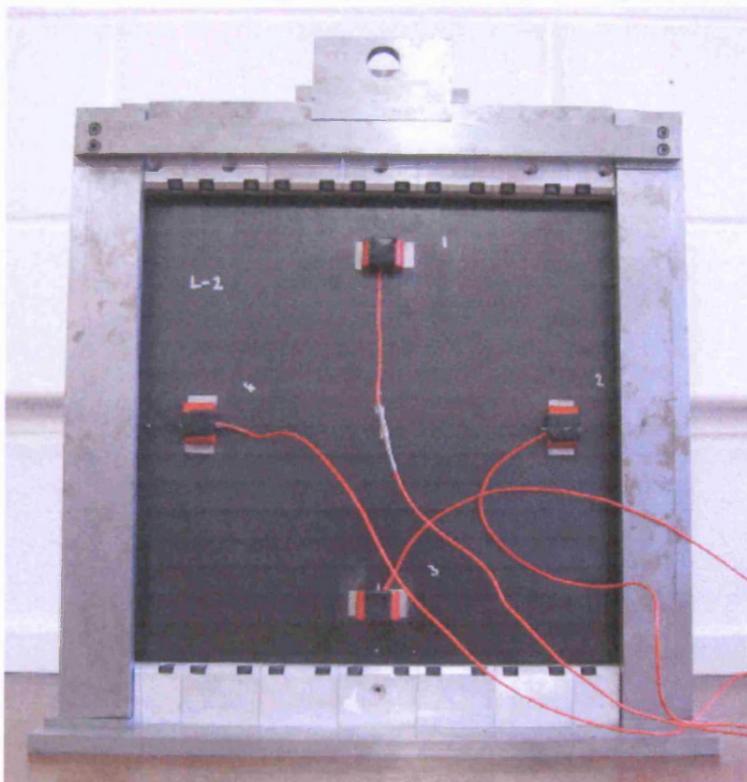
Figure 5.3 - Sensor arrangement for first stage buckling tests
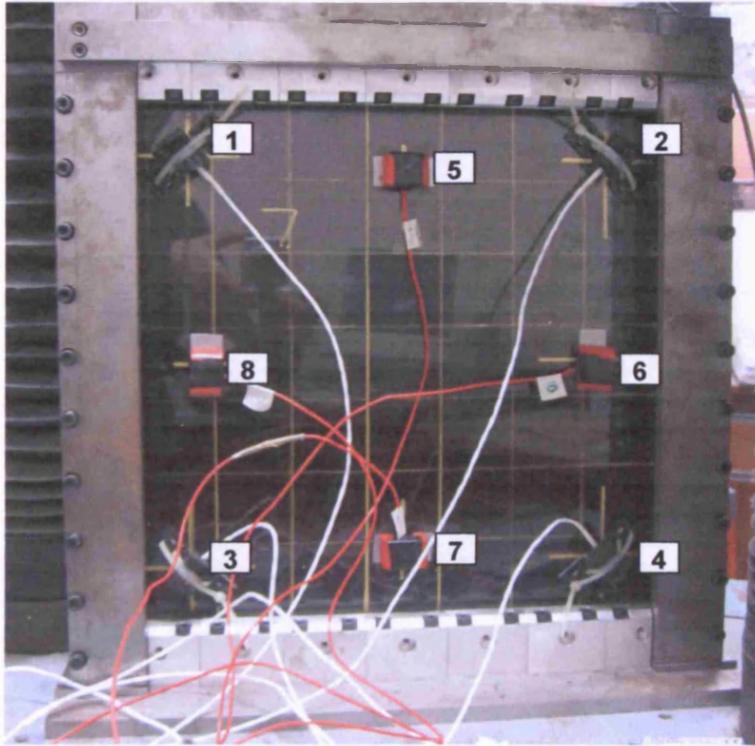
Figure 5.4 - Sensor arrangement for second stage buckling tests
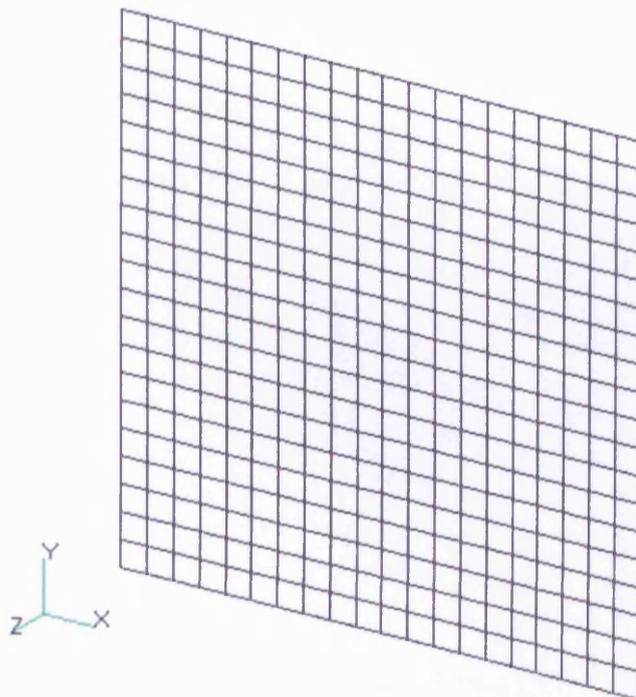
Figure 5.5 - FE mesh of undamaged plate
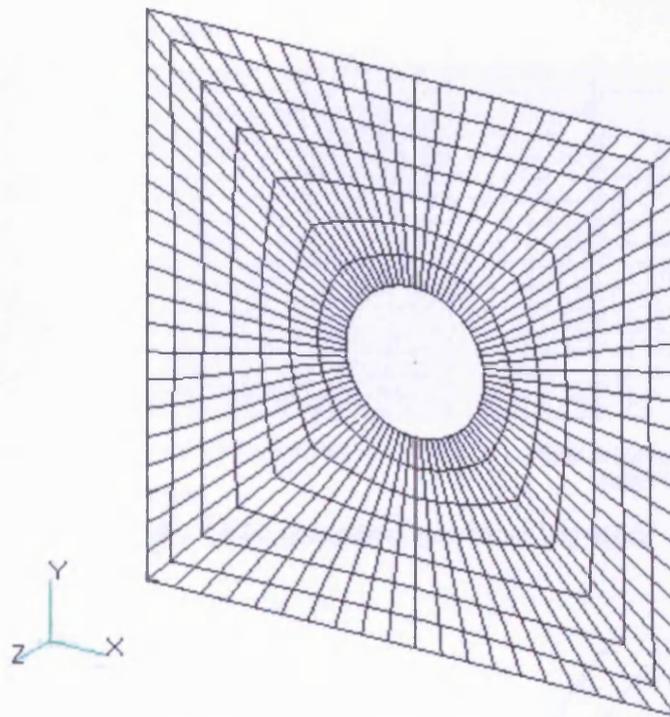
Figure 5.6 - FE mesh for 100mm hole model
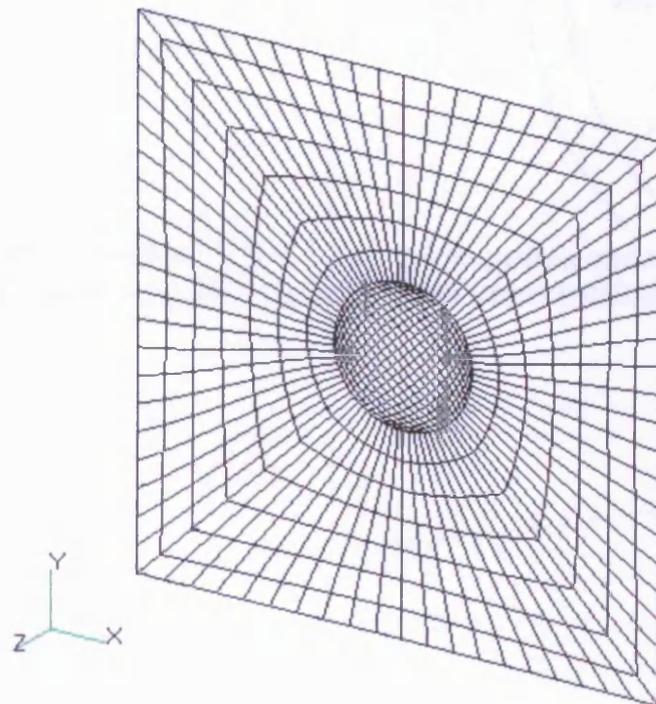
Figure 5.7 - FE mesh for 100mm delamination model
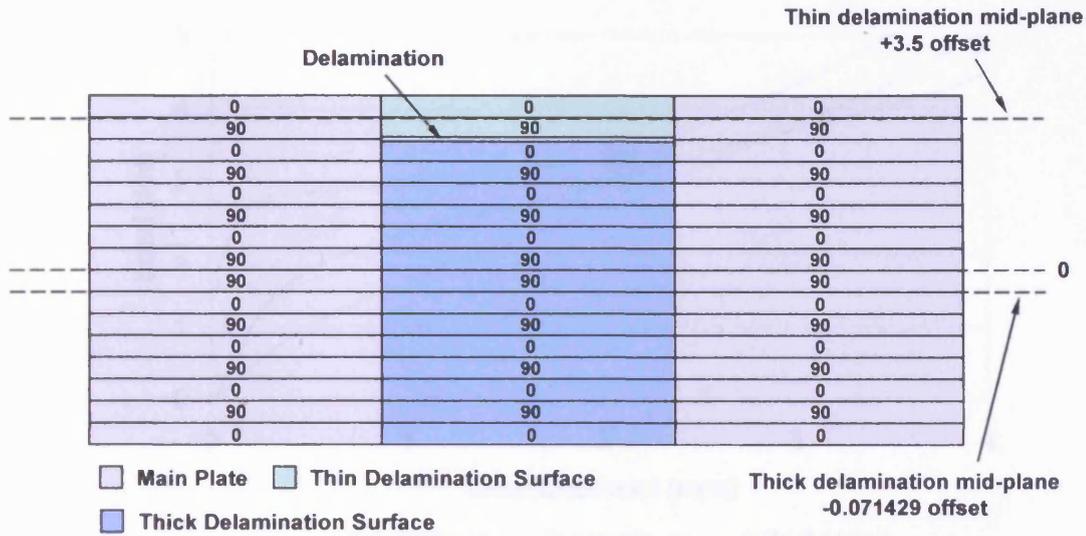
Figure 5.8 - Delamination surface lay-ups
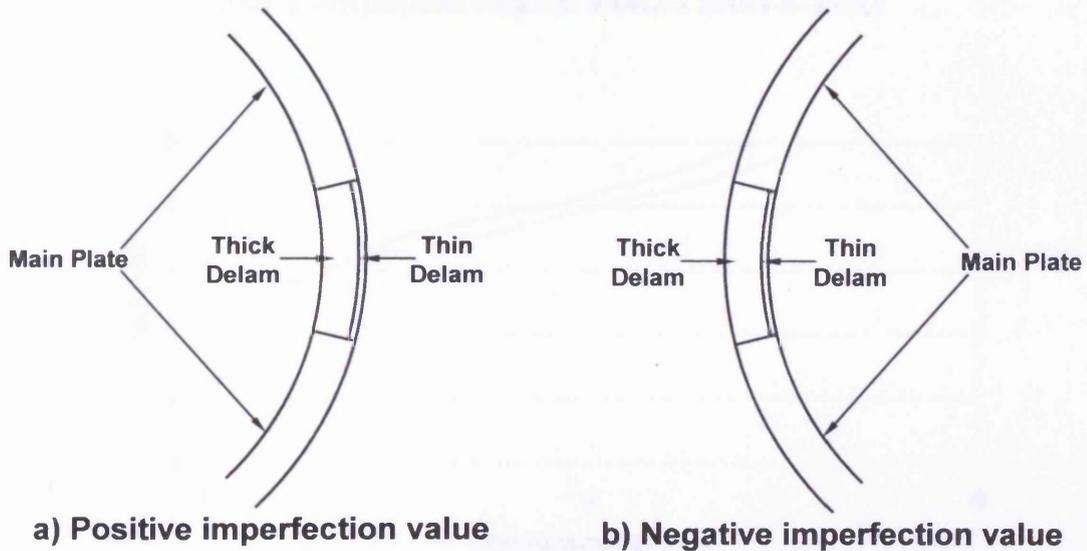
a) Positive imperfection value   b) Negative imperfection value
Figure 5.9 - Delamination model overall imperfection orientation
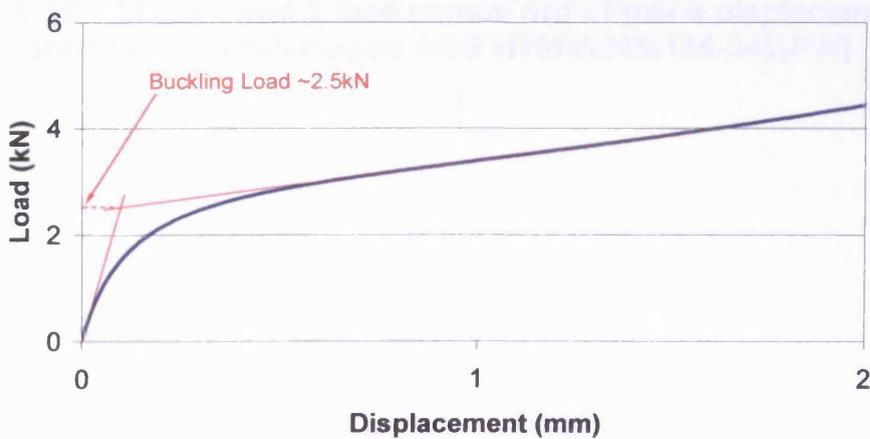
Figure 5.10 - Buckling load extraction
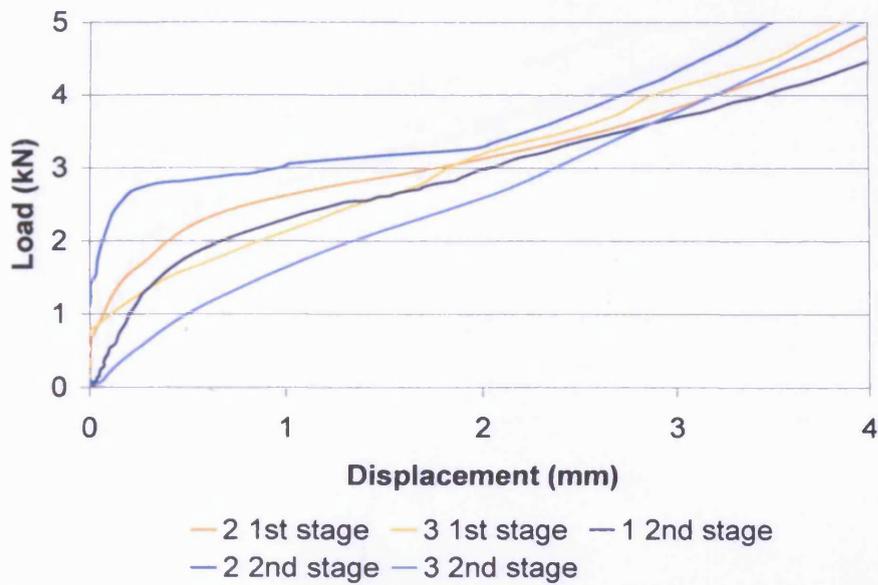
Figure 5.11 - Stage 1 and 2 load versus displacement for specimens 1, 2 and 3 (Impacted Hexcel 914C-T300H-5-34%)
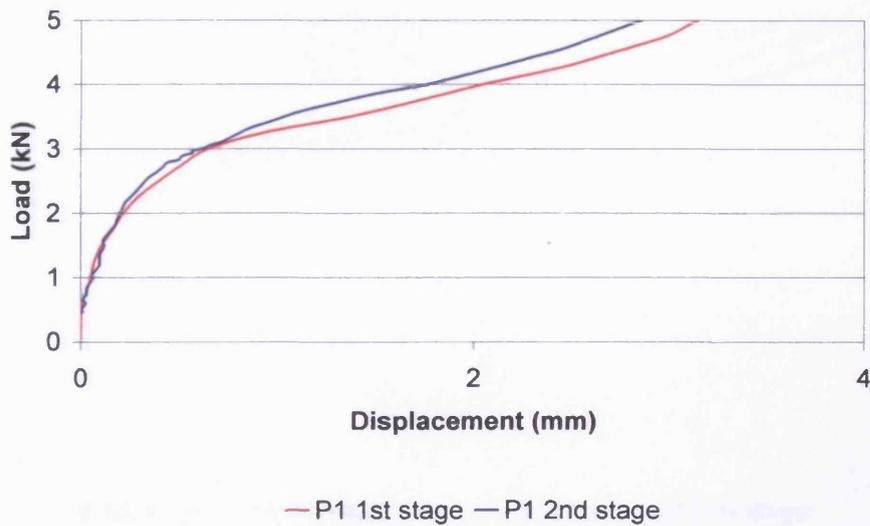
Figure 5.12 – Stage 1 and 2 load versus out-of-plane displacement for specimen 4 (undamaged ACG HTM45/HS-135-34%RW)
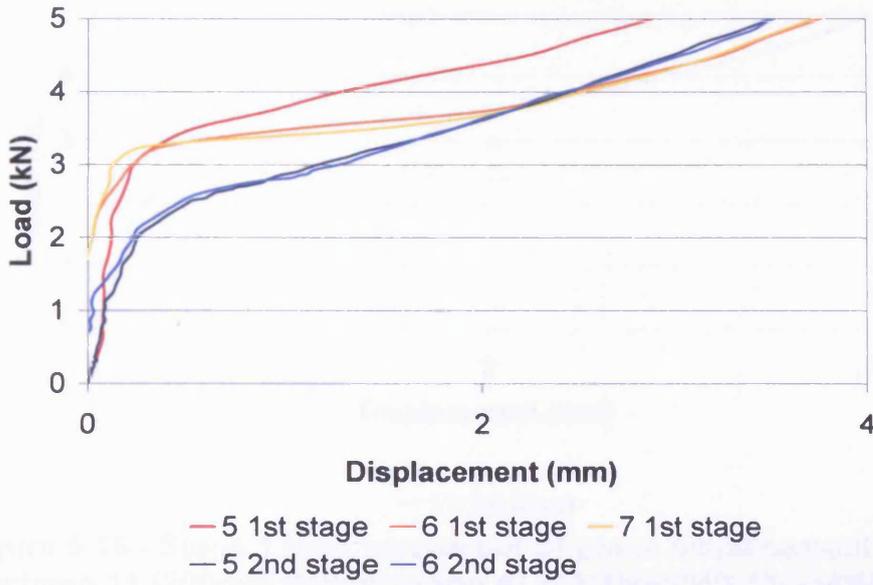
Figure 5.13 - Stage 1 and 2 load versus out-of-plane displacement for specimens 5, 6 and 7 (50mm delamination ACG HTM45/HS-135-34%RW)
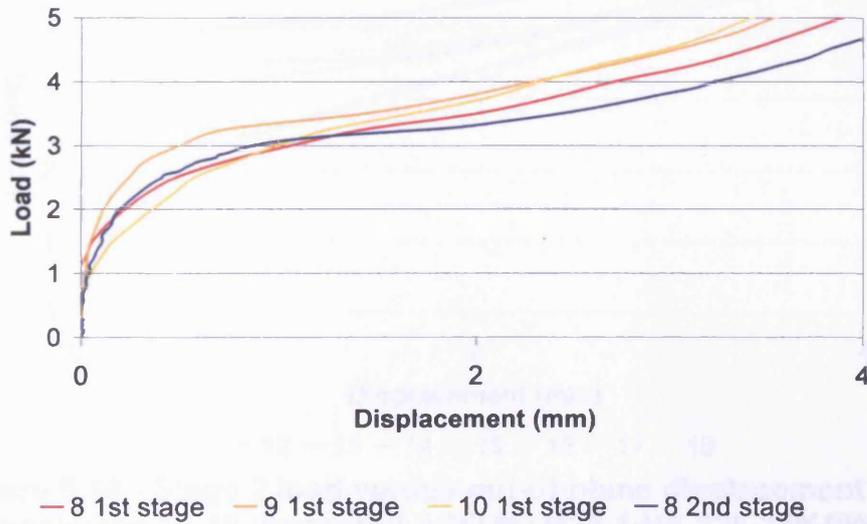
Figure 5.14 - Stage 1 and 2 load versus out-of-plane displacement for specimens 8, 9 and 10 (100mm delamination ACG HTM45/HS-135-34%RW)
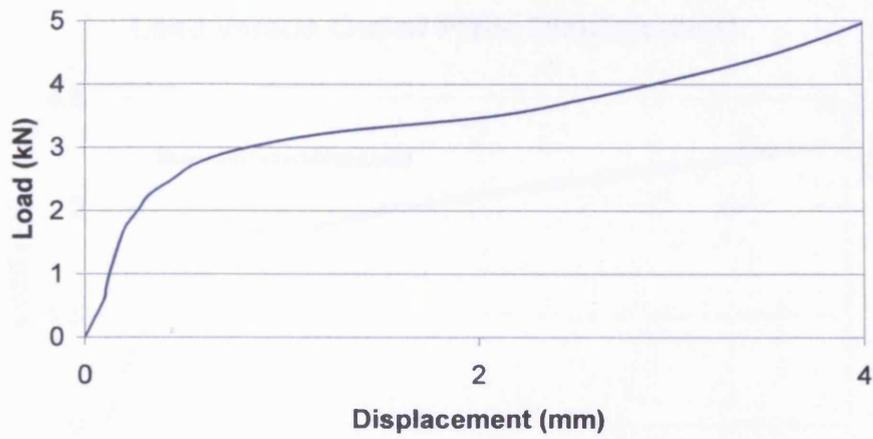
— 11 1st stage

Figure 5.15 - Stage 1 load versus out-of-plane displacement for specimen 11 (200mm delamination ACG HTM45/HS-135-34%RW)
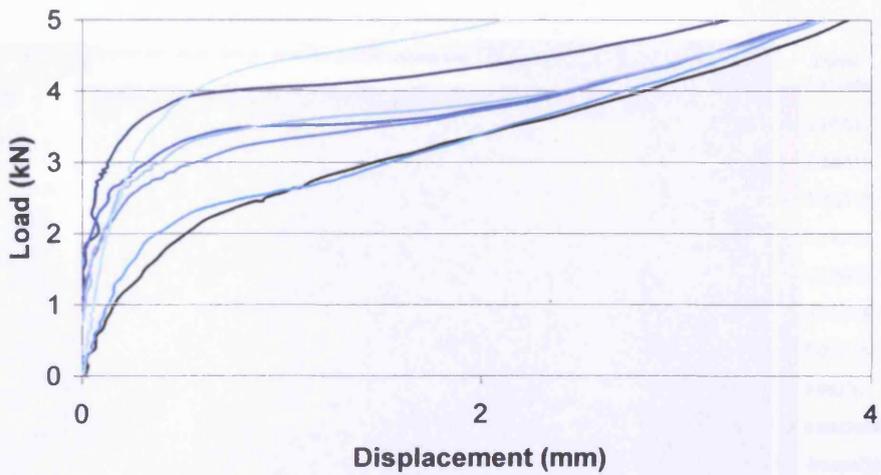
— 12 — 13 — 14 — 15 — 16 — 17 — 18

Figure 5.16 - Stage 2 load versus out-of-plane displacement for specimens 12-18 (Impacted ACG MTM28-1/HS-135-34%RW)
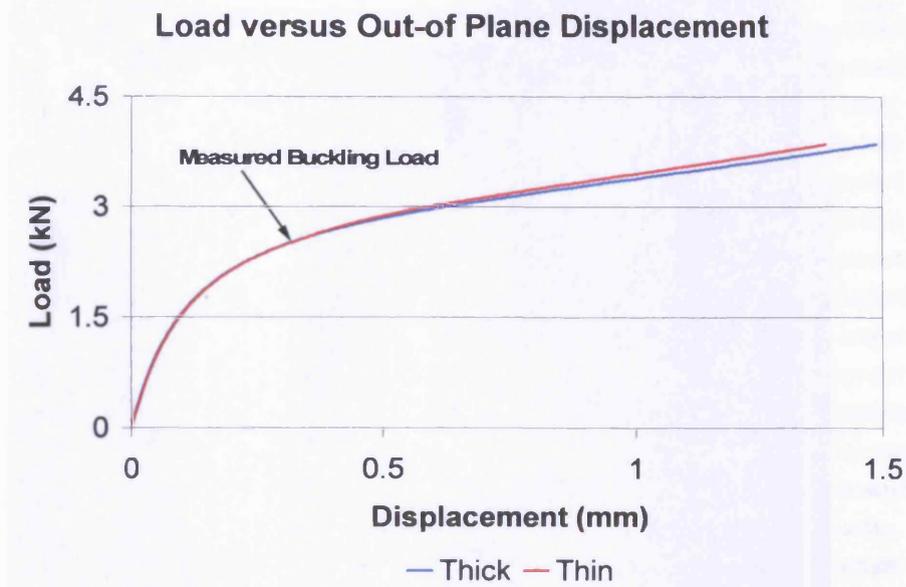
Figure 5.17 - Example of load displacement for 100mm negative Riks analysis
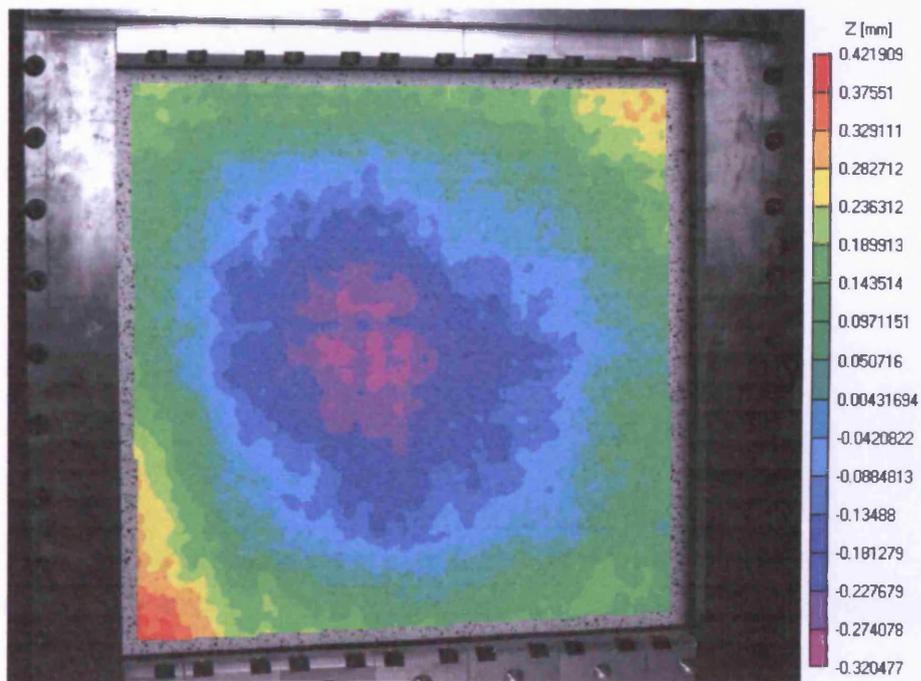
Figure 5.18 - Example of a negative buckling mode initial imperfection
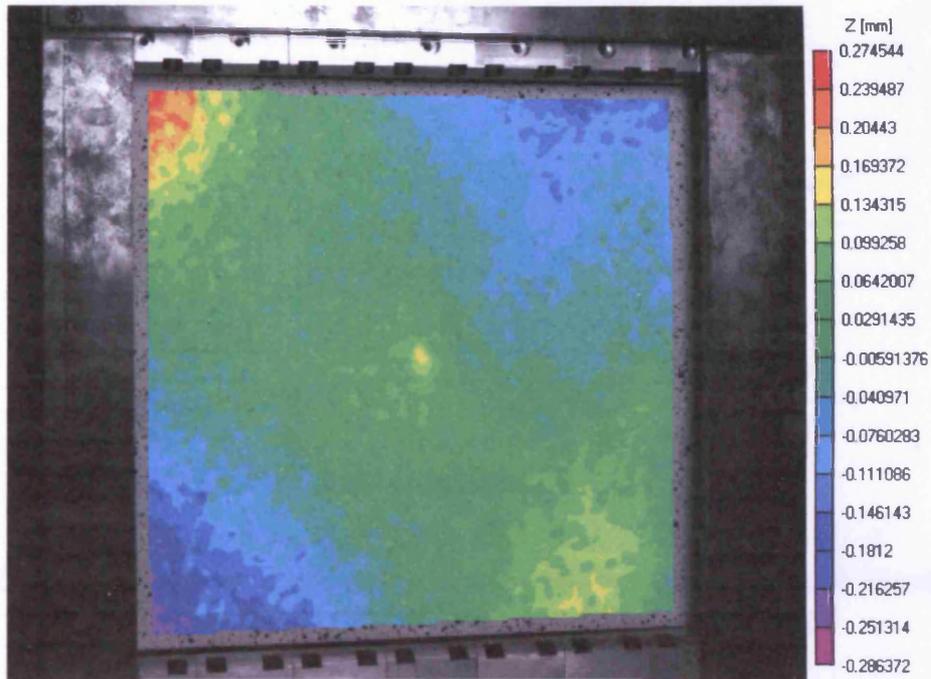
Figure 5.19 - Example of twisted initial imperfection
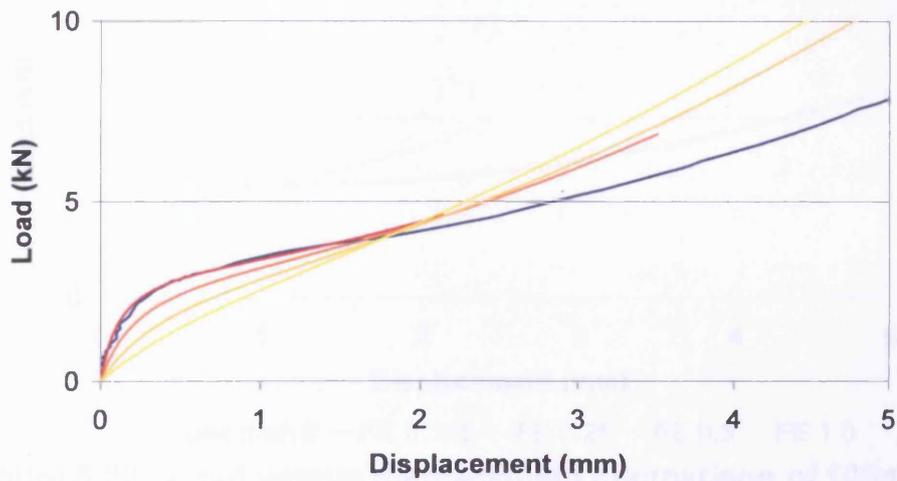
Figure 5.20 – Load versus displacement comparison of undamaged model with experimental results
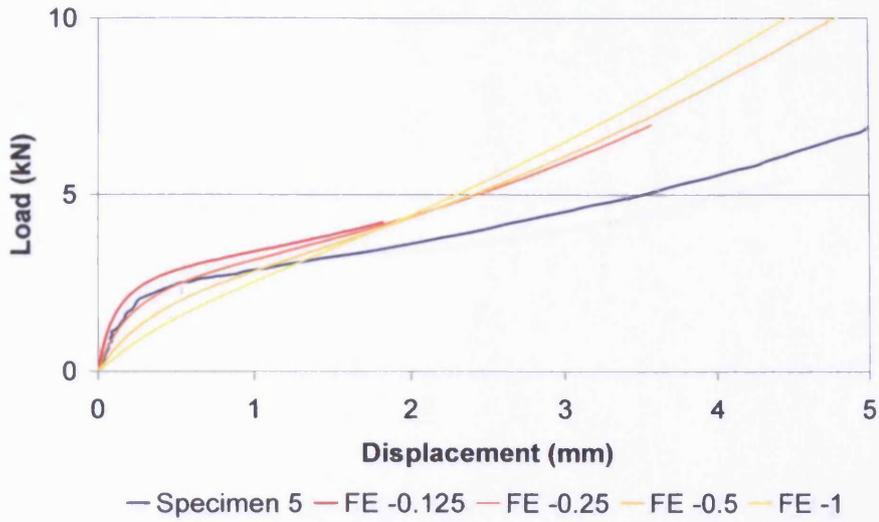
Figure 5.21 - Load versus displacement comparison of 50mm delamination model with experimental results
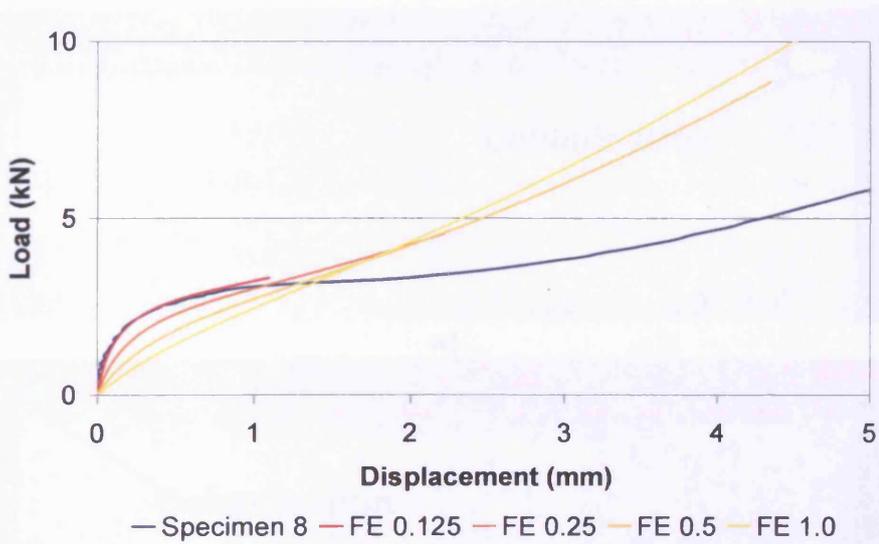
Figure 5.22 - Load versus displacement comparison of 100mm delamination model with experimental results
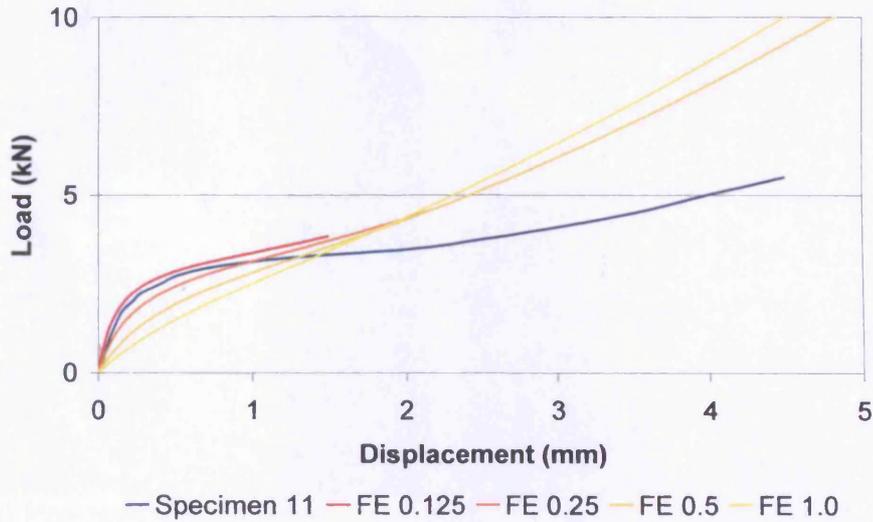
Figure 5.23 - Load versus displacement comparison of 200mm delamination model with experimental results

a)

b)
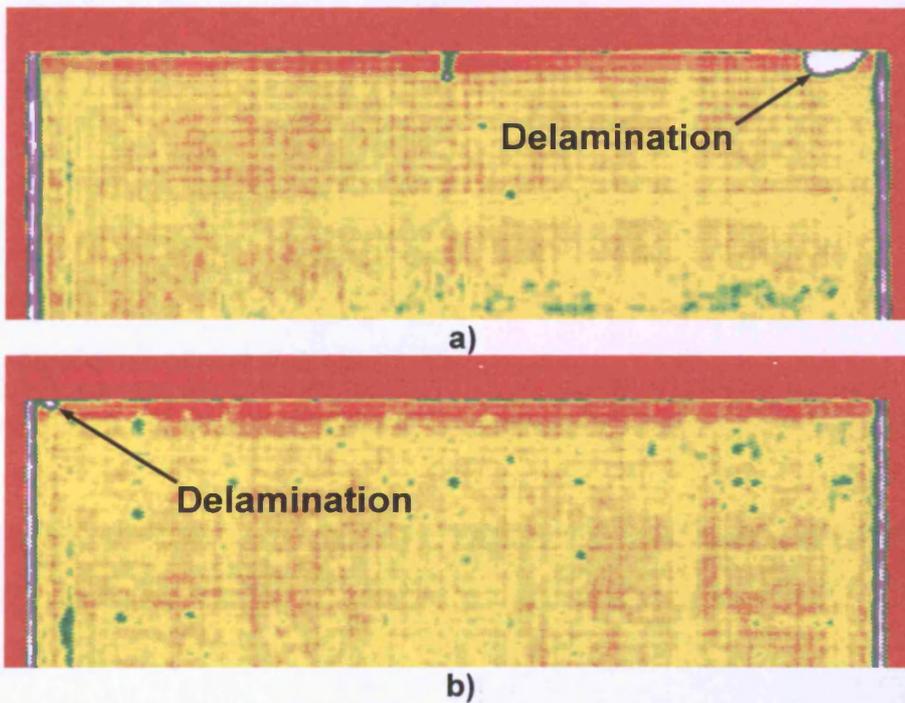
Figure 5.24 - Delamination observed in C-scan images of a) specimen 4 and b) specimen 7

a) Pre-test specimen 5　　　　　c) Pre-test specimen 1
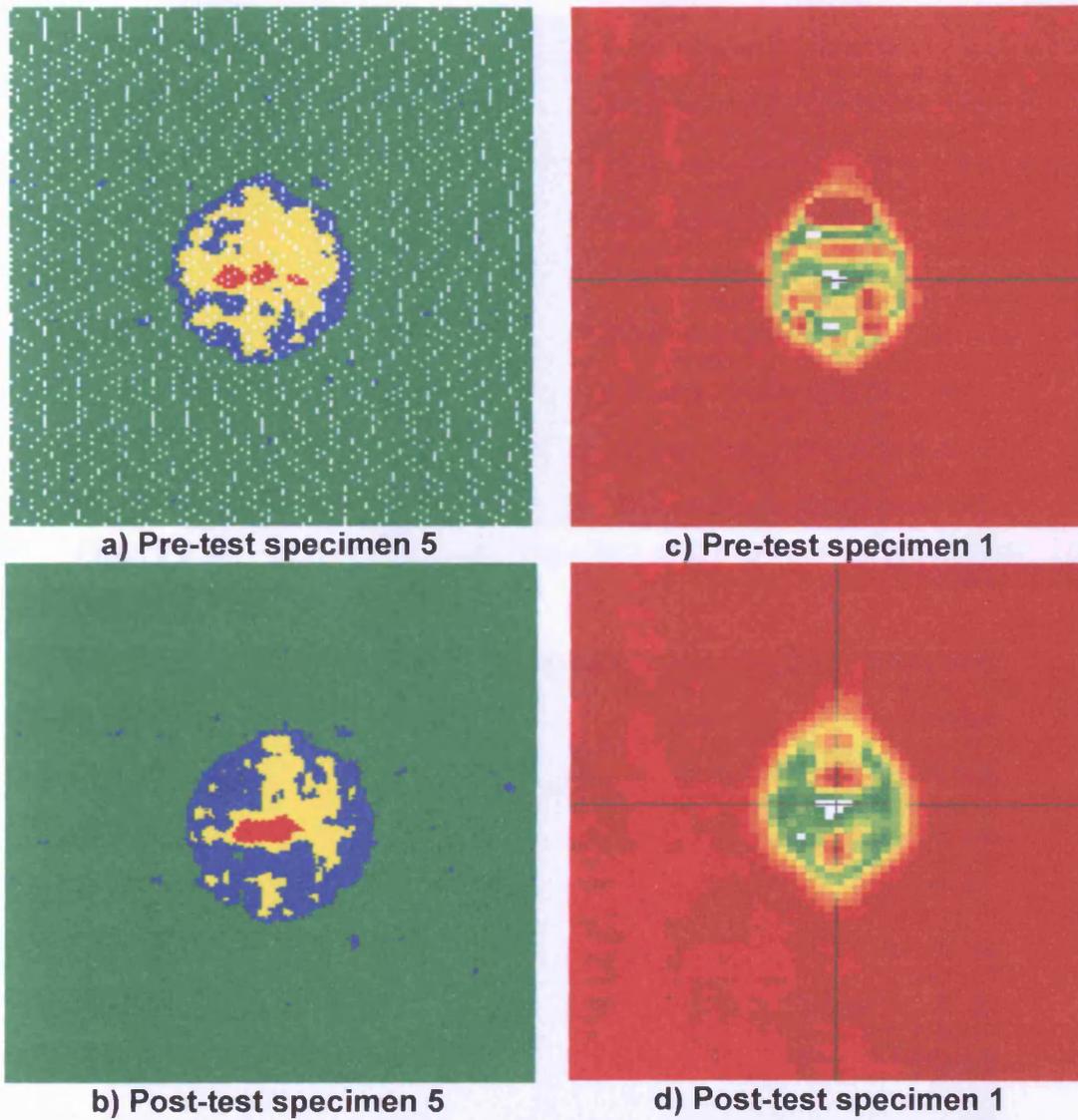
b) Post-test specimen 5　　　　d) Post-test specimen 1
Figure 5.25 - C-scan images of delamination from pre and post-test
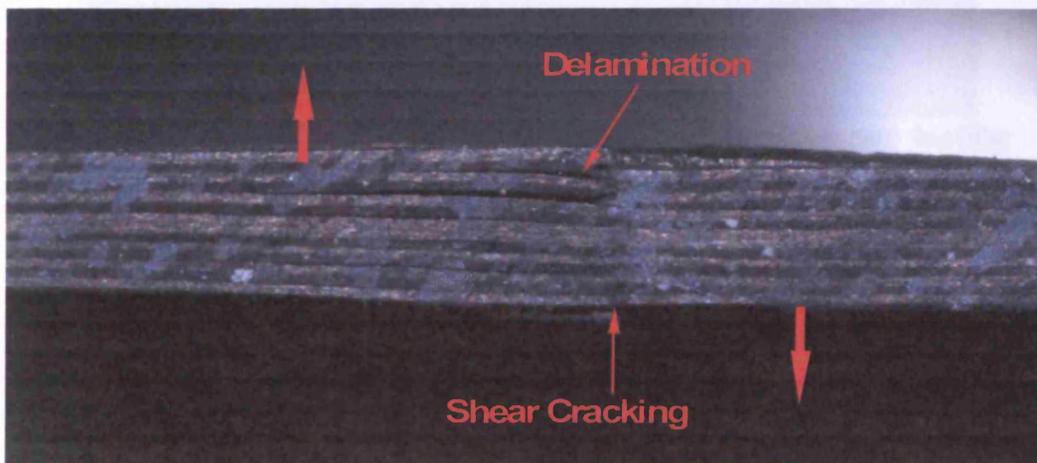
Figure 5.26 - Shear cracking and delamination observed at failure site
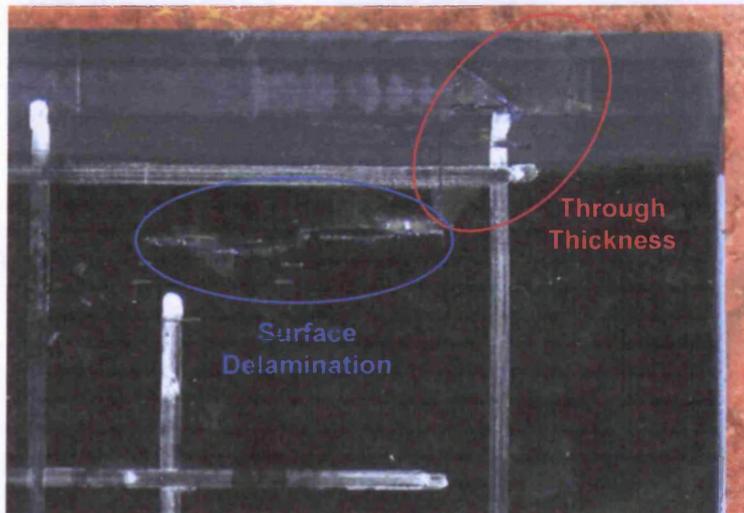
Figure 5.27 - Shear crack propagation and surface delamination
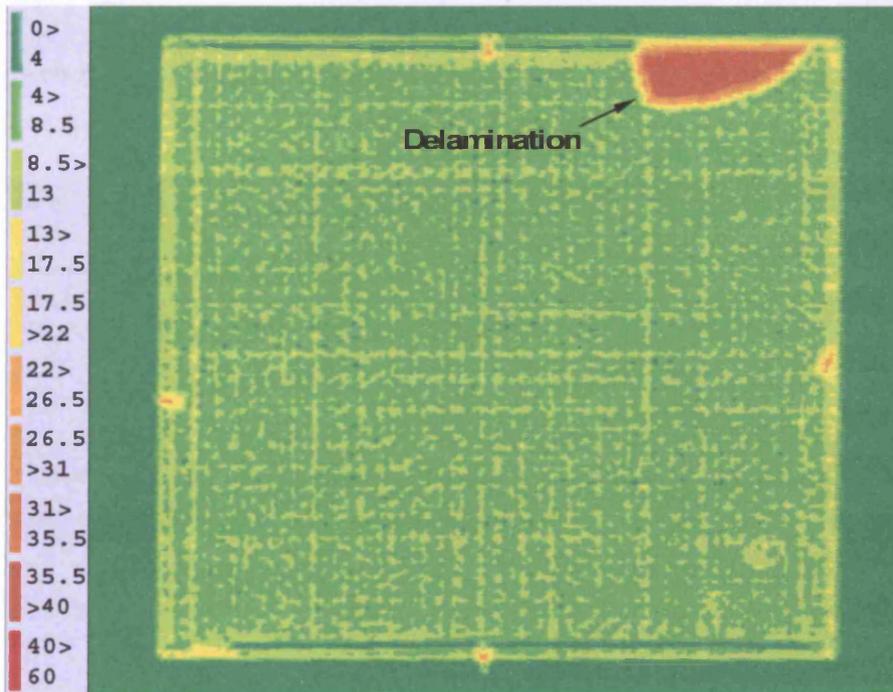
Figure 5.28 - C-scan image of specimen 4 after stage two testing
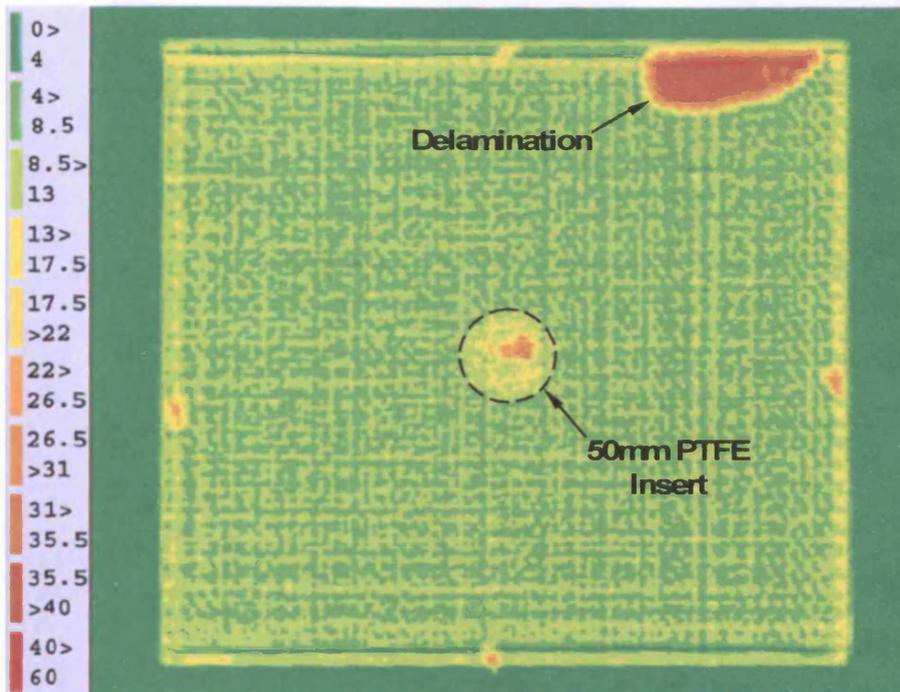
Figure 5.29 - C-scan image of specimen 7 after stage two testing
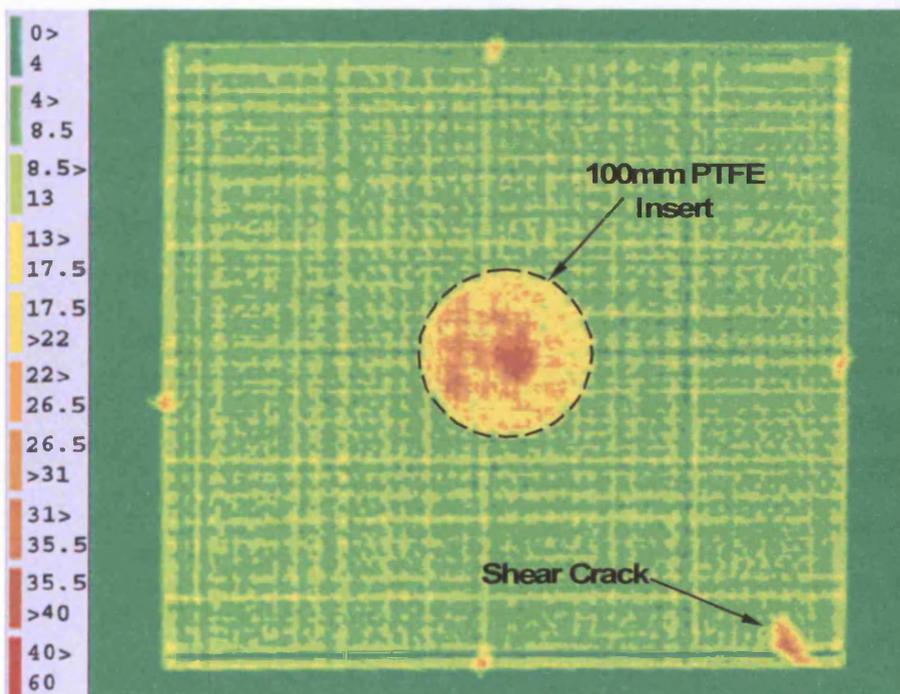
Figure 5.30 - Specimen 8 C-scan Image after stage two testing
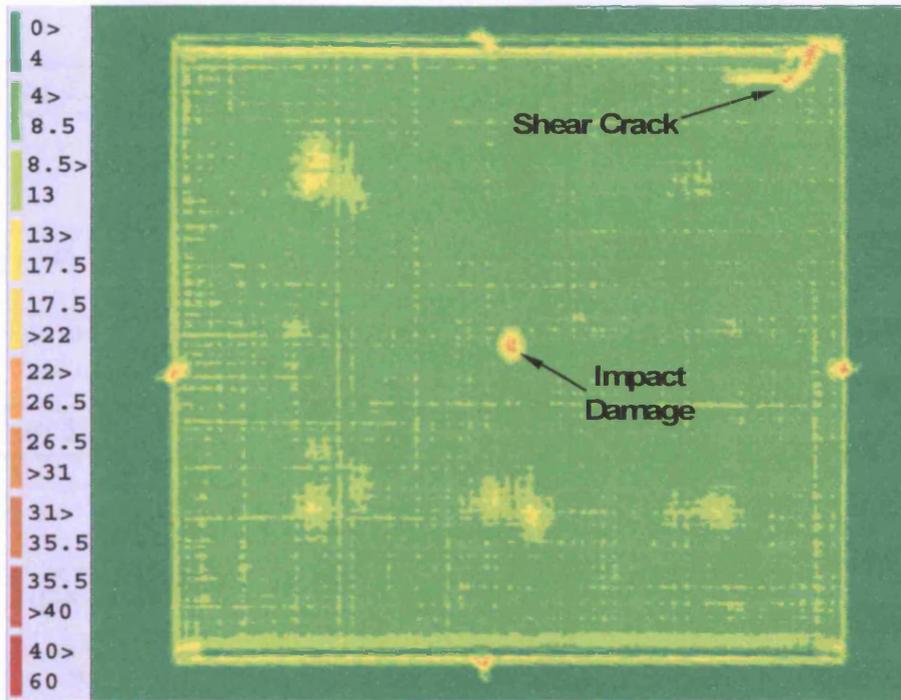
Figure 5.31 - Specimen 12 C-scan image after stage two testing
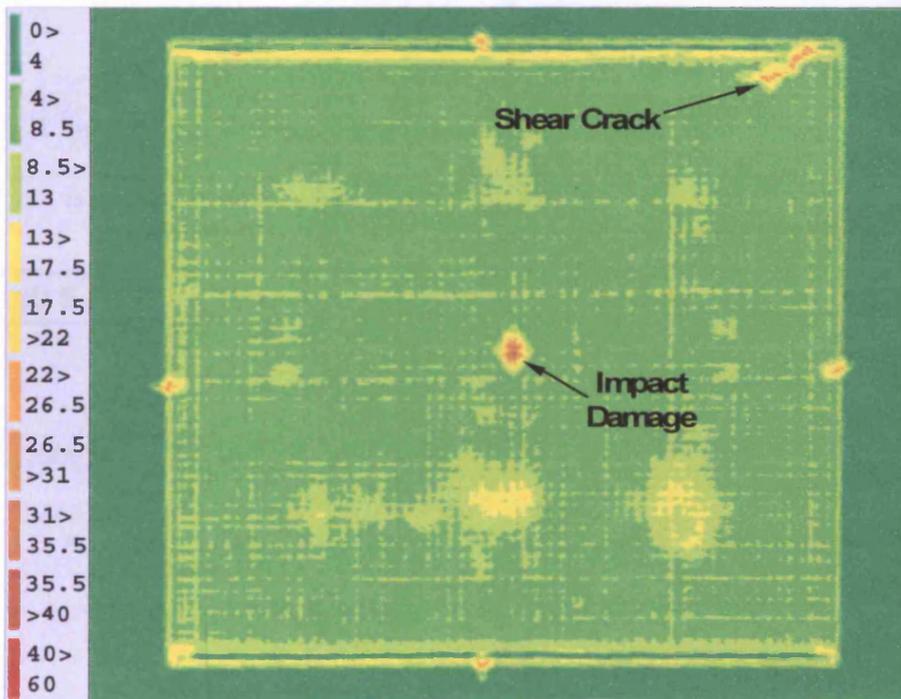
Figure 5.32 - Specimens 15 C-scan images after stage two testing
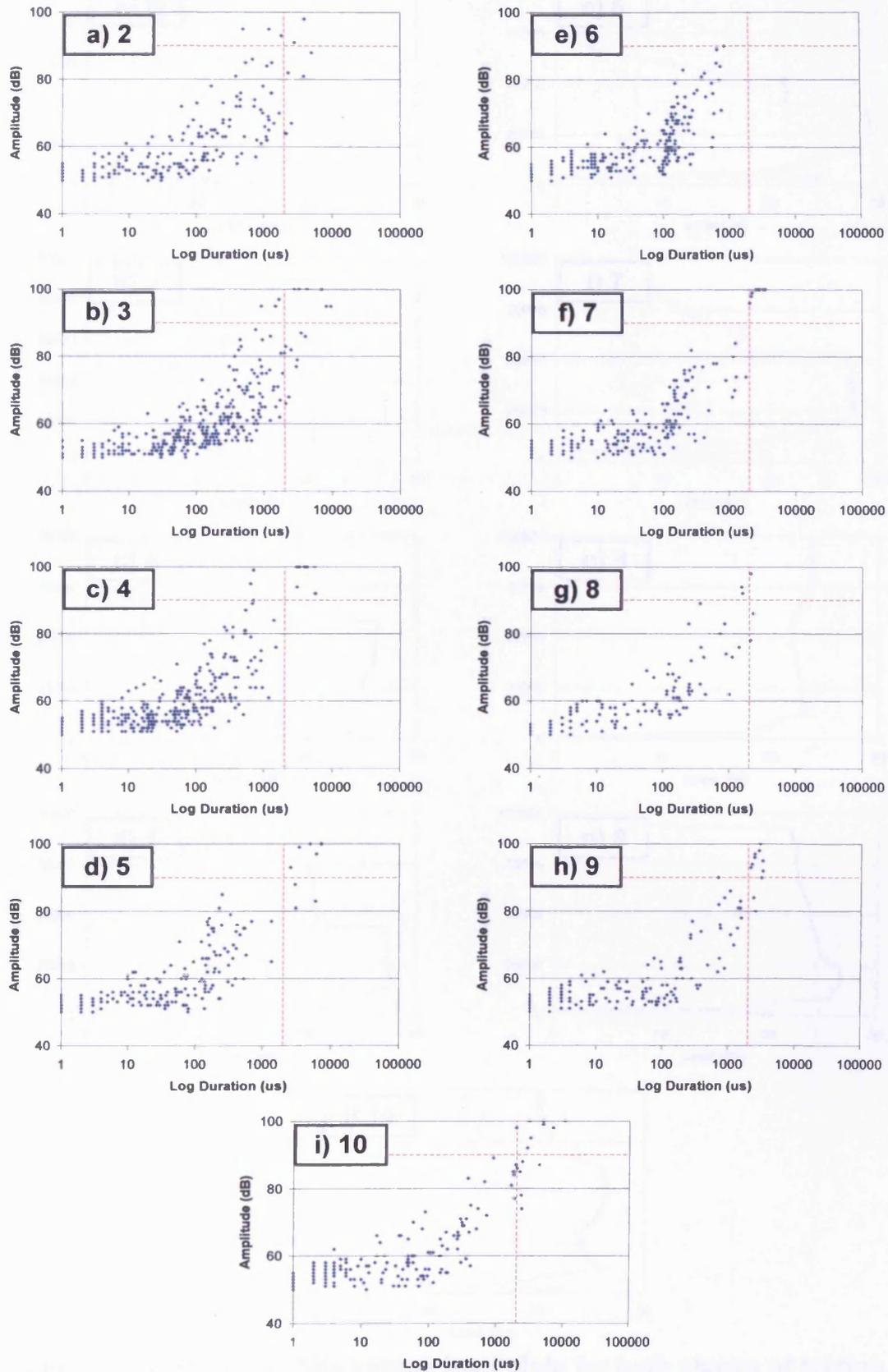
Figure 5.33 Amplitude versus duration correlation plots from first stage buckling tests
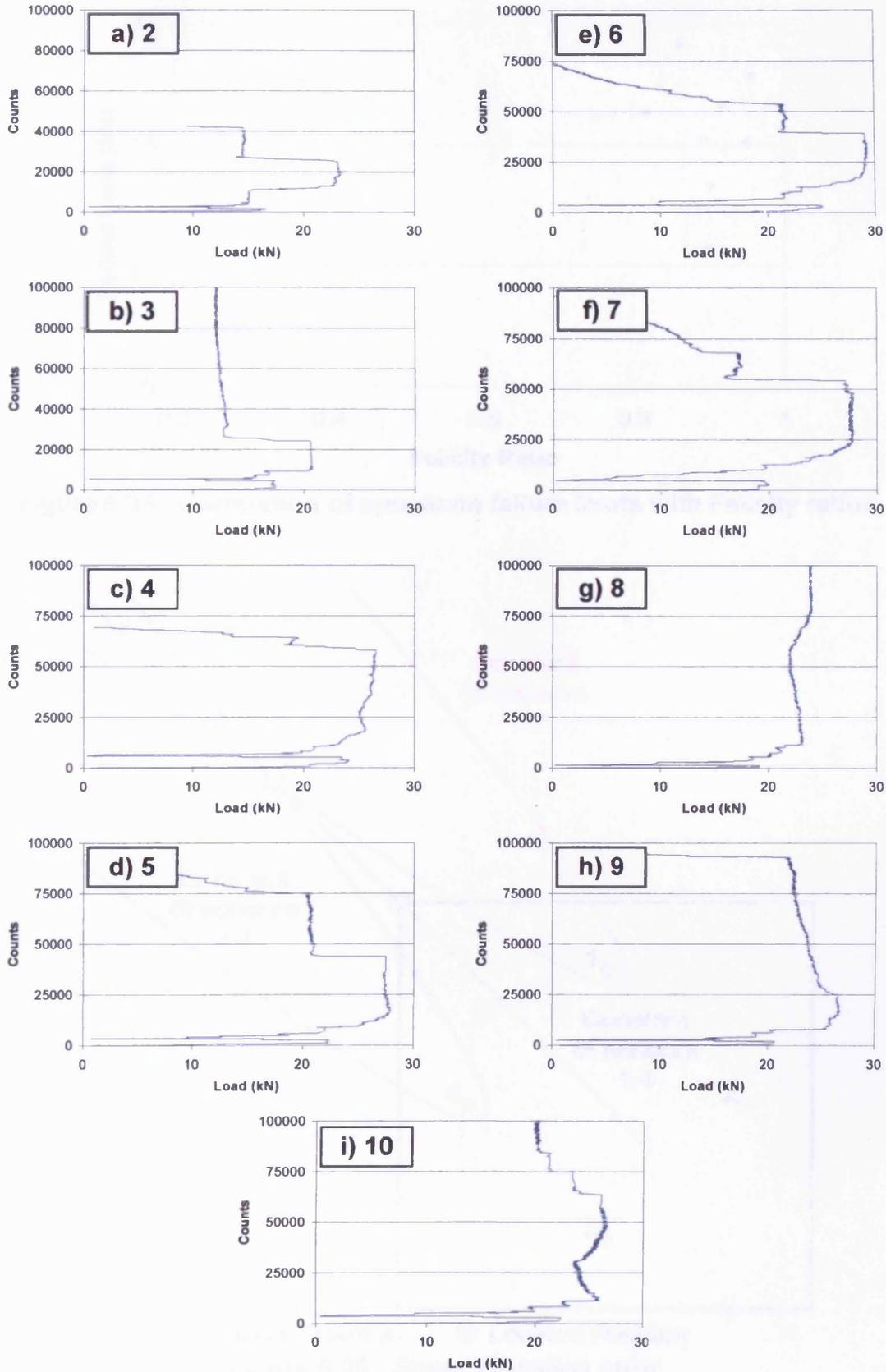
Figure 5.34- Cumulative hits versus load plots for both stages of testing, demonstrating the Felicity effect
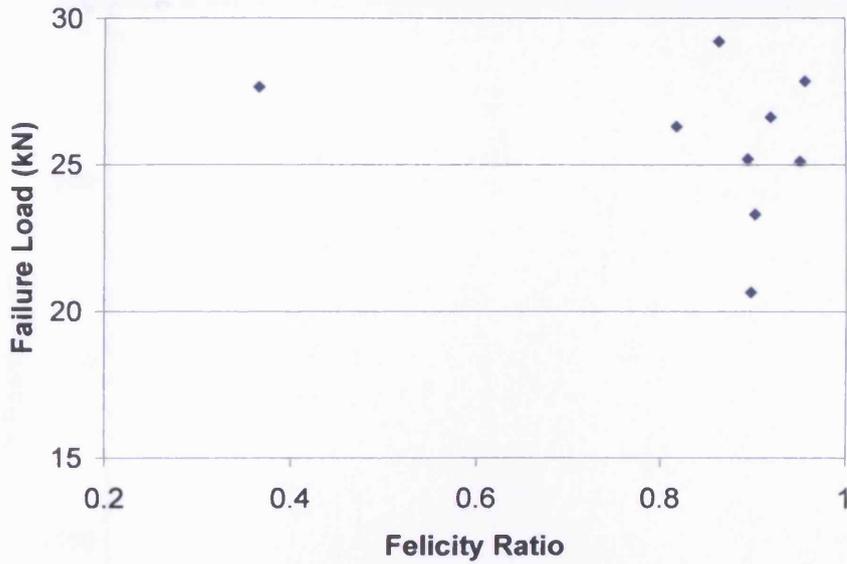
Figure 5.35 - Correlation of specimen failure loads with Felicity ratios
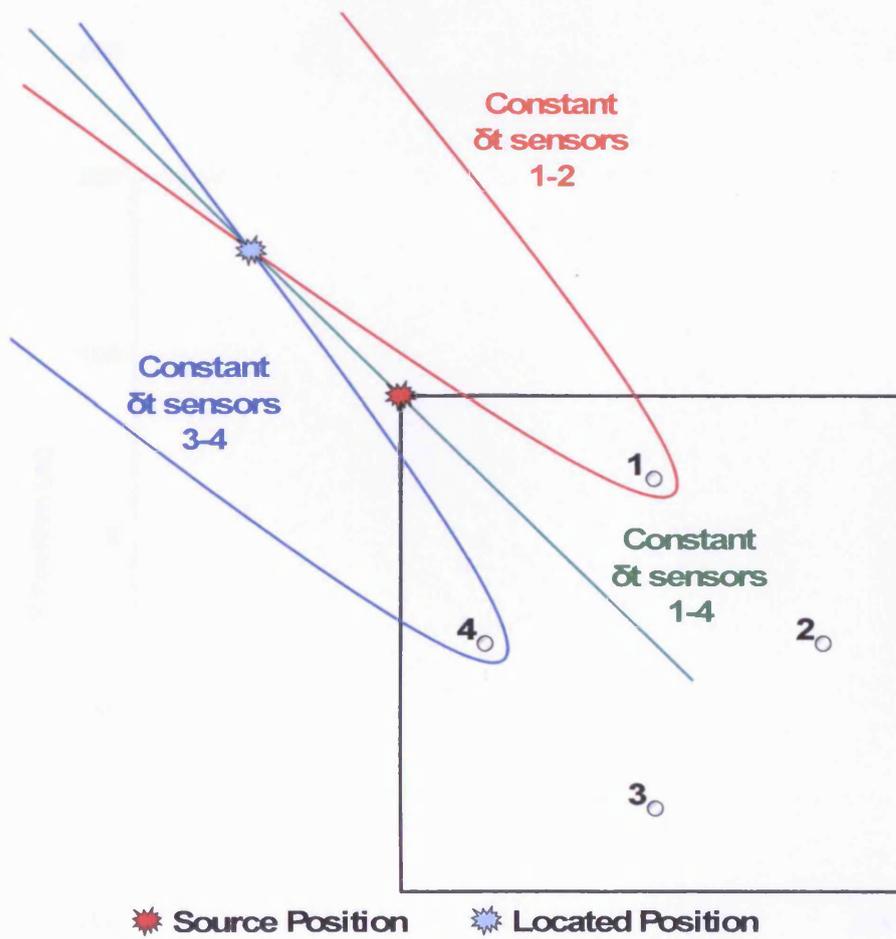
Figure 5.36 - Stage 1 location error
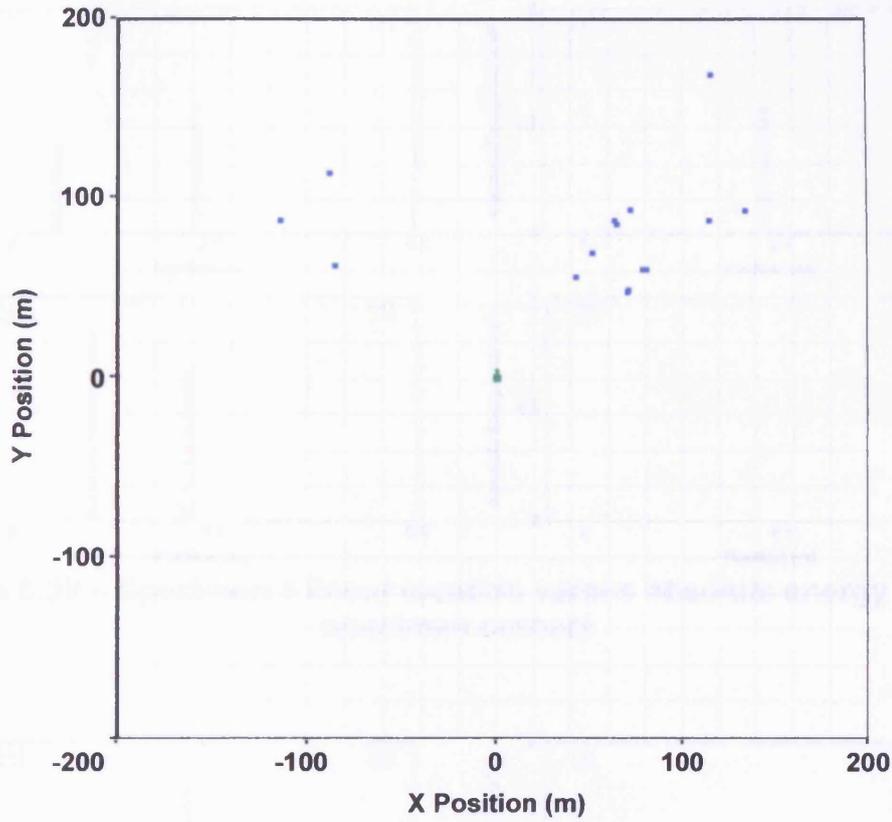
a) Specimen 4
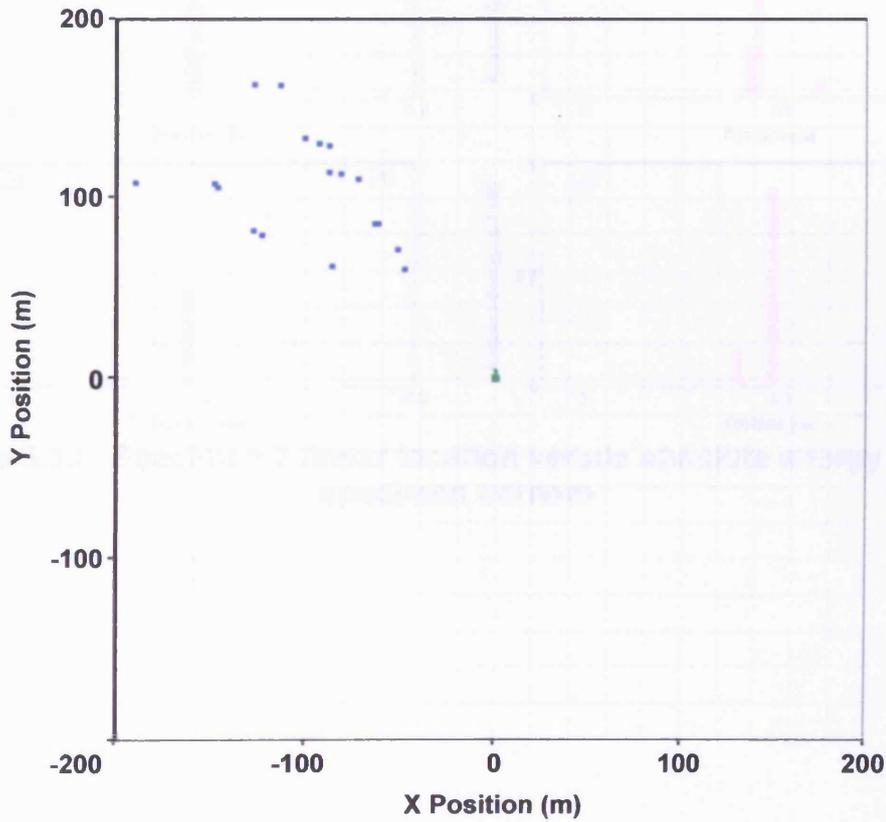
b) Specimen 7

Figure 5.37 - TOA locations from stage 1 testing
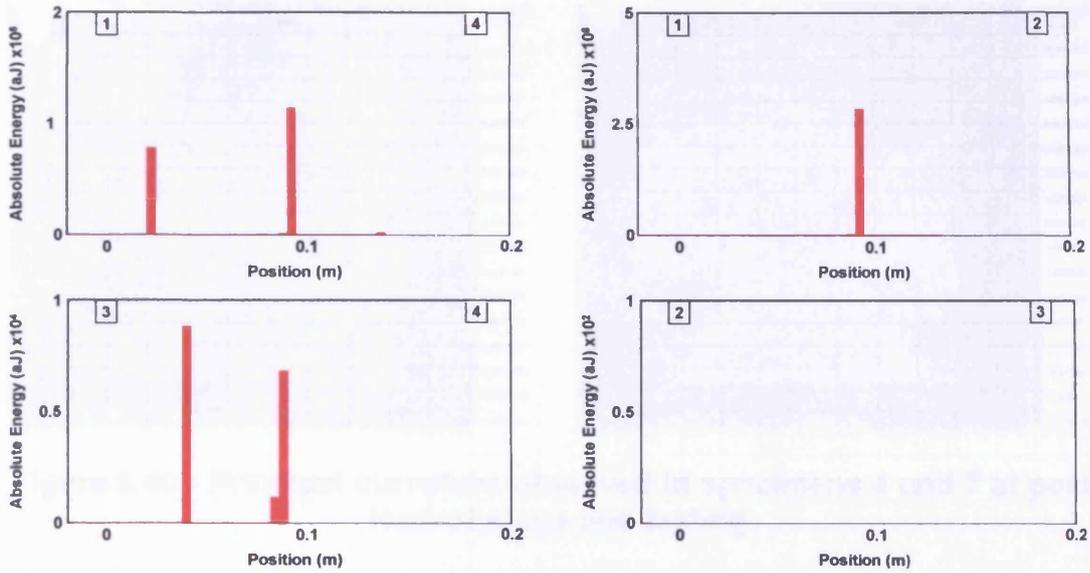
Figure 5.38 – Specimen 4 linear location versus absolute energy across specimen corners
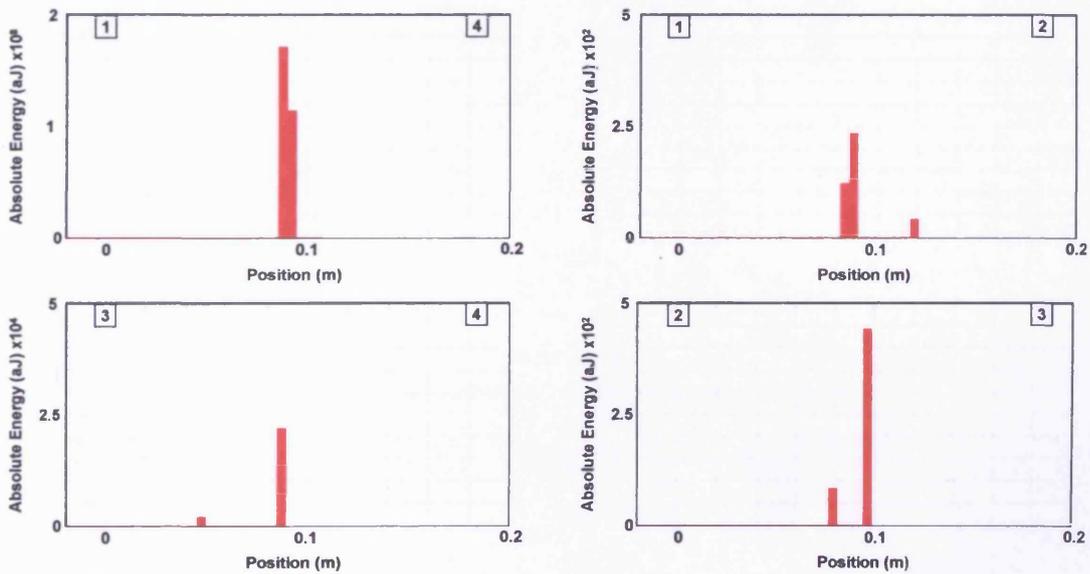
Figure 5.39 - Specimen 7 linear location versus absolute energy across specimen corners
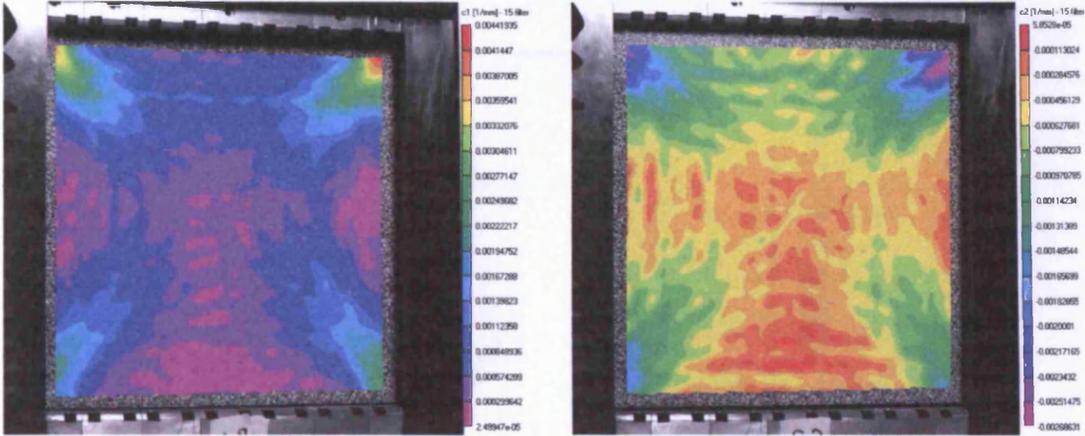
Figure 5.40 - Principal curvature observed in specimens 4 and 7 at peak load of stage one testing
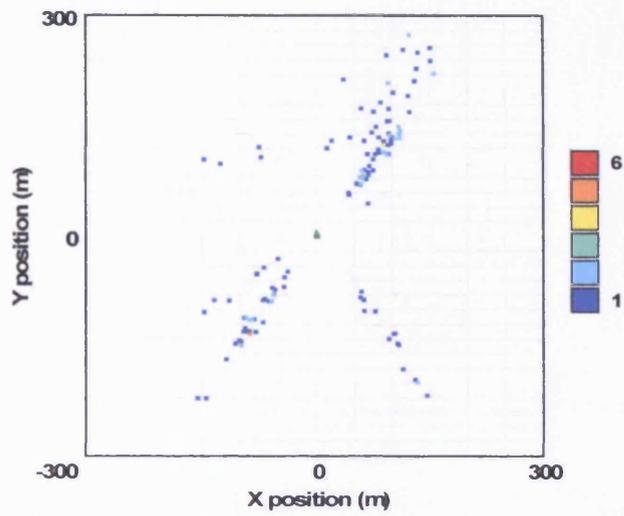
a) TOA Nano 30 sensor array (sensors 5-8)
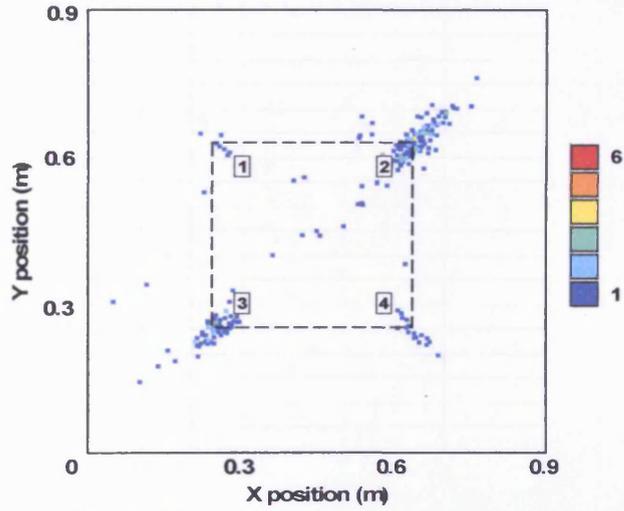
b) TOA WD sensor array (sensors 1-4)
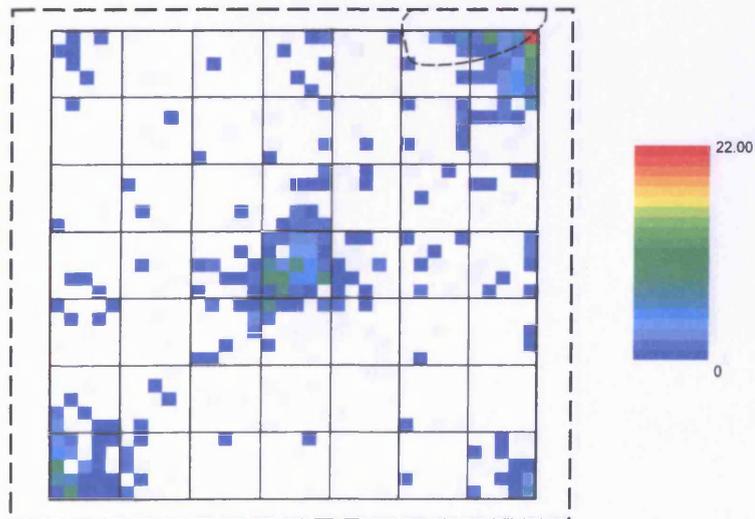
c) DeltaT locations (sensors 1-8)

**Figure 5.41 - Two-dimensional locations from specimen 4 second stage testing**

a) TOA Nano 30 sensor array (sensors 5-8)

b) TOA WD sensor array (sensors 1-4)

c) DeltaT locations (sensors 1-8)
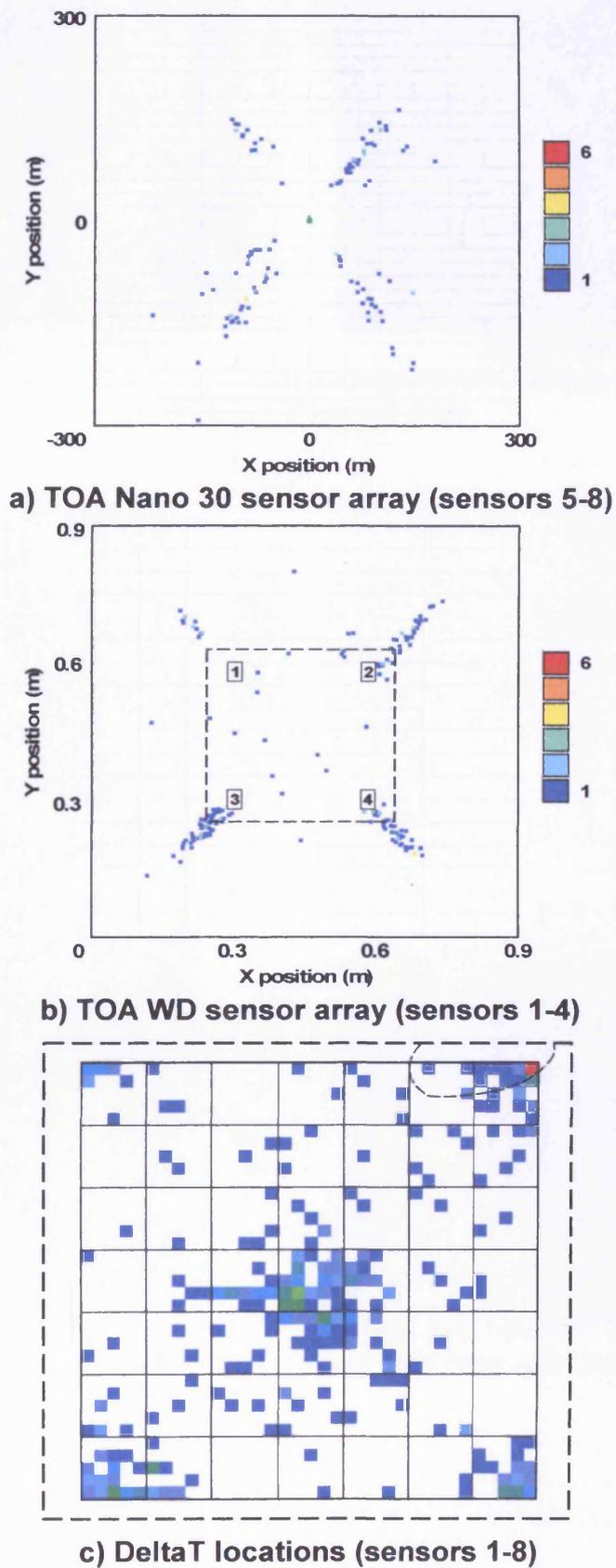
Figure 5.42 - Two-dimentional locations from specimen 7 second stage testing
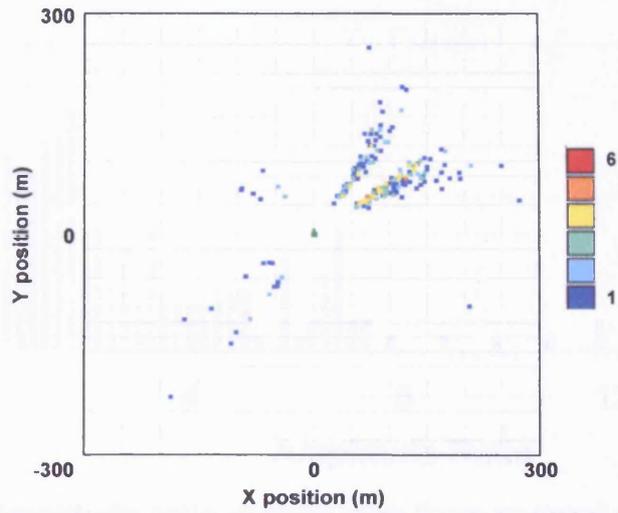
a) Specimen 4   b) Specimen 7

Figure 5.43 - Principal curvature measured just before failure under second stage loading

a) 1 - 5   b) 4 - 6

c) 1 - 4   d) 1-5, 4-6, and 1-4 overlaid

Figure 5.44 - DeltaT location grids from specimen 4

a) TOA Nano30 sensor array (sensors 5-8)
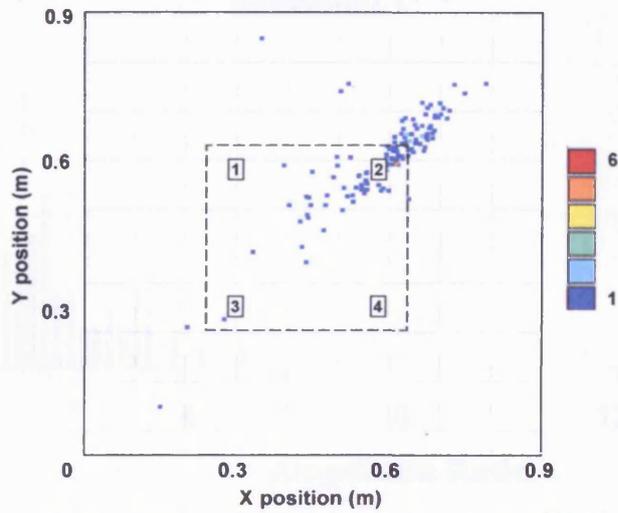
b) TOA WD sensor array (sensors 1-4)
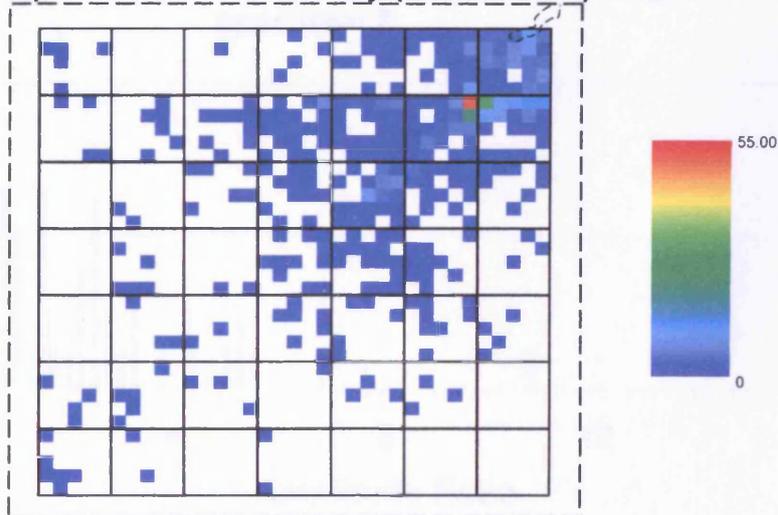
c) DeltaT locations (sensors 1-8)

Figure 5.45 – Two-dimensional locations from specimen 15 second stage testing
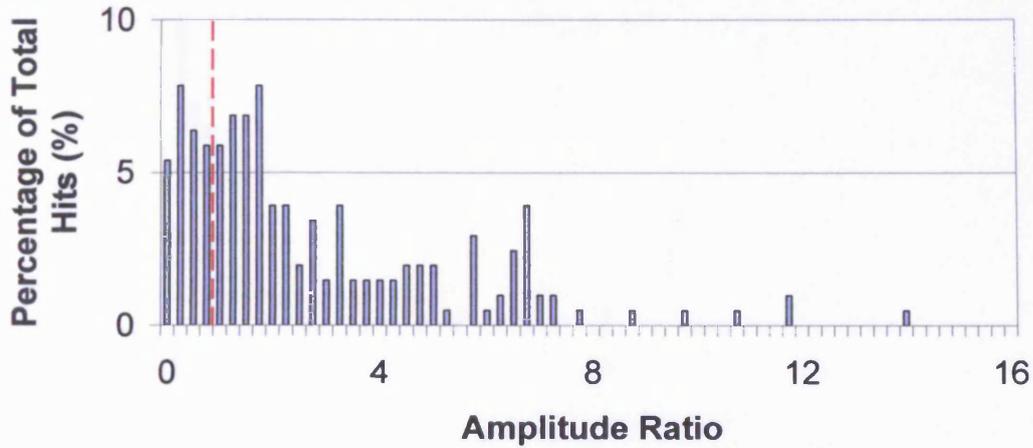
Figure 5.46 - Amplitude ratio distribution from second stage testing of specimen 1
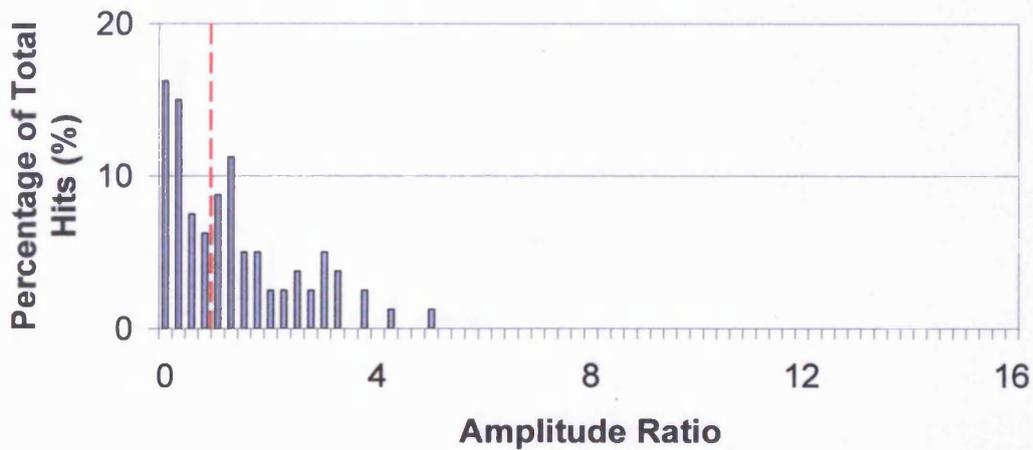
**Figure 5.47 - Amplitude ratio distribution from second stage testing of specimen 2**
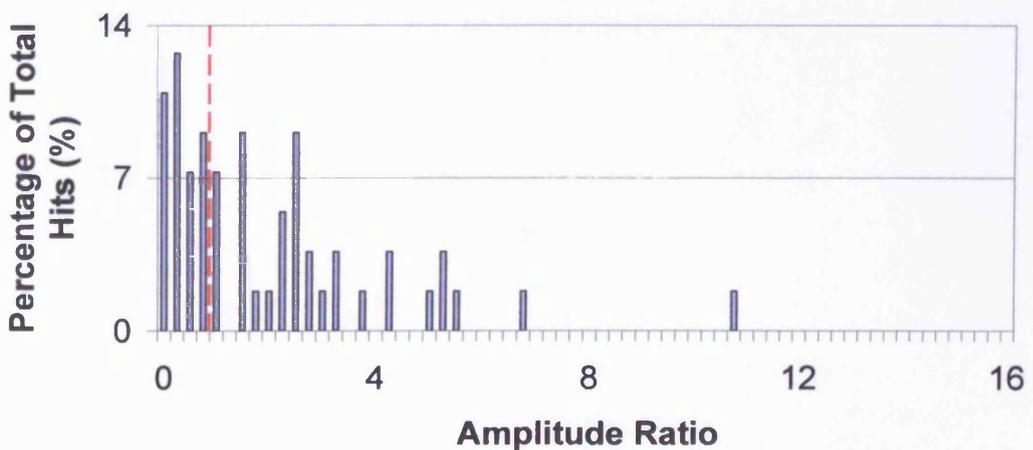
Figure 5.48 - Amplitude ratio distribution from second stage testing of specimen 3
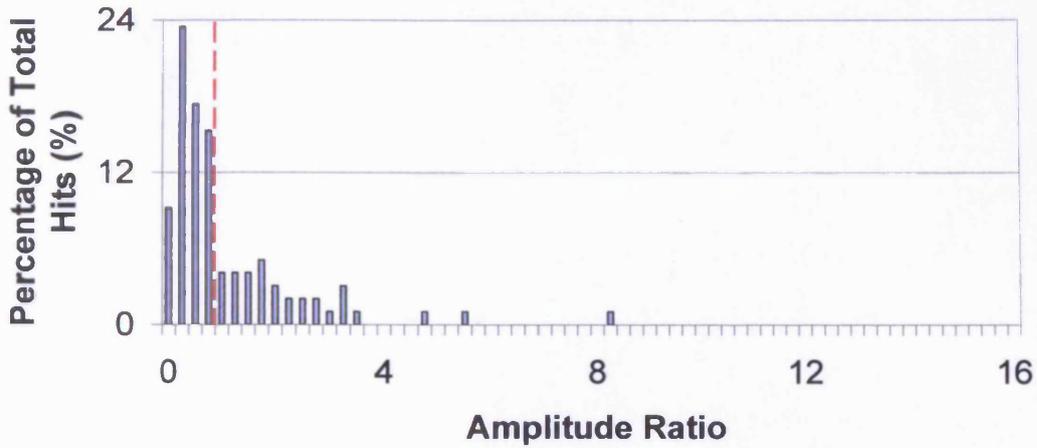
Figure 5.49 - Amplitude ratio distribution from second stage testing of specimen 4
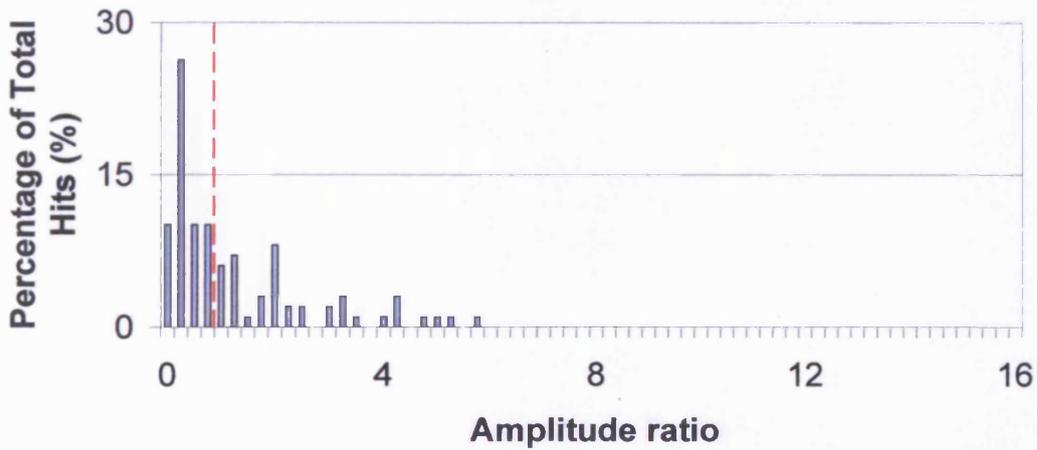
Figure 5.50 - Amplitude ratio distribution from second stage testing of specimen 5
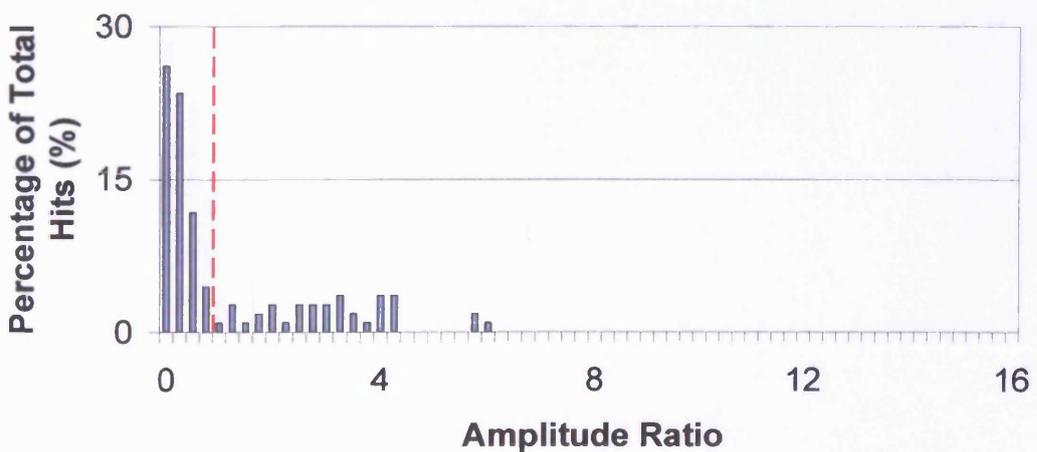

Figure 5.51 - Amplitude ration distribution from second stage testing of specimen 6
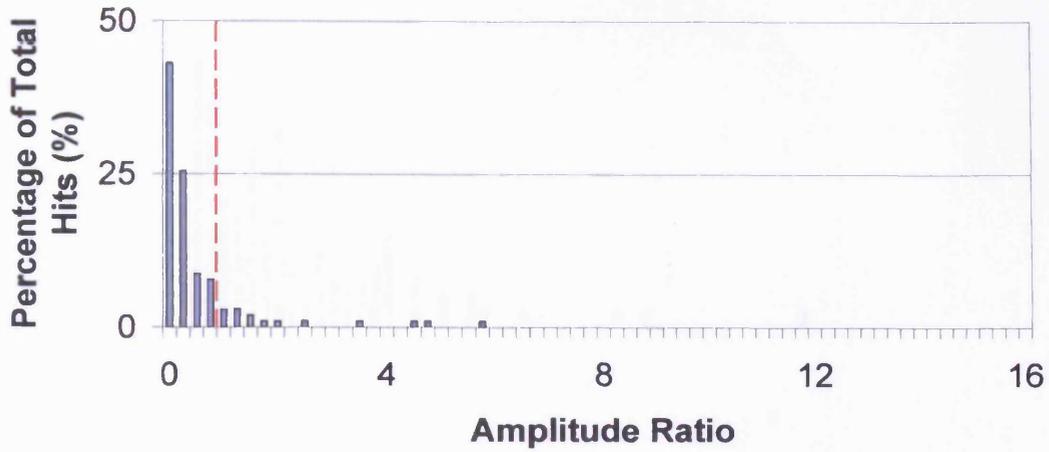
Figure 5.52 - Amplitude ratio distribution from second stage testing of specimen 7
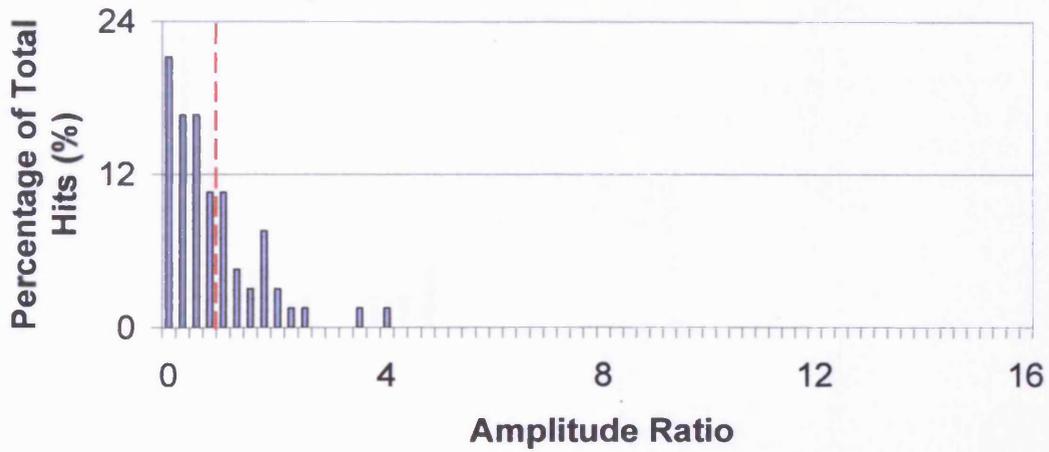

Figure 5.53 - Amplitude ratio distribution from second stage testing of specimen 8
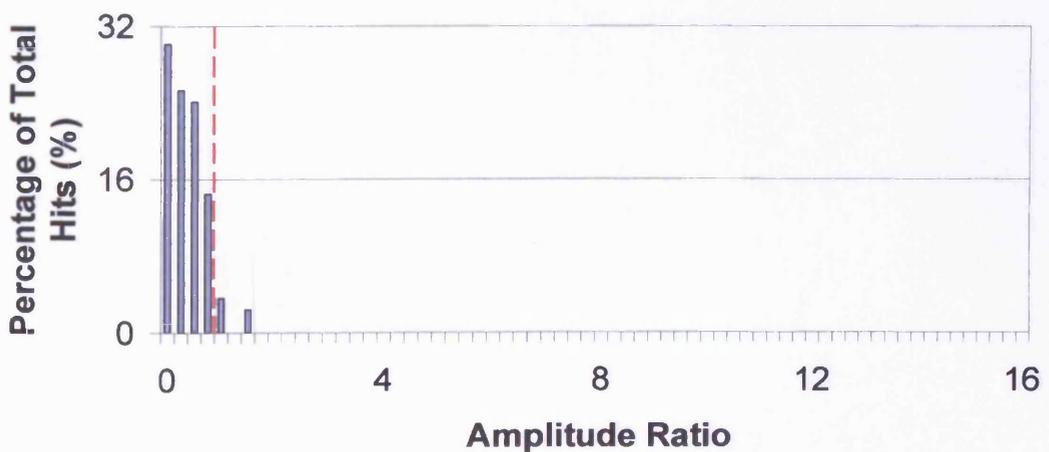

Figure 5.54 - Amplitude ratio distribution from second stage testing of specimen 9
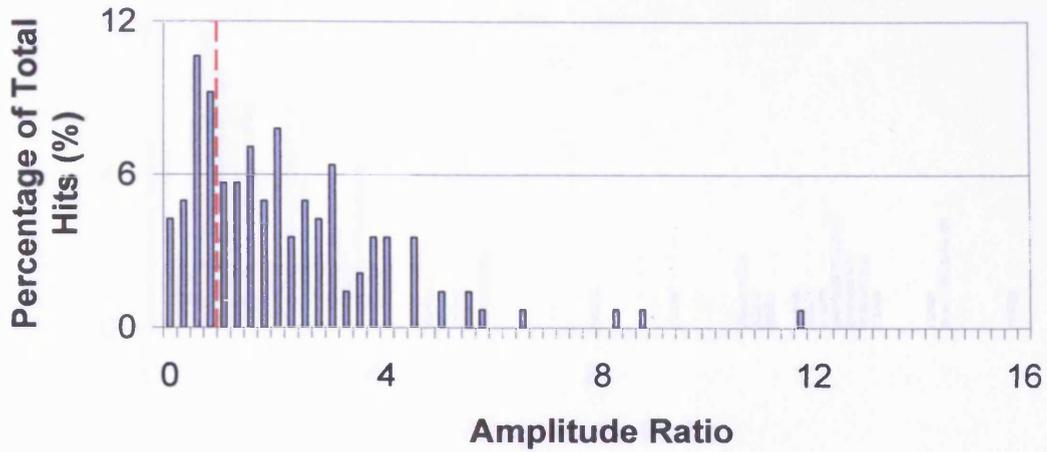
Figure 5.55 - Amplitude ratio distribution from second stage testing of specimen 10
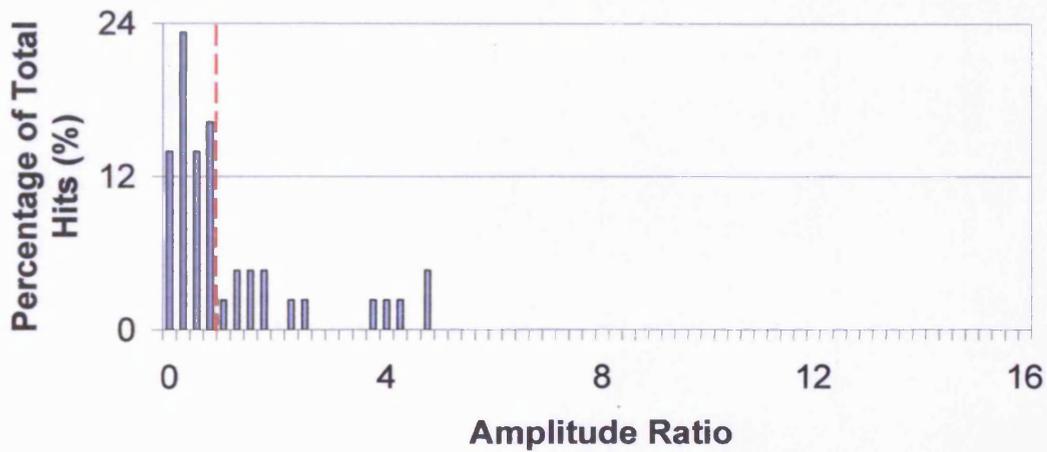
Figure 5.56 - Amplitude ratio distribution from second stage testing of specimen 11
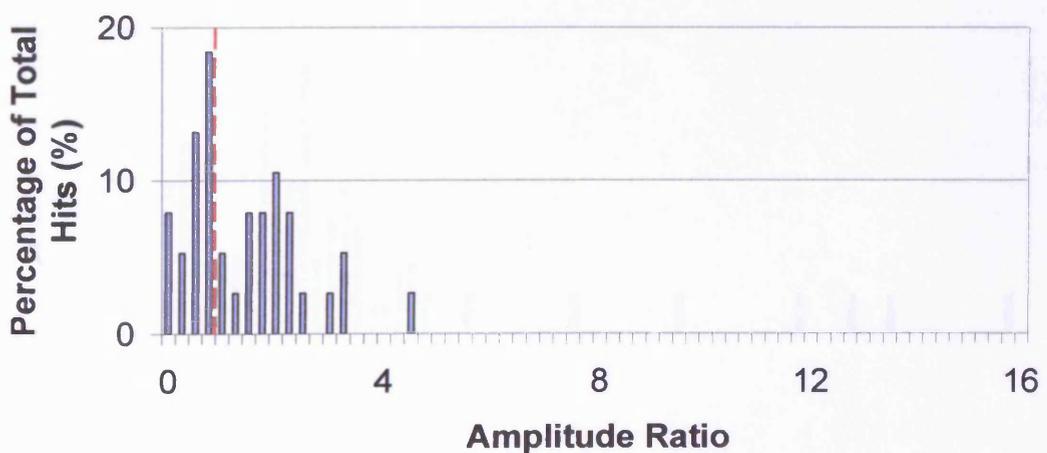
Figure 5.57 - Amplitude ratio distribution from second stage testing of specimen 12
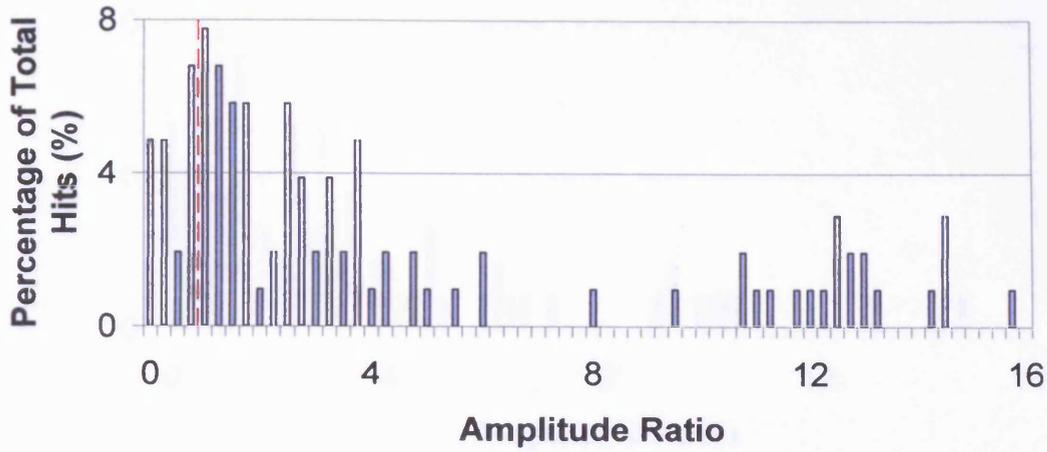
Figure 5.58 - Amplitude ratio distribution from second stage testing of specimen 13
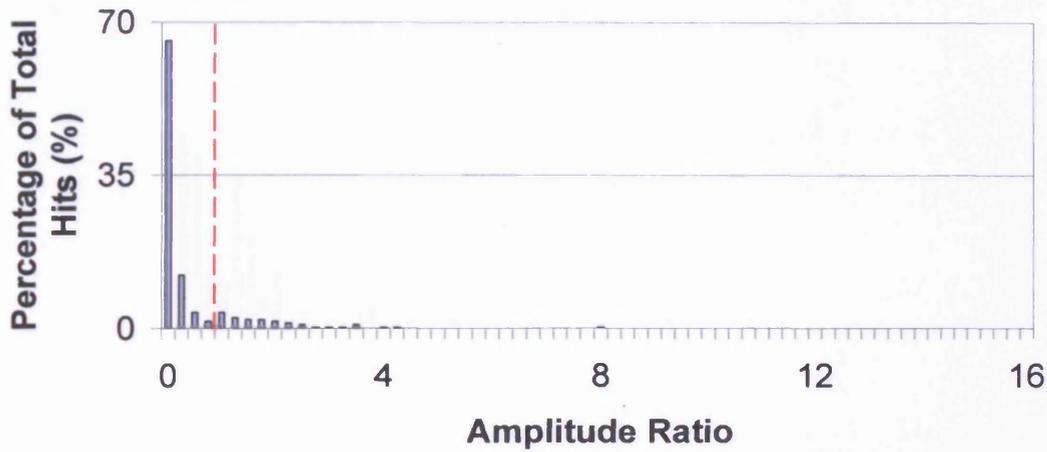
Figure 5.59 - Amplitude ratio distribution from second stage testing of specimen 14
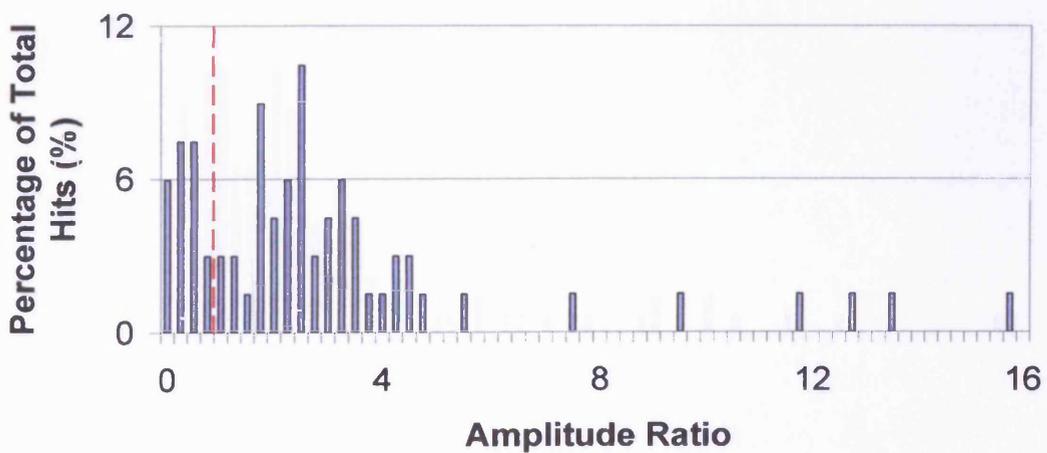
Figure 5.60 - Amplitude ratio distribution from second stage testing of specimen 15
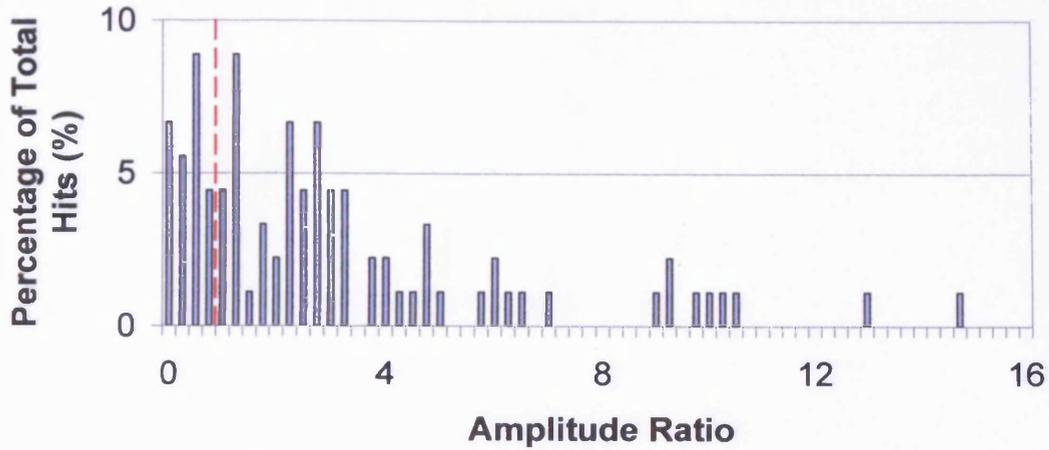
Figure 5.61 - Amplitude ratio distribution from second stage testing of specimen 16
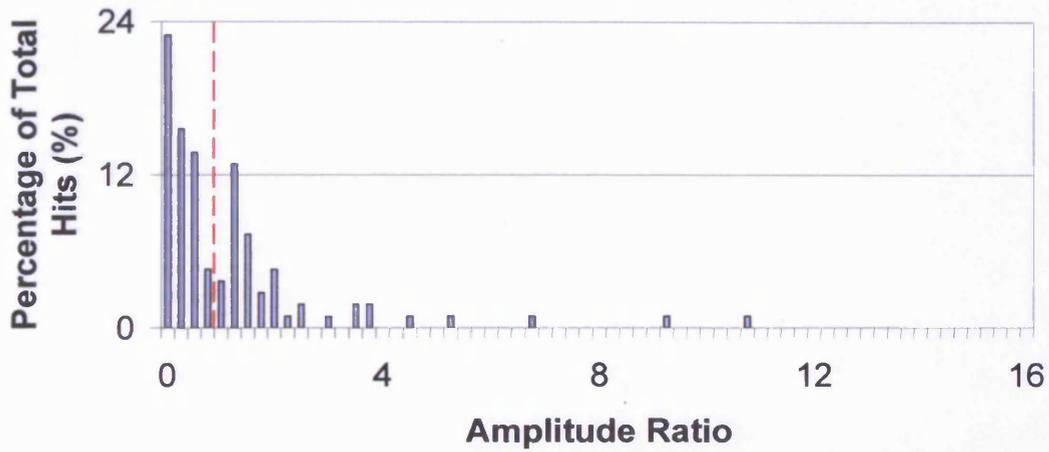
Figure 5.62 - Amplitude ratio distribution from second stage testing of specimen 17
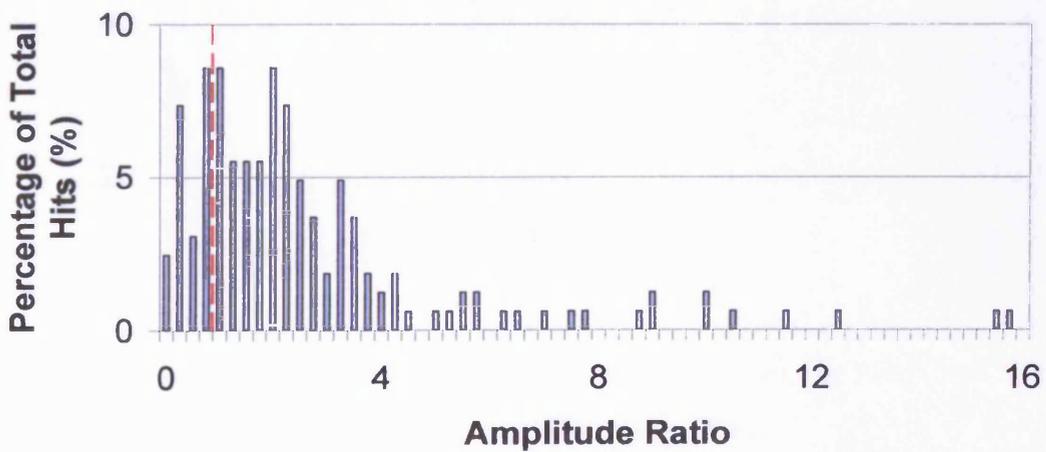
Figure 5.63 - Amplitude ratio distribution from second stage testing of specimen 18
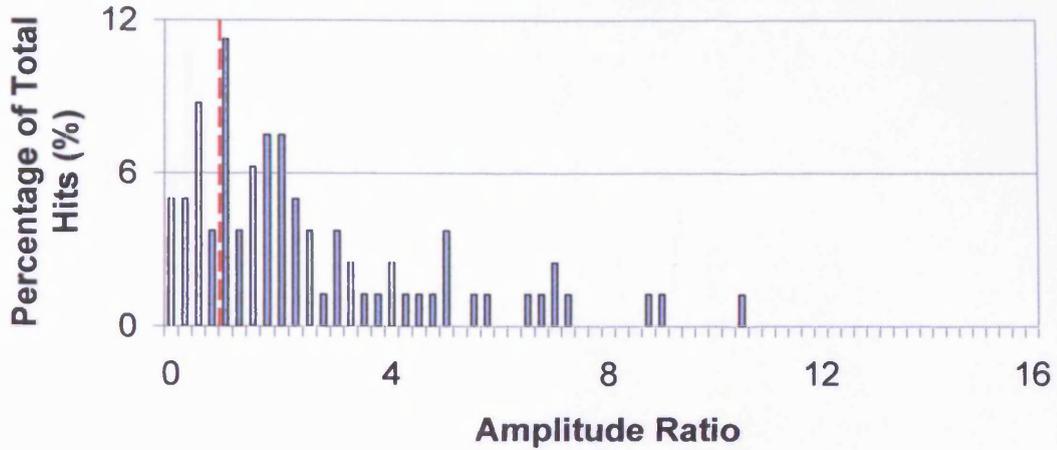
**Figure 5.64 - Amplitude ratio distribution from second stage testing of specimen 19**
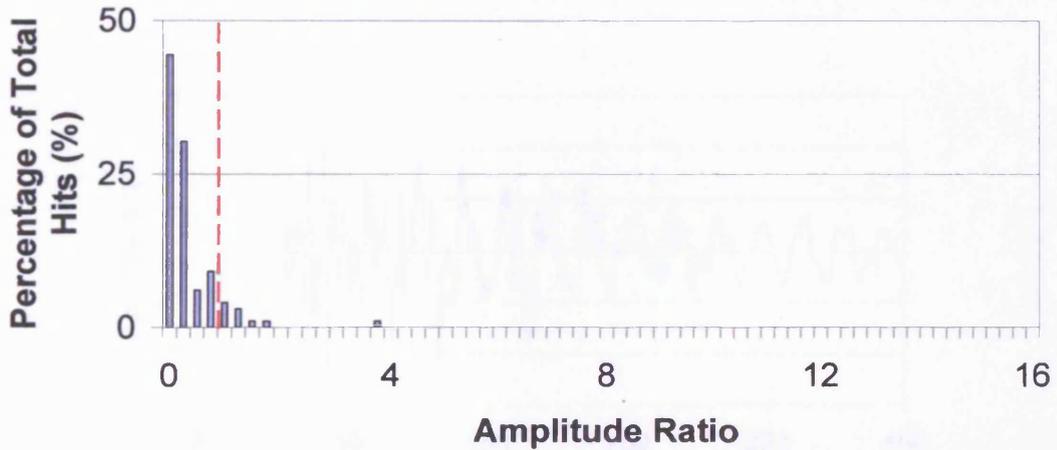
Figure 5.65 - Channel 3 amplitude ratio distribution from second stage testing of specimen 5
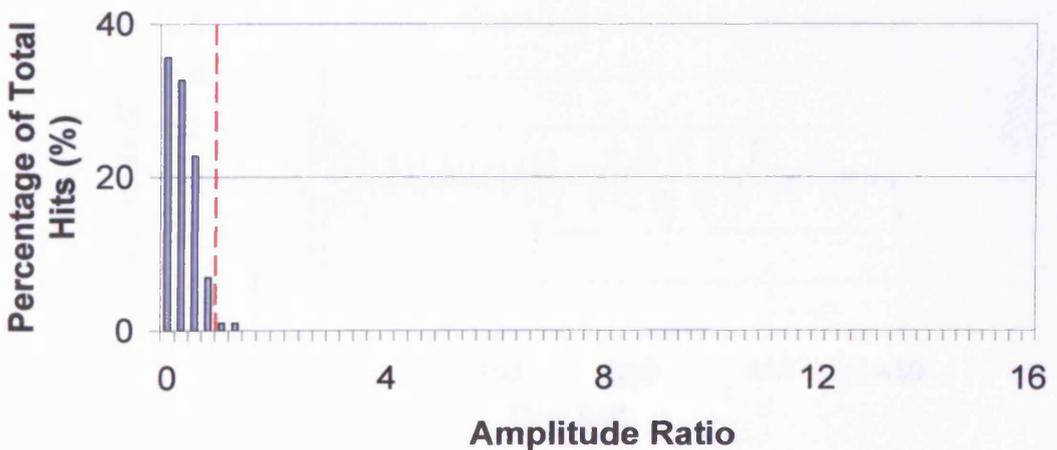
Figure 5.66 - Channel 2 amplitude distribution from second stage testing of specimen 12
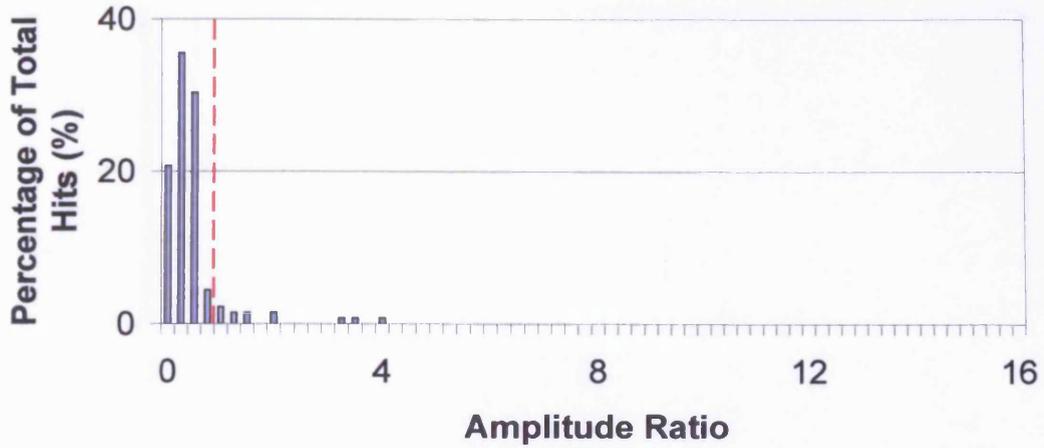
Figure 5.67 - Channel 2 amplitude ratio distribution from second stage testing of specimen 15
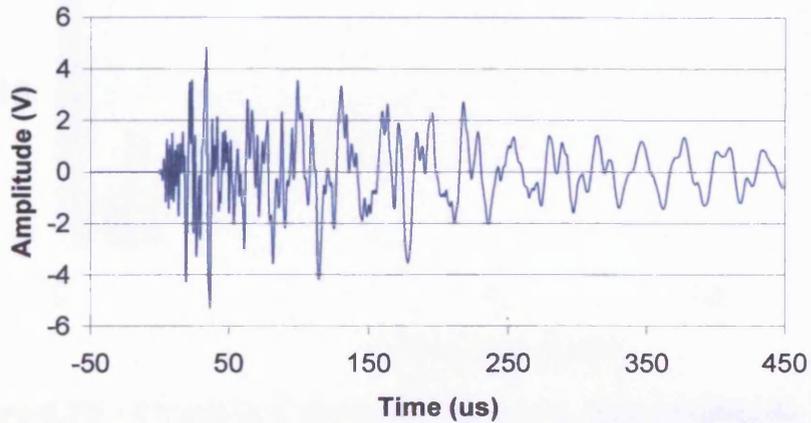

a) Channel 2 – arrival time = 641.0774487 amplitude ratio = 0.323
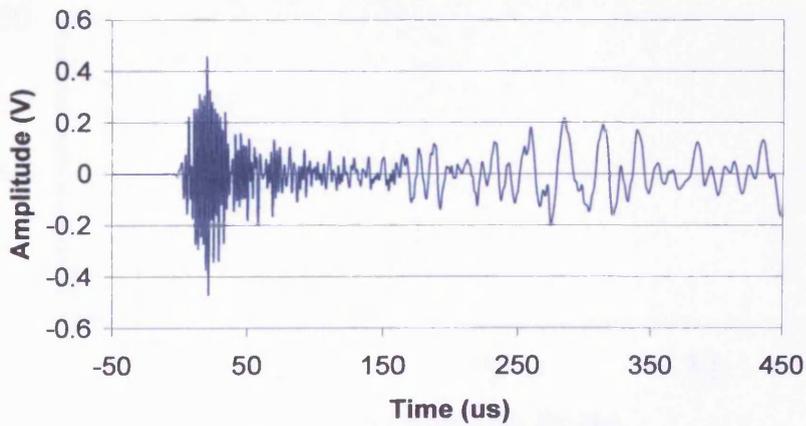
b) Channel 1 – arrival time = 641.0774945 amplitude ratio = 2.181

Figure 5.68 - Waveforms resulting from the same event in Specimen 14 recorded by sensors 1 and 2
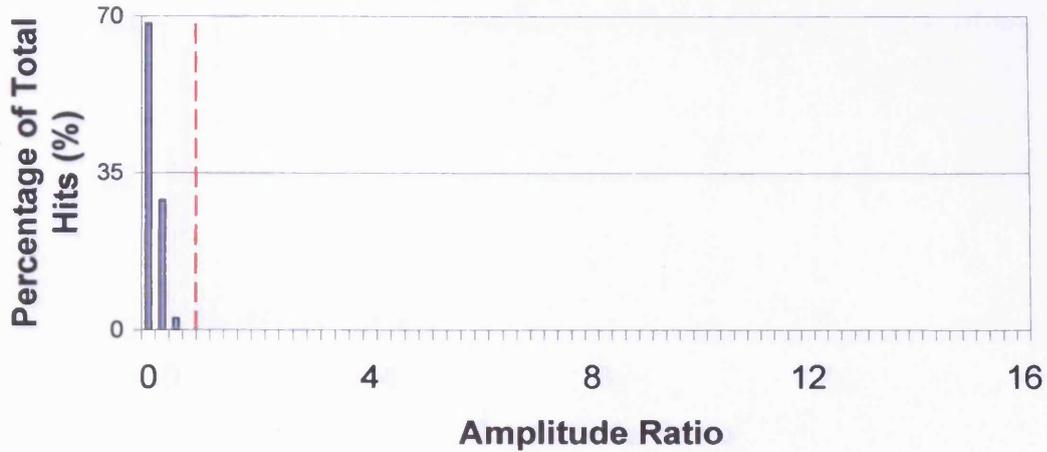
Figure 5.69 - Channel 1 propagation corrected amplitude ratio distribution from second stage testing of specimen 12
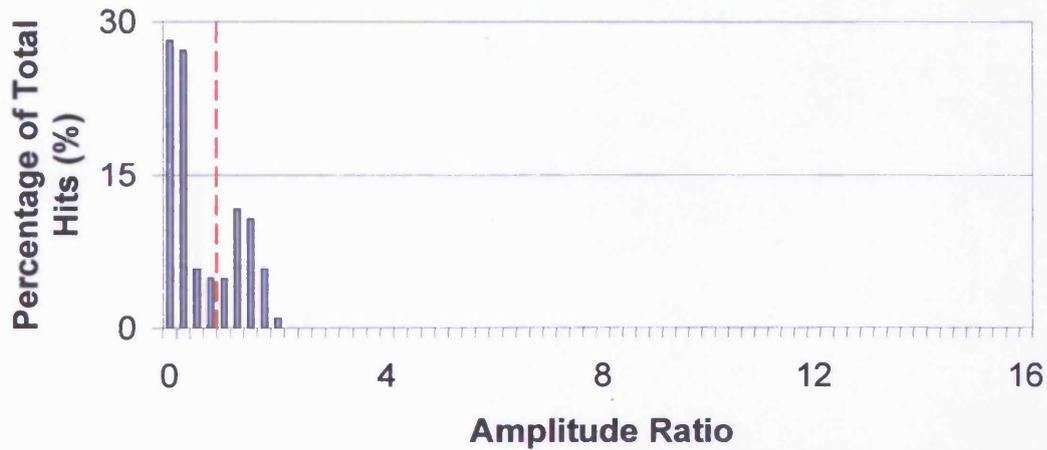
Figure 5.70 - Channel 1 propagation corrected amplitude ratio distribution from second stage testing of specimen 13
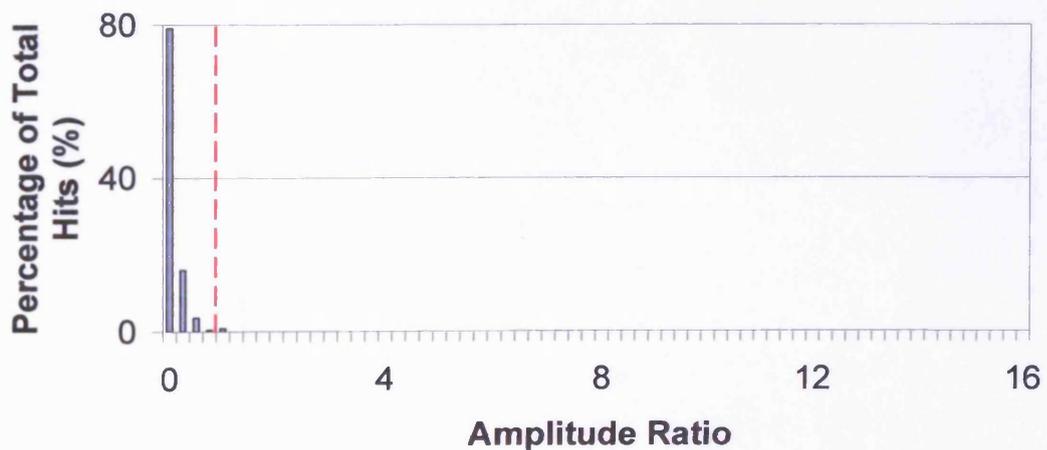
Figure 5.71 - Channel 1 propagation corrected amplitude ratio distribution from second stage testing of specimen 14
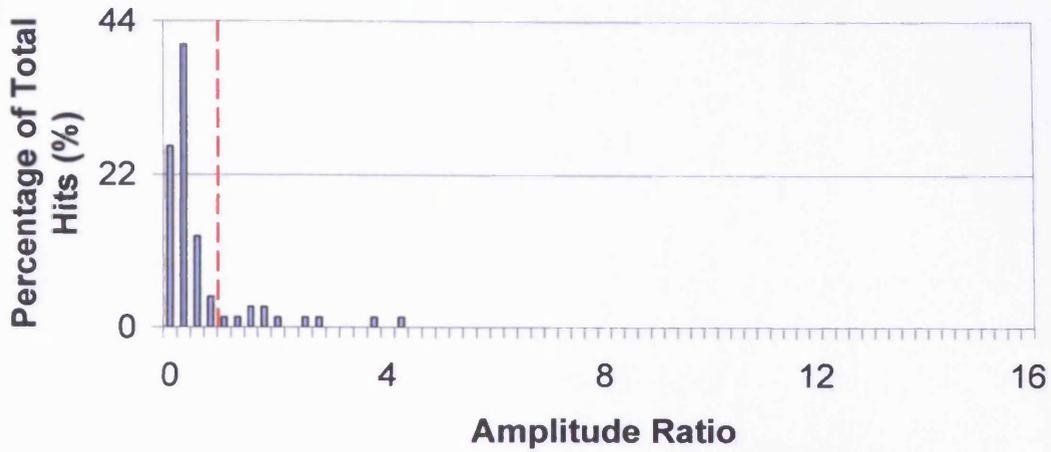
Figure 5.72 - Channel 1 propagation corrected amplitude ratio distribution from second stage testing of specimen 15
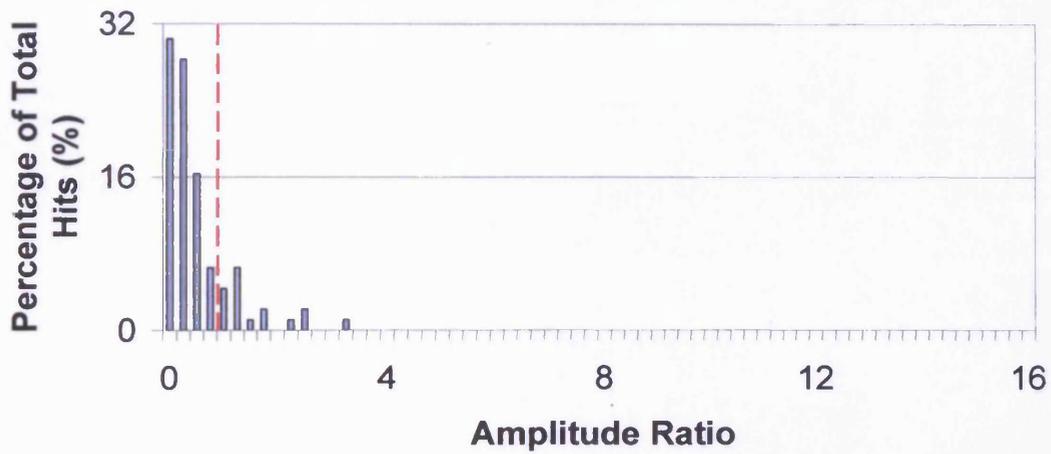
Figure 5.73 - Channel 1 propagation corrected amplitude ratio distribution from second stage testing of specimen 16
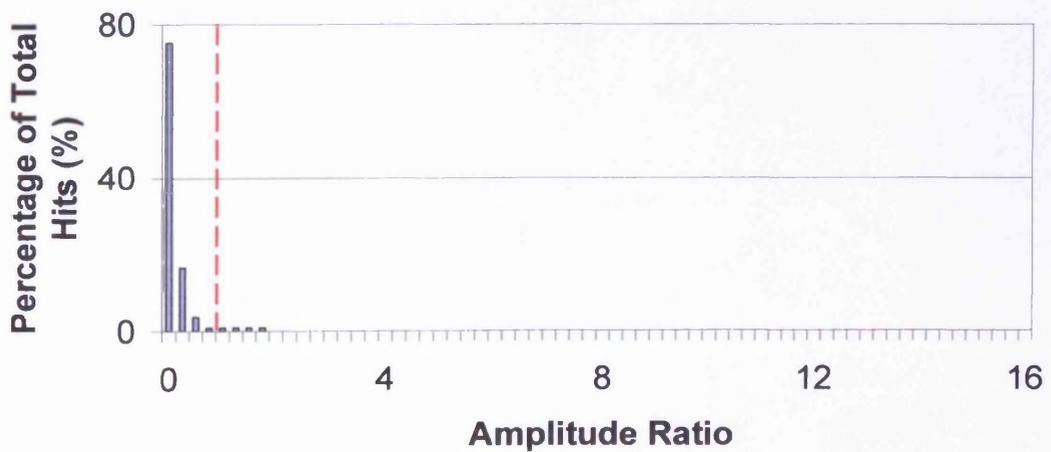
Figure 5.74 - Channel 1 propagation corrected amplitude ratio distribution from second stage testing of specimen 17
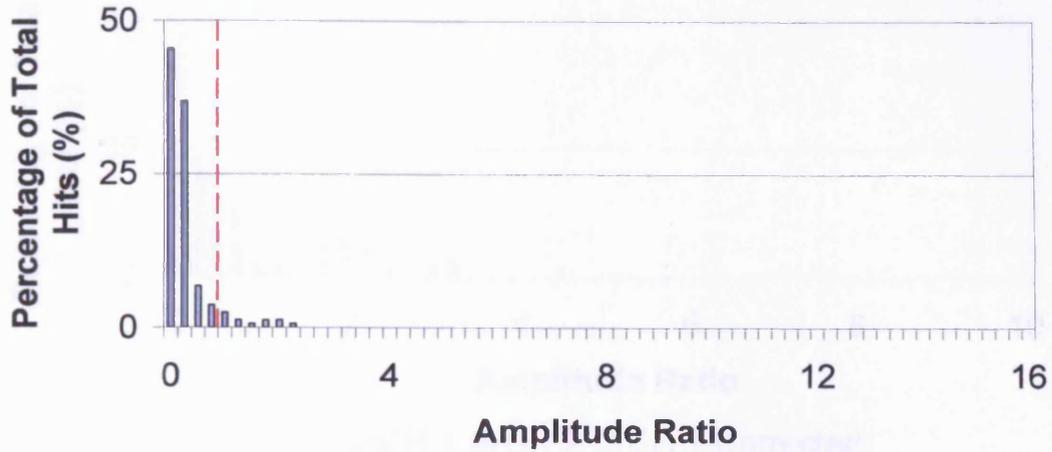
Figure 5.75 - Channel 1 propagation corrected amplitude ratio distribution from second stage testing of specimen 18
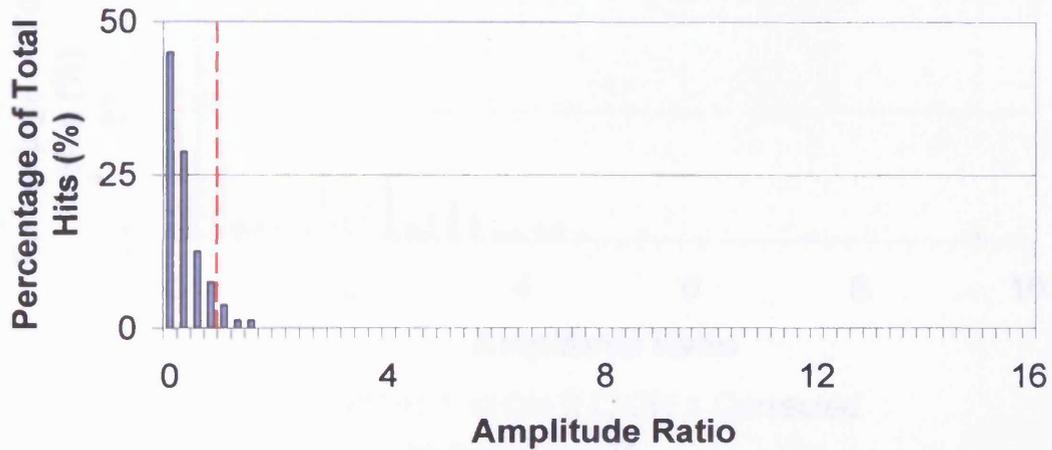
Figure 5.76 - Channel 1 propagation corrected amplitude ratio distribution from second stage testing of specimen 19

a) Specimen I2
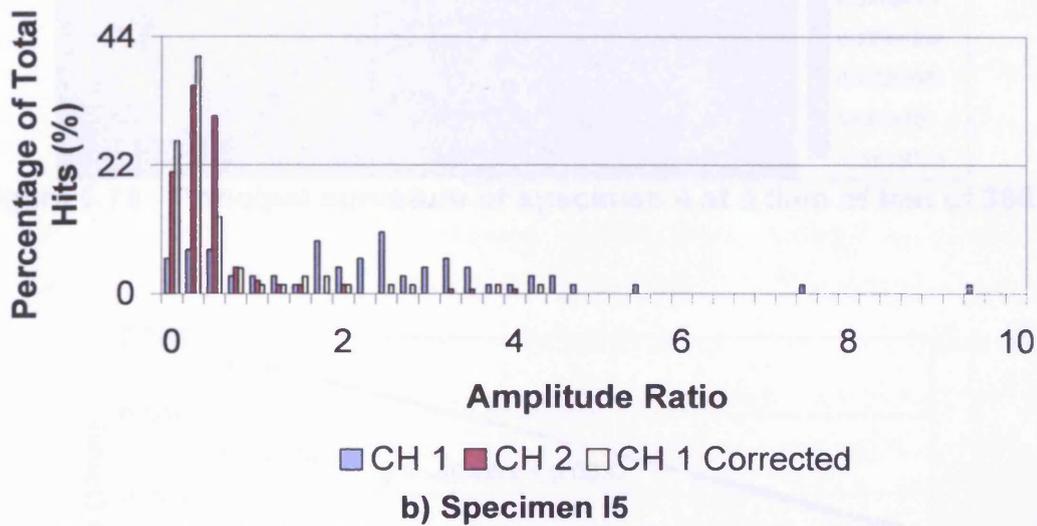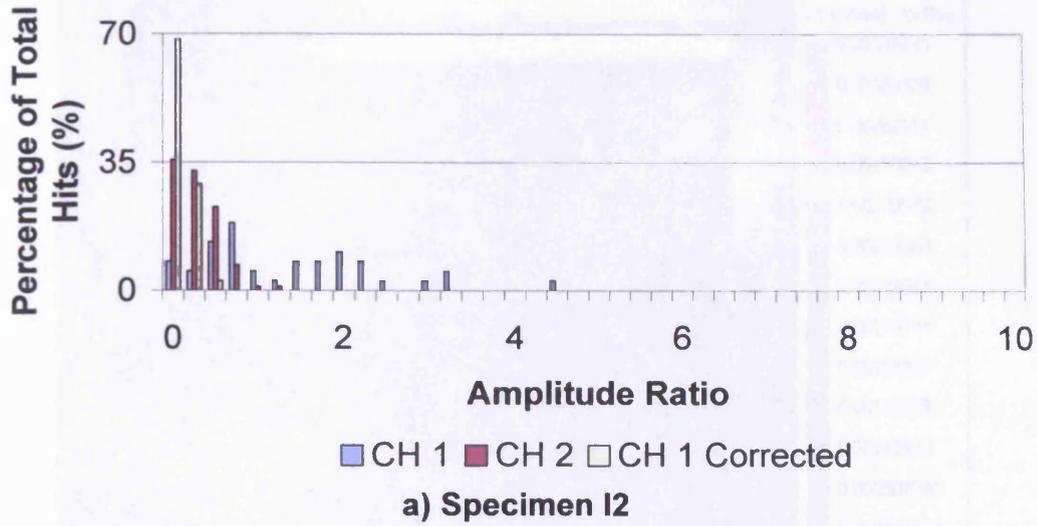
b) Specimen I5

Figure 5.77 - Comparison of amplitude ratio distributions

388.39s
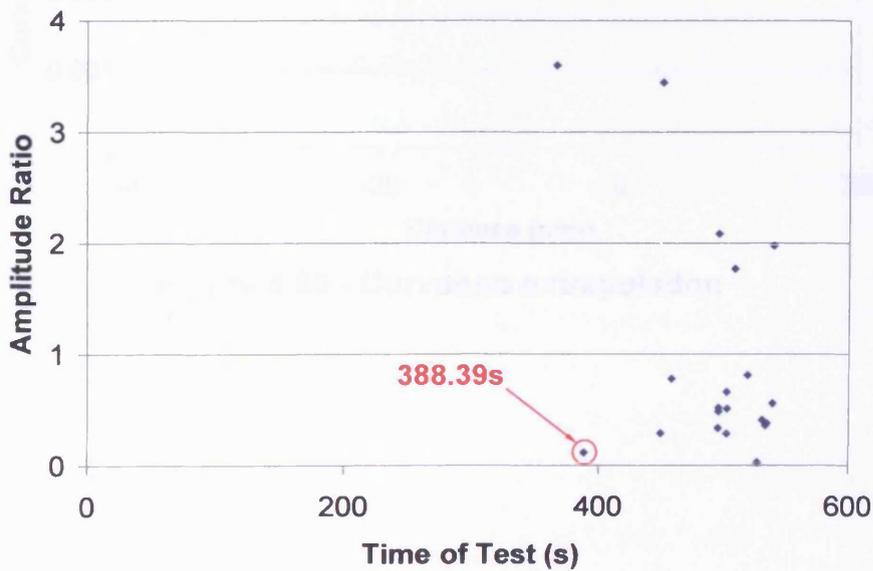
Figure 5.78 - Specimen 4 amplitude ratio versus time of test for signals with amplitude greater than 90dB
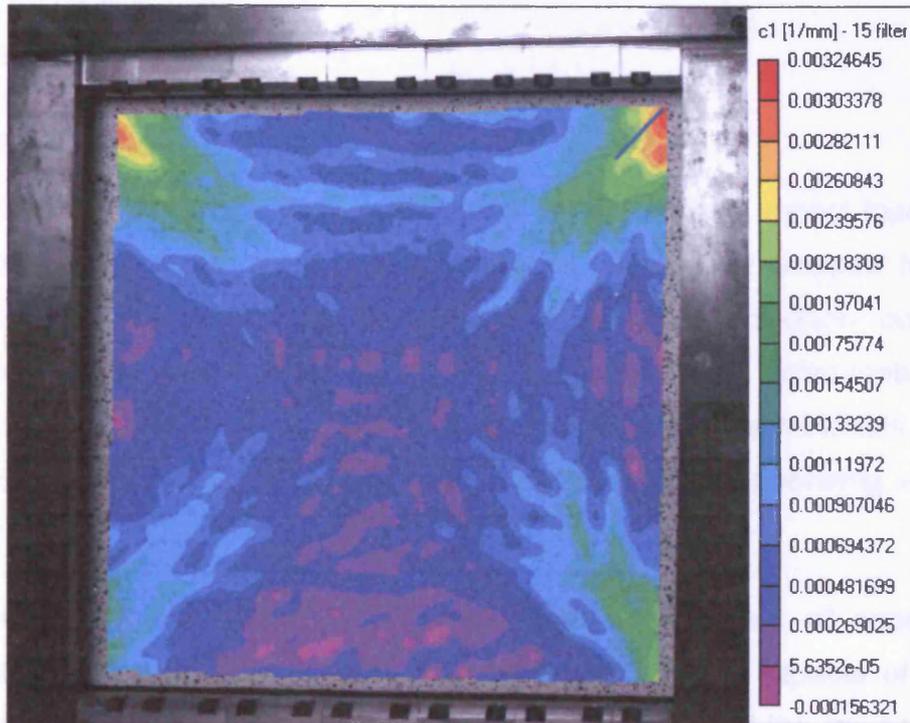
Figure 5.79 - Principal curvature of specimen 4 at a time of test of 388s
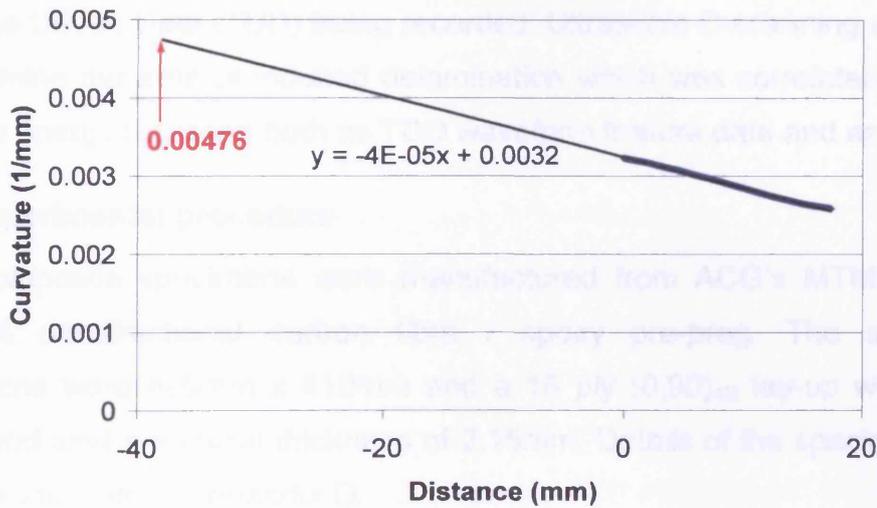
Figure 5.80 - Curvature extrapolation

6 Impact Testing

6.1 Introduction

The response of carbon fibre composites to low velocity impact loads is an area of great concern. Low velocity impacts, such as a dropped tool, can induce large areas of inter-ply delamination that can often be barely detectable by visual inspection. The presence of delamination can substantially reduce the mechanical properties of composite materials, leading to unexpected premature failure of a component that is operating within its design limits.

The work in this chapter details the results of a series of experiments subjecting 8 carbon fibre / epoxy panels to low velocity impacts of varying energies, using a drop weight impactor. AE monitoring of the impact events was conducted on four simultaneous levels, with continuous waveform signals, discrete waveform signals, Hit Driven Data (HDD) waveform features and Time Driven Data (TDD) being recorded. Ultrasonic C-scanning was used to determine the area of induced delamination which was correlated with the absolute energy recorded both as TDD waveform feature data and as HDD.

6.2 Experimental procedure

Eight composite specimens were manufactured from ACG's MTM21-1/HS-125-38% uni-directional carbon fibre / epoxy pre-preg. The specimen dimensions were 400mm x 410mm and a 16 ply $(0,90)_{4S}$ lay-up was used, which produced a nominal thickness of 2.15mm. Details of the specimen cure cycle are included in Appendix D.

Impact damage was induced into the specimens using an instrumented drop weight impact test rig. The impact conditions were designed in accordance with the British Standard for Impact Behaviour of Rigid Plastics (BSI 2000). As such the specimens were clamped rigidly between two large clamping plates that restrained movement of the entire specimen apart from a circular unsupported area, of 120mm diameter, at its centre, shown schematically in Figure 6.1. The impactor consisted of a polished hemispherical tup (or striker)

with a 12.7mm diameter. The tup was attached to an inertial-mass that accelerates down a guided channel, due to gravity. Released by an electromagnet, the impactor can be dropped from any height up to 5m and has a combined mass of 1.46kg. Each specimen was impacted once only with a 5J, 6J, 8J or 10J impact energy, controlled by the release height of the impactor in accordance with the equation for potential energy. The rebounded impactor was restrained by a rebound capture mechanism to avoid a second impact with the specimen. A pair of light gates measured the impactor velocity just prior to impact and just after rebound, allowing the kinetic energy to be calculated pre and post impact, therefore providing a measure of the energy absorbed by the specimen as damage. The impact details are presented in Table 6.1.

AE monitoring of the impact events was conducted with a single PAC Pico sensor, selected for its broad operating frequency range and in particular its small size, due to space restrictions in the test rig. A cyanoacrylate adhesive was used as both a couplant and to secure the sensor in position at the edge of the unsupported area. The sensor was attached to a PAC PCI-2 system via a PAC 0/2/4 pre-amplifier with a 0dB gain and an internal filter of 10-1200kHz. A gain of 0dB was selected in order to avoid the saturation of the system due to the large amplitude signals expected from the impact events. The data acquisition was conducted simultaneously on four levels. Continuous waveform signals were recorded throughout the impact events using the PCI-2 system's wave streaming facility. Discrete waveforms were recorded for signals with amplitudes greater than the 80dB threshold and TDD waveform features were extracted. The relevant AE channel settings are presented in Table 6.2. Additionally TDD was recorded throughout the impact event at a rate of 100Hz, meaning that during a 10ms period all the energy recorded was summed.

Post-impact ultrasound C-scan inspection of the specimens was used to assess the extent of the induced damage. The size estimation of the resulting delaminations was evaluated using a the "–6dB drop" method, discussed in section 5.2.1.

6.3 Results and Discussion

The graphical results of the C-scan investigation are presented in Figure 6.2, where lighter colours represent the areas of delamination. Details of the delamination areas resulting from the investigation can be seen in Table 6.3 along with the energy absorbed (calculated from pre and post impact velocity). Close examination revealed specimen 7 to be approximately two plies thicker than the nominal thickness of 2.15mm of the other specimens, due to a manufacturing error. It is for this reason and because the impact energy applied to the specimen was close to the limit of damage onset for the expected 2.15mm thickness, that the specimen sustained no damage. This illustrates how seemingly small changes in impact condition can produce considerably different results. The lack of observed damage in specimen 7 has a correspondingly small amount of absorbed energy recorded.

A comparison of the delamination area with both the impact energy level and the calculated energy absorbed is presented in Figure 6.3. The results from specimen 7 have been omitted from the comparison due to the lack of induced damage. The comparison of impact energy with delamination area highlights the variation in damage that can occur for a given level of impact. The greatest difference, of over 60mm², was observed at an impact level of 10J. The calculated absorbed energy shows a good correlation with the delamination area, as shown by the trend line in Figure 6.3. The notable exception was specimen 4, impacted at 10J, which has a much larger absorbed energy recorded than all the other specimens and has a smaller delamination area than that of specimen 3, also impacted at 10J. Possible sources of error in the presented trends have been identified as variations in manufacturing quality of the specimens, timing errors from the light gates that are likely to be greater at higher speeds and the assumption of perfect linear motion of the impactor without energy losses due to friction, heat or noise. This approach to impact investigation may be of use in a controlled laboratory environment, however in practical situations it is unlikely that a measure of impact energy or pre and post impact velocities would be available. This highlights a need for a different approach to damage estimation for composite impact events.

Figure 6.4a-h presents the continuous waveform data recorded during the impact event for specimens 1-8 respectively and clearly shows that no noise contamination or extraneous noise signals were recorded during the investigation. The time of arrival of the first reflection was calculated to be approximately 55μs, however, due to the high attenuation levels observed in this material (section 4.2.2) it is not thought that reflections will have a discernable effect on the results. Three regions have been proposed for each signal (excluding specimen 7); they are identified as follows. Region A begins at the point of contact between the impactor and the specimen, region B begins when the load on the plate is sufficient to initiate damage and region C is the unloading of the specimen during impactor rebound. The point at which region B ends and region C begins is difficult to predict accurately without data for the load trace of the impact event, which was not available for this investigation, however this is an area identified for further investigation. For the purposes of this investigation, the start of region C is selected manually as the point at which the signal amplitude exhibits significant loss relative to the high signal amplitudes observed in the damage region (B). The durations of regions A and B are detailed in Table 6.4, where it can be seen that as the impact energy reduces and hence the velocity and momentum of the impactor reduce, the duration of region A increases, because it takes longer for the load to reach the level at which damage initiates. The largest duration of region A was observed in specimen 8 at 1982μs and the smallest was observed in specimen 3 at 983μs. Additionally it can be seen that the duration of Region B increases with impact energy, corresponding to the increase in damage observed at higher impact energies. The duration of region B for specimen 3 is the largest at 1404μs and specimen 8 has the smallest at 266μs. The total length of both region A and B is observed to be between 1900 and 2400μs in all cases with specimens 3 and 4 (impacted at 10J) having the longest total, however a trend of increased total length with impact energy is not observed in the other specimens. The time window in which the signals are presented is 10ms in length, which is equivalent to the binning period used for the TDD. Hence it is evident that the signals could be split between two samples, however it would be unfortunate if the damage region (B) were also split. The corresponding discrete waveforms (apart from

specimen 6 which was not recorded due to user error) are presented in Figure 6.5a-g for specimens 1-5, 7 and 8 respectively. The discrete waveforms match the continuous waveforms, presented in Figure 6.4a-h, demonstrating the potential to use threshold triggered discrete waveforms for impact analysis. The main difference observed in the discrete waveforms is the loss of region A from specimen 1 (Figure 6.5a), this occurred because the signal amplitude of region A dropped below the 80dB threshold for longer than the 50μs HDT before damage occurred. As such the damage region (region B) was recorded in the subsequent discrete waveform, presented in Figure 6.5a. The previous discrete waveform containing region A of the signal for the specimen 1 impact event is presented in Figure 6.6. Additionally, some signal loss was seen in region C, resulting from the discrete waveforms being cut-off when the signal drops below the threshold for longer than the HDT. The use of a lower threshold may have ensured that the capture of the impact event in specimen 1 was recorded in a single discrete waveform, however this would also make the system more susceptible to noise. A more appropriate solution would be to increase the HDT to ensure the full waveform is collected, the operator must take care not to extend the HDT so much as to include noise from additional sources, such as rebound capture. This serves to highlight the importance of selecting appropriate settings when using AE software for acquisition.

The HDD and TDD energy values are presented in Table 6.5, where the HDD energy value for specimen 1 is a summation of the two hits over which the impact event is split. Figure 6.7a and b show two plots of absolute energy against time of test (starting at the arming of the acquisition system) for HDD and TDD respectively, for specimen 4. Absolute energy was selected as a parameter for investigation as it can be traced back to S.I. units of Joules at the sensor face. The obvious difference between the two plots, is that the HDD only displays information from events with amplitudes above the 80dB threshold and the TDD displays the energy value over every 10ms period. To facilitate a simple evaluation of the data, the highest energy value for the HDD and the TDD were chosen and are assumed to be the energy for the impact event. A comparison of delamination area with the absolute energy recorded

by both the HDD and the TDD is presented in Figure 6.8. The data from specimen 7 is included because it provides a measure of the energy recorded by an impact where damage does not occur, however TDD for specimens 2 and 6 was not recorded due to operator error. The TDD measurement of absolute energy shows a very good correlation with the area of delamination, the trend line passes close to the origin and approaches 4×10^{10} atto-J absolute energy for a 400mm^2 delamination size, suggesting an approximate relationship of 1×10^8 atto-J for every 1mm^2 of delamination area. The same level of correlation is not observed between the HDD and the delamination area, however there are a number of HDD data points that lie directly on top of those from the TDD. The three HDD data points that do not match the TDD are from specimens 1, 2 and 6. The TDD for specimens 2 and 6 was lost due to operator error and therefore it is difficult to asses whether or not the same deviation would have been observed in the TDD. The variation observed in specimen 1, despite the summation of the two hits containing the impact event, occurs because of the signal lost during the hit lock out time of 200µs. Plus additional signal loss that occurs after the hit lock out, because the AEwin software will not allow a channel to rearm until the hit and waveform data is transferred from the card buffer to the hard drive for storage, the length of delay is related to the length of waveform recorded. For this reason there is no signal present in the pre-trigger region for the second discrete waveform containing the impact event from specimen 1. The observations of variation in the HDD resulting from the timing parameters may offer some explanation as to why previous researchers (Liu et al 1999; Okafor et al 2001) found limited success when correlating energy recorded as HDD with delamination size and impact energy for composite materials.

6.4 Conclusions

The mechanically calculated and measured values of impact energy and absorbed energy were shown to be limited in their capability to estimate the extent of impact damage induced in composite materials. Furthermore their use in practical situations is unlikely to be possible. AE monitoring was shown to have good potential as a method for monitoring damage and the estimation of its extent in impact critical composite specimens. Acquisition of AE data on

numerous levels allowed for a detailed investigation of the impact events. The continuous waveforms provided exact timings of damage development during the impact events and the potential for discrete waveforms to replicate these results was shown. Correlation of the impact event load trace with the waveform data is required to confirm the predicted stages of damage development.

The TDD was shown to have a very good correlation with the area of delamination, however it is not certain that the missing results of specimens 2 and 6 would fit the correlation as closely. The HDD did not provide such a good correlation with delamination area because of the signal loss experienced due to the AE timing parameters. Adjustments to the test set-up could provide an improved correlation for the HDD.

Table 6.1 – Impactor drop heights

Specimen	Impact Energy (J)	Drop Height (m)
1	8	0.56
2	8	0.56
3	10	0.70
4	10	0.70
5	6	0.42
6	6	0.42
7	5	0.35
8	5	0.35

Table 6.2 - AE channel settings

Threshold	PDT	HDT	HLT	Sample Rate	Hit Length
80dB	20µs	50µs	200µs	2MSPS	15k

Table 6.3 - Impact details

Specimen	Impact (J)	Calculated Absorbed Energy (J)	Delamination Area (mm^2)
1	8	3.8	165
2	8	3.4	180
3	10	4.6	342
4	10	7.6	283
5	6	2.5	133
6	6	2.6	128
7	5	1.5	0
8	5	2.5	110

Table 6.4 - Continuous waveform timings of identified regions

Specimen	Region A (µs)	Region B (µs)	Total (A+B) (µs)
1	1085	892	1977
2	1136	881	2077
3	983	1404	2387
4	1010	1335	2345
5	1641	516	2157
6	1394	580	1974
7	-	-	-
8	1982	266	2248

Table 6.5 - HDD and TDD energy values

Specimen	HDD Absolute Energy (atto-J)	TDD Absolute Energy (atto-J)
1	1.25×10^{10}	1.82×10^{10}
2	2.56×10^{10}	-
3	3.92×10^{10}	3.92×10^{10}
4	2.87×10^{10}	2.88×10^{10}
5	1.50×10^{10}	1.50×10^{10}
6	3.76×10^{8}	-
7	7.27×10^{8}	7.39×10^{8}
8	9.66×10^{9}	9.66×10^{9}
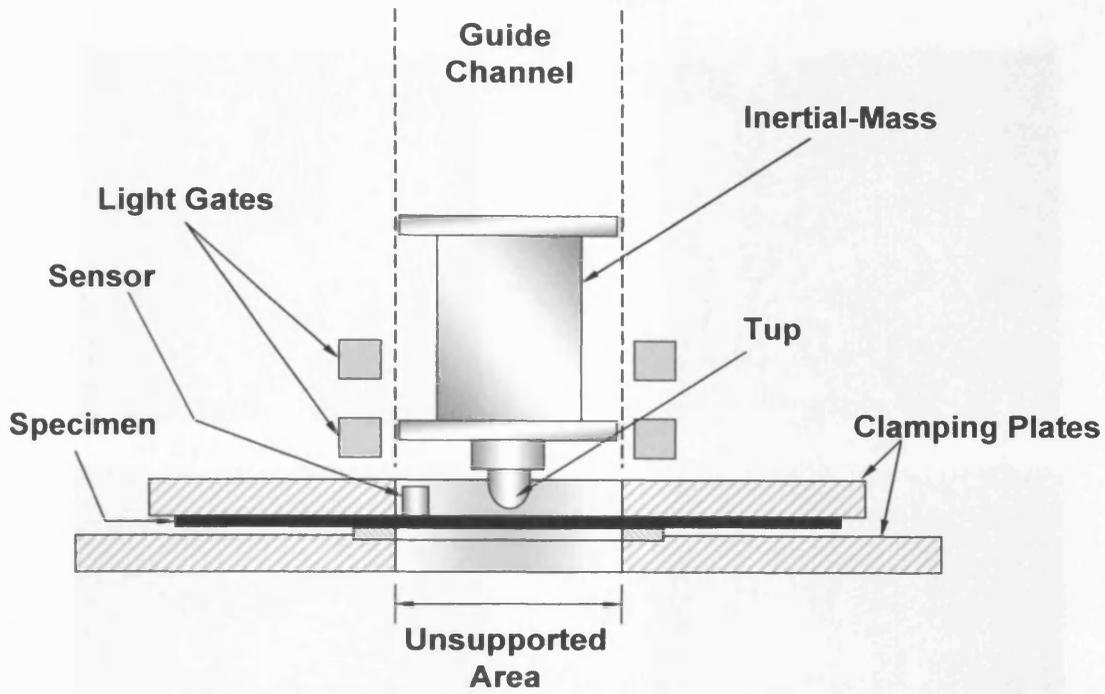
Figure 6.1 - Instrumented drop weight impact test rig
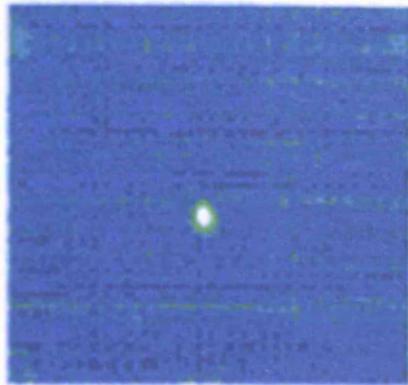
a) Specimen 1 – 8J
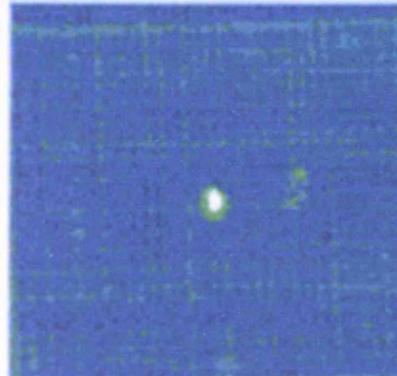
b) Specimen 2 – 8J
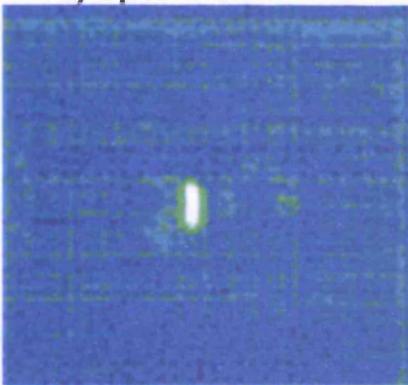
c) Specimen 3 – 10J
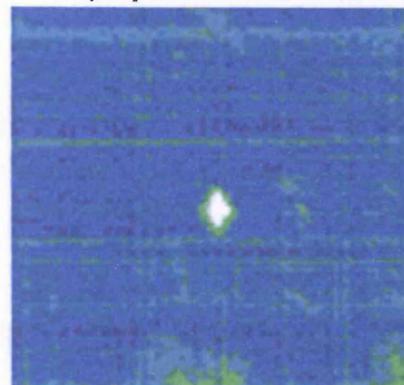
d) Specimen 4 – 10J
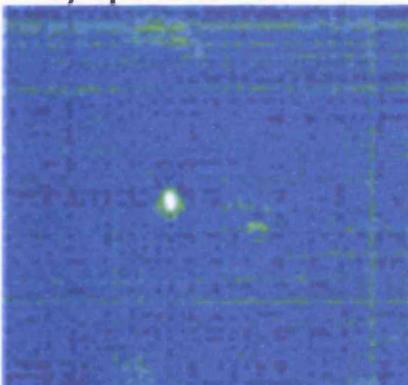
e) Specimen 5 – 6J
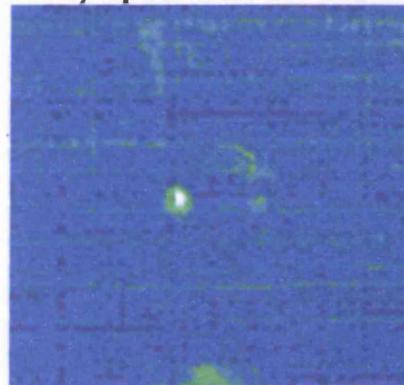
f) Specimen 6 – 6J
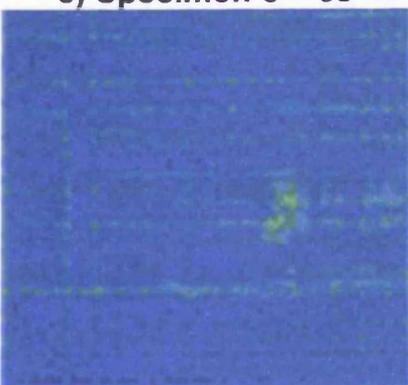
g) Specimen 7 – 5J
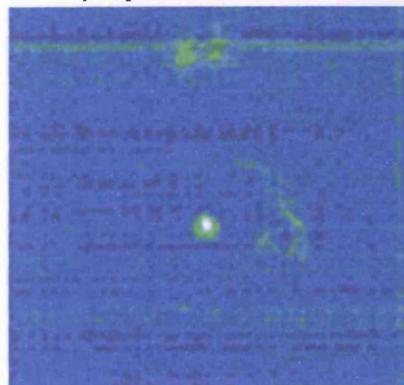
h) Specimen 8 – 5J

Figure 6.2 - C-scan images of impacted specimens
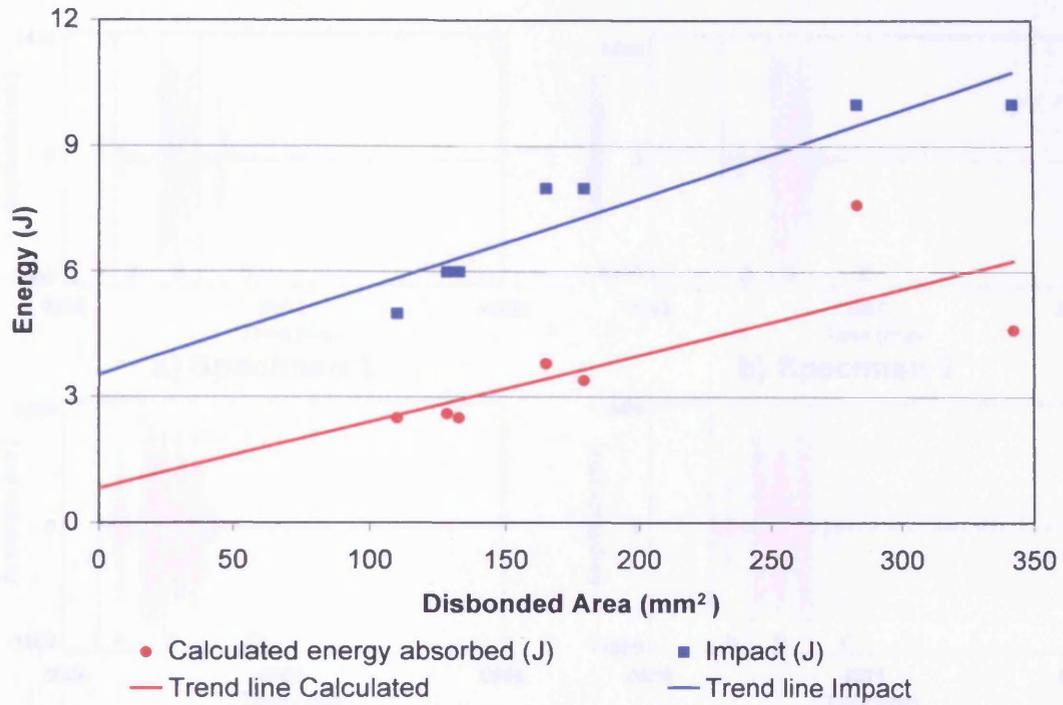
Figure 6.3 - Comparison of delamination area with impact and absorbed energy
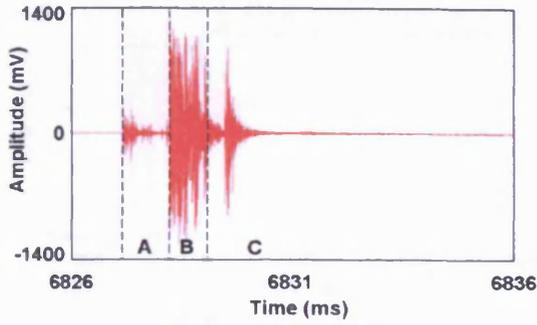
a) Specimen 1
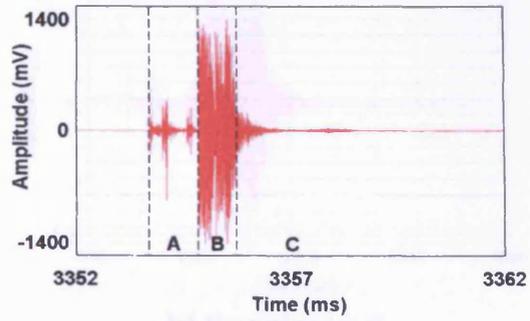
b) Specimen 2
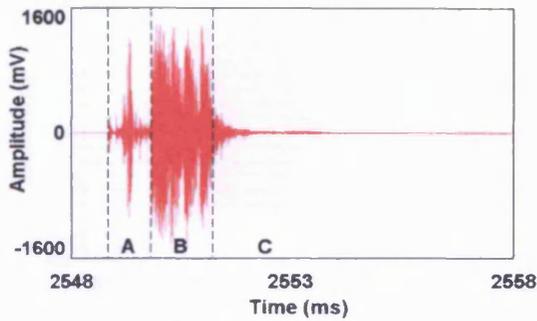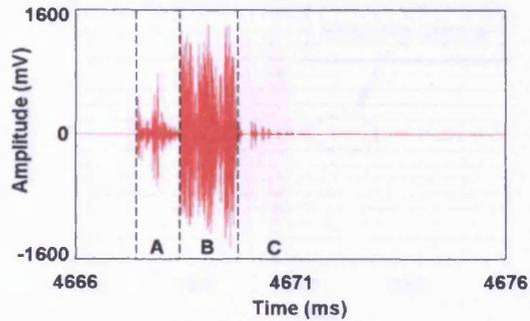
c) Specimen 3
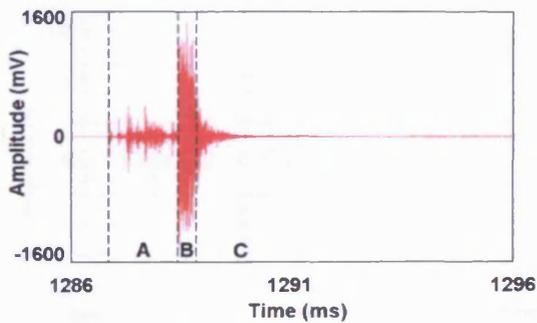
d) Specimen 4
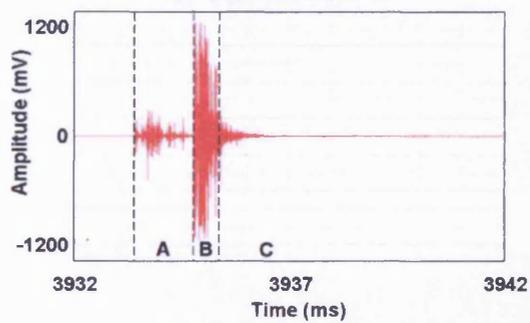
e) Specimen 5

f) Specimen 6
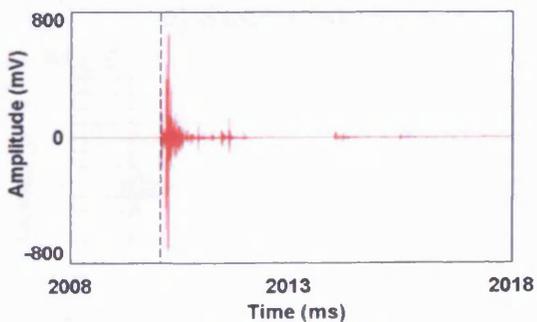
g) Specimen 7
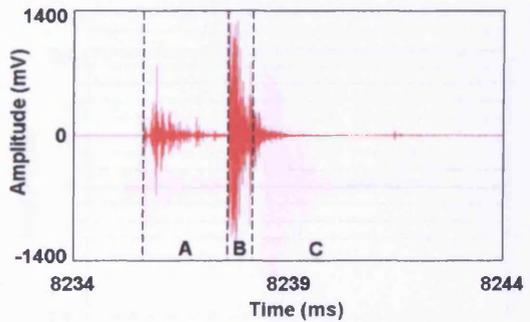
h) Specimen 8

Figure 6.4 - Continuous waveforms recorded during the impact event
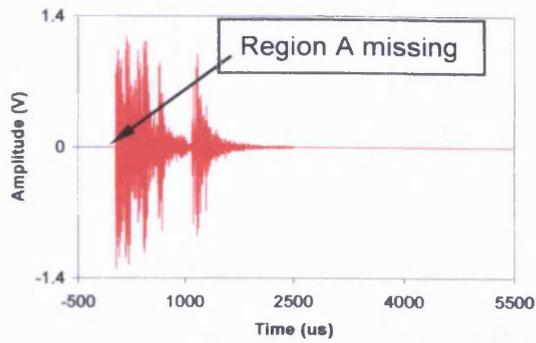
a) Specimen 1
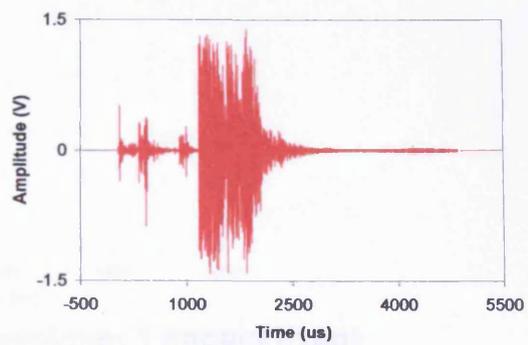
b) Specimen 2
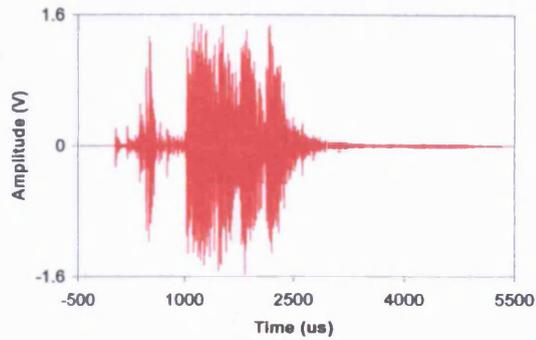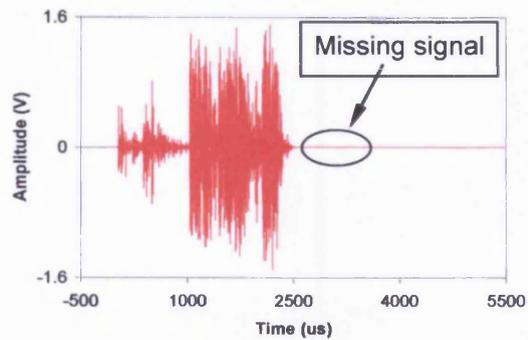
c) Specimen 3
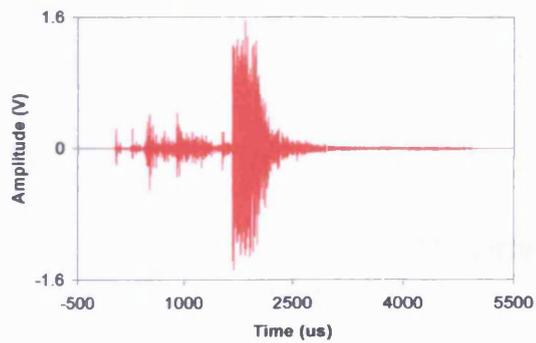
d) Specimen 4
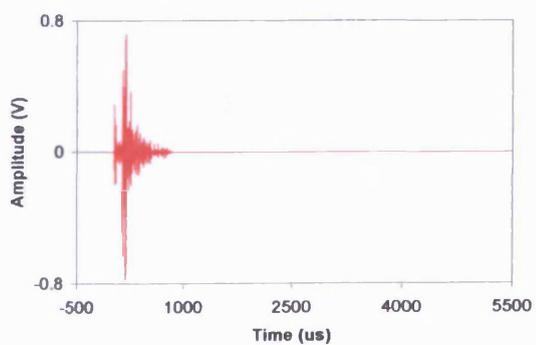
e) Specimen 5

f) Specimen 7
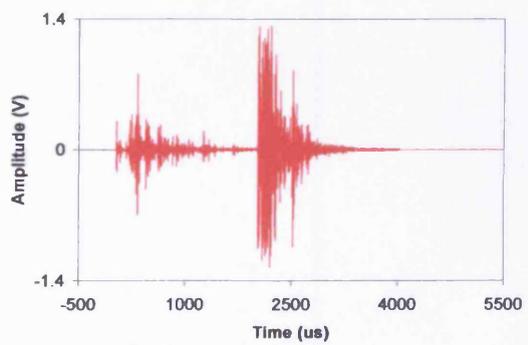
g) Specimen 8

Figure 6.5 - Discrete waveforms recorded from the impact event
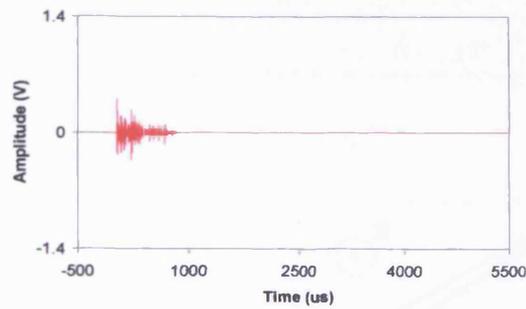
Figure 6.6 - Region A of specimen 1 impact event
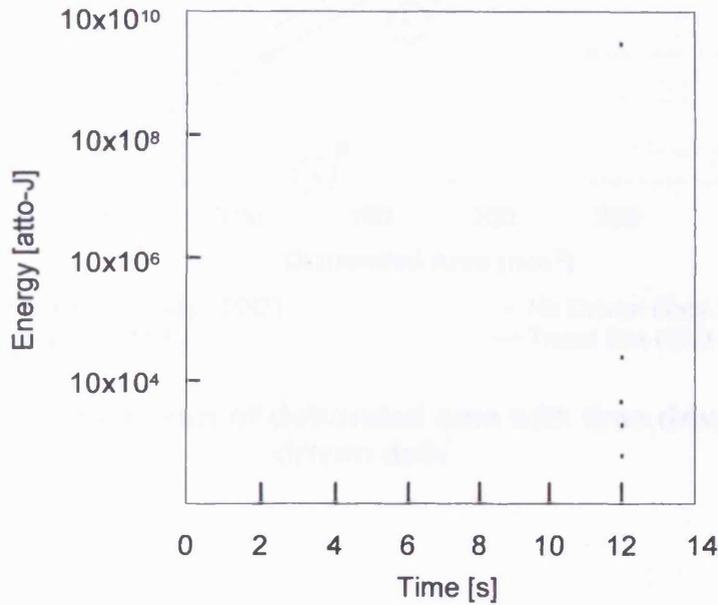
a) Hit Driven Data (HDD)
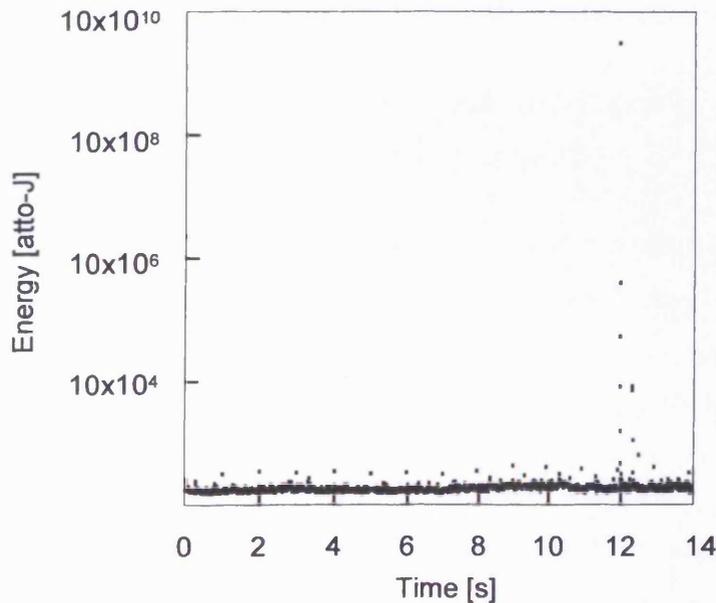
b) Time Driven Data (TDD)
Figure 6.7 - Recorded AE data from 10J impact on specimen 4, a) HDD, b) TDD
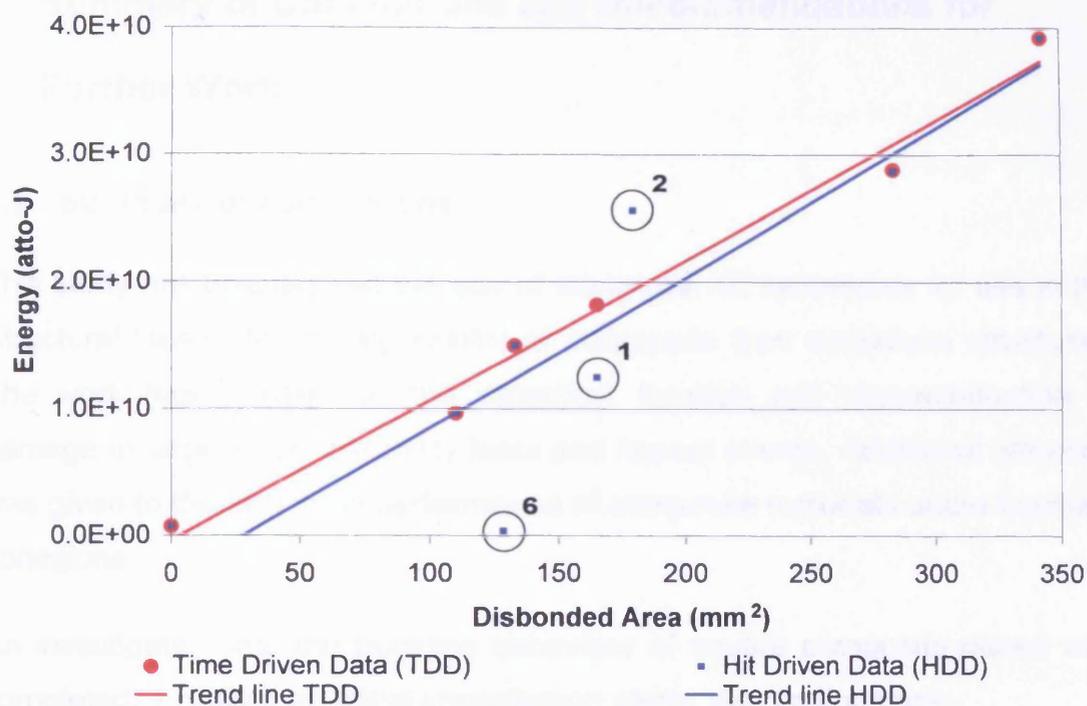
Figure 6.8 - Comparison of debonded area with time driven and hit driven data

7 Summary of Conclusions and Recommendations for Further Work

7.1 Summary of conclusions

This study has investigated the use of advanced AE techniques for use in the Structural Health Monitoring (SHM) of aerospace type composite structures. The work has focused on the detection, location and characterisation of damage in large scale instability tests and impact events. Additional attention was given to the structural performance of composite materials under buckling conditions.

An investigation into the buckling behaviour of square composite plates was completed, including an initial imperfection study. Key findings are:-

- FE results were shown to be in good agreement with experimental results in the initial buckling stage.

- A trend for specimens with twisted initial imperfection geometries to produce increased buckling loads was identified, highlighting the need for the precise manufacture of structures susceptible to buckling.

A thorough investigation of wave propagation in composite materials was completed and the following conclusions were drawn:-

- The velocity of the s_0 mode exhibited a strong directional dependency resulting from the change in in-plane stiffness with propagation direction. However the same directional dependency was not observed for the a_0 mode velocity, its velocity depending more on geometry and flexural stiffness.

- Dispersion curves were theoretically calculated for the 0° and 90° material directions in which the s_0 mode was non-dispersive below ~400kHz and highly dispersive above. The a_0 mode was highly dispersive below ~100kHz and non-dispersive above.

- Dispersion curves were successfully measured using wavelet transforms and good agreement was shown with theoretically calculated curves.

- High attenuation rates of up to $100dB.min^{-1}$ were observed for composite materials and the principal plate wave modes displayed different rates of attenuation. Identifying the potential for erroneous characterisation of signals using the Measured Amplitude Ratio at distance from a source.

A study of signal characterisation was completed in which both frequency content and the MAR of signals was investigated. The MAR approach was further utilised to characterise damage during large scale buckling experiments. The main results were:-

- Geometry and sensor response were shown to have a dominant effect on the frequency content of recorded signals, making the use of frequency as a signal discriminator inappropriate.

- The Measured Amplitude Ratio (MAR) was found to be an excellent discriminator of in-plane and out-of-plane sources.

- The use of propagation-corrected amplitude ratios provided reliable characterisation of source orientation in large scale structures.

AE monitoring was conducted throughout a series of large scale instability experiments. Key findings from these experiments were:-

- Classical acoustic emission analysis techniques proved useful for damage detection, however they provided limited quantitative information regarding the structural integrity of specimens and the extent to which they can be misconstrued was demonstrated.

- The DeltaT location technique was successfully used for the first time in composite materials, resulting in up to 61% improvement in location error over commercial techniques, however some limitations were observed.

A series of controlled impact events were undertaken and AE data acquisition was conducted on four levels throughout. The following results were identified:-

- Good correlation was demonstrated between delamination size and recorded absolute energy values resulting for impact events of varying energy. Time driven data provided the best correlation with delamination size, however hit driven data has the potential to produce a similar level of correlation with adjustments made to the timing parameters.

- The stages of damage development throughout an impact event were identified using continuous wavestreaming data and discrete waveforms.

7.2 Recommendations for further work

This work has highlighted many areas of interest for future investigation, in particular the correlation between experimental and FEA buckling behaviour. The use of smart meshing techniques to produce FE models with representative imperfection geometries from the DIC measurements will provide more realistic FE results. Additionally correlation with experimental results can be improved in the postbuckling region through refined modelling of the specimen supports and the inclusion a damage material model to allow accurate prediction of failure beyond the buckling point.

A study of the optimum sensor positioning for DeltaT location will greatly reduce the number of erroneous signal locations observed. Additionally, the linking of hit\event data with the DeltaT locations would greatly increase the efficiency of analysis for the operator.

Further impact tests instrumented to allow the acquisition of impact force throughout the impact event would enable confirmation of the damage stages observed in the continuous wavestream data.

The use of embedded sensor technology will enable the continuous SHM of composite structures throughout their service life with minimal intrusion into their operation. This however requires investigation into the effects of such sensors on both the material properties and the AE propagation.

In-order to utilise the methods presented in this research for the SHM of composite structures, extensive testing is required to ensure the techniques can produce reliable and accurate detection, location and characterisation. Development of standard composite structures will allow comparison with traditional NDT techniques and the investigation of damage tolerance in composite structures. Implementation of such a SHM system for composite structures would require standardisation, including information on the probability of detection.

References

Abrate, S. 1991. Impact on Laminated Composite Materials. *Applied Mechanics Review.* 44(4), pp. 155-189.

Abrate, S. 1994. Impact on Laminated Composites: Recent Advances. *Applied Mechanics Review.* 47(11), pp. 517-544.

Airbus. 2007. *Airbus Military Website* [Online]. Available at: http://www.airbusmilitary.com/ [Accessed: 15/3/07].

ASTM. 1982. Standard Definitions of Terms Relating to Acoustic Emission. *American Society for Testing and Materials,* E610-82.

ASTM. 1985. Standard Guide for Mounting Piezoelectric Acoustic Emission Sensors. *American Society for Testing and Materials,* E650-85.

ASTM. 1986. Standard Method for Primary Calibration of Acoustic Emission Senseors. *American Society for Testing and Materials,* E1106-86.

ASTM. 1989. Standard Practice for Acoustic Emission Examination of Fibreglass Rienforced Plastic Resin (FRP) Tanks/Vessels. *American Society for Testing and Materials,* E1067-89.

ASTM. 1994. A standard guide for determining the reproducibility of acoustic emission sensor response. *American Society for Testing and Materials,* E976.

Autieri, M. R. V. 2007. *Acoustic emission characterisation of damage in CFRP composites*. University of Southampton.

Baxter, M. G. 2007. *Damage Assessment by Acoustic Emission (AE) During Landing Gear Fatigue Testing*. Cardiff University.

Black, S. 2004. *Composite Rib Structure for Airbus A380 Vertical tail* [Online]. Available at: http://www.compositesworld.com/hpc/issues/2004/March/412 [Accessed: 15/3/2007].

Boeing. 2007. *777 Family* [Online]. Available at: http://www.boeing.com/commercial/777family/background/back5.html [Accessed: 05/08/07].

Bohse, J. 2000. Acoustic Emission Characteristics of Micro-Failure Processes in Polymer Blends and Composites. *Composites Science and Technology,* 60, pp. 1213-1226.

Bohse, J., Mair, G. and Novak, P. 2006. Acoustic Emission Testing of High-Pressure Composite Cylinders. *Advanced Materials Research,* 13-14, pp. 267-272.

Broughton, W. R., Sims, G. D., and Lodeiro, M. J. 1998. Overview of DTI-Funded Programme on "Standardised Procedures for Ultrasonic Inspection of

Polymer Matrix Composites". *Insight: Non-Destructive Testing and Condition Monitoring,* 40(1), pp. 8-11.

Brush, D. O., and Almroth, B. O. 1975. *Buckling of Bars, Plates and Shells.* McGraw-Hill.

BSI 2000. *Plastics: Determination of Multi-Axial Impact Behaviour of Rigid Plastics, Instrumented Puncture testing.* British Standards Institute.

Bulson, P. S. 1970. *Stability of Flat Plates.* Chatto and Windus.

Cantwell, W. J., Morton, J. 1989. Comparison of Low and High Velocity Impact Response of CFRP. *Composites,* 20(6), pp. 545-551.

Cantwell, W. J., Morton, J. 1991. The Impact Resistance of Composite Materials - A Review. *Composites,* 22(5), pp. 347-362.

Carter, D. 2000. *Acoustic emission techniques for structural integrity monitoring of steel bridges.* Cardiff University.

Davies, G. A., Zhang, X. 1995. Impact Damage Prediction in Carbon Composite Structures. *International Journal of Impact Energy,* 16(1), pp. 149-170.

de Groot, P. J., Wijnen, P.A.M., Janssen, R.B. F. 1995. Real-Time Frequency Determination of Acoustic Emission for Different Fracture Mechanisms in Carbon/Epoxy Composites. *Composites Science and Technology,* 55, pp. 405-412.

Drouillard, T. F. 1996. A History of Acoustic Emission. *Journal of Acoustic Emission,* 14(1), pp. 1-34.

Dunegan, H. 1997. Global Flaw Location with One Transducer. *The DECI Report #9709,* http://www.deci.com/decireport.9.97.html.

Eurofighter. 2007. *Eurofighter-Typhoon Website* [Online]. Available at: http://www.eurofighter-typhoon.co.uk/Eurofighter/structure.html [Accessed: 15/3/07].

Gorman, M. R. 1990a. Plate wave acoustic emission. *Journal of Acoustic Society of America,* 90(1), pp. 358-364.

Gorman, M. R., and Prosser, W.H. 1991. AE source orientation by plate wave analysis. *Journal of Acoustic Emission,* 9(4), pp. 283-288.

Gorman, M. R., and Ziola, S.M. 1990b. Plate waves produced by transverse matrix cracking. *Ultrasonics,* 29, pp. 245-251.

Hensman, J. J. 2006. Unpublished research. *Private communication.*

Hill, R. a. E.-D., M. A. 1976. The effects of geometry on acoustic emission. In: *Fundamental aspects and applications of acoustic emission.* Chelsea College, London, 1976.

Holford, K. M. 2000. Acoustic Emission - Basic Principles and Future Directions. *Strain*, 36(2), pp. 51-54.

Holford, K. M., and Carter, D. C. 1999. Acoustic Emission Source Location. *Key Engineering Materials*, 167-168, pp. 162-171.

Hong, S., and, Liu, D. 1989. On the relationship between impact energy and delamination area. *Experimental Mechanics*, 29(2), pp. 115-120.

Hsu, N. N., and Breckenridge, F. R. 1981. CharacteriZation and Calibration of Acoustic Emission Sensors. *Materials Evaluation*, 39(1), pp. 60-68.

Jeong, H. 2001. Analysis of plate wave propagation in anisotropic laminates using a wavelet transform. *NDT&E International*, 34, pp. 185-190.

Jeong, H., and Jang, Y.-S. 2000. Wavelet analysis of plate wave propagation in composite laminates. *Composite Structures*, 49, pp. 443-450.

Johnson, M. 2003. Classification of AE transients based on numerical simulations of composite laminates. *NDT & E International*, 36, pp. 319-329.

Johnson, M., and, Gudmundson, P. 2001. Experimental and theoretical characterisation of acoustic emission transients in composite laminates. *Composites Science and Technology,* 61, pp. 1367-1378.

Kaiser, J. 1950. *Untersuchung uber das Aufreten von Gerauschen biem Zugversuch.* University of Munich (TUM).

Lanza di Scalea, F., and McNamara, J. 2004. Measuring High-Frequency Wave Propagation in Railroad Tracks by Joint Time-Frequency Analysis. *Journal of Sound and Vibration,* 273, pp. 637-651.

Lindahl, D., and, Knuuttila, M. 1999. Acoustic Emission Monitoring of the JAS 39 Gripen Combat Aircraft. In: *USAF Aircraft Structural Integrity Program (ASZP99) Conference.* San Antonio, 30th Nov - 2nd Dec 1999.

Liu, N., Zhu, Q.M. Wei, C.Y., Dykes, N.D., and Irving, P.E. 1999. Impact damage detection in carbon fibre composites using neural networks and acoustic emission. *Key Engineering Materials,* 167-168, pp. 43-54.

Loughlan, J. ed. 2000. *Buckling of Specially Orthotropic Laminates, Uni-Axial Compression - All Edges Simply Supported.* Composite Material Structures. Cranfield College of Aeronautics, Bedfordshire, UK, 24th - 28th July 2000.

Lowe, M. J. S., Neau, G., and Deschamps, M. 2004. Properties of Guided Waves in Composite Plates, and Implications for NDE. *Review of Quantitative Nondestructive Evaluation,* 23, pp. 214-221.

Maji, A. K., and Setpathi, D. 1995. Acoustic Emission Source Location Based on Lamb Waves. *Engineering Mechanics,* 1, pp. 597-600.

Miller, R. K., McIntire, P. 1987. Acoustic Emission Testing. *NDT Handbook Vol 5.* American Society for Non-destructive Testing.

Neau, G., Deschamps, M., and Lowe, M. J. S. 2001. Group Velocity of Lamb Waves in Anisotropic Plates: Comparison Between Theory and Experiments. *Review of Quantitative Nondestructive Evaluation,* 20, pp. 81-88.

Nielson, A. 1980. *Acoustic Emission Source Based on Pencil Lead Breaking.* Report 80-15, Danish Welding Institute.

Okafor, A. C., Otieno, A. W., Dutta, A. and Rao, V. S. 2001. Detection and Characterization of High-Velocity Impact Damage in Advanced Composite Plates Using Multi-Sensing Techniques. *Composite Structures,* 54, pp. 289-297.

Olson, K. 2004. *SAAB JAS-39 (A, B, C, D) "Gripen"* [Online]. Available at: http://www.robotechresearch.com/rpg/vehicles/EBSIS/Gripen/gripen.htm [Accessed: 15/3/07].

PAC 2003a. AEwin for DiSP User's Mannual. *Physical Acoustics Corporation, Princeton Junction, New Jersey, USA.*

PAC 2003b. WaveGen1410 Arbitrary Waveform Generator Subsystem User's Mannual Rev.2. *Physical Acoustics Corporation, Princeton Junction, New Jersey, USA.*

PAC 2004. PCI-2 Based AE System User's Manual. *Physical Acoustics Corporation, Princeton Junction, New Jersey, USA.*

PAC 2006a. AE Level II Course Notes. In: *Acoustic Emission Level II Training Course.* Princeton Junction, New Jersy, USA.

PAC. 2006b. *Physical Acoustics Website* [Online]. Available at: http://www.pacndt.com/index.aspx?go=products&focus=/sensors/wideband.ht m [Accessed: 21/2/06].

Pavlakovic, B., and Lowe, M. 2003. *DISPERSE User's Manual.* Non-destructive Testing Laboratory, Imperial College London.

Pollock, A. A. ed. 1986. *Classical Plate Theory in Practical AE Testing.* Progress in Acoustic Emission III, Proceedings of the Eighth International Acoustic Emission Symposium, The Japanese Society for Nondestructive Testing, 708-721.

Prosser, W. H. 1991. *The propagation Characteristics of the Plate Modes of Acoustic Emission Waves in Thin Aluminium Plates and Thin Graphite/Epoxy Composite Plates and Tubes.* John Hopkins University.

Prosser, W. H. 1996. Advanced AE Techniques in Composite Materials Research. *Journal of Acoustic Emission,* 14, pp. 1-11.

Prosser, W. H., and Seale, M. D. 1999. Time-frequency analysis of the dispersion of Lamb modes. *Journal of Acoustic Society of America,* 105(5), pp. 2669-2676.

Prosser, W. H., Jackson, K.E., Kellas, S., Smith, B.T, McKeon, J, and Friedman, A. 1995. Advanced, Waveform Based Acoustic Emission Detection of Matrix Cracking in Composites. *Materials Evaluation,* 53(9), pp. 1052-1058.

Prosser, W. H., Seale, M.D. & Smith, B.T. 1997. Aplication of the pseudo wigner-ville distribution to the measurement of the dispersion of Lamb modes in graphite/epoxy plates. *8th International Symposium on Nondestructive Characterisation of Materials.*

Pullin, R. 2001. *Structural Integrity Monitoring of Steel Bridges Using Acoustic Emission Techniques.* Cardiff University.

Pullin, R., Baxter, M. G., Eaton, M. J., Holford, K. M. and Evans, S. L. 2007a. Novel Acoustic Emission Source Location. In: *6th International Conference on Acoustic Emission.* Lake Tahoe-Nevada, 29th October-2nd November 2007.

Pullin, R., Holford, K. M., Evans, S. L. and Baxter, M. G. 2007b. Advanced Location and Characterisation of Damage in Complex Metallic Structures using Acoustic Emission. In: *13th International Conference on Experimental Mechanics.* Alexandroupolis- Greece, 1st-6th July 2007.

Pullin, R., Holford, K.M., and Baxter, M.G. 2005. Modal acoustic emission signals from artificail and fatigue crack sources in aerospace grade steel. *Key Engineering Materials,* 293-294, pp. 217-224.

Pullin, R., Theobald, P., Holford, K.M., and, Evans, S. 2006. Experimental validation of dispersion curves in plates for acoustic emission. *Advanced Materials Research,* 13-14, pp. 53-60.

Ramirez-Jimenez, C. R., Papadakis, N., Reynolds, N., Gan, T.H., Purnell, P., and, Pharaoh, M. 2004. Identification of failure modes in glass/polypropylene composites by means of the primary frequency content of the acoustic emission event. *Composites Science and Technology,* 64, pp. 1819-1827.

Rindorf, H. J. 1981. Acoustic emission source location in theory and in practice. *Bruel and Kjaer Technical Review,* 2, pp. 3-44.

Rose, J. L. 1999. *Ultrasonic Waves in Solid Media.* Cambridge University Press.

Rowland, C. 2004. Acoustic Emission Technique to Assist the Formula One Designer in Structural Design. In: *26th European Conference on Acoustic Emission Testing.* Berlin, Germany, 15-17th September.

Smith, R. A., Jones, L. D., Willsher, S. J., and Marriott, A. B. 1998a. Diffraction and Shadow Errors in the -6dB Defect Sizing of Delaminations in Composites. *Insight: Non-Destructive Testing and Condition Monitoring,* 40(1), pp. 44-49.

Smith, R. A., Jones, L. D., Zeqiri, B., and Hodnett, M. 1998b. Ultrasonic C-scan Standardisation for Fibre-Reinforced Polymer Composites - Minimising the Uncertainties in Attenuation Measurements. *Insight: Non-Destructive Testing and Condition Monitoring,* 40(1), pp. 34-43.

Smith, R. A., Zeqiri, B., Jones, L. D., and Hodnett, M. 1998c. Nonlinear Propagation in Water and its Effect on Ultrasonic C-scanning. *Insight: Non-Destructive Testing and Condition Monitoring,* 40(1), pp. 12-19.

Surgeon, M., and Wevers, M. 1999a. Modal analysis of acoustic emission signals from CFRP laminates. *NDT & E International,* 32, pp. 311-322.

Surgeon, M., and Wevers, M. 1999b. One Sensor Linear Location of Acoustic Emission Events Using Plate Wave Theories. *Materials Science and Engineering,* A625, pp. 254-261.

Suzuki, H., Takemoto, M., and Ono, K. 1996. The Fracture Dynamics in a Dispative Glass-Fibre/Epoxy Model Composite with AE Source Simulation. *Journal of Acoustic Emission,* 14(1), pp. 35-50.

Tensi, H. M. 1961. *Piezoelektrische Impulsmessung zur Untersuchung von Vorgangen in Metallen bei Phasenanderungen und bei mechanischer Beanspruchung.* University of Munich (TUM).

Theobald, P. D. 2004. Towards Traceable Calibration of Acoustic Emission Measurement Systems: Development of a Reference Source at the UK's National Physical Laboratory. In: *26th European Conference on Acoustic Emission Testing.* Berlin, Germany, 15 – 17 September.

Turvey, G. J., and Marshall, T. H. 1995. *Buckling and Postbuckling of Composite Plates.* 1st ed. Chapman and Hall.

Vallen. 2006. *Vallen Systems Website* [Online]. Available at: http://www.vallen.de/wavelet/index.html [Accessed: 05/05/06].

Vallen, H. 2002. AE Testing Fundamentals, Equipment, Applications. *The e-Journal of Nondestructive Testing,* 7(9).

Wang, L., and Yuan, F. G. 2007. Group Velocity and Characteristic Wave Curves of Lamb Waves in Composites: Modeling and Experiments. *Composites Science and Technology,* 67, pp. 1370-1384.

Zaal, K. 1998. *Buckling and Postbuckling of a Square Plate Subjected to Uniform Edge Loads - An Experimental Investigation.* Technion Israel Institute of Technology, Department of Aeronautical Enginnering.

Zeqiri, B., and Hodnett, M. 1998a. A Systematic Investigation of the Effects of Collimators on the Characteristics of Ultrasonic NDT Transducers. *Insight: Non-Destructive Testing and Condition Monitoring,* 40(1), pp. 28-33.

Zeqiri, B., Hodnett, M., Smith, R. A., and Scudder, L. P. 1998b. An Assessment of Pulse-Echo and Hydrophone Methods for Charactersing Ultrasonic NDT Transducers. *Insight: Non-Destructive Testing and Condition Monitoring,* 40(1), pp. 20-27.

Appendix

Appendix A – Thin plate buckling

The development of the governing differential equations for the behaviour of a thin plate are found from Classical plate theory by Bulson (1970)

For small deflections the following assumptions are required:-

1. Deflections are small.

2. The middle plane of the plate does not stretch during bending.

3. Plane sections rotate during bending to remain normal to the neutral surface and do not distort.

4. Loads are entirely resisted by bending and twisting of the plate elements and the effects of shear forces are neglected.

5. The thickness of the plate is small in comparison to other dimensions.

It is important to recognise the limitations of the assumption that deflections are small. However the analysis is greatly simplified by the assumption of small deflections and can still provide the correct linear elastic buckling load for a problem. It is also possible to differentiate between undeformed stable and unstable conditions. However it is not possible to determine the equilibrium paths after bifurcation.

Considering equilibrium of the element in Figure A1 leads to the following:

Resolving forces in the z direction

$$\frac{\partial Q_x}{\partial x}\,dxdy + \frac{\partial Q_y}{\partial y}\,dydx = 0 \qquad\qquad \textbf{(A1)}$$

where Q_x and Q_y are shear forces per unit width.

Similarly resolving in the x and y directions assuming $sin\dfrac{\partial w}{\partial x} = \dfrac{\partial w}{\partial x}$ gives:

$$Q_x \frac{\partial w}{\partial x} - p_x = 0 \qquad \text{(A2)}$$

and

$$Q_y \frac{\partial w}{\partial y} - p_y = 0 \text{ respectively.} \qquad \text{(A3)}$$
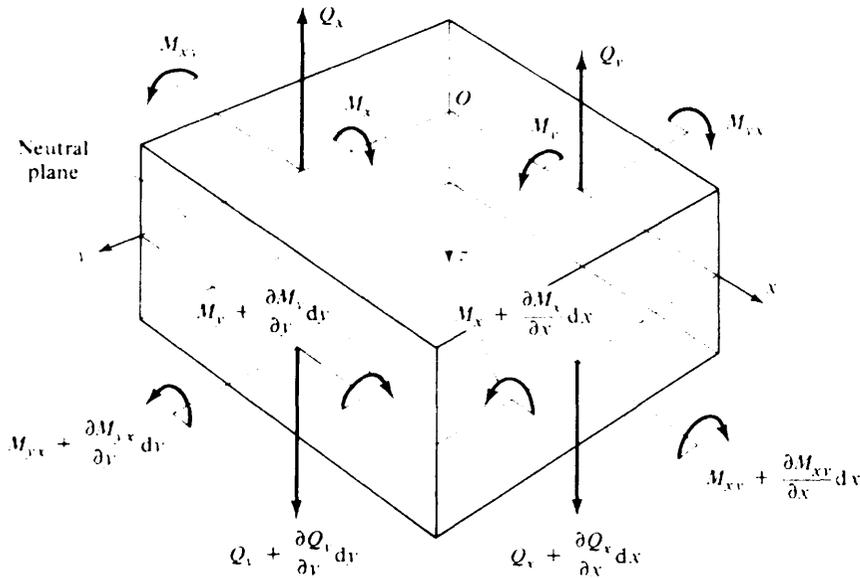
Figure A0.1- Plate element in bending and shear

Taking moments about the *x* axis,

$$-\left(M_{xy} + \frac{\partial M_{xy}}{\partial x} dx \right) dy + M_{xy} dy + M_y dx$$

$$-\left(M_y + \frac{\partial M_y}{\partial y} dy \right) dx + \left(Q_y + \frac{\partial Q_y}{\partial y} dy \right) dxdy = 0 \qquad \text{(A4)}$$

which can be simplified to,

$$\frac{\partial M_{xy}}{\partial x} + \frac{\partial M_y}{\partial y} - Q_y = 0 \qquad \text{(A5)}$$

when derivatives of Q_y are neglected.

Similarly taking moments about the y axis,

$$-\left(M_{yx}+\frac{\partial M_{yx}}{\partial y}\,dy\right)dx+M_{yx}dx$$

$$-\left(M_x+\frac{\partial M_x}{\partial x}\,dx\right)dy+\left(Q_x+\frac{\partial Q_x}{\partial x}\,dx\right)dydx=0 \qquad \textbf{(A6)}$$

Which neglecting derivatives of Q_x simplifies to

$$\frac{\partial M_{yx}}{\partial y}+\frac{\partial M_x}{\partial x}-Q_x=0 \qquad \textbf{(A7)}$$

Combining equations (A5) and (A7) after differentiating with respect to y and x respectively gives

$$\frac{\partial^2 M_x}{\partial x^2}+2\frac{\partial^2 M_{xy}}{\partial x\partial y}+\frac{\partial^2 M_y}{\partial y^2}=\frac{\partial Q_x}{\partial x}+\frac{\partial Q_y}{\partial y} \qquad \textbf{(A8)}$$

The sum of the shear forces is equal to a distributed lateral load of intensity q (which in this case will be 0) such that

$$-q=\frac{\partial Q_x}{\partial x}+\frac{\partial Q_y}{\partial y} \qquad \textbf{(A9)}$$

Combining (8) and (9) gives

$$\frac{\partial^2 M_x}{\partial x^2}+2\frac{\partial^2 M_{xy}}{\partial x\partial y}+\frac{\partial^2 M_y}{\partial y^2}=-q \qquad \textbf{(A10)}$$

The internal forces, M_x, M_y and M_{xy}, representing the stress resultants over the plate thickness and per unit width of the plate are defined as

$$M_x = -\int_{h/2}^{h/2} \sigma_x z.dz \ , \quad M_y = -\int_{h/2}^{h/2} \sigma_y z.dz \ , \quad M_{xy} = -\int_{h/2}^{h/2} \tau_{xy} z.dz \quad \textbf{(A11)}$$

where

$$\sigma_x = E_x \varepsilon_x + E_{xy} \varepsilon_y \ , \quad \sigma_y = E_{xy} \varepsilon_x + E_y \varepsilon_y \ , \quad \tau_{xy} = G_{xt} \gamma_{xy} \quad \textbf{(A12)}$$

in which

$$\varepsilon_x = -\frac{\partial^2 w}{\partial x^2}.z \ , \quad \varepsilon_y = -\frac{\partial^2 w}{\partial y^2}.z \ , \quad \gamma_{xy} = -\frac{\partial^2 w}{\partial x \partial y}.z \quad \textbf{(A13)}$$

and

$$E_x = E_y = \frac{E}{(1-v^2)} \ , \quad E_{xy} = vE_x \ , \quad G_{xy} = \frac{\frac{1}{2}E}{(1+v)} \quad \textbf{(A14)}$$

Combining equations (A11), (A12), (A13) and (A14) leads to

$$M_x = D\left(\frac{\partial^2 w}{\partial x^2} + v\frac{\partial^2 w}{\partial y^2}\right)$$

$$M_y = D\left(\frac{\partial^2 w}{\partial y^2} + v\frac{\partial^2 w}{\partial x^2}\right)$$

$$M_{xy} = M_{yx} = D(1-v)\frac{\partial^2 w}{\partial x \partial y} \quad \textbf{(A15)}$$

where

$$D = \frac{Eh^3}{12(1-v^2)} \quad \text{(bending stiffness parameter)} \quad \textbf{(A16)}$$

Substituting into equation (A15) into equation (A10) gives

$$\frac{\partial^4 w}{\partial x^4} + 2\frac{\partial^4 w}{\partial x^2 \partial y^2} + \frac{\partial^4 w}{\partial y^4} = \frac{q}{D} \quad \textbf{(A17)}$$

Finally the edge loads acting on the middle plane, as shown in Figure A2, must be considered.
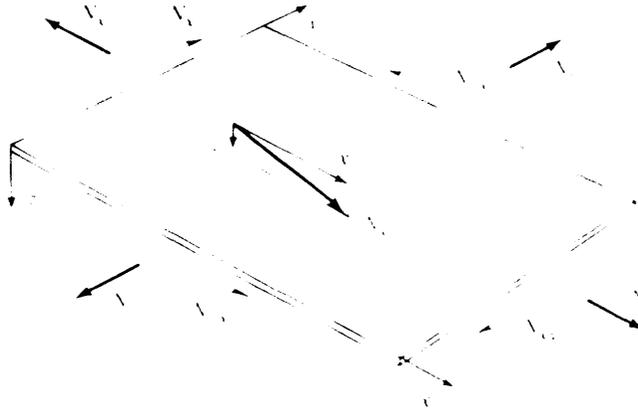
Figure A2 - Edge forces on a rectangular plate

By resolving in the x direction,

$$\left(N_x + \frac{\partial N_x}{\partial x} dx\right) dy - N_x dy + \left(N_{yx} + \frac{\partial N_{yx}}{\partial y} dy\right) dx - N_{yx} dx = 0 \qquad \textbf{(A18)}$$

which reduces to (ignoring second order terms),

$$\frac{\partial N_x}{\partial x} + \frac{\partial N_{yx}}{\partial y} = 0 \qquad \textbf{(A19)}$$

Similarly, for y direction forces,

$$\frac{\partial N_y}{\partial y} + \frac{\partial N_{xy}}{\partial x} = 0 \qquad \textbf{(A20)}$$

Equations (A2) and (A3) now become

$$\frac{\partial N_x}{\partial x} + \frac{\partial N_{xy}}{\partial y} - Q_x \frac{\partial w}{\partial x} + p_x = 0 \qquad \textbf{(A21)}$$

and

$$\frac{\partial N_{xy}}{\partial x} + \frac{\partial N_y}{\partial y} - Q_y \frac{\partial w}{\partial y} + p_y = 0 \qquad \textbf{(A22)}$$

In order to introduce the forces from the x and y directions into equation (A17) it is necessary to resolve them in the z direction, in which case the small angle the middle surface makes with the horizontal must be taken into account. Again assuming $\sin\left(\dfrac{\partial w}{\partial x}\right) = \dfrac{\partial w}{\partial x}$ and referring to Figure 16 the projection of N_x on the z axis is

$$\left(N_x + \frac{\partial N_x}{\partial x}dx\right)\left(\frac{\partial w}{\partial x} + \frac{\partial^2 w}{\partial x^2}dx\right)dy - N_x \frac{\partial w}{\partial x}dy \qquad \textbf{(A23)}$$

which reduces to

$$N_x \frac{\partial^2 w}{\partial x^2}dxdy \qquad \textbf{(A24)}$$

Similarly the projections of N_y, N_{xy}, and N_{yx} are

$$N_y \frac{\partial^2 w}{\partial y^2}dxdy, \qquad N_{xy}\frac{\partial^2 w}{\partial x\partial y}dxdy \quad \text{and} \quad N_{yx}\frac{\partial^2 w}{\partial x\partial y}dxdy. \qquad \textbf{(A25)}$$

Adding the components from (A25) and noting $N_{xy} = N_{yx}$ the resulting force in the z direction is

$$\left(N_x \frac{\partial^2 w}{\partial x^2} + 2N_{xy}\frac{\partial^2 w}{\partial x\partial y} + N_y \frac{\partial^2 w}{\partial y^2}\right)dxdy \qquad \textbf{(A26)}$$

Adding equation (A26) to equation (A17) gives

$$\frac{\partial^4 w}{\partial x^4} + 2\frac{\partial^4 w}{\partial x^2\partial y^2} + \frac{\partial^4 w}{\partial y^4} = \frac{1}{D}\left(q + N_x \frac{\partial^2 w}{\partial x^2} + 2N_{xy}\frac{\partial^2 w}{\partial x\partial y} + N_y \frac{\partial^2 w}{\partial y^2}\right) \qquad \textbf{(A27)}$$

Which is the governing equation for thin plate elastic buckling problems involving only small deflections.

Appendix B – Laminate Constitutive Equation

The following derivation of the laminate constitutive equation is taken from Barbero (1998).

Classical Thin Plate Theory gives

$$\varepsilon_x = \frac{du_0}{dx} - z\frac{d^2 w_0}{dx^2}$$

$$\varepsilon_y = \frac{dv_0}{dy} - z\frac{d^2 w_0}{dy^2}$$

$$\varepsilon_{xy} = \frac{du_0}{dx} + \frac{dv_0}{dy} - z\frac{2d^2 w_0}{dxdy} \qquad\qquad \textbf{(B1)}$$

Where u_0 is the laminate mid-plane displacement in the x-direction

v_0 is the laminate mid-plane displacement in the y-direction

w_0 is the laminate mid-plane displacement in the y-direction

z is the distance from the mid-plane varying from $-t/2$ to $t/2$

t is the laminate thickness

As seen in figure B1.
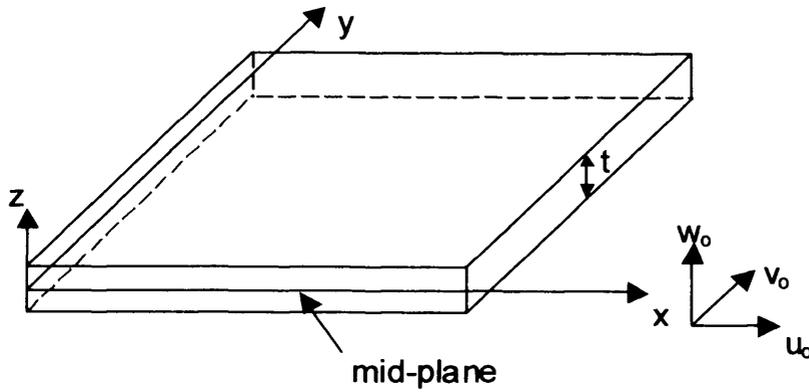
Figure B1 – Laminate Notation

The following abbreviated matrix notation can be used, for convenience, to replace the above equations (B1):

ϵ^0 (mid-plane in-plane strains)

$$\begin{pmatrix} \varepsilon_x^0 \\ \varepsilon_y^0 \\ \varepsilon_{xy}^0 \end{pmatrix} = \begin{pmatrix} \dfrac{du_0}{dx} \\ \dfrac{dv_0}{dy} \\ \dfrac{du_0}{dx} + \dfrac{dv_0}{dy} \end{pmatrix}$$

(B2)

k (mid-plane curvatures)

$$\begin{pmatrix} k_x \\ k_y \\ k_{xy} \end{pmatrix} = \begin{pmatrix} \dfrac{d^2 w_0}{dx^2} \\ \dfrac{d^2 w_0}{dy^2} \\ \dfrac{2d^2 w_0}{dxdy} \end{pmatrix}$$

(B3)

The total strain is therefore

$$\varepsilon = \varepsilon^0 - zk \tag{B4}$$

or

$$\begin{pmatrix} \varepsilon_x \\ \varepsilon_y \\ \varepsilon_{xy} \end{pmatrix} = \begin{pmatrix} \varepsilon_x^0 \\ \varepsilon_y^0 \\ \varepsilon_{xy}^0 \end{pmatrix} - z \begin{pmatrix} k_x \\ k_y \\ k_{xy} \end{pmatrix} \tag{B5}$$

Figure B2 shows the resultant laminate forces.
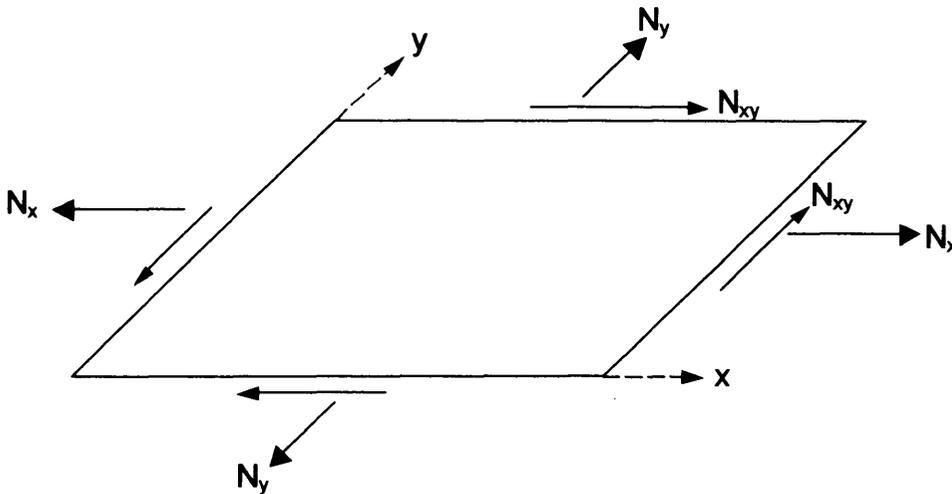
Figure B2 – Resultant Laminate Forces

where

N_x is the resultant in-plane force intensity on the x-direction per unit width

of the laminate cross section

N_y is the resultant in-plane force intensity in the y-direction per unit width

of the laminate cross section

N_{xy} is the resultant in-plane shear force intensity in the x (y) – axis per unit width of the laminate cross section

The resultant laminate moments are shown in Figure B3.
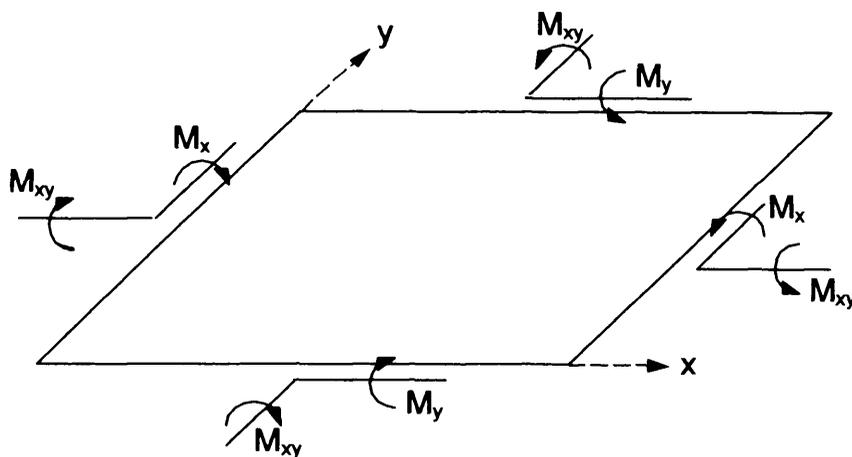
Figure B3 – Resultant Laminate Moments

where

M_x is the resultant in-plane moment intensity about the y-direction per unit width of the laminate cross section

M_y is the resultant in-plane moment intensity about the x-direction per unit width of the laminate cross section

M_{xy} is the resultant in-plane twisting moment intensity about the x (y) – axis per unit width of the laminate cross section

By definition, the resultant force and the moment intensities are given by the following expressions:

$$N_x = \int_{-\frac{t}{2}}^{\frac{t}{2}} \sigma_x dz \qquad\qquad N_y = \int_{-\frac{t}{2}}^{\frac{t}{2}} \sigma_y dz \qquad\qquad N_{xy} = \int_{-\frac{t}{2}}^{\frac{t}{2}} \sigma_{xy} dz$$

$$M_x = -\int_{-\frac{t}{2}}^{\frac{t}{2}} \sigma_x z dz \qquad M_y = \int_{-\frac{t}{2}}^{\frac{t}{2}} \sigma_y z dz \qquad M_{xy} = \int_{-\frac{t}{2}}^{\frac{t}{2}} \sigma_{xy} z dz \quad \textbf{(B6)}$$

In the case when the loading axis coincide with the material axis Hooke's Law may be written as

$$\begin{Bmatrix} \sigma_1 \\ \sigma_2 \\ \sigma_{12} \end{Bmatrix} = \begin{bmatrix} Q_{11} & Q_{12} & Q_{16} \\ Q_{12} & Q_{22} & Q_{26} \\ Q_{16} & Q_{26} & Q_{66} \end{bmatrix} \begin{Bmatrix} \varepsilon_1 \\ \varepsilon_2 \\ \varepsilon_{12} \end{Bmatrix} \qquad\qquad \textbf{(B7)}$$

where

σ_1 = Stress in material direction 1

σ_2 = Stress in material direction 2

σ_{12} = Shear stress in material 1-2 plane

And

Q_{ij} =material stiffness constants

However in most cases the load axis and material axis do no coincide, so the stresses are related thus

$$\begin{Bmatrix} \sigma_1 \\ \sigma_2 \\ \sigma_{12} \end{Bmatrix} = \begin{bmatrix} \cos^2\theta & \sin^2\theta & 2\sin\theta\cos\theta \\ \sin^2\theta & \cos^2\theta & -2\sin\theta\cos\theta \\ -\sin\theta\cos\theta & \sin\theta\cos\theta & \cos^2\theta - \sin^2\theta \end{bmatrix} \begin{Bmatrix} \sigma_x \\ \sigma_y \\ \sigma_{xy} \end{Bmatrix}$$ **(B8)**

Combining equations (B7) and (B8) an expression for stress in terms of strain

is obtained

$$\begin{Bmatrix} \sigma_x \\ \sigma_y \\ \sigma_{xy} \end{Bmatrix} = [T]^{-1}[Q][T]\begin{Bmatrix} \varepsilon_x \\ \varepsilon_y \\ \varepsilon_{xy} \end{Bmatrix}$$ **(B9)**

This can be written as

$$\begin{pmatrix} \sigma_x \\ \sigma_y \\ \sigma_{xy} \end{pmatrix} = \begin{pmatrix} \overline{Q_{11}} & \overline{Q_{12}} & \overline{Q_{16}} \\ \overline{Q_{12}} & \overline{Q_{22}} & \overline{Q_{26}} \\ \overline{Q_{16}} & \overline{Q_{26}} & \overline{Q_{66}} \end{pmatrix} \begin{pmatrix} \varepsilon_x \\ \varepsilon_y \\ \varepsilon_{xy} \end{pmatrix}$$ **(B10)**

Where

$$\overline{Q_{11}} = m^4 Q_{11} + m^2 n^2 (2Q_{12} + 4Q_{66}) + n^4 Q_{22}$$

$$\overline{Q_{12}} = m^2 n^2 (Q_{11} + Q_{22} - 4Q_{66}) + (m^4 + n^4)Q_{22}$$

$$\overline{Q_{16}} = m^3 n (Q_{11} - Q_{12} - 2Q_{66}) + mn^3 (Q_{12} - Q_{22} + Q_{66})$$

$$\overline{Q_{21}} = Q_{12}$$

$$\overline{Q_{22}} = n^4 Q_{11} + m^2 n^2 (2Q_{12} + 4Q_{66}) + m^4 Q_{22}$$

$$\overline{Q_{26}} = mn^3 (Q_{11} - Q_{12} - 2Q_{66}) + m^3 n (Q_{12} - Q_{22} + Q_{66})$$

$$\overline{Q_{61}} = Q_{16}$$

$$\overline{Q_{62}} = Q_{26}$$

$$\overline{Q_{66}} = m^2 n^2 (Q_{11} + Q_{22} - 2Q_{12} - 2Q_{66}) + (m^4 + n^4)Q_{66} \qquad \textbf{(B11)}$$

and

$$m = \cos\theta$$

$$n = \sin\theta \qquad \textbf{(B12)}$$

Substituting for ε_x, ε_y and ε_{xy} in terms of mid-plane strains and curvatures from equation (B5) gives

$$\begin{pmatrix} \sigma_x \\ \sigma_y \\ \sigma_{xy} \end{pmatrix} = \begin{pmatrix} \overline{Q_{11}} & \overline{Q_{12}} & \overline{Q_{16}} \\ \overline{Q_{12}} & \overline{Q_{22}} & \overline{Q_{26}} \\ \overline{Q_{16}} & \overline{Q_{26}} & \overline{Q_{66}} \end{pmatrix} \begin{pmatrix} \varepsilon_x^0 \\ \varepsilon_y^0 \\ \varepsilon_{xy}^0 \end{pmatrix} - \begin{pmatrix} \overline{Q_{11}} & \overline{Q_{12}} & \overline{Q_{16}} \\ \overline{Q_{12}} & \overline{Q_{22}} & \overline{Q_{26}} \\ \overline{Q_{16}} & \overline{Q_{26}} & \overline{Q_{66}} \end{pmatrix} z \begin{pmatrix} k_x \\ k_y \\ k_{xy} \end{pmatrix} \qquad \textbf{(B13)}$$

This equation relates the mid-plane strains and curvatures to the stresses for a single ply.

Consider now a laminate made from N plies with the bottom ply being ply 1 and the top ply being ply N, shown in figure B4.
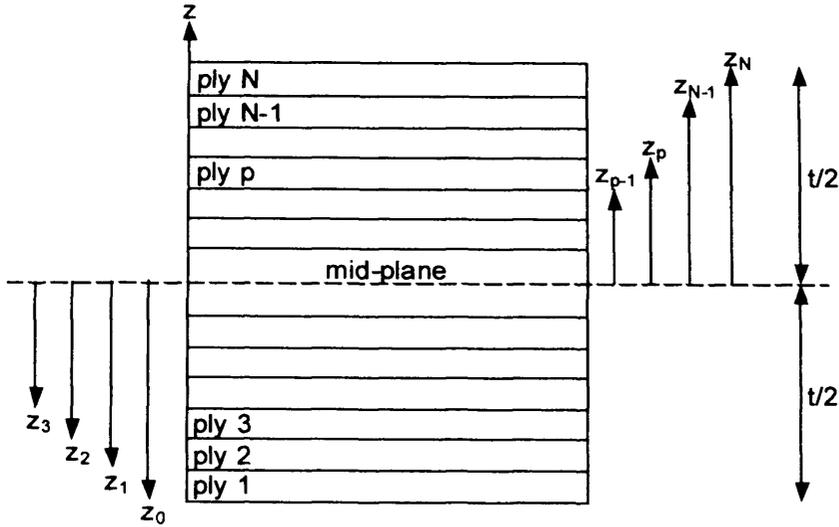
Figure B4 – Laminate Consisting of N Plies

The resultant force and moment intensities, relative to the mid-plane, per unit width of the ply cross section, acting on an individual ply, say Ply p are

$$(N_x)_p = \int_{z_{p-1}}^{z_p} \sigma_x dz \qquad (N_y)_p = \int_{z_{p-1}}^{z_p} \sigma_y dz \qquad (N_{xy})_p = \int_{z_{p-1}}^{z_p} \sigma_{xy} dz$$

$$(M_x)_p = -\int_{z_{p-1}}^{z_p} \sigma_x z dz \qquad (M_y)_p = -\int_{z_{p-1}}^{z_p} \sigma_y z dz \qquad (M_{xy})_p = -\int_{z_{p-1}}^{z_p} \sigma_{xy} z dz \qquad \textbf{(B14)}$$

Substituting for σ_x in the above equation for $(N_x)_p$ gives

$$(N_x)_p = \int_{z_{p-1}}^{z_p} \left\{ \begin{pmatrix} \overline{Q_{11}} & \overline{Q_{12}} & \overline{Q_{16}} \end{pmatrix}_p \begin{pmatrix} \varepsilon_x^0 \\ \varepsilon_y^0 \\ \varepsilon_{xy}^0 \end{pmatrix} - \begin{pmatrix} \overline{Q_{11}} & \overline{Q_{12}} & \overline{Q_{16}} \end{pmatrix}_p z \begin{pmatrix} k_x \\ k_y \\ k_{xy} \end{pmatrix} \right\} dz \qquad \textbf{(B15)}$$

Now ε_x, ε_y, ε_{xy}, k_x, k_y, k_{xy} and the Q are all independent of the variable z and can therefore come out of the integral term. So the above expression for $(N_x)_p$ becomes

$$(N_x)_p = \int_{z_{p-1}}^{z_p} 1\,dz \overline{(\overline{Q_{11}}\quad \overline{Q_{12}}\quad \overline{Q_{16}})}_p \begin{pmatrix} \varepsilon_x^0 \\ \varepsilon_y^0 \\ \varepsilon_{xy}^0 \end{pmatrix} - \int_{z_{p-1}}^{z_p} z\,dz \overline{(\overline{Q_{11}}\quad \overline{Q_{12}}\quad \overline{Q_{16}})}_p \begin{pmatrix} \varepsilon_x^0 \\ \varepsilon_y^0 \\ \varepsilon_{xy}^0 \end{pmatrix} \quad \textbf{(B16)}$$

Evaluating the integral gives

$$(N_x)_p = (z_p - z_{p-1})(\overline{Q_{11}}\quad \overline{Q_{12}}\quad \overline{Q_{16}})_p \begin{pmatrix} \varepsilon_x^0 \\ \varepsilon_y^0 \\ \varepsilon_{xy}^0 \end{pmatrix}$$

$$-\frac{1}{2}(z_p^2 - z_{p-1}^2)(\overline{Q_{11}}\quad \overline{Q_{12}}\quad \overline{Q_{16}})_p \begin{pmatrix} \varepsilon_x^0 \\ \varepsilon_y^0 \\ \varepsilon_{xy}^0 \end{pmatrix} \qquad \textbf{(B17)}$$

Expressions for $(N_y)_p$ and $(N_{xy})_p$ are obtained in a similar manner, leading to

$$(N_y)_p = (z_p - z_{p-1})(\overline{Q_{12}}\quad \overline{Q_{22}}\quad \overline{Q_{26}})_p \begin{pmatrix} \varepsilon_x^0 \\ \varepsilon_y^0 \\ \varepsilon_{xy}^0 \end{pmatrix}$$

$$-\frac{1}{2}(z_p^2 - z_{p-1}^2)(\overline{Q_{12}}\quad \overline{Q_{22}}\quad \overline{Q_{26}})_p \begin{pmatrix} k_x \\ k_y \\ k_{xy} \end{pmatrix} \qquad \textbf{(B18)}$$

$$(N_{xy})_p = (z_p - z_{p-1})(\overline{Q_{16}}\quad \overline{Q_{26}}\quad \overline{Q_{66}})_p \begin{pmatrix} \varepsilon_x^0 \\ \varepsilon_y^0 \\ \varepsilon_{xy}^0 \end{pmatrix}$$

$$-\frac{1}{2}(z_p^2 - z_{p-1}^2)(\overline{Q_{16}}\quad \overline{Q_{26}}\quad \overline{Q_{66}})_p \begin{pmatrix} k_x \\ k_y \\ k_{xy} \end{pmatrix} \qquad \textbf{(B19)}$$

Alternatively equations (B17), (B18) and (B19) can be written in matrix form as

$$
\begin{pmatrix} N_x \\ N_y \\ N_{xy} \end{pmatrix} = (z_p - z_{p-1}) \begin{pmatrix} \overline{Q}_{11} & \overline{Q}_{12} & \overline{Q}_{16} \\ \overline{Q}_{12} & \overline{Q}_{22} & \overline{Q}_{26} \\ \overline{Q}_{16} & \overline{Q}_{26} & \overline{Q}_{66} \end{pmatrix}_p \begin{pmatrix} \varepsilon_x^0 \\ \varepsilon_y^0 \\ \varepsilon_{xy}^0 \end{pmatrix}
$$

$$
-\frac{1}{2}(z_p^2 - z_{p-1}^2) \begin{pmatrix} \overline{Q}_{11} & \overline{Q}_{12} & \overline{Q}_{16} \\ \overline{Q}_{12} & \overline{Q}_{22} & \overline{Q}_{26} \\ \overline{Q}_{16} & \overline{Q}_{26} & \overline{Q}_{66} \end{pmatrix}_p \begin{pmatrix} k_x \\ k_y \\ k_{xy} \end{pmatrix} \qquad \textbf{(B20)}
$$

The total resultant force intensities on the laminate are given by the summation of the force intensities of the individual plies

$$
\begin{pmatrix} N_x \\ N_y \\ N_{xy} \end{pmatrix} = \sum_{p=1}^{N}(z_p - z_{p-1}) \begin{pmatrix} \overline{Q}_{11} & \overline{Q}_{12} & \overline{Q}_{16} \\ \overline{Q}_{12} & \overline{Q}_{22} & \overline{Q}_{26} \\ \overline{Q}_{16} & \overline{Q}_{26} & \overline{Q}_{66} \end{pmatrix}_p \begin{pmatrix} \varepsilon_x^0 \\ \varepsilon_y^0 \\ \varepsilon_{xy}^0 \end{pmatrix}
$$

$$
+\sum_{p=1}^{N}\left(-\frac{1}{2}\right)(z_p^2 - z_{p-1}^2) \begin{pmatrix} \overline{Q}_{11} & \overline{Q}_{12} & \overline{Q}_{16} \\ \overline{Q}_{12} & \overline{Q}_{22} & \overline{Q}_{26} \\ \overline{Q}_{16} & \overline{Q}_{26} & \overline{Q}_{66} \end{pmatrix}_p \begin{pmatrix} k_x \\ k_y \\ k_{xy} \end{pmatrix} \qquad \textbf{(B21)}
$$

The mid-plane strains and curvatures are common to all plies and can therefore come out of the summation terms. The Q terms vary from ply to ply depending on the ply angle and ply material and therefore cannot come out of the summation terms. So equation (B21) becomes

$$
\begin{pmatrix} N_x \\ N_y \\ N_{xy} \end{pmatrix} = \left\{ \sum_{p=1}^{N}(z_p - z_{p-1}) \begin{pmatrix} \overline{Q}_{11} & \overline{Q}_{12} & \overline{Q}_{16} \\ \overline{Q}_{12} & \overline{Q}_{22} & \overline{Q}_{26} \\ \overline{Q}_{16} & \overline{Q}_{26} & \overline{Q}_{66} \end{pmatrix}_p \right\} \begin{pmatrix} \varepsilon_x^0 \\ \varepsilon_y^0 \\ \varepsilon_{xy}^0 \end{pmatrix}
$$

$$+ \left\{ \sum_{p=1}^{N} \left(-\frac{1}{2} \right) \left(z_p^2 - z_{p-1}^2 \right) \begin{pmatrix} \overline{Q_{11}} & \overline{Q_{12}} & \overline{Q_{16}} \\ \overline{Q_{12}} & \overline{Q_{22}} & \overline{Q_{26}} \\ \overline{Q_{16}} & \overline{Q_{26}} & \overline{Q_{66}} \end{pmatrix}_p \right\} \begin{pmatrix} k_x \\ k_y \\ k_{xy} \end{pmatrix} \quad \textbf{(B22)}$$

Equation (B22) is usually written in a condensed matrix form using abbreviations for terms in the curly bracket

$$\begin{pmatrix} N_x \\ N_y \\ N_{xy} \end{pmatrix} = \begin{pmatrix} A_{11} & A_{12} & A_{16} \\ A_{12} & A_{22} & A_{26} \\ A_{16} & A_{26} & A_{66} \end{pmatrix} \begin{pmatrix} \varepsilon_x^0 \\ \varepsilon_y^0 \\ \varepsilon_{xy}^0 \end{pmatrix} + \begin{pmatrix} B_{11} & B_{12} & B_{16} \\ B_{12} & B_{22} & B_{26} \\ B_{16} & B_{26} & B_{66} \end{pmatrix} \begin{pmatrix} k_x \\ k_y \\ k_{xy} \end{pmatrix} \quad \textbf{(B23)}$$

Where

$$A_{ij} = \sum_{p=1}^{N} \left(z_p - z_{p-1} \right) \left(\overline{Q_{ij}} \right)_p$$

$$B_{ij} = \sum_{p=1}^{N} \left(-\frac{1}{2} \right) \left(z_p^2 - z_{p-1}^2 \right) \left(\overline{Q_{ij}} \right)_p \quad \textbf{(B24)}$$

The resultant moment intensities can be treated in a similar manner to achieve the following expression

$$\begin{pmatrix} M_x \\ M_y \\ M_{xy} \end{pmatrix} = \begin{pmatrix} B_{11} & B_{12} & B_{16} \\ B_{12} & B_{22} & B_{26} \\ B_{16} & B_{26} & B_{66} \end{pmatrix} \begin{pmatrix} \varepsilon_x^0 \\ \varepsilon_y^0 \\ \varepsilon_{xy}^0 \end{pmatrix} + \begin{pmatrix} D_{11} & D_{12} & D_{16} \\ D_{12} & D_{22} & D_{26} \\ D_{16} & D_{26} & D_{66} \end{pmatrix} \begin{pmatrix} k_x \\ k_y \\ k_{xy} \end{pmatrix} \quad \textbf{(B25)}$$

Where

$$B_{ij} = \sum_{p=1}^{N} \left(-\frac{1}{2} \right) \left(z_p^2 - z_{p-1}^2 \right) \left(\overline{Q_{ij}} \right)_p$$

$$D_{ij} = \sum_{p=1}^{N} \left(\frac{1}{3}\right)\left(z_p^3 - z_{p-1}^3\right)\overline{(Q_{ij})}_p \tag{B26}$$

Therefore the laminate constitutive equation giving the relationship between the loads and the deformations combines equations (B23) and (B25), and is written in matrix form as

$$\begin{pmatrix} N_x \\ N_y \\ N_{xy} \\ M_x \\ M_y \\ M_{xy} \end{pmatrix} = \begin{pmatrix} A_{11} & A_{12} & A_{16} & B_{11} & B_{12} & B_{16} \\ A_{12} & A_{22} & A_{26} & B_{12} & B_{22} & B_{26} \\ A_{16} & A_{26} & A_{66} & B_{16} & B_{26} & B_{66} \\ B_{11} & B_{12} & B_{16} & D_{11} & D_{12} & D_{16} \\ B_{12} & B_{22} & B_{26} & D_{12} & D_{22} & D_{26} \\ B_{16} & B_{26} & B_{66} & D_{16} & D_{26} & D_{66} \end{pmatrix} \begin{pmatrix} \varepsilon_y^0 \\ \varepsilon_y^0 \\ \varepsilon_{xy}^0 \\ k_x \\ k_y \\ k_{xy} \end{pmatrix} \tag{B27}$$

Or in condensed matrix form

$$\begin{pmatrix} N \\ M \end{pmatrix} = \begin{pmatrix} A & B \\ B & D \end{pmatrix} \begin{pmatrix} \varepsilon^0 \\ k \end{pmatrix} \tag{B28}$$

Note that the individual (3x3) A, B, and D matrices are symmetric about their leading diagonals and the whole (6x6) matrix is symmetric about its leading diagonal.

By inverting the above matrix, the laminate constitutive equation can be expressed in terms of a deformation-load relationship

$$\begin{pmatrix} \varepsilon_y^0 \\ \varepsilon_y^0 \\ \varepsilon_{xy}^0 \\ k_x \\ k_y \\ k_{xy} \end{pmatrix} = \begin{pmatrix} a_{11} & a_{12} & a_{16} & b_{11} & b_{12} & b_{16} \\ a_{12} & a_{22} & a_{26} & b_{12} & b_{22} & b_{26} \\ a_{16} & a_{26} & a_{66} & b_{16} & b_{26} & b_{66} \\ b_{11} & b_{12} & b_{16} & d_{11} & d_{12} & d_{16} \\ b_{12} & b_{22} & b_{26} & d_{12} & d_{22} & d_{26} \\ b_{16} & b_{26} & b_{66} & d_{16} & d_{26} & d_{66} \end{pmatrix} \begin{pmatrix} N_x \\ N_y \\ N_{xy} \\ M_x \\ M_y \\ M_{xy} \end{pmatrix} \tag{B29}$$

Or in condensed matrix form

$$\begin{pmatrix} \varepsilon^0 \\ k \end{pmatrix} = \begin{pmatrix} a & b \\ b & d \end{pmatrix} \begin{pmatrix} N \\ M \end{pmatrix}$$

(B30)

References

Barbero, E. J., "Introduction to Composite Materials Design", Taylor and Francis Inc., 1998.

Appendix C – Composite Buckling theory

The governing equation for buckling of a thin composite plate is formed by substituting the constitutive equation into the general equation for elastic buckling of a homogeneous thin plate. The following is covered in (Turvey 1995)

Starting with the equations of resolved forces in the x and y directions

$$\frac{\partial N_x}{\partial x} + \frac{\partial N_{xy}}{\partial y} - Q_x \frac{\partial w}{\partial x} + p_x = 0 \quad \text{and} \quad \frac{\partial N_{xy}}{\partial x} + \frac{\partial N_y}{\partial y} - Q_y \frac{\partial w}{\partial y} + p_y \quad \text{(C1)}$$

the internal moment forces representing the stress resultants over the plate thickness per unit width

$$M_x = D\left(\frac{\partial^2 w}{\partial x^2} + v\frac{\partial^2 w}{\partial y^2}\right)$$

$$M_y = D\left(\frac{\partial^2 w}{\partial y^2} + v\frac{\partial^2 w}{\partial x^2}\right)$$

$$M_{xy} = M_{yx} = D(1-v)\frac{\partial^2 w}{\partial x \partial y} \quad \text{(C2)}$$

And the governing equation for homogeneous thin plate elastic buckling

$$\frac{\partial^4 w}{\partial x^4} + 2\frac{\partial^4 w}{\partial x^2 \partial y^2} + \frac{\partial^4 w}{\partial y^4} = \frac{1}{D}\left(q + N_x \frac{\partial^2 w}{\partial x^2} + 2N_{xy} \frac{\partial^2 w}{\partial x \partial y} + N_y \frac{\partial^2 w}{\partial y^2}\right) \quad \text{(C3)}$$

Assuming that the transverse shear forces Q_x and Q_y as well as the slopes $\frac{\partial w}{\partial x}$ in Equations C1 are typical small and back substituting Equations C2 into Equation C3 gives

$$\frac{\partial N_x}{\partial x} + \frac{\partial N_{xy}}{\partial y} + p_x = 0$$

$$\frac{\partial N_{xy}}{\partial x} + \frac{\partial N_y}{\partial y} + p_y = 0$$

$$\frac{\partial^2 M_x}{\partial x^2} + 2\frac{\partial^2 M_{xy}}{\partial x \partial y} + \frac{\partial^2 M_y}{\partial y^2} + N_x \frac{\partial^2 w}{\partial x^2} + 2N_{xy}\frac{\partial^2 w}{\partial x \partial y} + N_y \frac{\partial^2 w}{\partial y^2} + q = 0 \textbf{ (C4)}$$

Substitution of the composite constitutive equation (B29) into equations C4 yields

$$\begin{bmatrix} L_{11} & L_{12} & L_{13} \\ L_{21} & L_{22} & L_{23} \\ L_{31} & L_{32} & (L_{33} - F) \end{bmatrix} \begin{Bmatrix} u \\ v \\ w \end{Bmatrix} = \begin{Bmatrix} 0 \\ 0 \\ 0 \end{Bmatrix} \tag{C5}$$

where L_{ij} are differential operators representing the plate stiffness,

$$L_{11} = A_{11} \frac{\partial^2}{\partial x^2} + 2A_{16} \frac{\partial^2}{\partial x \partial y} + A_{66} \frac{\partial^2}{\partial y^2}$$

$$L_{22} = A_{22} \frac{\partial^2}{\partial y^2} + 2A_{26} \frac{\partial^2}{\partial x \partial y} + A_{66} \frac{\partial^2}{\partial x^2}$$

$$L_{33} = D_{11} \frac{\partial^4}{\partial x^4} + 4D_{16} \frac{\partial^4}{\partial x^3 \partial y} + 2(D_{12} + 2D_{66}) \frac{\partial^4}{\partial x^2 \partial y^2}$$

$$+ 4D_{26} \frac{\partial^4}{\partial x \partial y^3} + D_{22} \frac{\partial^4}{\partial y^4}$$

$$L_{12} = L_{21} = A_{16} \frac{\partial^2}{\partial x^2} + (A_{12} + A_{66})\frac{\partial^2}{\partial x \partial y} + A_{26} \frac{\partial^2}{\partial y^2}$$

$$L_{13} = L_{31} = -B_{11} \frac{\partial^3}{\partial x^3} - 3B_{16} \frac{\partial^3}{\partial x^2 \partial y} - (B_{12} + 2B_{66})\frac{\partial^3}{\partial x \partial y^2} - B_{26} \frac{\partial^3}{\partial y^3}$$

$$L_{23} = L_{32} = -B_{16} \frac{\partial^3}{\partial x^3} - (B_{12} + 2B_{66})\frac{\partial^3}{\partial x^2 \partial y} - 3B_{26} \frac{\partial^3}{\partial x \partial y^2} - B_{22} \frac{\partial^3}{\partial y^3} \textbf{ (C6)}$$

and *F* is a differential operator representing the in-plane loading,

$$F = N_x \frac{\partial^2}{\partial x^2} + 2N_{xy} \frac{\partial^2}{\partial x \partial y} + N_y \frac{\partial^2}{\partial y^2} \qquad \text{(C7)}$$

Equations (C5) are an eighth order set of partial differential equations. It is the coupling between bending and stretching, due to the asymmetric lamination, that causes the order to go from four, in the case of a homogeneous material, to eight.

For symmetrically laminated plates $B_{ij} = 0$ and the L_{13} and L_{23} operators in equations C6 are seen to vanish, uncoupling the in-plane part of the problem from the transverse part in equation C5. The in-plane part of the problem results in $u = v = 0$ in the buckled configuration, whereas the transverse displacements are governed by

$$D_{11} \frac{\partial^4 w}{\partial x^4} + 4D_{16} \frac{\partial^4 w}{\partial x^3 \partial y} + 2(D_{12} + 2D_{66}) \frac{\partial^4 w}{\partial x^2 \partial y^2} + 4D_{26} \frac{\partial^4 w}{\partial x \partial y^3} + D_{22} \frac{\partial^4 w}{\partial y^4}$$

$$= N_x \frac{\partial^2 w}{\partial x^2} + 2N_{xy} \frac{\partial^2 w}{\partial x \partial y} + N_y \frac{\partial^2 w}{\partial y^2} \qquad \text{(C8)}$$

Equation C8 is the governing differential equation for a symmetric laminate, in the absence of any transverse loading and subject to in-plane force intensities N_x, N_y and N_{xy}.

Appendix D – Specimen manufacture

Three different carbon fibre / epoxy Uni-directional pre-preg materials with similar properties were used to manufacture specimens for the research. Table D1, Table D2 and Table D3 detail the material properties for 914C-T300H-5-34%RW (Hexcel), HTM45/HS-135-34%RW (Advanced Composite Group) and MTM28-1/HS-135-34%RW (Advanced Composite Group) materials respectively. The cure cycles used for the three materials are shown in Table D4, Table D5 and Table D6 for 914C-T300H-5-34%RW (Hexcel), HTM45/HS-135-34%RW (Advanced Composite Group) and MTM28-1/HS-135-34%RW (Advanced Composite Group) materials respectively.

The processes utilised in the manufacture for each type of specimen are detailed below:

Tensile specimens – 120mm x 240mm plates with a 1.075mm nominal thickness were layed-up by hand from Advanced Composite Group's HTM45/HS-135-34%RW material and cured in a horpress (Table D2). Specimens were cut to size using a water cooled, diamond tipped cutting wheel and edges were finished with emery cloth. Additionally aluminium end tabs were bonded on with epoxy resin.

Beam buckling specimens – 120mm x 240mm plates with a 2.15mm nominal thickness were layed-up up by hand from Advanced Composite Group's HTM45/HS-135-34%RW material and cured in a horpress (Table D2). Specimens were cut to size using a water cooled, diamond tipped cutting wheel and edges were finished with emery cloth.

Large Plate – Used for the propagation investigation the large plate had dimensions of 500mm x 1400mm with a nominal thickness of 2.15mm. Hand layed-up from Advanced Composite Group's MTM28-1/HS-135-34%RW the plate was clamped between two aluminium plates, to ensure flatness, and vacuum bagged before curing in accordance with the cycle presented in Table D6.

Large scale buckling specimens – All the specimens were hand lay-ed up, resulting in a nominal thickness of 2mm for Hexcel's 914C-T300H-5-34%RW

material and a 2.15mm nominal thickness for Advanced Composite Group's HTM45/HS-135-34%RW and MTM28-1/HS-135-34%RW materials. The specimens manufactured from Hexcel's 914C-T300H-5-34%RW and Advanced Composite Group's HTM45/HS-135-34%RW materials were cured in an autoclave in accordance with their individual curing cycles (Table D4 and Table D5). The specimens manufactured from Advanced Composite Group's MTM28-1/HS-135-34%RW material were clamped between aluminium plates, to ensure flatness, and vacuum bagged before curing in accordance with the cycle presented in Table D6.

Material properties

Table D1 - 914C-T300H-5-34%RW (Hexcel) material properties

E_{11} (MPa)	E_{22} (MPa)	G_{12} (MPa)	v_{12}	v_{21}	Ply thickness (mm)
132800	8870	3000	0.3	0.02	0.125

Table D2 - HTM45/HS-135-34%RW (Advanced Composite Group) material properties

E_{11} (MPa)	E_{22} (MPa)	G_{12} (MPa)	v_{12}	v_{21}	Ply thickness (mm)
124400	8900	4430	0.33	0.02	0.135

Table D3 - MTM28-1/HS-135-34%RW (Advanced Composite Group) material properties

E_{11} (MPa)	E_{22} (MPa)	G_{12} (MPa)	v_{12}	v_{21}	Ply thickness (mm)
118100	8400	4060	0.34	0.02	0.135

Curing cycles

Table D4 - 914C-T300H-5-34%RW (Hexcel) cure cycle

Pressure	Ramp Rate	Cure Temperature and Time	Ramp Rate	Post-Cure Temperature and Time	Cooling
7bar	2°C/min	175°C / 60min	2°C/min	190°C / 240min	n/a

Table D5 - HTM45/HS-135-34%RW (Advanced Composite Group) cure cycle

Pressure	Ramp Rate	Cure Temperature / Time	Ramp Rate	Post-Cure Temperature and Time	Cooling
6bar	3°C/min	175°C / 120min	n/a	None Required	n/a

Table D6 – MTM28-1/HS-135-34%RW (Advanced Composite Group) cure cycle

Pressure	Ramp Rate	Cure Temperature and Time	Ramp Rate	Post-Cure Temperature and Time	Cooling
0.98bar	3°C/min	120°C / 60min	n/a	None Required	3°C/min